An Experimental and Theoretical Study of Active Flow Control

Thesis by
Damian George Hirsch

In Partial Fulfillment of the Requirements
for the Degree of
Doctor of Philosophy

CALIFORNIA INSTITUTE OF TECHNOLOGY
Pasadena, California

2017
(Defended May 30, 2017)

I have been impressed with the urgency of doing. Knowing is not enough; we must apply. Being willing is not enough; we must do.

— Leonardo da Vinci

Abstract

The accelerating growth of environmental awareness has not stopped at the aerospace industry. The need for greener and more efficient airplanes threatens to outpace the flow of new technology. This has ignited development in several fields, one of which is active flow control (AFC). Active flow control has quickly proven its tremendous potential for real applications. Even though the roots of this technology date back a century, we still lack fundamental understanding. This thesis combines both modern and traditional approaches to lay out a new foundation for future research.

The thesis first focuses on the rising stars of active flow control: the so-called fluidic oscillators or sweeping jet actuators. These devices consist of simple, rigid internal geometries that create a sweeping output jet motion. The fluid dynamic interactions with the internal geometry are studied in detail using high-speed Schlieren imaging. Additionally, the influence of adjacent sweeping jets is investigated. It is revealed that the internal driving mechanism is far stronger than the fluid dynamic interactions at the outlet, resulting in a completely independent jet behavior.

Next, a high-lift airfoil design is combined with active flow control, and an extensive wind tunnel study is carried out. It is shown that for the given wing design active flow control leads to much higher lift benefits when applied to the trailing edge. Applied to the leading edge active flow control disrupts the vortex lift of the high-lift airfoil, resulting in a deleterious lift effect; however, it shows potential for pitch moment control. This project also underlines the advantages of jet-like active flow control over steady blowing actuation at limited available mass flow rates.

The momentum input coefficient as an important parameter in active flow control is discussed in detail, identifying common misconceptions and difficulties that hinder its proper calculation. An innovative, much simpler approach is introduced. This allows a detailed study of the underlying physics, unveiling unknown limitations of active flow control. The approach is then used as a model to derive the novel concept of thermal active flow control. Experimental studies, including a wind tunnel test campaign, are performed to confirm the viability of the concept for practical applications.

The new calculation method of the input momentum coefficient emphasizes its weakness as a similarity parameter in active flow control studies. The extended mass flow coefficient is introduced as a

new parameter. It is shown that it can overcome the deficiencies of the input momentum coefficient without suffering other disadvantages. Its further investigation leads to a deeper understanding of active flow control, which is supported by PIV experiments. The main findings of this investigation divide active flow control into three different "states": boundary layer thickening, separation control, and supercirculation.

Acknowledgements

First of all, I would like to express my gratitude to my advisor, Professor Mory Gharib, for giving me the opportunity to work on an exciting and fulfilling research project. I would like to thank him for his inspiring guidance, invaluable support, comprehensive understanding, and great trust over the last few years. I am also grateful to the members of my thesis committee, namely Professors Hans Hornung, Joseph Shepherd, and Tim Colonius, for the encouraging discussions and resourcefulness advice. A special thanks goes to my last committee member Professor Israel Wygnanski for his tremendous mentorship and collaboration.

I thank the entire Gharib research group members for all the scientific and non-scientific discussions: Chris Roh, Morgane Grivel, Cong Wang, Nathan Martin, Jinglin Huang, Cecilia Huertas-Cerdeira, Chris Dougherty, Marcel Veismann, Sean Mendoza, Emilio Graff, David Jeon, Francisco Pereira, David Kremmers, and Masoud Beizaie. In particular, I want to thank Stephanie Rider and Manuel Bedrossian for their help throughout my PhD and for enduring me in the same office for such a long time. I would also like to thank Martha Salcedo, Peggy Blue, Christine Ramirez, and Dimity Nelson for their priceless administrative support. A big thanks goes to Ali Kiani, Matavos Zargarian, and Joe Haggerty for creating usable parts out of my impossible drawings. I am also grateful to all visiting students who worked with me in the Lucas Wind Tunnel: Yann Glauser, Damien Fulliquet, Justin Mercier, Mark Vujicic, Albéric Gros, Nicolas Bosson, and Raimondo Pictet.

I would like to acknowledge Boeing for their financial support of my research throughout my entire time at Caltech, as well as Northrop Grumman for their funding during my second and third year.

Among my friends, I would like to especially thank Phillipe Tosi, Nicholas Burali, Kazuki Maeda, Georgios Rigas, Oliver Schmidt, Christian Kettenbeil, Thibaud Talon, Ryan McMullen, Rich Kennedy, Ian Brownstein, and Silvio Tödtli for their morale support and for keeping me a responsible human being these last few years.

Last, but not least, I am incredibly grateful to my family for their constant support and encouragement throughout my life.

Table of Contents

List of Illustrations

List of Tables

Nomenclature

Acronyms

AFC	Active Flow Control
AFRL	Air Force Research Laboratory
AHLLE	Advanced High Lift Leading Edge
BL	Boundary Layer
CFD	Computational Fluid Dynamics
DDPIV	Defocusing Digital Particle Image Velocimetry
ERA	Environmentally Responsible Aviation
FFT	Fast Fourier Transform
LAVLET	Laminar Airfoil Virtual Leading Edge Technology
LE	Leading Edge
MAC	Mean Aerodynamic Chord
MOLEC	Multi-Objective Leading Edge Concept
NACA	National Advisory Committee for Aeronautics
NASA	National Aeronautics and Space Administration
OML	Outer Mold Line
PIV	Particle Image Velocimetry
TAFC	Thermal Active Flow Control
TE	Trailing Edge
ZNMF	Zero-Net-Mass-Flux

Greek Symbols

α	Angle of attack	[°]
δ_F	Flap deflection angle	[°]
ε	Relative error	[-]
η	System efficiency	[-]
γ	Heat capacity ratio	[-]
Λ	Leading edge sweep	[°]
ν	Kinematic viscosity	$[m^2/s]$
ω	Angular frequency	$[rad/s]$
ϕ	Phase angle	[°]
Π	Power	[W]
ρ	Density	$[kg/m^3]$
θ	Jet deflection angle	[°]

Roman Symbols

A	Area	$[m^2]$
a	Speed of sound	$[m/s]$
AF	Axial force measure by balance	[N]
AR	Aspect ratio	[-]
b	Wing span	[m]
c	Wing chord	[m]
C_μ	Coefficient of momentum input	[-]

C_Π	Power coefficient	[-]
C_D	Drag coefficient	[-]
C_d	Discharge coefficient	[-]
c_f	Relative flap chord	[-]
C_J	Total momentum coefficient	[-]
C_L	Lift coefficient	[-]
C_m	Pitching moment coefficient	[-]
C_p	Pressure coefficient	[-]
c_p	Heat capacity at constant pressure	$[\mathrm{J}/(\mathrm{kg}\cdot\mathrm{K})]$
C_Q	Flow input coefficient	[-]
c_v	Heat capacity at constant volume	$[\mathrm{J}/(\mathrm{kg}\cdot\mathrm{K})]$
d	Actuator spacing	[m]
F	Force	[N]
f	Frequency	[Hz]
h	Specific enthalpy	$[\mathrm{J}/\mathrm{kg}]$
L	Lift force	[N]
M	Mach number	[-]
$\dot{m}$	Mass flow rate	$[\mathrm{kg}/\mathrm{s}]$
n	Number of actuators	[-]
p	Pressure	[Pa]
PM	Pitch moment measure by balance	$[\mathrm{N}\cdot\mathrm{m}]$

$\dot{Q}$	Volume flow rate	$[m^3/s]$
R	Specific gas constant	$[J/(kg \cdot K)]$
Re_c	Chord Reynolds number	[-]
S	Planform area	$[m^2]$
SF	Side force measure by balance	[N]
T	Temperature	[K]
u	Fluid velocity in the x or freestream direction	[m/s]
v	Fluid velocity in the y-direction	[m/s]
x	Coordinate or distance	[m]
y	Coordinate or distance	[m]

Superscripts

$'$	Normalized

Subscripts

0	Zero mass flow rate input
∞	Freestream
ac	Aerdodynamic center
act	Actuator
atm	Atmospheric
bal	Balance
c	Calibration value
calc	Calculated value

cold	Value at the lower temperature	
crit	Critical value	
e	Effective value	
hot	Value at the higher temperature	
i	Induced	
jet	Value at the jet exit of an AFC device	
m	Measured value	
min	Minimum required value	
net	Velocity-corrected value	
ref	Reference	
s	Static	
sup	Supply	
t	Total	

Other Symbols

$\mathcal{A}$	Actuator area ratio	[-]
$\mathcal{M}$	Extended mass flow coefficient	[-]
$\mathcal{P}$	Pressure ratio	[-]
$\mathcal{S}$	Spacing ratio	[-]
$\mathcal{T}$	Temperature ratio	[-]
$\mathcal{V}$	Velocity magnitude divided by freestream velocity	[-]

Important Definitions

$C_\mu = \frac{\dot{m} u_{\text{jet}}}{\frac{1}{2}\rho_\infty u_\infty^2 S}$

$C_\Pi = \frac{\frac{\gamma}{\gamma-1} p_\infty \dot{m}\left[\left(\frac{p_{\text{sup}}}{p_\infty}\right)^{\frac{\gamma-1}{\gamma}} - 1\right]}{\frac{1}{2}\rho_\infty^2 u_\infty^3 S}$

$C_D = \frac{\text{SF}\sin\alpha - \text{AF}\cos\alpha}{\frac{1}{2}\rho_\infty u_\infty^2 S} = \frac{D}{\frac{1}{2}\rho_\infty u_\infty^2 S}$

$C_L = \frac{\text{SF}\cos\alpha + \text{AF}\sin\alpha}{\frac{1}{2}\rho_\infty u_\infty^2 S} = \frac{L}{\frac{1}{2}\rho_\infty u_\infty^2 S}$

$C_m = \frac{\text{PM} + L(x_{\text{ac}} - x_{\text{bal}})}{\frac{1}{2}\rho_\infty u_\infty^2 S c}$

$C_p = \frac{p - p_\infty}{\frac{1}{2}\rho_\infty u_\infty^2}$

$C_Q = \frac{\dot{m}}{\rho_\infty u_\infty S} = \frac{\rho_s \dot{Q}}{\rho_\infty u_\infty S}$

$\text{Re}_c = \frac{u_\infty c}{\nu}$

Chapter 1

Introduction

1.1 Motivation

Commercial airlines spend billions of dollars on jet fuel every year. If one can offer new ways to save millions of gallons of jet fuel, the airlines' attention is practically guaranteed. Tighter environmental regulations and higher fuel prices will further accelerate this process in the near future. Yet even the coming generation of new commercial airplane models will, within a few years, inevitably struggle to meet these criteria. The accelerating growth of environmental awareness threatens to outpace the flow of new technology. In response, NASA's Environmentally Responsible Aviation (ERA) Project aimed to increase the technology advancement's pace and set it to fast-track the introduction of several "green" developments that have been tested since 2009 (Norris, 2014).

As one of many other technologies developed and tested under the ERA Project, one particular research objective focused on the size of the vertical tail. As of today, its size is determined by the eventuality of losing an engine during takeoff or landing while being exposed to strong crosswinds. Yet the vertical tail is a large surface that is barely used during nominal flight conditions. On top of that, manufacturing constraints still lead to a family of airplanes sharing the same vertical tail, sized for the shortest body and forcing the longer planes to carry unnecessarily large tails (Seele, Graff, Lin, et al., 2013). This is well visualized in Fig. 1.1, where the Airbus 320 family shows

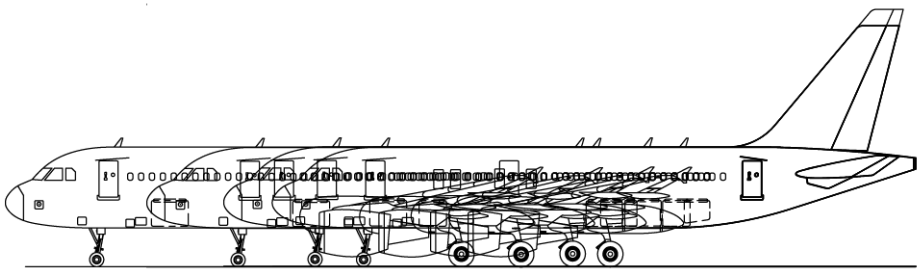

Figure 1.1: Airbus A320 family with only small differences between tail sizes.

a "clipped span" tail on the longest fuselage as the only difference between its family members. During the NASA ERA program it was shown that active flow control (AFC) has the potential to

enhance the performance of a vertical tail to reduce its size in future designs. A smaller vertical tail would lead to a reduction of weight and drag of an airplane, which can improve fuel efficiency and aerodynamic performance. The ERA project also demonstrated that the concept does not only work in a laboratory environment, such as the Lucas Wind Tunnel at Caltech, but also at full-scale at the NASA Ames wind tunnel. Most recently in 2015, Boeing took it a step further and tested the technology on a real, full-sized Boeing 757 airplane called the ecoDemonstrator 757. It was concluded that this technology has the potential to make a big impact on commercial airplanes, and that there could be a significant change to airplane design.

Extensive research on this topic was performed during the early discoveries of active flow control in the 1950s and early 1960s, when the technology was tested on wings of military aircraft, mainly to reduce their takeoff and landing speed. Examples are the Grumman F9F-4 Panther Jet, the Lockheed T2V-1 Seastar U.S. Navy Jet Trainer, and the U.S.A.F. Lockheed F104 Starfighter among many others. Most of the current understanding and theory of AFC is from that time. However, the traditional theory presents itself with a variety of inconsistencies and unsolved questions, such as "[...] a favorable Reynolds number effect [...] was experienced during the flight tests" (Attinello, 1961). This phenomenon could also be observed during the ERA project comparing data between the Lucas Wind Tunnel model and the NASA Ames model. Conclusively, there is still a significant lack of fundamental fluid dynamic understanding that hasn't been resolved for over half a century.

1.2 Study Objectives

While the technique of active flow control has been proven to work well, the lack of understanding impedes the next step of an application to an airplane. The unanswered question about the interaction of AFC devices with the boundary layer and the freestream is one of the core problems. Even though there is a large desire to get quantitative data to understand the interplay between these vastly different flow states, the practical reality looks quite different. The large fundamental differences between the boundary layer (small-scale, transient and spatial changes, low subsonic velocity, incompressible regime), the freestream (large-scale, stationary and spatially constant, mediocre subsonic velocity, incompressible regime), and the jets itself (small-scale, transient and spatial changes, sonic velocity, compressible regime) make any attempt of a quantitative experiment extremely challenging. The second main issue is that the currently used similarity parameters, such as the input momentum

coefficient C_μ, are not able to cover the whole spectrum of active flow control and fail in certain situations. If these two major issues can be resolved, the industry would be more willing to adapt current airplane models with AFC. The long-term goal should be to increase the fundamental understanding to a point where a new generation of airplanes would be built from scratch, incorporating AFC at the start of the design process. This would certainly trigger another revolution in the aircraft industry in terms of effectiveness and possibilities. Airplanes would most likely look completely different compared to today's design, which has not evolved much over the last couple of decades.

Several specific objectives have been formulated as a guidance for this thesis and are described as follows:

(a) Gain insight into the internal flow structure of sweeping jets, one of the currently most popular active flow control devices. Investigate the interaction between adjacent sweeping jets with the absence of freestream flow.

(b) Combine the effects of a high-lift airfoil and active flow control. Identify the importance of the flow control location along the chord of a wing, and compare different actuation devices.

(c) Elucidate the problems with the input momentum coefficient C_μ, simplify its calculation, and understand its underlying mechanisms.

(d) Investigate the concept of thermal active flow control (TAFC).

(e) Derive a new similarity parameter to replace the flawed momentum input coefficient C_μ.

1.3 Scope of Study

Flow control is the attempt to alter a flow field, i.e. around a wing, in a favorable way. Many definitions exist; a short and concise one was given by Flatt, 1961: "Boundary layer control includes any mechanism or process through which the boundary layer of a fluid flow is caused to behave differently than it normally would [...]." Most definitions take it a step further and differentiate between active and passive flow control. Passive flow control incorporates techniques that do not require any auxiliary power and no control loop. Passive techniques include geometric shaping, wing morphing, the use of vortex generators, the placement of grooves and trip-wires on an airfoil

surface, and many more. Active flow control require energy expenditure. From a control standpoint of view active flow control can be divided further into open-loop and closed-loop active flow control. Closed-loop active flow control defines all techniques that make use of a control loop to manipulate the flow. As a consequence, these techniques usually require a sensor to gather information of the current flow state as well as a processing unit to calculate the next manipulation steps. Open-loop active flow control can be defined as techniques that do not make us of a control loop. Thus, they do not require sensing and processing of data. However, they usually can be turned on, off, and often have intermediate settings. Examples of open-loop active flow control methods include steady suction or blowing, the use of synthetic jets, and of course unsteady suction and blowing. The techniques described in this thesis are part of the latter with some use of steady blowing as comparison. All used techniques are part of the open-loop active flow control subgroup but will further be referred to as active flow control or AFC.

The modern use of flow control was certainly pioneered by Ludwig Prandtl during his Nobel-prize-worthy presentation at the Third Congress of Mathematicians at Heidelberg, Germany in 1904. His paper “Über Flüssigkeitsbewegung bei sehr kleiner Reibung”, which translates to "On Fluid Motion at Very Small Friction”, introduced the boundary-layer theory in just eight pages (as required for acceptance by the congress). By applying his theory to flow separation, he was able to clearly explain the concept of stall for the first time. This opened the way for understanding the motion of real fluids and fueled the research in aerodynamics for the next three decades. Stimulated by political tension during the years 1940 to 1970, flow control research accelerated even more. Flow control played a major role to achieve the military needs for the development of fast, highly maneuverable, efficient aircraft, missiles, ships, submarines, and torpedoes. Natural laminar flow, laminar flow control, and polymer drag reduction were discovered during this era. The years 1970-1990 were dominated by the energy crises and brought a noticeable shift of interest from the military to the civilian sector. The appearance of the first inexpensive computers supported the development of more complex flow control devices such as the reduction of skin-friction drag in turbulent boundary layers. Since the 1990s more complex control devices have been pursued (Gad-el-Hak, 2007).

In the subgroup of AFC devices various actuation methods have been investigated (Cattafesta III and Sheplak, 2011) and have shown different degrees of effectiveness. Fluidic oscillators, also called

sweeping jet actuators, proved themselves as an attractive option because they have no moving parts and are believed to be highly efficient AFC devices. However, they do require a steady supply of compressed air, and in this regard, they resemble steady blowing although they use less air. A schematic drawing of a typical modern actuator used as an AFC device is shown in Section 1.3.

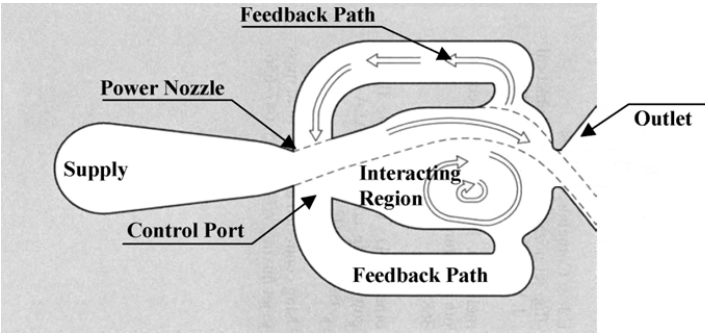

Figure 1.2: Conceptual design of a sweeping jet actuator.[1]

Sweeping jet actuators were used in aeronautical experiments for the purpose of delaying separation on airfoils (Seele, Tewes, et al., 2009; Phillips, Woszidlo, and Wygnanski, 2010; Desalvo, E. Whalen, and Glezer, 2012) and on wings (Tewes, Taubert, and Wygnanski, 2010). The usefulness of these devices prompted the need to understand their working principle (Vatsa, Koklu, and Wygnanski, 2012) and their effect on boundary layers that are about to separate from the surface. In the interim one may improve the efficiency of these actuators for a specific application by using dimensional analysis that enables one to determine the leading parameters controlling the process (Woszidlo and Wygnanski, 2011; Woszidlo, Nawroth, et al., 2010). They also found application as drag-reduction devices on trucks (Seifert, Stalnov, et al., 2008) and as active combustion control devices (Guyot, Paschereit, and Raghu, 2009).

Next, Rathay et al., 2014 applied synthetic jet actuators, also called zero-net-mass-flux (ZNMF) actuators, to a typical vertical stabilizer of a commercial airplane model. Their actuators were placed in a linear array next to the hinge of the rudder for the purpose of attaching the flow over the rudder surface at large rudder deflection angles, thereby increasing its effectiveness. Seele, Graff, Gharib, et al., 2012 and Seele, Graff, Lin, et al., 2013 discuss recent significant findings of active flow control on a typical vertical stabilizer. The former paper focuses on sweeping jet actuation that was applied directly to the rudder, while the later evaluates the effects of actuation from the trailing

[1] Raman and Raghu, 2004.

edge of the main element. Both show that sweeping jets can provide significant improvements in lift and drag with minimal input. Smaller jets spaced farther apart make better use of air unless extreme gains are required. This so called "air fence effect" or "fluidic fence effect" at high actuator spacings could prove useful to increase the sweep angle of wings while delaying tip stall at low speed (Graff and Wygnanski, 2014). The scope of this study is to build onto these recent results employed on the vertical tail and to improve their predictability.

1.4 Thesis Outline

Chapter 2 investigates the working principle of sweeping jet actuators via high-speed Schlieren imaging. It discusses their unique characteristics and tries to connect the findings to the promising performance as an AFC device.

Chapter 3 discusses the interaction between two adjacent sweeping jet actuators without an overlaying crossflow. The jet positions are tracked visually and then analyzed using FFT. The spacing between the actuators was varied and two different input pressures were compared. The tracked data also allowed to plot the mass distribution of a sweeping jet actuator for these two different cases.

Chapter 4 explores the use of active flow control on a high-lift airfoil design. The interaction between the virtual leading edge of the airfoil and the active flow control is exemplified. Additionally, this chapter analyzes the effects of different chordwise flow control locations and possible combinatory effects. It also compares the traditional steady blowing actuation with the more modern use of sweeping jets. This comparison eventually leads to the discussions in Chapter 7.

Chapter 5 is dedicated to the importance of the momentum input coefficient C_μ in the area of active flow control. Furthermore, the chapter tries to properly define C_μ and point out common problems and misconceptions. A simplification of its calculation is introduced, which will be used as a baseline in the following chapters.

Chapter 6 introduces Thermal Active Flow Control (TAFC). The chapter derives the concept mathematically, and proceeds with a bench-top experiment to get a practical proof of concept. In a last step, TAFC is applied to a vertical tail model and its effects on lift performance are studied.

Chapter 7 debunks the weaknesses of C_μ and proceeds with the identification of key variables that drive AFC. These key variables are then combined into a new similarity coefficient, which is then

applied to different AFC actuation devices to show the new parameter's superior characteristics. Lastly, the parameter is extended to account for TAFC.

Chapter 8 summarizes the results of this thesis. Their implications on future work and possible applications are discussed.

Chapter 2

An Investigation of Sweeping Jets

Sweeping jets play an important role in recent AFC research as they seem to be more efficient in terms of lift generation compared to other actuator types. They were born as fluidic analogs of electronics components at the Harry Diamond Labs in the 1950's. As such they found few applications, though the thrust reverser actuator system of both the DC-10 and the Concorde employed fluidic operational amplifiers. An example of an amplifier is shown in Fig. 2.1a; small amounts of flow in the control ports C_1 and C_2 divert the main jet, thus increasing the flow rate ("current") in the desired output port. Vented outputs can also be used to amplify "voltage" (pressure). Many geometries self-oscillate when the control ports are not connected, and this type of oscillator has found its way into shower

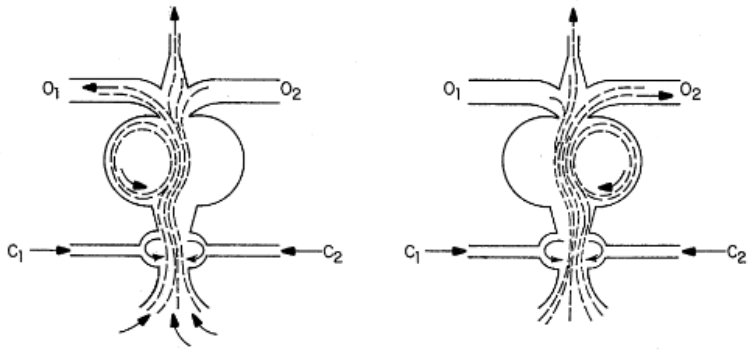

(a) Example of a fluidic amplifier.[2]

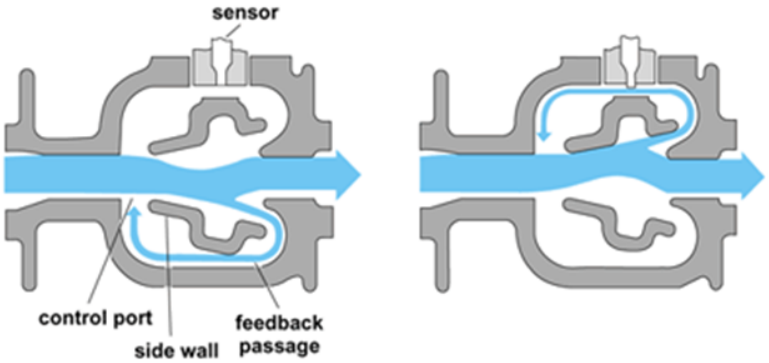

(b) Flow meter using self-oscillation to convert flow rate to frequency.[3]

Figure 2.1: Examples of other uses of fluidic oscillators.

[2] Freeman, 1977.
[3] Bailey, 1980.

heads, paint sprayers, and wind shield wiper nozzles. In Fig. 2.1b an implementation of a flow meter which uses the self-oscillation to convert flow rate to frequency is illustrated.

In order to visualize the internal and external flow of a sweeping jet actuator, several transparent models were built to be used in a Schlieren setup. Fig. 2.2 shows a model made with optical glass sandwiching aluminum parts which form the sweeping jet actuator. The vertical line in the image represents the edge of the glass plates, and the entire geometry is quasi two-dimensional with a thickness of 0.1 inches, a jet throat width of 0.2 inches, and an opening angle of 100°. At lower speeds the jet is visualized by a temperature difference using cold gas (tetrafluoroethane) in the air hose but eventually pressure differences are sufficient.

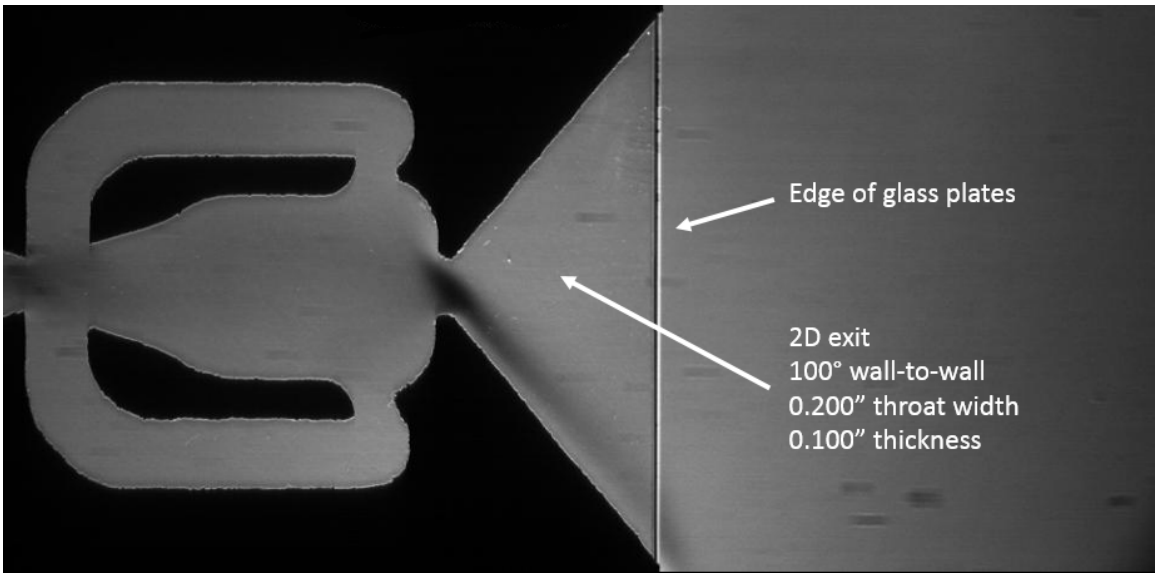

Figure 2.2: Sweeping jet sandwiched between two optical glass plates visualized in a Schlieren setup.

Fig. 2.3 shows the early stages of a scenario where a valve connecting the sweeping jet actuator with a pressurized air reservoir is suddenly opened. At startup, the standing gas in the oscillator is pushed into the two feedback passages by the incoming jet. Two vortices appear at the inlet and exit throat (Fig. 2.3a). The flow in the feedback passages flows towards the central inlet jet. At this point the flow is still largely symmetric (Fig. 2.3b). The first sign of asymmetry in the internal flow shows up in Fig. 2.3c. The internal jet is titling toward the lower island. It is believed that this is governed by slight asymmetries in the construction of the jet. The first sign of impending oscillation is a wavering of the internal jet, but not yet completely decisive to one island or the other (Fig. 2.3d). The wavering eventually favors one direction (in this case, down; see Fig. 2.3e) which feeds more

fluid to one feedback passage than the other (here the upper one). In Fig. 2.3f, oscillations have now begun; the internal jet has flipped from one side to the other, attaching itself to one of the solid surfaces ("islets") forming the main cavity of the actuator. The feedback passages are now fed by

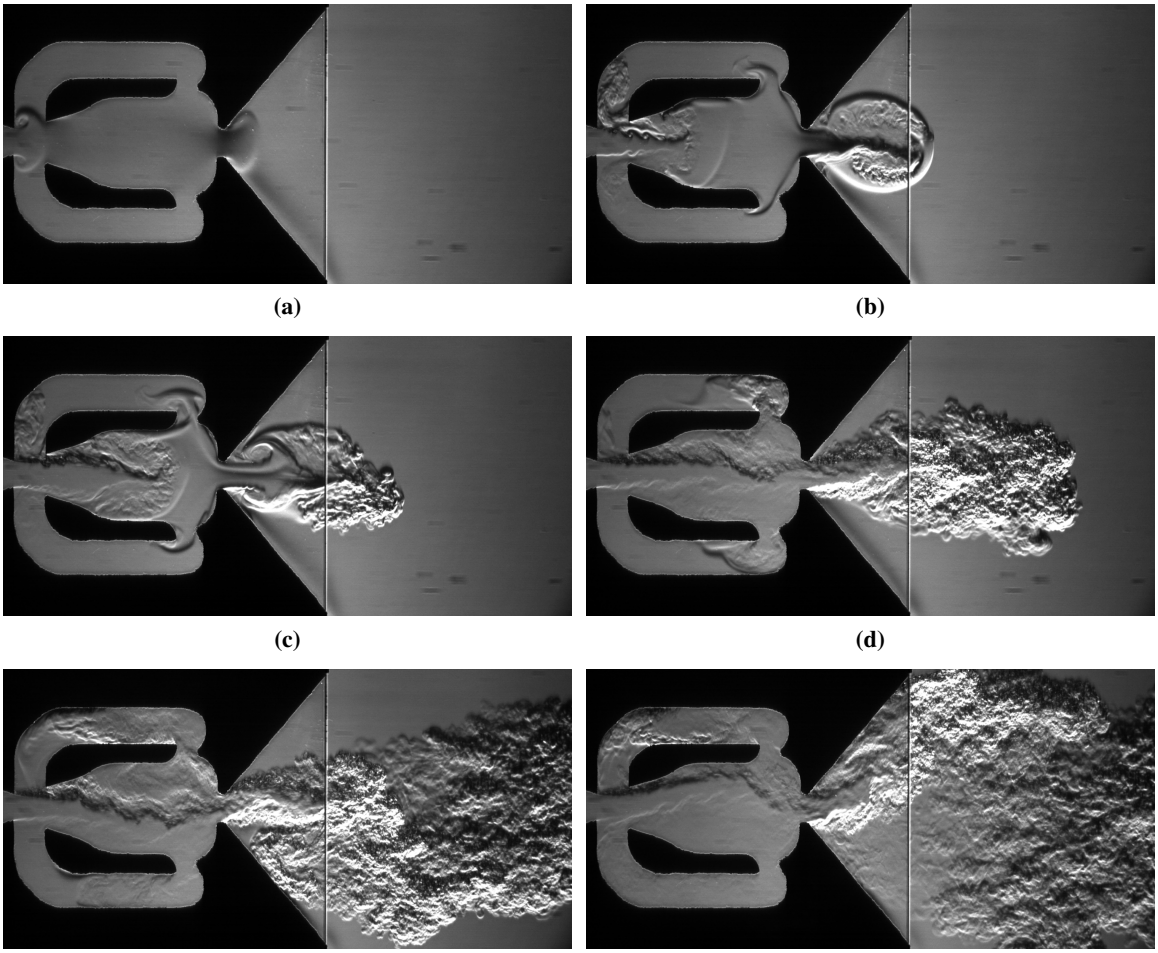

Figure 2.3: Startup flow and first oscillation of a sweeping jet actuator.

the jet impinging on the walls on either side of the exit throat, creating a flow that eventually pushes the inlet jet back to the opposite surface: systematic and sustained oscillations are created. The oscillation is two-dimensional in nature, and its frequency is mainly determined by the length of the feedback passage (Schmidt et al., 2016) and the pressure ratio between inlet and outlet. Its spanwise sweep angle depends on the detailed design of the actuator. In some designs (Guyot, Paschereit, and Raghu, 2009; Cerretelli, Gharaibah, et al., 2009; Cerretelli and Kirtley, 2009) a wedge was placed in the center of the exit nozzle to ensure that the resulting oscillatory jet dwells at two prescribed angles. The actuator does not have to be internally rounded as the one shown in Section 1.3. In

fact, many previous experiments were carried out using rectangular actuators as described by (Lucas et al., 2008). The whole geometry could be made slightly asymmetric and it would then oscillate in a "syncopated" fashion. However, all the sweeping jet actuators in this thesis were carefully built with the intention of making them symmetric.

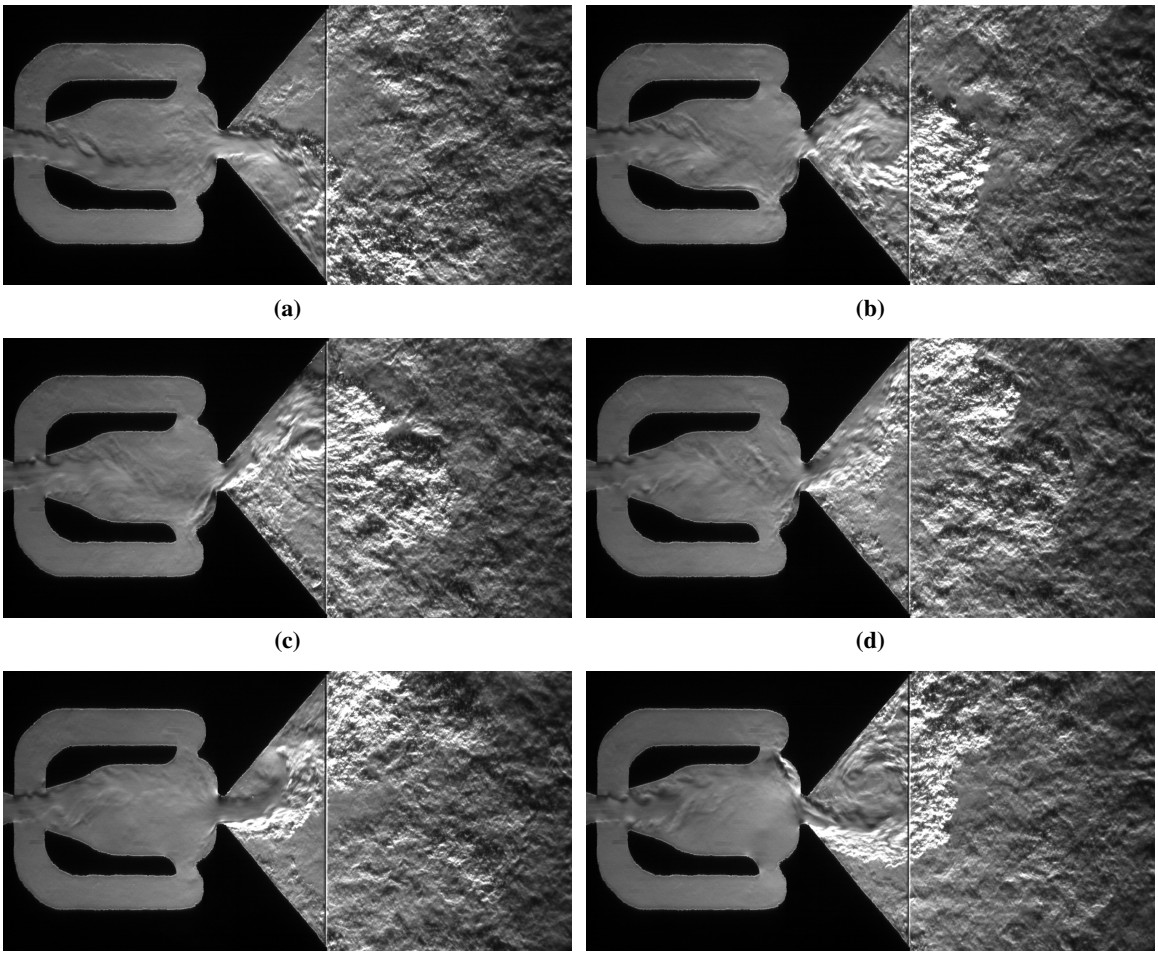

Figure 2.4: Creation of vortices during the sweeping cycle.

During the subsonic oscillations phase the flipping of the jet generates vortices. The vortices get created in the exit trapezoid while the jet is separating itself from the outer wall during the first phase of the flipping cycle (Fig. 2.4a). In the provided example, a clockwise-rotating vortex is created during the upward sweep. The jet drags the vortex to the other side while it is enlarging at the same time (Fig. 2.4b). Once the jet reaches the other wall, the vortex is pushed outward (Fig. 2.4c). Because of the additional flow "trapped" inside this vortex, a pulse of flow is created at the outlet. In a time-integrated sense, a sweeping jet looks similar to two distinct pulsed jets

(see Section 3.3.6). When the vortex leaves the exit trapezoid, which corresponds to a transition from a quasi two-dimensional space to a three-dimensional space, it immediately interacts with the ambient air and rapidly dissipates (Fig. 2.4d). While the dissipation of the previous vortex is still ongoing, the jet starts to separate itself from the wall again. This downward motion now creates a counterclockwise-rotating vortex (Fig. 2.4e). This newly created vortex is now pulled downwards with the sweeping motion and the whole process repeats (Fig. 2.4f). These vortices significantly enhance the mixing capabilities of the sweeping jets. It is believed that these distinct characteristics play a major role in the sweeping jets' promising performances in AFC applications.

As the pressure continues to increase the outlet jet reaches the speed of sound (Fig. 2.5a), and the first signs of shocks appear. In its subsonic state the jet fully attaches to the exit walls and creates the vortices before the jet switches sides. As the back pressure further increases the now sonic jet stays no longer attached to the walls and reduces its sweeping angle (Figs. 2.5b to 2.5d).

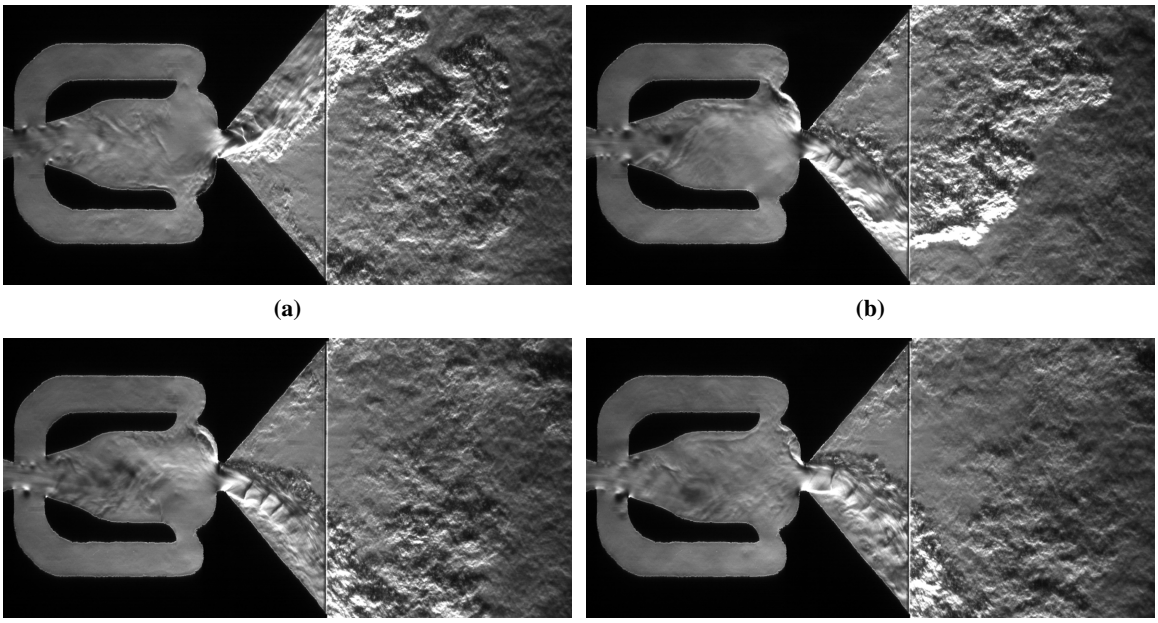

Figure 2.5: Transition to sonic exit jet and reduction of sweep angle.

At this point the cold gas (tetrafluoroethane) has run out, and the flow is primarily visible due to pressure variations. Looking at the images in Fig. 2.6, it is evident that the oscillation frequency immediately increases due to the reduction of the sweeping angle. The jet is nowhere near the side walls anymore; the sweep angle is reduced by about $\pm 18°$ (see Section 3.3.6).

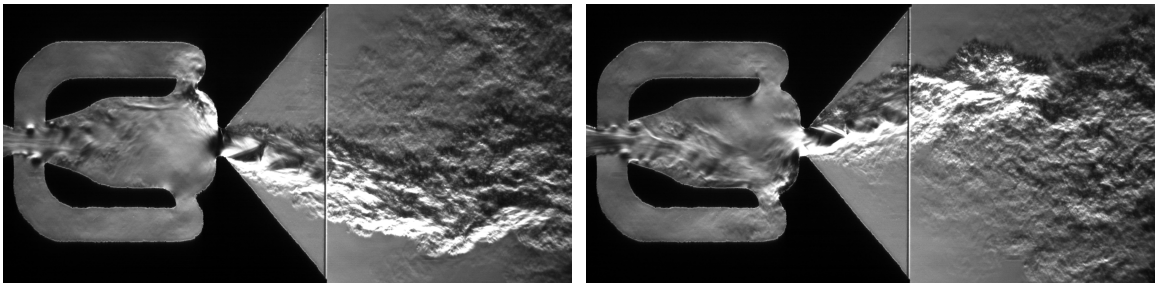

(a) **(b)**

Figure 2.6: Sonic exit jet at higher flow rate with increased frequency and large reduction of sweep angle.

Fig. 2.7a is at the maximum pressure ratio (about 6) between the inlet and outlet (ambient) the given setup is able to provide. The outlet jet is now underexpanded, and this allows it to reattach to the side walls. In Fig. 2.7b one can see circular black stripes that emit from the center of the jet exit. These stripes represent sound waves created by the jet noise. At this condition, the sweeping jets can be extremely loud to a point where the sound waves are getting visible in Schlieren.

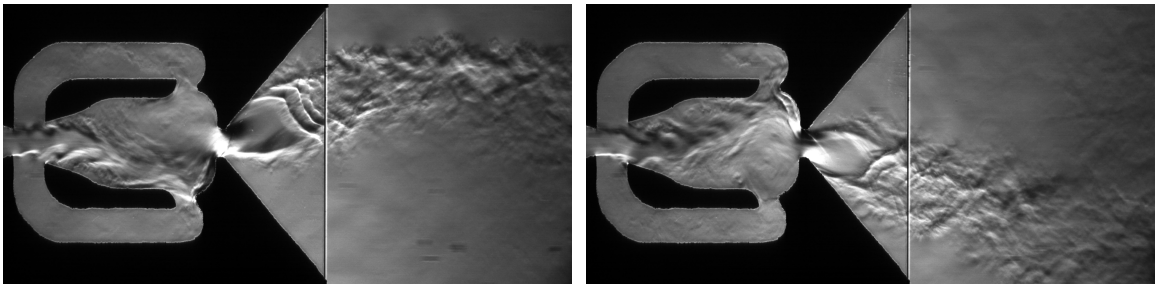

(a) **(b)**

Figure 2.7: Underexpanded jet at a high inlet to outlet pressure ratio.

Chapter 3

The Influence of Adjacent Sweeping Jets

3.1 Introduction

In recent years, the interaction of sweeping jet actuators with the separating boundary layer became of particular interest. Woszidlo, 2011 used surface flow visualization (China clay) on a two-dimensional airfoil to address this question. He discovered that two adjacent sweeping jets form a "necklace vortex" downstream of the jet exits when an overlaying freestream velocity is present. He further identified that the location of the "necklace vortex" agrees well with the expected interaction zone derived from the sweeping angle of the adjacent jets and does not change noticeably at higher jet velocities. Downstream of of the "necklace vortex" footprints of two quasi-stationary counter-rotating vortices were observed. Tewes, 2015 continues this investigation and argues that the combined effect of the sweeping wall jet and the streamwise vortices are the reason for keeping the flow attached, and thus enhancing the lift of the airfoil. He further states that the flow of two adjacent actuators is similar to flow in a wake that's globally unstable when its center is close to stagnation (Huerre and Monkewitz, 1985). The formation of such spatially and transiently stable flow features is surprising, because sweeping jet actuators represent the exact opposite of this. The question now is whether these features are generated by "external" fluid interactions, or if sweeping jet actuators start to "communicate" with each other, such as matching their frequencies or positions. While it is believed that sweeping jet actuators do oscillate randomly relative to each other, this is contradicted by the current knowledge about adjacent jet interactions (Tam and Seiner, 1987). For sweeping jets no experiments have been performed so far, even though it seems to be of particular importance in the current discussion about the origins of the sweeping jet actuator's promising performances. For example if the jets do have an influence on each other, do they synchronize their sweeping? How close to they have to be that this happens?

3.2 Experimental Setup

To answer some of these questions a bench-top model was built where the distance between two adjacent sweeping jet actuators could easily be changed. The experimental setup is shown in Fig. 3.1a. Actuators can be freely moved along a slot to change their respective spacing and more

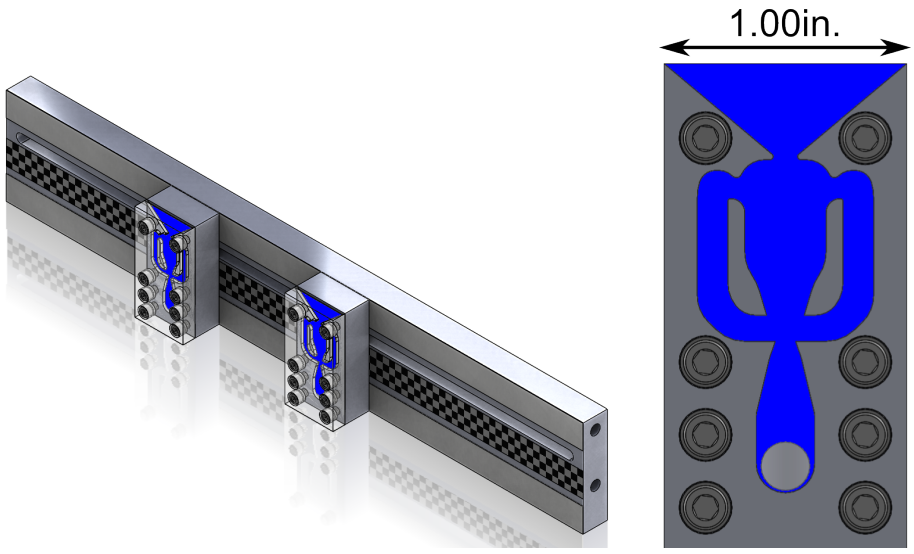

(a) Bench-top model to study the influence of adjacent jets on each other depending on the separation distance. The sweeping jets actuators are colored in blue.

(b) Single sweeping jet actuator that was used for the experiment.

Figure 3.1: Bench-top model setup.

actuators can be added if necessary; experiments with three or more actuators are possible. However, the data shown here will only be used to discuss the case of two adjacent sweeping jet actuators in quiescent ambient air. The absence of a freestream flow ensures that solely the interaction between the two adjacent sweeping jets depending on their separation distance can be examined. A schematic drawing of the sweeping jet actuator design is shown in Fig. 3.1b, where the actuator height is 0.050 inches and the nozzle width is 0.100 inches. To ensure identical pressure, each actuator has a separate connection to a manifold. To observe their respective interaction, the sweeping jet actuators were placed in the same Schlieren setup that was used to acquire the images in Chapter 2. For this experiment, the IDT MotionPro Y7 high-speed camera acquired images at a frame rate of 9000 Hz. Due to the physical size of the setup, the separation distance of the two actuators was limited to 1.25 inches to observe both of them simultaneously. For higher separation distances, the second actuator was out-of-view of the camera. The analysis is then solely based on comparison with the reference case of a single sweeping jet actuator.

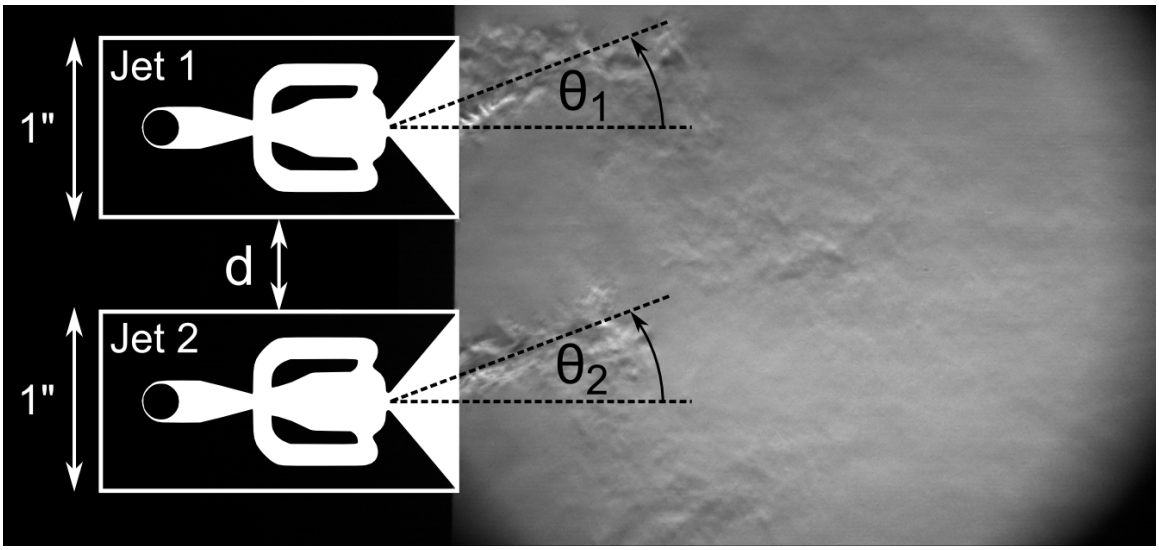

Figure 3.2: Definition of the deflection angle for the top (θ_1) and bottom (θ_2) sweeping jet actuator. The spacing between the actuators is labeled with d.

It was believed, that any influence the actuators exhibit would translate into a position or frequency adjustments of one or even both jets to accommodate the presence of the other. To put "position" into an actual quantitative value, it was decided to record the jet deflection angles of the actuators as defined in Fig. 3.2. To extract the angle deflections θ_1 and θ_2 from the images an algorithm was written to track the jets and calculate their respective deflection angles. The images were analyzed using an edge detection method introduced by Canny, 1986. The method calculates the gradient of

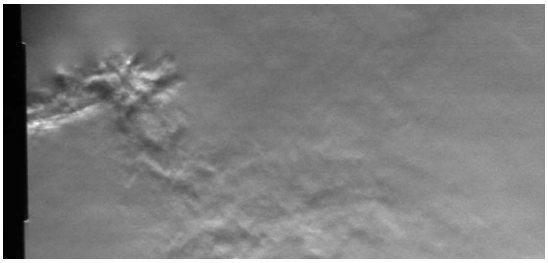

(a) Raw image

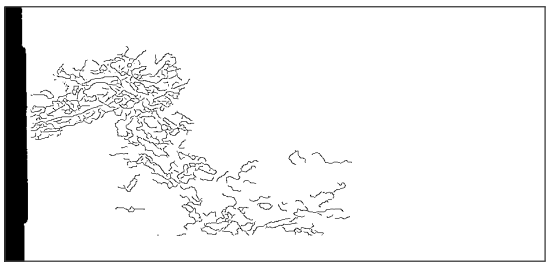

(b) Processed image

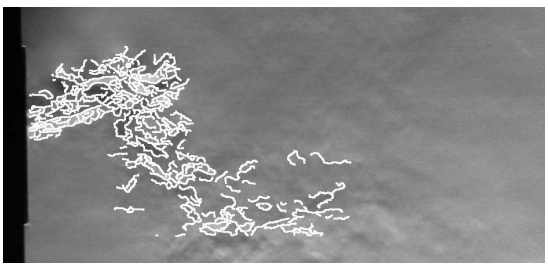

(c) Overlay

Figure 3.3: Detection of the jets using the Canny edge detection method.

an intensity image using the derivative of a Gaussian filter. This method applies two thresholds to the gradient: a high threshold for low edge sensitivity and a low threshold for high edge sensitivity. It starts with the low sensitivity result and then grows it to include connected edge pixels from the high sensitivity result. This helps fill in gaps in the detected edges and makes the Canny method less likely to be fooled by noise compared to other methods and more likely to detect true weak edges. In Fig. 3.3 one can see a comparison between a raw image, the processed version, and an overlay of both. It's evident that this method is fully capable of tracking the jets without much difficulty. However, the main interest is acquiring the deflection angle and not tracking the jets themselves. A simple way to do so is by calculating the center of mass of the tracked pixels of the processed image (3.3b). This is more difficult than it sounds because the large wake region that has already mixed well with the surrounding air lags considerably behind the actual jet deflection angle. Fig. 3.4a

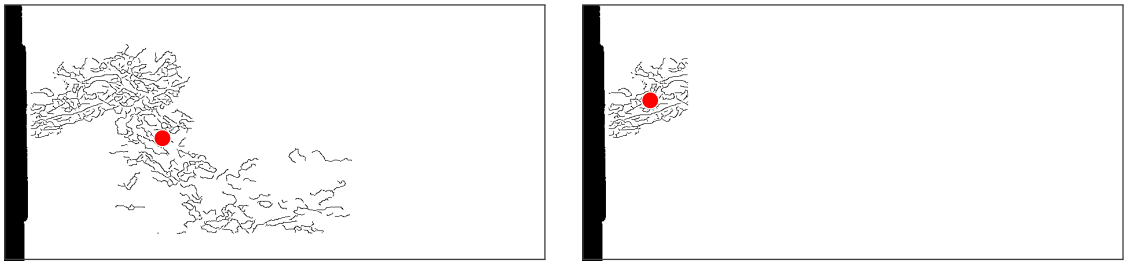

(a) Full detection area with inaccurate center of mass calculation (dot).

(b) Detection area limited to a narrow band right after the jet.

Figure 3.4: Reduction of the detection area significantly improves the accuracy of the center of mass calculation (dots).

exemplifies this problem: The large wake region of the jet lags behind the actual exit jet and causes the center of mass calculation to be inaccurate (dot in the images). Fortunately, by limiting the tracking area to a small band closer to the actuator exit, where the jet has not started its mixing and wake interactions, this can be resolved. Fig. 3.4b uses a much narrower band and the accuracy of the calculated center of mass is significantly improved. By knowing the location of the jet, simple trigonometric calculations lead to the sought-after deflection angle.

The first images taken showed that two adjacent sweeping jet actuators went through cycles with three distinguishable states: parallel-sync, crossed-sync, and async. These states are defined as:

$$\text{parallel-sync: } \theta_1 = \theta_2, \tag{3.1}$$

$$\text{cross-sync: } \theta_1 = -\theta_2, \tag{3.2}$$

$$\text{async: } \theta_1 \neq \theta_2. \tag{3.3}$$

Parallel-sync is a parallel motion of the jet with respect to each other, while cross-sync means the jets are mirrored along the horizontal center line resulting in a criss-cross behavior. Async describes all the other jet orientations where the jets are in a random orientation to each other. The two in-sync states are illustrated in Fig. 3.5.

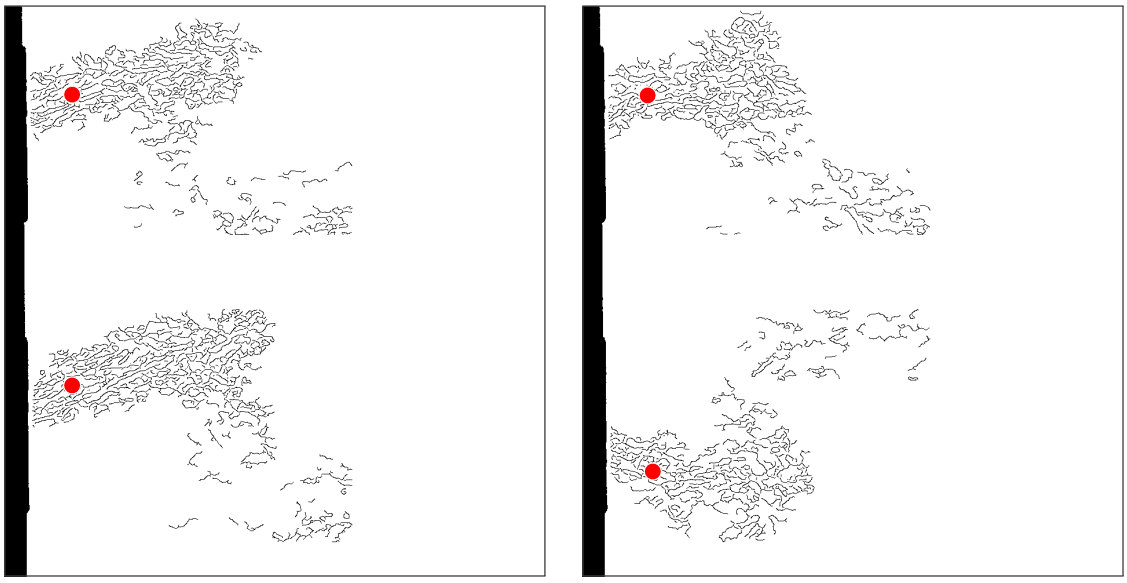

(a) Parallel-sync: $\theta_1 = \theta_2$ **(b)** Cross-sync: $\theta_1 = -\theta_2$

Figure 3.5: Illustration of the two in-sync states of the jets.

3.3 Results and Discussion

During the experiment data samples with a single jet (as a reference) and a jet spacing ranging from 0 inches to 1.25 inches in increments of 0.125 inches were taken. Both actuators were visible in the Schlieren and a mass flow rate of about 10 kg/hr through each of the actuators was supplied. An extended data set at the same mass flow rate was taken with only one jet visible in the Schlieren (due to the limitation of the observable area) at increments of 0.250 inches from 1.5 inches to 3.5 inches.

Thus, the spacing ratio $\mathcal{S}$ defined as the ratio between the jet exit trapezoidal width (1 inch) and jet spacing d lies between 0 and 3.5 covering the case of approximately 2 for the real models.

There are three distinct ways to evaluate the adjacent actuators' influence:

Cross-Correlation: The cross-correlation between two signals in the original time-domain is calculated with this method. In this case, either the time dependent jet deflection angles between two jets of the same recording θ_1 and θ_2 or the same jet for two different recordings at different spacing can be evaluated. If there is an interaction between two actuators, the former can give insight into a time-dependent dependence as the correlation value is expected to change with increasing time-shifts (assuming windows are used to get rid of edge effects). The latter would reveal if there is a change to the correlation over the whole time-domain by changing the distance between two jets. It would be expected that the correlation coefficients stay the same if there is no interaction between the actuators.

Unfortunately, this technique has a few major drawbacks. First, the signal of the jet angles is oscillating, which means that a correlation would also be an oscillating "signal" with values between -1 and 1. One could either average the results for comparison or focus on the maximum and minimum correlations values only. However, the much bigger drawback is that cross-correlation relies on a clean signal. The tracked images of the jet recordings can't live up to that due to noise in tracking, varying supply-pressure, and tiny geometry differences between the two actuators. These issues cause small frequency differences between the actuators on the order of 1%, which is sufficient to prevent any success with this approach.

Frequency Domain: Here the signals are converted into the frequency domain using a Fast Fourier Transform (FFT). If the signals have a, more or less, constant frequency, this is an excellent approach because it naturally rejects all noise and interference at other frequencies. Therefore, one can compare the frequency content of a reference actuator with actuators at a certain spacing. If the actuators have no interaction, one would not expect a frequency change between the reference jet and a jet that was subjected to the influence of an adjacent actuator. However, this is not sufficient as a proof: for example, the jets could go into a parallel-sync mode and conserve their frequency. Thus, this approach would miss this characteristic change, and can't yield the correct answer. But there is

a work-around: it is possible to look at the frequency domain of the phase time-domain signal. The phase angle ϕ is defined as

$$\phi = \theta_1 - \theta_2. \tag{3.4}$$

If one looks at the frequency domain of the phase angle, one would now expect to see changes even if two adjacent actuators are in a parallel-sync or cross-sync state.

Hilbert Transform: Another interesting technique is to convert the time-domain signal into an analytic signal via the Hilbert transform. This transforms the signal into a vector of complex numbers. The angle deflection which are of sinusoidal form will be converted into complex numbers whose magnitudes are constant and whose phase is changing with the original sinusoidal wave. Thus, this technique allows one to get the instantaneous phase lag between two signals. The major limitation of this approach is that the signal needs to be mono-component, which means that the signal of interest needs to dominate the recording. Any substantial interference must be filtered out.

3.3.1 FFT of a Single Jet and Comparison to Reference

First, a Fast Fourier Transform is taken for the reference jet and every jet spacing. A typical FFT that was acquired for all the cases is shown in Fig. 3.6. The frequency of the jet is clearly dominating the amplitude. The next higher peak corresponds to the second harmonic of the jet frequency. The first harmonic of the jet frequency is very weak and barely visible. A possible reason might be that right next to it there is another peak from an unknown source. This peak is also visible for the reference jet, and hence it is not an interaction frequency. It might have to do with the pressure source that runs the experimental setup, meaning it could be connected to the compressor's RPM.

Table 3.1 summarizes the frequency analysis for all spacing ratios $\mathcal{S}$ comparing the reference jet to one of the two adjacent jets. One can see that all the calculated frequencies are basically the same with a maximum deviation of less than 0.35%. This suggest two things: first, the experimental setup and the jet tracking worked really well leading to a small experimental error; second, because the tiny differences in frequency can be accounted for by experimental error, and there are also no characteristic tendencies distinguishable, one can conclude that two adjacent sweeping jet actuators do not have an interaction that would lead to a frequency change; the frequency is solely driven by the sweeping jet actuator itself.

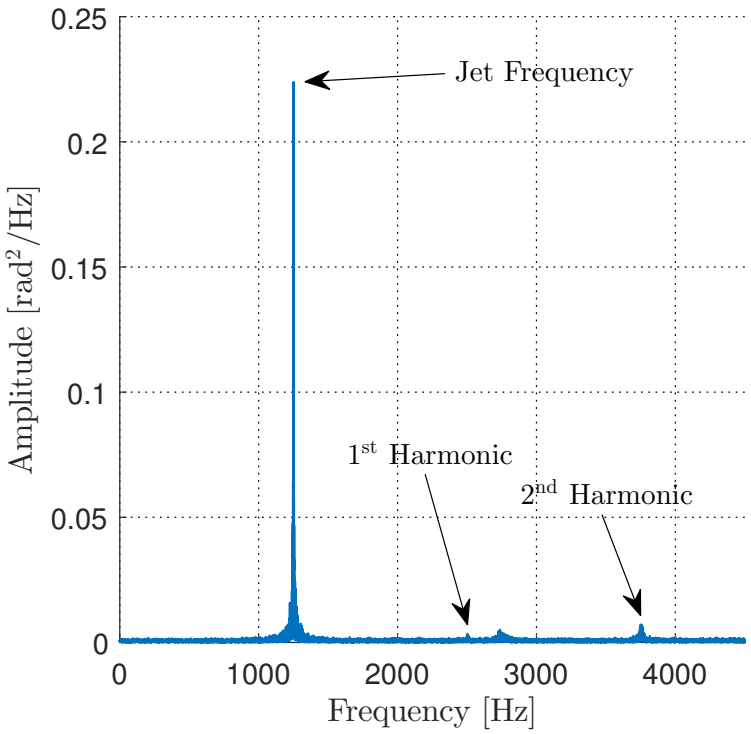

Figure 3.6: Typical FFT of a sweeping jet actuator with its jet frequency clearly dominating. The first harmonic is very weak while the second harmonic is a bit stronger. There is also another frequency that is slightly stronger than the first harmonic frequency that is most likely connected with the pressure source that runs the experimental setup.

3.3.2 Comparison of the FFT Results to a Fourier Type Fit

To verify that the FFT from the previous section calculates the correct frequencies, a different approach can be used that was not mentioned in the introductory part. Because the jet deflection angle follows approximately a sinusoidal wave over time, it is possible to fit the data to a sine function where the angular frequency ω is directly linked to the jet frequency f. A simple sine function as fit seemed to be a little too simple and wouldn't have given enough degrees of freedom to acquire a good result. Thus, it was decided to use a first-order Fourier series

$$f\left(a_0, a_1, b_1, \omega, x\right) = a_0 + a_1 \cos\left(\omega x\right) + b_1 \sin\left(\omega x\right) \tag{3.5}$$

and nonlinear least squares as evaluation method. The results are summarized in Table 3.2 and show a high agreement between the two methods with a maximum deviation of only 0.08%. The worst results come from the reference case and the one with 0.000 spacing ratio. The reason is most likely found in the darker images of these two cases that make the tracking a bit tougher. The spacing ratios from 1.500 to 3.500 have an average deviation of about 0.03%. This group only consists of 5000 images per spacing, and is thus not as accurate as the cases from 0.125 to 1.250 with over 20,000

Table 3.1: Calculated frequency of the different jet cases. The maximum deviation from the reference case is less than 0.35% suggesting that there is no change in frequency due to any possible interaction of the actuators.

$\mathcal{S}$ [-]	Jet Frequency [Hz]	Difference [Hz]	Deviation [%]
Reference	1249.4	-	-
0.000	1248.0	-1.4	0.11
0.125	1253.5	4.1	0.33
0.250	1248.0	-1.4	0.11
0.375	1248.0	-1.4	0.11
0.500	1252.4	3.0	0.24
0.625	1247.5	-1.9	0.15
0.750	1251.1	1.7	0.14
0.875	1249.1	-0.3	0.02
1.000	1251.1	1.7	0.14
1.125	1253.3	3.9	0.31
1.250	1250.2	0.8	0.06
1.500	1248.0	-1.4	0.11
1.750	1250.2	0.8	0.14
2.000	1248.0	-1.4	0.06
2.250	1248.0	-1.4	0.11
2.500	1248.0	-1.4	0.11
2.750	1246.9	-2.5	0.20
3.000	1248.0	-1.4	0.11
3.250	1246.9	-2.5	0.20
3.500	1246.9	-2.5	0.20

images each. In general it can be stated that both methods have an outstanding agreement, and that there is a large confidence in the results including the drawn conclusion that there is no evidence for any actuator interaction.

3.3.3 FFT of Phase Angle

The next step is to look at the phase angles defined in Eq. (3.4) for the different spacing ratios. The phase should be more prone to reveal any synchronization by the jet when performing an FFT. The frequency of the synchronization would reveal itself as its own frequency peak. Fig. 3.7a shows that the frequency domain of the phase angle looks exactly like the one for the “raw” jet angle. However, zooming into the main peak (see Fig. 3.7b) reveals that there are in fact two peaks present close to each other. This has to be expected, because with the phase the two jet angles are now interconnected and the FFT will not only reveal the frequency of a single jet, but also of the second one. In other words, the second peak is nothing else than the jet frequency of the adjacent jet. Because there is a distinct peak visible and there is no smearing between those peaks, one can again conclude that

Table 3.2: Calculated frequency of the different jet cases using a Fourier fit and comparison to the FFT approach. The approaches get to similar results with a maximum deviation of 0.08%.

$\mathcal{S}$ [-]	Fourier Fit [Hz]	FFT [Hz]	Difference [Hz]	Deviation [%]
Reference	1248.4	1249.4	-1.0	0.08
0.000	1249.0	1248.0	1.0	0.08
0.125	1253.5	1253.5	0.0	0.00
0.250	1248.0	1248.0	0.0	0.00
0.375	1248.0	1248.0	0.0	0.00
0.500	1252.4	1252.4	0.0	0.00
0.625	1247.6	1247.5	0.1	0.01
0.750	1251.2	1251.1	0.1	0.01
0.875	1249.2	1249.1	0.1	0.01
1.000	1251.2	1251.1	0.1	0.01
1.125	1253.3	1253.3	0.0	0.00
1.250	1250.2	1250.2	0.0	0.00
1.500	1247.6	1248.0	-0.4	0.03
1.750	1249.9	1250.2	-0.3	0.02
2.000	1248.2	1248.0	0.2	0.02
2.250	1248.4	1248.0	0.4	0.03
2.500	1248.4	1248.0	0.4	0.03
2.750	1247.3	1246.9	0.4	0.03
3.000	1247.9	1248.0	-0.1	0.01
3.250	1247.2	1246.9	0.3	0.02
3.500	1247.4	1246.9	0.5	0.04

the jets don't seem to have any influence on each other; they are completely independent of each other. Table 3.3 shows that the FFT of the phase indeed unveils the separate jet frequencies when

Table 3.3: FFT of the phase angle reveals two peaks for each of the jet frequencies.

$\mathcal{S}$ [-]	Jet 1		Jet 2	
	FFT Angle [Hz]	FFT Phase [Hz]	FFT Angle[Hz]	FFT Phase [Hz]
0.000	1248.0	1248.0	1256.6	1256.6
0.125	1253.5	1253.5	1262.9	1262.9
0.250	1248.0	1248.0	1261.0	1261.0
0.375	1248.0	1248.0	1264.0	1263.7
0.500	1252.4	1252.4	1263.2	1263.2
0.625	1247.5	1247.5	1256.3	1256.3
0.750	1251.1	1250.0	1262.3	1262.3
0.875	1249.1	1249.1	1258.8	1258.8
1.000	1251.1	1251.1	1263.7	1263.7
1.125	1253.3	1253.3	1265.1	1264.8
1.250	1250.2	1250.2	1261.0	1260.4

comparing them to the FFT results of the "raw" angle deflections. The data is limited for spacing ratios between 0.000 and 1.250 due to the absence (reference case) or non-observability of the second jet in the other cases. Most of the frequencies also match perfectly with the direct analysis of the

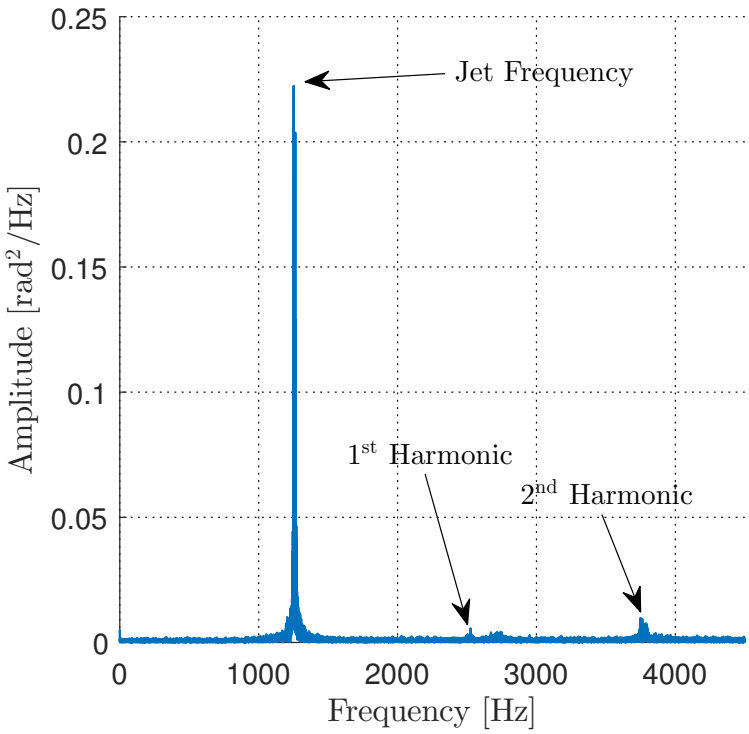

(a) FFT of the phase angle.

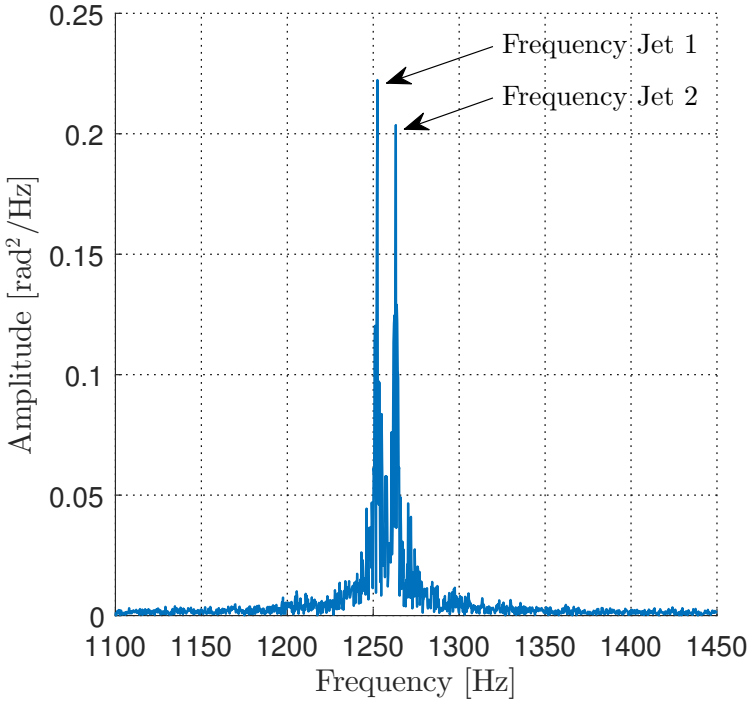

(b) Zoom: Two peaks are distinguishable.

Figure 3.7: FFT of the phase looks exactly like the FFT of the jet deflection angles. However, a closer look at the plot reveals a second peak which corresponds to the frequency of the second jet.

deflection angle even though the phase signal is much noisier in the frequency domain (creates wider peaks). This is also the reason why a few small differences can be observed when comparing direct deflection to phase angle FFT.

3.3.4 Hilbert Transform of Phase Angle

To support the previous results a Hilbert transform of the phase angles was performed. Because the phase is used again, this technique is limited to the cases with two observable jets. Fig. 3.8 summarizes the phase lags for the different spacing ratios. The phase lag continuously increases

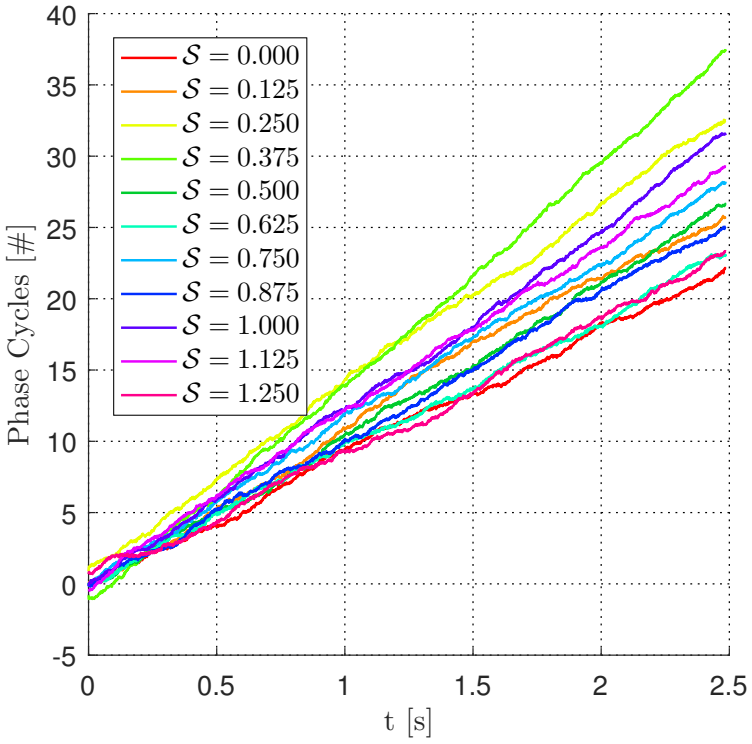

Figure 3.8: Hilbert transform of the phase angle. A continuously increasing phase lag can be observed for all the signals.

for all the cases going through 20 to 35 cycles depending on the case. The number of cycles is not dependent on the spacing ratio and seems to be completely random. As stated previously, the phase lag is created because of the slight frequency difference of the two jets, where the faster one (higher frequency) slowly gets ahead of the slower one. Thus, the number of cycles can be directly linked to a frequency difference between the two jets. Table 3.4 compares the frequency difference predicted by the FFT calculation of the deflection angles with the Hilbert transform of the phase angle. Both values show a high agreement throughout the data with a low error considering the

Table 3.4: Comparison between the frequency difference calculated by an FFT of the angle deflection versus the Hilbert transform.

$\mathcal{S}$ [-]	Δf_{FFT} [Hz]	$\Delta f_{\text{Hilbert}}$ [Hz]
0.000	8.6	8.9
0.125	9.4	10.4
0.250	13.0	12.8
0.375	16.0	15.4
0.500	10.8	10.6
0.625	8.8	9.3
0.750	11.2	11.3
0.875	9.7	10.2
1.000	12.6	12.8
1.125	11.8	12.0
1.250	10.8	9.2

underlying frequencies are around 1250 Hz. An FFT of the Hilbert transform will again result in the same frequency results, but the distinct frequencies of the two jets are now smeared out (Fig. 3.9).

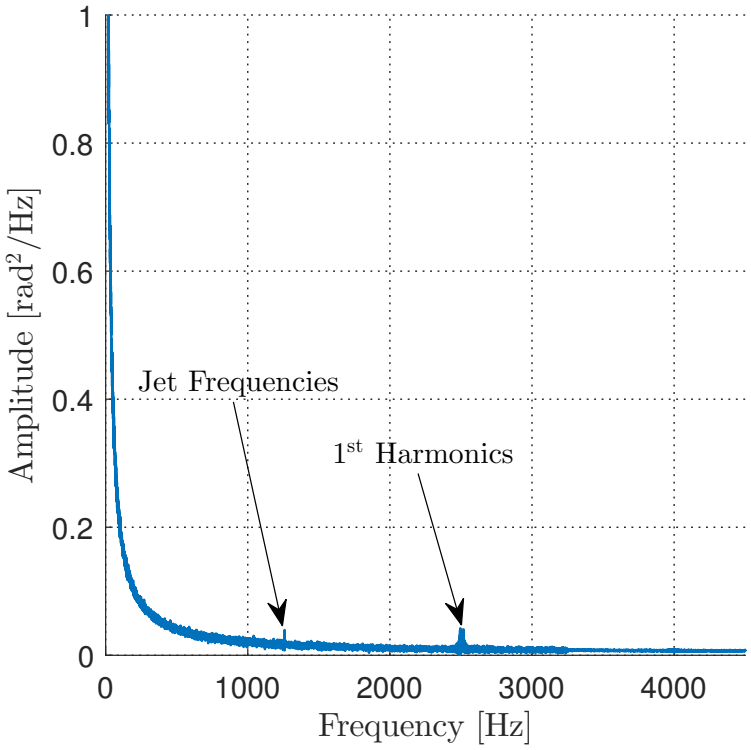

Figure 3.9: FFT of the Hilbert transform.

3.3.5 Reduction of Mass Flow Rate

The experiments up until this point were conducted at a mass flow rate of 10 kg/h for each jet. However, this mass flow rate chokes the actuator's nozzle, creating shocks in the exit trapezoid.

One could argue that if a shock is obstructing the path to the inside of the actuator, no information can travel upstream of the nozzle, and thus the actuator can't be influenced by any external flow features. To resolve this issue, another experimental test series was performed with a reduced mass flow rate of only 3 kg/h per jet, assuring a subsonic nozzle exit velocity. Data points were taken between spacing ratios of 0.000 and 1.500 in steps of 0.250, and only one jet was observed as the increased sweep angle (see Section 3.3.6) made it extremely difficult to track two jets at the same time (crossing of jets, observability).

Table 3.5 shows the acquired results using an FFT of the deflection angle and a first-order Fourier fit. Agreeing with the previous results, the frequency for different spacing ratios do not seem to change

Table 3.5: FFT of the deflection angle at a reduced mass flow rate of 3 kg/h per jet.

$\mathcal{S}$ [-]	FFT of Angle [Hz]	Fourier Fit [Hz]
Reference	1155.8	1156.8
0.000	1173.3	1172.6
0.250	1153.6	1153.2
0.500	1175.5	1174.5
0.750	1173.3	1173.1
1.000	1164.6	1164.6
1.250	1158.0	1159.0
1.500	1160.2	1159.8

in a characteristic fashion. The deviation, both in absolute numbers and the difference between FFT and Fourier fit, is increased due to the fact that a reduced number of images was acquired for every case. The frequency of the jet also reduced from around 1250 Hz to about 1150 Hz as expected due to the reduction of the mass flow rate, which leads to a reduction of input pressure. Based on these results the conclusions previously drawn also hold for the subsonic case, and thus hold in general; two adjacent sweeping jet actuators are not influenced by each other independent of the spacing between them. The internal geometry as a driver is much stronger than any external influences.

3.3.6 Mass Flow Rate Distribution of Sweeping Jet Actuators

The collected data can also be used to answer the question how a sweeping jet actuator distributes its mass flow rate along its sweep axis. Therefore, the collected angle deflection data was used to acquire a normalized histogram with a bin size of 0.5°.

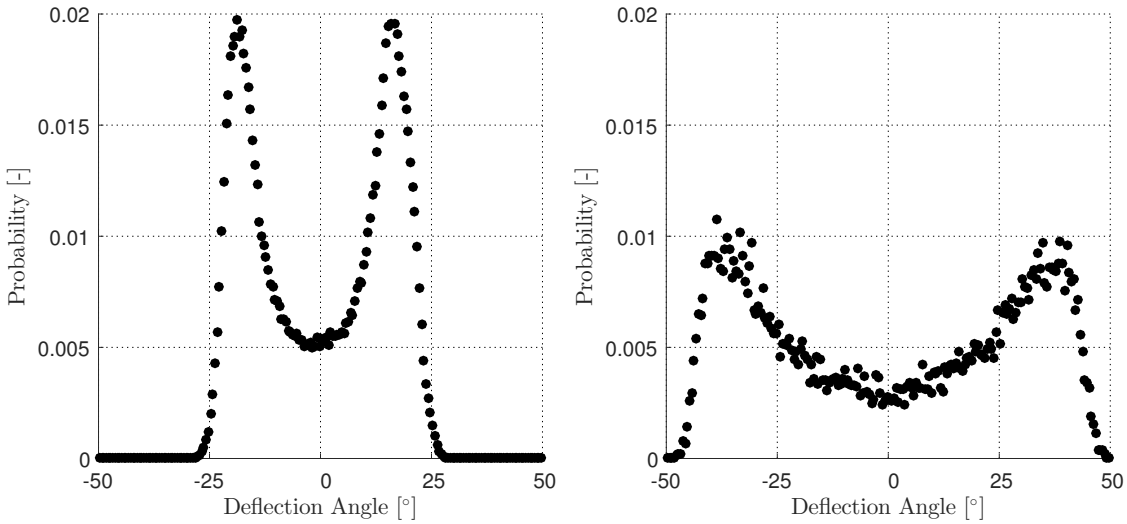

(a) Mass flow distribution at choked conditions. **(b)** Mass flow distribution at subsonic conditions.

Figure 3.10: Mass flow distribution for a standard sweeping jet with an opening angle of 100°.

Fig. 3.10a shows the mass flow distribution for a mass flow rate of 10 kg/h through one of the actuators, which represents a choked flow condition in the nozzle. The y-axis represents the probability of the jet being at that specific deflection angle, and the x-axis corresponds to the bins. The first observation is that the actuator restricts its sweep angle from $-25°$ to $25°$, which is half the opening angle of the trapezoid exit. Because the actuator is choked the sweep angle is damped, which is also observed in the Schlieren images, for example in Fig. 2.5. Secondly, the actuator does not distribute the mass flow evenly along the range of motion but deposits larger mass at the turning points and leaves a deficit in the center. This is an interesting observation, as it is not obvious by looking at the jet visualizations. Fig. 3.10b shows the case with a mass flow rate of 3 kg/h through the actuator, and thus subsonic conditions at the throat. By reducing the mass flow rate through the actuator, the range of motion increases to the full possible angle deflections from $-50°$ to $50°$. The jet now distributes the mass flow more evenly along the angles, and decreasing the probability for each of the individual bins. However, the deficit in the center is still present, although it is less pronounced. The data seem to be noisier as well; this is not an actuator property, but rather the consequence of a reduced amount of available data (about an order of magnitude lower than the other case) to perform the histogram. One might ask if it is possible to do a similar thing to acquire the momentum distribution. Experimentally, this would be a really challenging problem measuring the deflection angle and the momentum at every position at the same time. However, a much simpler approach

is to estimate the momentum based on its direct relation to the mass flow distribution by the jet velocity u_{jet}. Assuming the jet velocity is constant along the angles, which is not entirely correct based on Eq. (6.16), the momentum distribution would actually look exactly the same as the mass flow distribution.

3.4 Concluding Remarks

Using Schlieren and a high-speed camera it was shown that it is possible to accurately track a sweeping jet actuator's sweeping motion by using an edge detection method. A series of techniques, including Fast Fourier Transform, curve-fitting with a Fourier-fit, Hilbert Transform, and combinations thereof, were then applied to the tracking data to prove that sweeping jet actuators do not have any interactive ability even when brought right next to each other. The sweeping motion of the actuator is solely driven by its internal geometry, and is not easily disturbed by any external influences. Additionally, it was shown that this characteristic is independent of the nozzle exit velocity. The jet can neither be influenced in a subsonic nor in a sonic state with multiple shocks. It is not expected that these characteristics change when the sweeping jet actuators are applied as an AFC device. However, small differences in geometry and pressure supply change the sweeping frequencies of two, in theory, identical jets. This means that it is extremely difficult to create actuators that all sweep at the exactly same frequency without changing the "traditional" geometry. Additionally, the collected data made it possible to show the actuator's mass flow distribution along its sweep axis. Sweeping jet actuators show a large mass flow deficit at the center (low deflection angles) and distribute most of it at the maximum deflection angles.

Chapter 4

Active Flow Control Applied to a High-Lift Airfoil

4.1 Introduction

This project was initiated and funded by the Northrop Grumman Corporation via a bigger grant they received from the Air Force Research Laboratory (AFRL). Bright et al., 2013 developed an Advanced High Lift Leading Edge (AHLLE) technology for laminar flow wings. Based on a known laminar cruise airfoil they incorporated an integrated slot design into two steady-blowing leading edge concepts called the Laminar Airfoil Virtual Leading Edge Technology (LAVLET) and the Multi-Objective Leading Edge Concept (MOLEC). It was successfully demonstrated that these two concepts both provide high-lift capability. During the time these concepts were developed, AFC on a vertical stabilizer rudder as described in Seele, Graff, Lin, et al., 2013 showed great potential for high-lift concepts. This project's objective was to combine the two previous investigations, and examine the effects of a swept wing with sweeping jet actuators embedded near the leading edge as well as the trailing edge. Previous tests at Northrop (internal reports only) and Iowa State (Clemons and Wlezien, 2016; Jairam, Clemons, and Wlezien, 2016) have focused on two-dimensional sectional lift properties using leading edge blowing. The purpose of the Caltech test was to gain an understanding of the flow physics when AFC is applied at the leading and trailing edge in a three-dimensional configuration.

4.2 Experimental Setup

4.2.1 Lucas Wind Tunnel

The tests were conducted at the California Institute of Technology's Lucas Wind Tunnel. The closed loop test section is 6 ft (1.828m) wide and 5ft (1.524m) high and is operated at speeds of up to about 65 m/s. During this project most experiments were run at 50 m/s. The full-rotatable turn table, which also houses the six component strain gauge balance, was used to support the model through a strake. The tunnel features a cooling system that is capable of holding the free stream temperature at a controlled level ranging from approximately 65°F (18°C) to 80°F (27°C). For the current test the

temperature was set to 75°F (24°C), and the cooling system is able to keep the temperature within 1-2°F (1°C).

4.2.2 Wing Model

The tested wing model is a 30° swept back wing based on the LAVLET design with a span of 50 inches and a chord of 25 inches which results in a semi-span aspect ratio of 2 (Fig. 4.1). AFC slots are located at 1%, 10%, and 80% with respect to the chord (Fig. 4.2). At each location the AFC

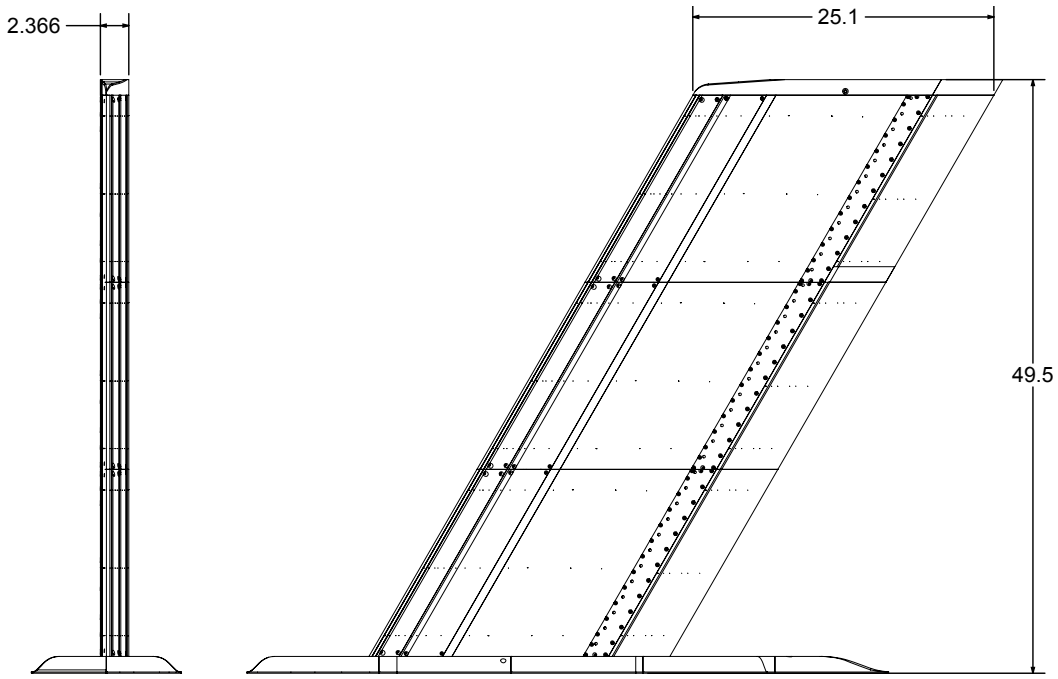

Figure 4.1: The Northrop wing model with its dimensions in inches. The full-span wing has roughly a chord of 25 inches and a span of 50 inches resulting in a semi-span aspect ratio of 2.

Figure 4.2: LAVLET airfoil shape with circled AFC locations at 1%, 10%, and 80% of chord.

actuator plates can be exchanged for varying configurations such as sweeping jet actuators or open slots for steady blowing. The 50-inch span of the model was divided into three subsections to enable to study the effect of aspect ratio, the ability to control the flow by section, and ease of assembly.

An aluminum fairing (see Fig. 4.3) was designed to provide a smooth aerodynamic transition from the tunnel floor to the model root. This way the creation of "edge effects" such as horseshoe vortices should be minimized.

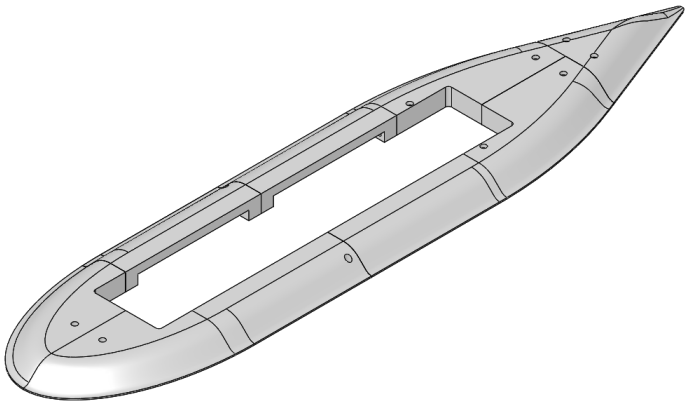

Figure 4.3: Fairing to provide a smooth aerodynamic transition from the tunnel floor to the model root.

The AFC devices (sweeping jet actuators and steady blowing) were embedded into so called actuator plates (see Fig. 4.4). These plates were machined from aluminum 0.040 inches deep. The sweeping jet actuator had a throat width of 0.080 inches, and a spacing of 1.50 inches. This allowed for 35 to 36 actuators at each AFC location at full span.The steady blowing plates were just open-ended with a few "bumps" for stabilization and screwing. This way they allow unobstructed blowing along the whole slot.

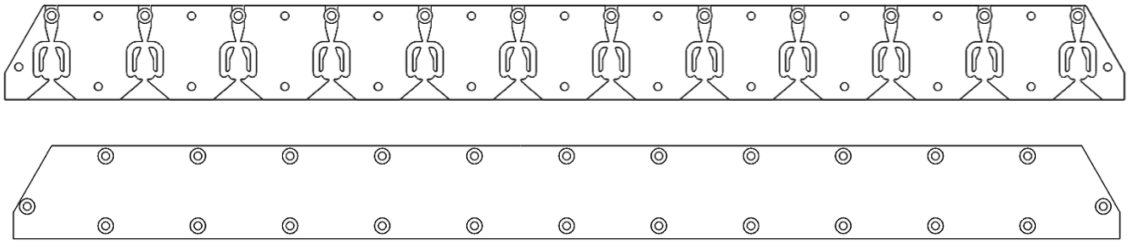

Figure 4.4: Sweeping jet actuator plate (top) and steady blowing plate (bottom).

A large amount of time went into the design of the exit geometry of the 1% and 10% AFC slots. Unlike the 80% location, the space at the tip of most airfoils is very limited and the airfoil thickness is usually rapidly growing which makes a proper plate alignment even more challenging. One solution would be to 3D print curved actuator plates that at the same time form the outer mold of the airfoil. Because it is not known if horizontally curved sweeping jet actuators would even work

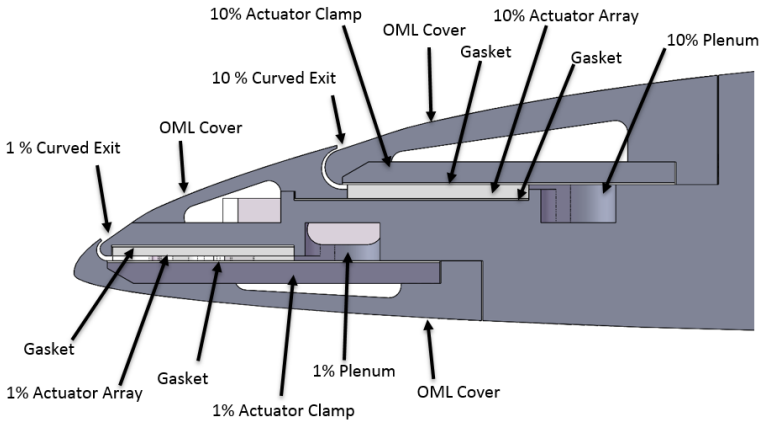

Figure 4.5: Schematic of leading edge design showing actuator arrays, gaskets, actuator clamps, plenums, and outer mold line (OML) covers for the 1% and 10% slot.

and the printing quality of such parts would be sufficient, it was decided to use a more conservative approach: the actuator plates were embedded into the wing pointing upstream and then an exit geometry was designed that curves the flow around tangentially with the wing surface. A short experiment confirmed that although the sweeping motion was weakened, it was still present at the outlet. A comparison between the two different designs of the leading and trailing edge is illustrated in Figs. 4.5 and 4.6.

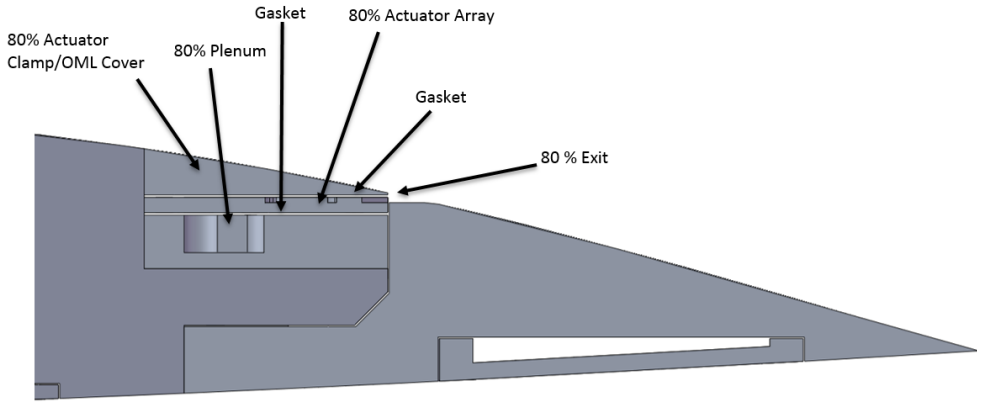

Figure 4.6: Schematic of trailing edge design showing actuator arrays, gaskets, actuator clamps, plenums, and outer mold line (OML) covers for the 80% slot.

During initial testing, it was discovered that the force balance used for testing was highly flexible and could freely rotate several degrees. The small rotation angles allowed for large deflections at the tip of the 50 inch span. At testing speeds, high amplitude oscillation of the model caused alarm. The model span appeared to remain rigid, which suggested that the deflections originated from the

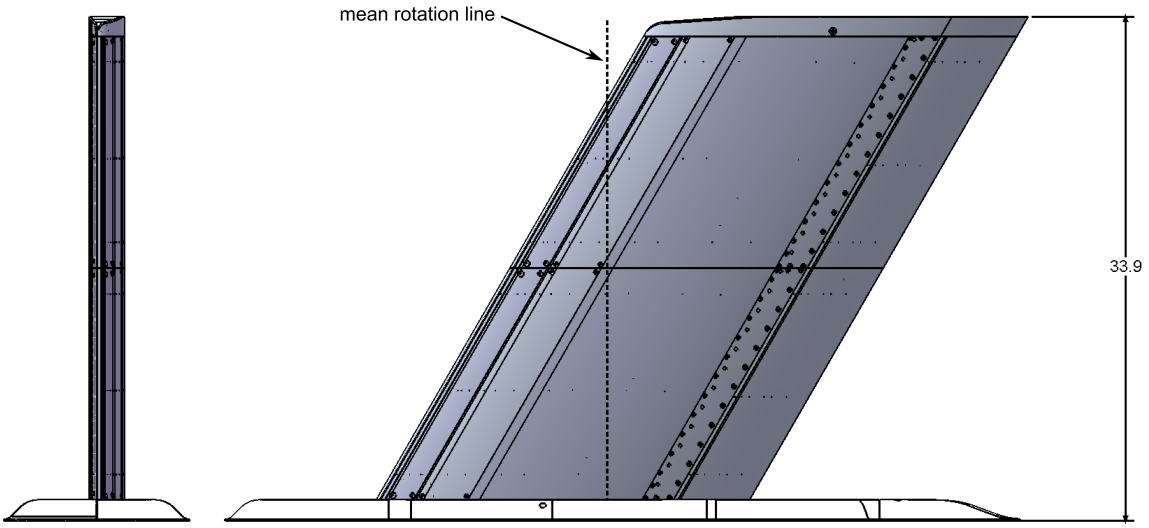

Figure 4.7: Reduced span configuration with only two spanwise sections. The span was reduced to limit the high amplitude oscillations caused by the flexible force balance. The dashed line represents the mean rotation line about which the pitch moment is measured (body coordinates).

force balance. Considering the high predicted loads, the span was reduced to avoid exceeding the balance limits with the unpredictable dynamic loads. It was decided to reduce the full span model to only two spanwise sections (see Fig. 4.7) which resulted in a span of 33.9 inches corresponding to an aspect ratio of around 1.3.

4.2.3 Instrumentation

Pressure taps were located in three spanwise rows. The 0.020 inch diameter taps are placed at about 33%, 50%, and 66% of the full span. With the reduction of span, the pressure taps reduced to two rows at 45% and 72% of the 33.9 inch span (see Fig. 4.8). A total of 52 pressure taps were evaluated with a Pressure Systems 8400.

To regulate the mass flow rate through the actuators, three Omega FMA-2621A mass flow controllers were purchased (Fig. 4.9). These units have on-board computers to regulate mass flow rate to a commanded setting, which greatly simplified operations, and are rated to supply up to 1500 SLM (about 108 kg/h). With these controllers, the main data acquisition computer only needs to send a set point and the controller will adjust itself to maintain the desired conditions, even if the supply air pressure or nozzle pressure ratio changes. These controllers also have a simple text based output giving continuous updates on the run conditions, including mass flow rate, volume flow rate,

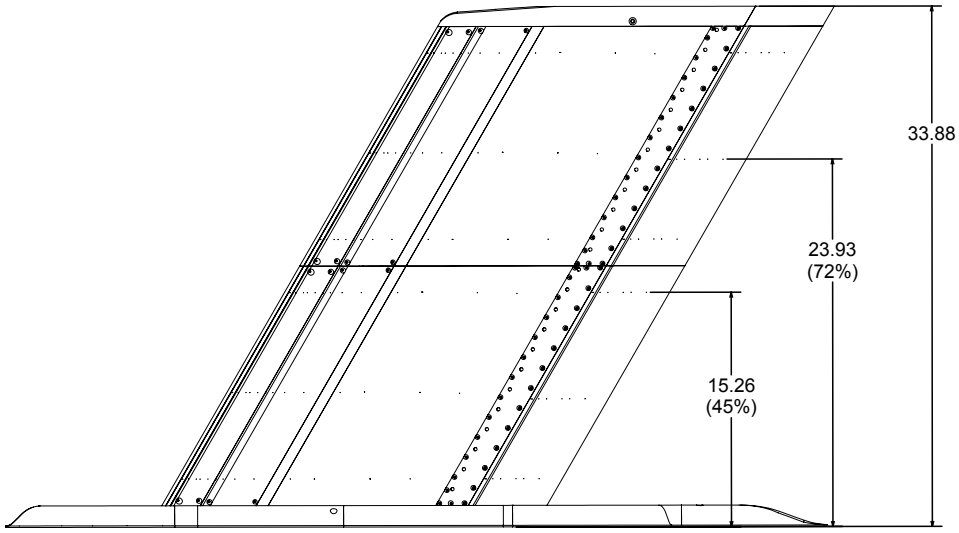

Figure 4.8: Spanwise pressure tap locations on the reduced span wing.

Figure 4.9: Omega FMA-2621A Mass Flow Controllers mounted beneath the test section regulate the mass flow rate into each bank of actuators.

temperature, and pressure. With one self-contained unit and two commands, the desired mass flow rate can be set and the inlet test conditions can be acquired. With three units, each bank of actuators can be controlled independently. The control and readout functionality was then integrated into the main data acquisition software.

The Lucas Wind Tunnel 3161-A balance limits were unable to support the predicted loads of this testing. With the help of AFRL and the Space Act Agreement, Caltech was able to loan a higher limit force balance from NASA Langley. The NASA 753 force balance has the following load limits:

1. Normal Force: ± 4000 lbs (18 kN)
2. Axial Force: ± 500 lbs (2.2 kN)
3. Pitch Moment: ± 10,000 in-lbs (1.1 kNm)
4. Roll Moment: ± 10,000 in-lbs (1.1 kNm)
5. Yaw Moment: ± 4500 in-lbs (0.51 kNm)
6. Side Force: ± 1800 lbs (8.0 kN)

A force balance adapter was designed and fabricated to couple the balance to the Lucas Wind Tunnel. The balance adapter was modeled after the 753 calibration fixture and fabricated from 17-4 stainless steel. Precision bores were honed to provide a slip fit around the balance shaft, and the part was heat treated per the NASA drawing specification.

4.3 Results and Discussion

The wing was tested in four different configurations:

- Steady blowing ("open" slot) with a flap deflection of 0°
- Steady blowing ("open" slot) with a flap deflection of 45°
- Unsteady blowing using sweeping jet actuators with a flap deflection of 0°
- Unsteady blowing using sweeping jet actuators with a flap deflection of 45°

All configurations were exposed to a range of angles of attack within -6° $\leq \alpha \leq$ 22°. The tested free stream velocities were originally set to 50 m/s corresponding to a chord Reynolds number of roughly 2,000,000, but were later reduced to 40 m/s corresponding to a chord Reynolds number of 1,600,000 to achieve higher coefficients of momentum input C_μ.

4.3.1 Baseline Characterization

The baseline of the wing consisted of two basic configurations: an undeflected configuration with a 0° flap and a deflected configuration with a 45° flap. The influence of the flap deflection δ_F on the

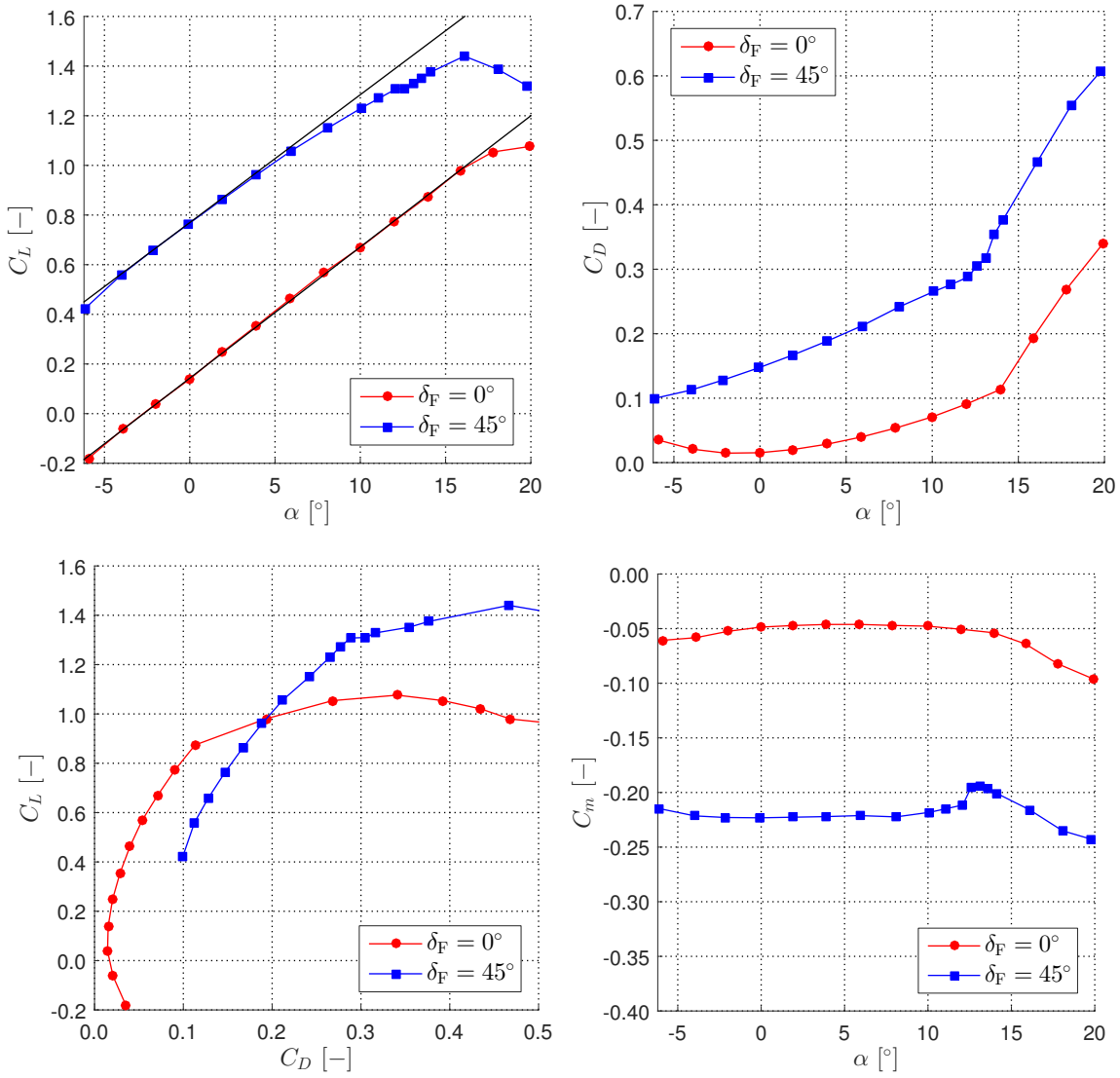

Figure 4.10: Comparison between the baselines of the two basic configurations with flap deflections $\delta_F = 0°$ and $\delta_F = 45°$.

baseline configuration is illustrated in Fig. 4.10. The plot on the top left shows the lift coefficient C_L vs. angle of attack α. For both configurations an increase in angle of attack α leads to a near-linear increase in lift coefficient as long as the wing is kept beneath the threshold angle of attack at which separation starts to occur. Additional lift of roughly $\Delta C_L \approx 0.6$ is generated by the deflected flap. The penalty one pays for the extra lift is additional drag as the C_D vs. α plot shows on the top right of Fig. 4.10. The maximum observable difference in drag is about $\Delta C_D \approx 0.2$ for angles of attack $\alpha > 10°$. The C_L vs. C_D plot shows that the flap is able to extend the drag polar. The bottom right figure showing the pitching moment coefficient C_m vs. α indicates that the flap decreases the

pitching moment (nose down), which corresponds to a lower (more negative) C_m value. In detail, one can also see that the pitching moment is constant for both cases (by definition of the aerodynamic center) until it reaches a certain α-threshold. This threshold corresponds to the threshold mentioned earlier and represents the beginning of separation. For $\delta_F = 45°$ this threshold is around $\alpha \approx 12°$, and is easily detectable by the rapid reduction of negative pitching moment. For the non-deflected case $\delta_F = 0°$, it is harder to pinpoint: the "transition" is much smoother and there is no growth of instabilities; the pitching moment simply deviates from its horizontal axis. However, looking at the C_D vs. α plot at the top right, it is evident that the wing starts to separate (sudden increase in drag) at $\alpha \approx 14°$. In other words, adding the flap causes the wing to start separating about 2° earlier. Another observation that can be made is that even though the separation begins above the aforementioned α-thresholds, the wing is still able to increase its lift until $\alpha \approx 16°$ with and $\alpha \approx 20°$ without flap deflection until stall is reached. Note that without flap deflection, the transition to stall and thereafter the loss of lift, is smooth and slow, while with flap deflection the wing suffers a sudden and severe loss of lift. Additionally, vortex lift, which is marked by an increase in $\partial C_L/\partial\alpha$, and its beneficial contribution to lift for swept back wings, might have been generated at $\alpha > 12°$ for the deflected configuration ($\delta_F = 45°$). The clear destabilizing effect on the pitching moment supports this assumption.

One can extract even more information by looking at the C_p vs. x/c plots for the case without deflection (Figs. 4.11 to 4.13) and with deflection (Figs. 4.14 to 4.16). The plots are divided into different angles of attack ranges to make them more readable. Every figure consists of two pressure tap rows which were taken at different spanwise locations of the wing (see Fig. 4.8). The lower spanwise location was located at 45% ($y/b = 0.45$) and the upper one at 72% ($y/b = 0.72$) of the wing span. Each row consisted of several pressure taps on the suction and pressure side of the wing. The pressure data was plotted in terms of the pressure coefficient C_p against the normalized chord location x/c.

Fig. 4.11 shows the pressure distribution for the non-deflected flap at low angles of attack. If one looks at the C_L vs. α plot in Fig. 4.10, it can be seen that the wing creates little, or even negative lift, for the two smallest angles. This becomes more apparent by looking at the left plot ($y/b = 0.45$). For both angles $\alpha = -6°$ and $\alpha = -4°$, an area is created under the closed curve (which correspond

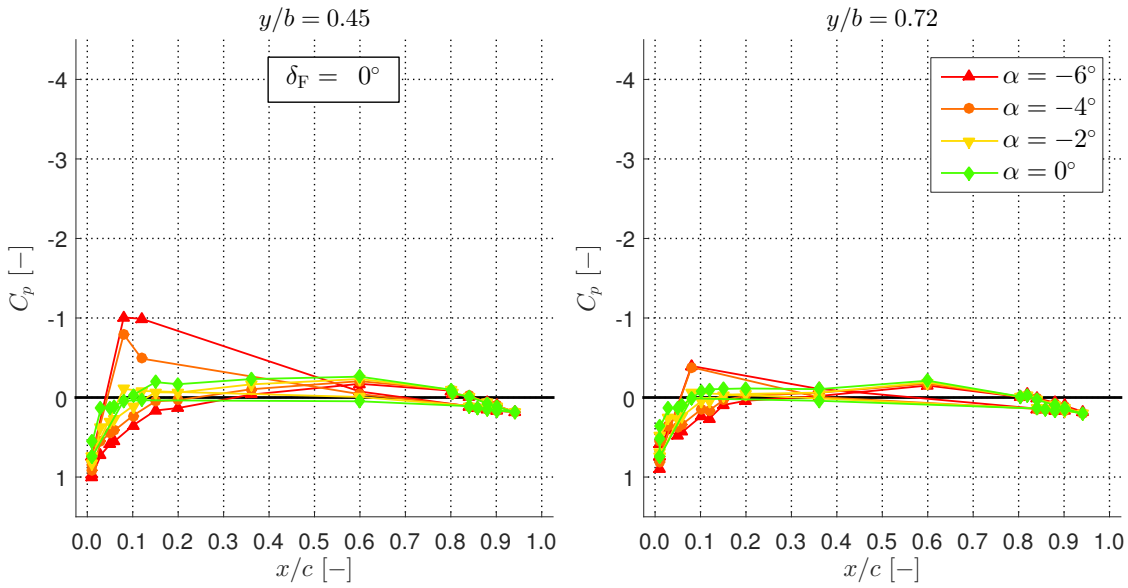

Figure 4.11: Pressure distribution C_p with $\delta_F = 0°$ for angles: -6°, -4°, -2°, and 0°.

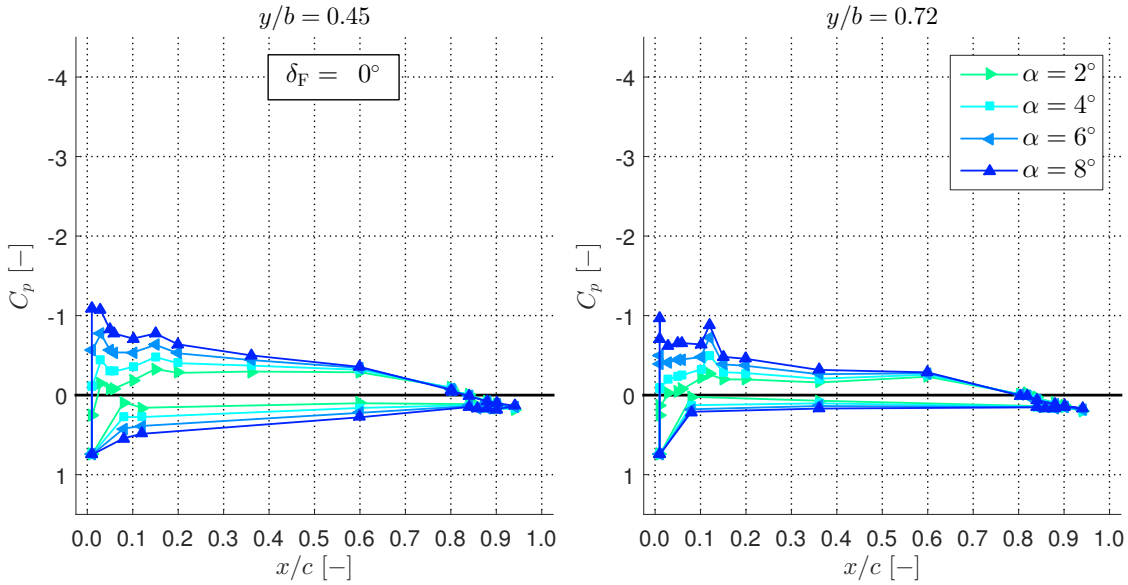

Figure 4.12: Pressure distribution C_p with $\delta_F = 0°$ for angles: 2°, 4°, 6°, and 8°.

to a pressure difference, which can be related to lift). The pressure (now suction) and suction (now pressure) side changed their signs, resulting in a "negative area", and thus negative lift. For the other two angles ($\alpha = -2°$ and $\alpha = 0°$) there is only a minor enclosed area, and therefore only minor lift. This matches perfectly with the results from the lift curve. Looking at the right plot of Fig. 4.11 ($y/b = 0.72$) one can observe that the closed curves follow the same trend as the lower pressure tap row; however, the created area (lift) is much smaller on the pressure and on the suction

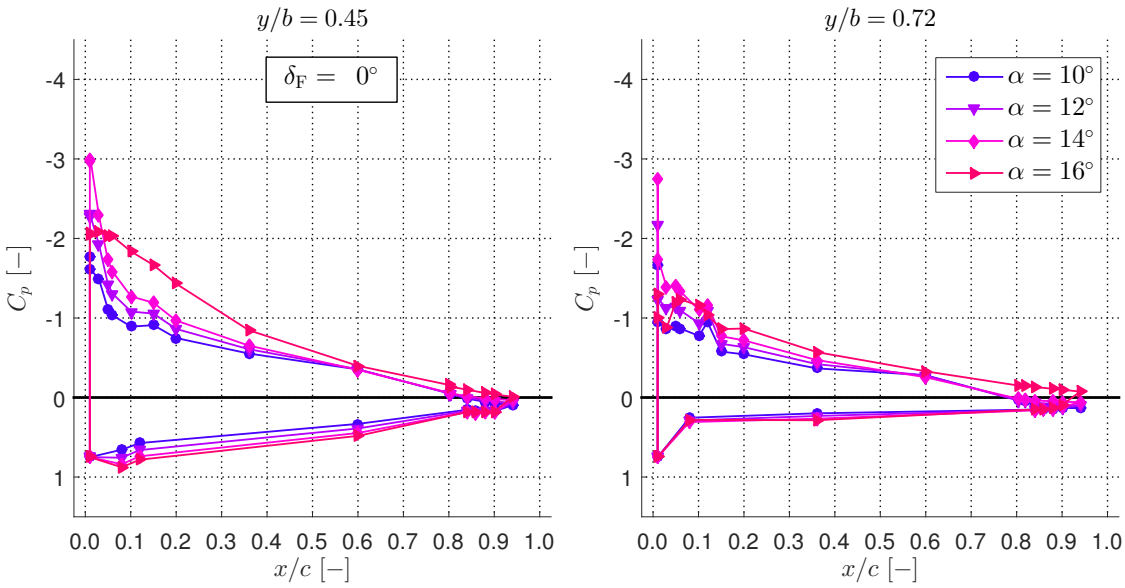

Figure 4.13: Pressure distribution C_p with $\delta_F = 0°$ for angles: 10°, 12°, 14°, and 16°.

side. This phenomena can also be observed in the following plots and can be explained by finite wing theory: because at the end of the wing ($y/b = 1$) the pressure difference between the suction and pressure side is lost as the flow rolls up into a vortex, the overall lift is reduced relative to the airfoil lift predicted for an infinite wing section and induced drag is created. The lift distribution has its maximum in the middle ($y/b = 0$) and decreases to 0 at the end of the wing ($y/b = 1$). As such, one should expect that the area under the closed C_p curve is lower for $y/b = 0.72$ than $y/b = 0.45$. In Fig. 4.12, the angles of attack belonging to the constant part of the lift curve without any separation are plotted. The plots illustrate how the area under the C_p curve consistently grows, which corresponds to the linear increase of the lift curve. The pressure tap rows indicate that the lift grows primarily in the first half ($x/c < 0.5$) of the wing chord, while the largest portion is contributed by the first 25% ($x/c = 0.25$) of the chord. Again, the lower spanwise pressure tap row shows higher values than the top row. Fig. 4.13 shows a range of angles that are still part of the linear lift growth ($\alpha = 10°$ and $\alpha = 12°$), as well as angles where separation starts to occur ($\alpha = 14°$ and $\alpha = 16°$) for $\delta_F = 0°$. The lower pressure tap row ($y/b = 0.45$) shows a steady increase of C_p until $\alpha = 16°$. Then there is a significant drop of C_p (less negative) on the suction side at the leading edge of the airfoil, and a minor increase at the trailing edge. However, the airfoil is still capable of increasing the lift because of an increase in "suction pressure" between $x/c > 0.05$ and $x/c < 0.35$. It seems that there is a large vortex at $\alpha = 16°$ that increases the "virtual" thickness of the airfoil

(vortex lift), and consequently produces a higher lift in that region. At $y/b = 0.72$, this phenomenon has been mitigated because the vortex has lifted and turned into the freestream direction. A drop in pressure ($C_p < 0$) at the trailing edge for $y/b = 0.72$ suggests a separation at this point.

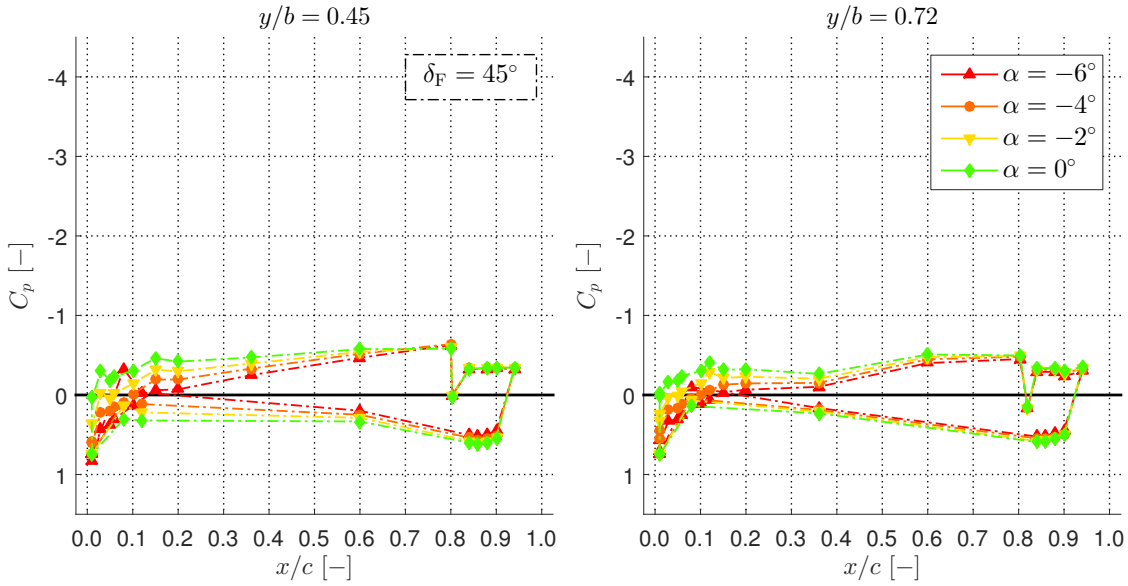

Figure 4.14: Pressure distribution C_p with $\delta_F = 45°$ for angles: -6°, -4°, -2°, and 0°.

Deflecting the flap to $\delta_F = 45°$ impacts the pressure distribution as well. At low angles (see Fig. 4.14) the deflected flap is still able to produce a considerable amount of lift that is created in the second half ($x/c > 0.5$) of the wing (flap effect). There are small differences for the two pressure tap rows at these low angles, due to the fact that the deflected flap dominates the flow regime. The suction pressure drop appears at $x/c = 0.8$, where the flap hinge is located. The pressure plot indicates a separation over the flap ($C_p < 0$, constant).

This continues for the angles that are part of the linear lift increase in Fig. 4.15. The additional lift compared to the non-deflected flap comes again from the second half of the wing ($x/c > 0.5$), and is a consequence of the flap deflection. However, the additional lift increments from increasing the angle of attack seem to come primarily from the first half of the wing ($x/c < 0.5$). The difference between the two pressure rows gets a little bit more apparent here, especially on the pressure side, where the lower row ($y/b = 0.45$) can cover a much larger area.

The higher angles of attack, illustrated in Fig. 4.16, show the most interesting flow features. As it can be seen in Fig. 4.10, the separation occurs about 2° earlier with the deflected flap. Similar to the

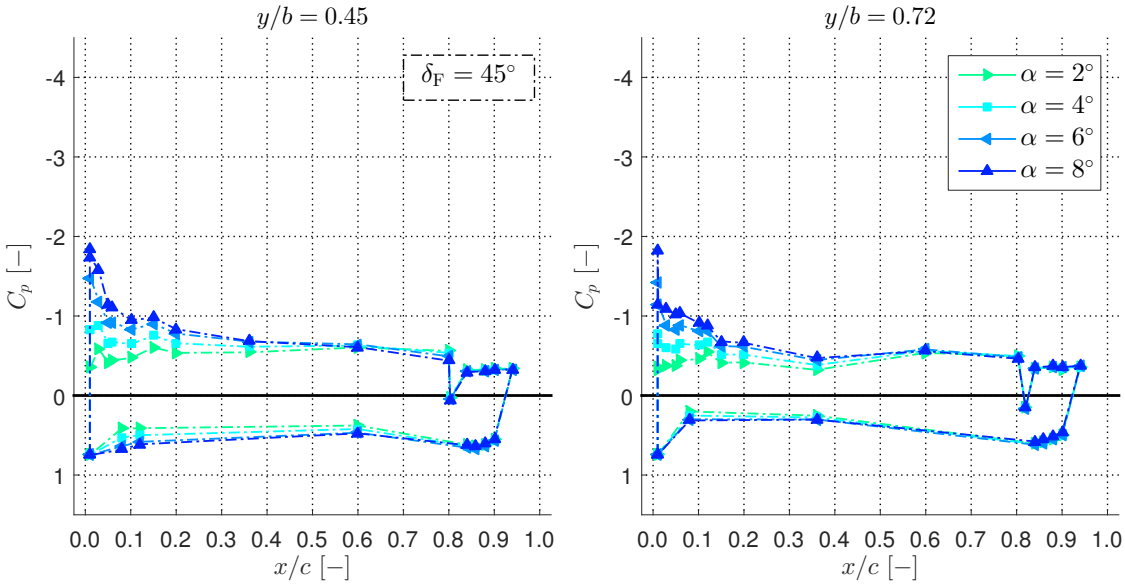

Figure 4.15: Pressure distribution C_p with $\delta_F = 45°$ for angles: 2°, 4°, 6°, and 8°.

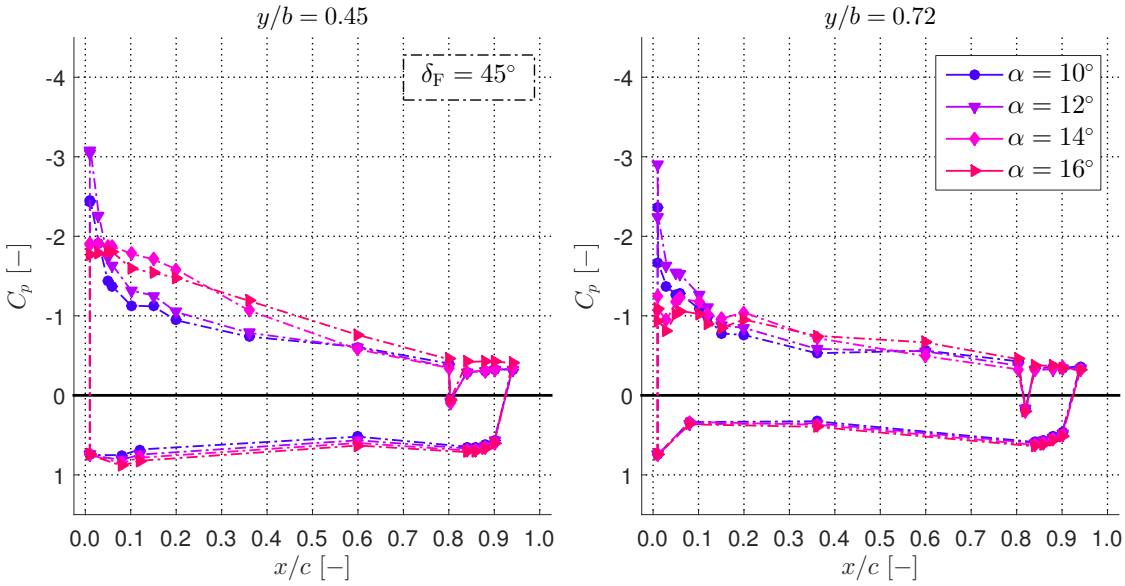

Figure 4.16: Pressure distribution C_p with $\delta_F = 45°$ for angles: 10°, 12°, 14°, and 16°.

non-deflected case, once the leading edge separation occurs, there's a decrease of suction pressure at the leading edge but an increased pressure between $x/c = 0.1$ and $x/c = 0.5$. This seems to be the separation bubble that "virtually" thickens the airfoil and therefore produces additional lift (vortex lift). The upper pressure tap row, like in the previous case, loses pressure (less suction) at the leading edge but can't recover it by making use of the separation bubble (vortex lift).

4.3.2 Reynolds Dependence of the Model

The statement of work stated a dynamic pressure of 30 psf (≈ 50 m/s). However, to achieve higher C_μ values it can be beneficial to reduce the wind tunnel speed. Looking at Eq. (5.1), one can conclude that any reduction in wind tunnel speed will be squared and therefore have a huge impact on the actual C_μ value. Nevertheless, it is important to verify that such a reduction in speed won't affect the results. A common way to do so is to prove Reynolds-independence of flow conditions, meaning that by changing the Reynolds number other dimensionless quantities such as C_L would still yield the same results. The obvious connection between the Reynolds number and C_μ is the wind tunnel speed.

The Reynolds independence test was done for both the non-deflected and the deflected flap. For both configurations the tunnel speed started at the prescribed 50 m/s (≈ 30 psf), and was then subsequently reduced to 20 m/s. Another reduction to 10 m/s would have been possible, but the Lucas Wind Tunnel and its instrumentation are not designed for such low speeds, and therefore testing was omitted. Fig. 4.17 summarizes the wing characteristics for the non-deflected flap at different wind tunnel speeds. On the top left, the lift coefficient remains constant up to about $\alpha = 5°$. Subsequently, the lowest speed (20 m/s) starts to deviate by about 10%. The case with a tunnel speed of 30 m/s is closer to the baseline case (50 m/s) with a deviation of less than 5%. When the wind tunnel speed is set to 40 m/s, it collapses with the 50 m/s baseline. The main explanation for this is that frictional losses in boundary layers decrease with increasing Reynolds number. In laminar flow the momentum thickness decreases with $\theta/x \sim \mathrm{Re}^{-1/2}$; however, in turbulent flow it is $\theta/x \sim \mathrm{Re}^{-0.2}$. Thus at lower Reynolds numbers the losses are larger, resulting in earlier separation of the flow, and hence non-linearity in C_L vs. α; in this case, this occurs at $\alpha = 5°$. The drag coefficient C_D vs. angle of attack α plot shows high agreement for all wind tunnel speeds except for the lowest one of 20 m/s. The drag in that case is lower, which contradicts the previous statement of the growing boundary layer thickness. This is due to the earlier separation and a reduction in lift that results in a reduction in induced drag $C_{D_i} \sim C_L^2$ based on the lifting-line theory. The C_L vs. C_D plot at the bottom left seems to closely follow the behavior of the C_L vs. α plot, with slightly higher deviation in terms of percentage. The pitching moment coefficient C_m seems to agree well for all wind tunnel speeds. Based on these observation, it can be concluded that the pitching moment of the non-deflected wing

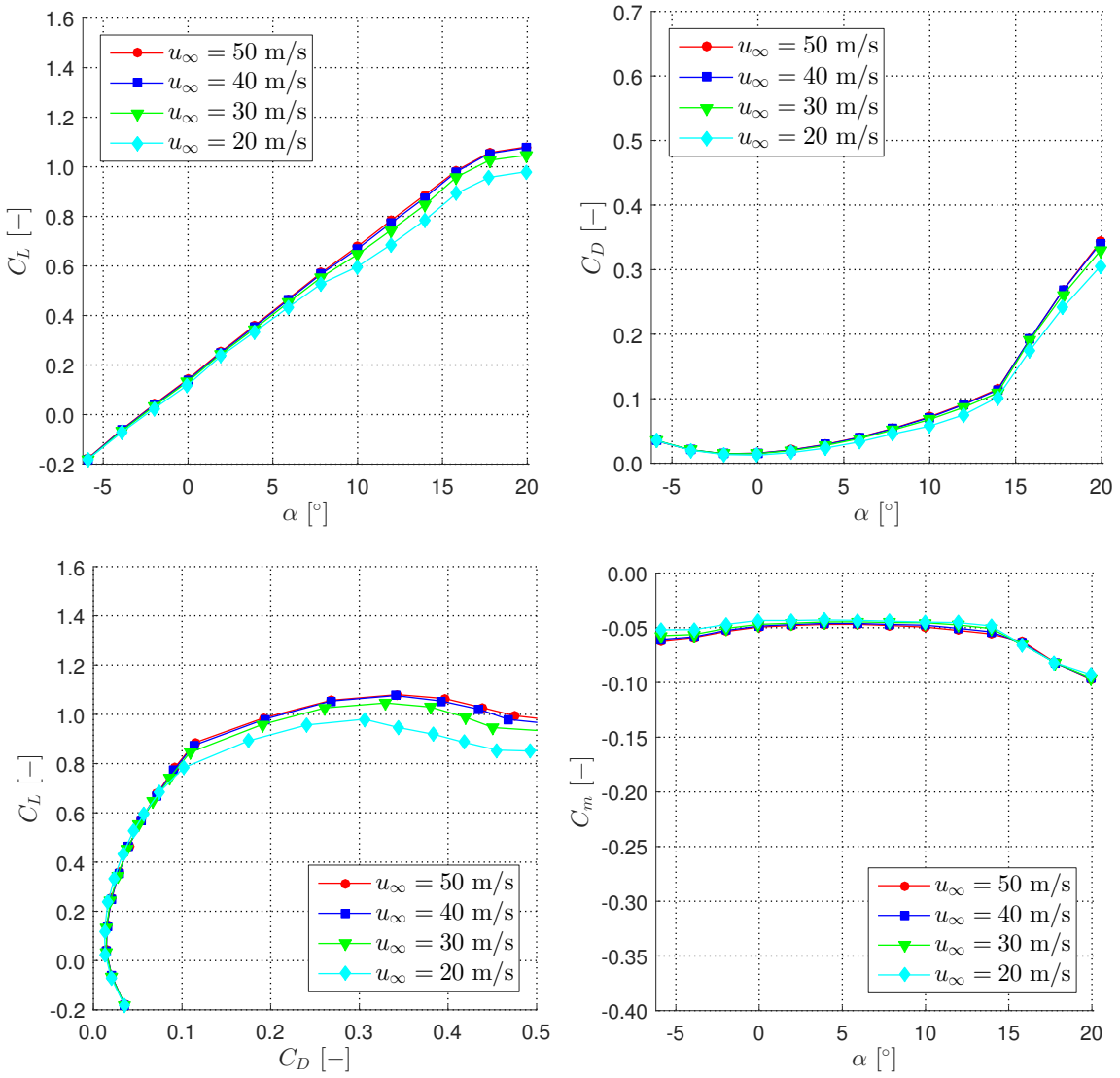

Figure 4.17: Reynolds independence for the non-deflected flap $\delta_F = 0°$.

is fully Reynolds-independent in the speed range of interest. However, the same thing can't be said about the lift coefficient C_L and the drag coefficient C_D. Both deviate from the proposed baseline case of 50 m/s, when the wind tunnel speed drops below 40 m/s. As a consequence, it was decided to not run the experiments at a speed lower than 40 m/s to provide full Reynolds-independence of the results. The reduction of wind tunnel speed from 50 to 40 m/s (25%) leads to an increase of C_μ by a factor of roughly 1.5.

The same test was repeated for the deflected flap. Due to the extreme flap deflection, it was not certain that the Reynolds-independence would stay the same because of the introduction of a "forced" separation over the flap. The results are presented in Fig. 4.18. Starting with lift coefficient C_L vs.

angle of attack α, one can see that this time, the data points are on top of each other until $C_{L,\max}$ is reached at $\alpha = 16°$. Afterwards the baseline case (50 m/s) is able to retain a slightly higher lift compared to all the other cases, yet the difference is minor on the order of 3%. Compared to the non-deflected flap, which is dominated by frictional losses in boundary layers, here the separation is initiated by the flap deflection. Thus the agreement at different Reynolds numbers is higher. For C_D vs. α the data points fully collapse, and the same is true for C_m vs. α. The minor difference in the bottom left plot (C_L vs. C_D) is a direct consequence of the small difference in lift. However, the data shows a high Reynolds-independence especially, in the region of major interest ($10° < \alpha < 14°$). To match the previous case, it was decided to also use a wind tunnel speed of 40 m/s for the deflected case.

4.3.3 Configuration 1: Steady Blowing with $\delta_F = 0°$

Configuration 1 represents steady blowing actuation for all slots at 1%, 10%, and 80% with the non-deflected flap $\delta_F = 0°$. Combinations of mass flow rates of 0 kg/h, 25 kg/h, and 50 kg were tested at every slot, which yields 27 cases in total. Additionally, every slot was subjected to a mass flow rate of 75 kg/h to reach higher C_μ values.

Because no combinatory effects could be observed, every AFC location will be discussed independent from the others. First, let's focus on the impact of the 1% slot. Data was taken at four different mass flow rates at 0 kg/h (baseline, no blowing), 25 kg/h, 50 kg/h, and 75 kg/h. The 10% and 80% slots were not subjected to any mass flow rate during this test. Fig. 4.19 summarizes the force balance data acquired. On the top left, the lift coefficient C_L vs. the angle of attack α: the curves are close together, which makes this plot difficult to interpret. The plot on the top right was created to highlight the differences of the lift coefficient C_L between the baseline and the actuated cases. Now it is evident that steady blowing at the 1% slot has no effect for 25 kg/h ($C_\mu = 0.011\%$) and 50 kg/h ($C_\mu = 0.042\%$). Even at 75 kg/h ($C_\mu = 0.095\%$) only a minor benefit in the attached region of the flow ($\alpha < 14°$) can be observed. Once separation occurs ($\alpha > 14°$), blowing is deleterious with regard to lift. The higher the mass flow rate, the more the lift is reduced. There is only a minor penalty in drag according to the plot at the bottom left. The pitching moment coefficient C_m doesn't seem to be affected at all. Note that the C_μ values are very low due to the large slot opening.

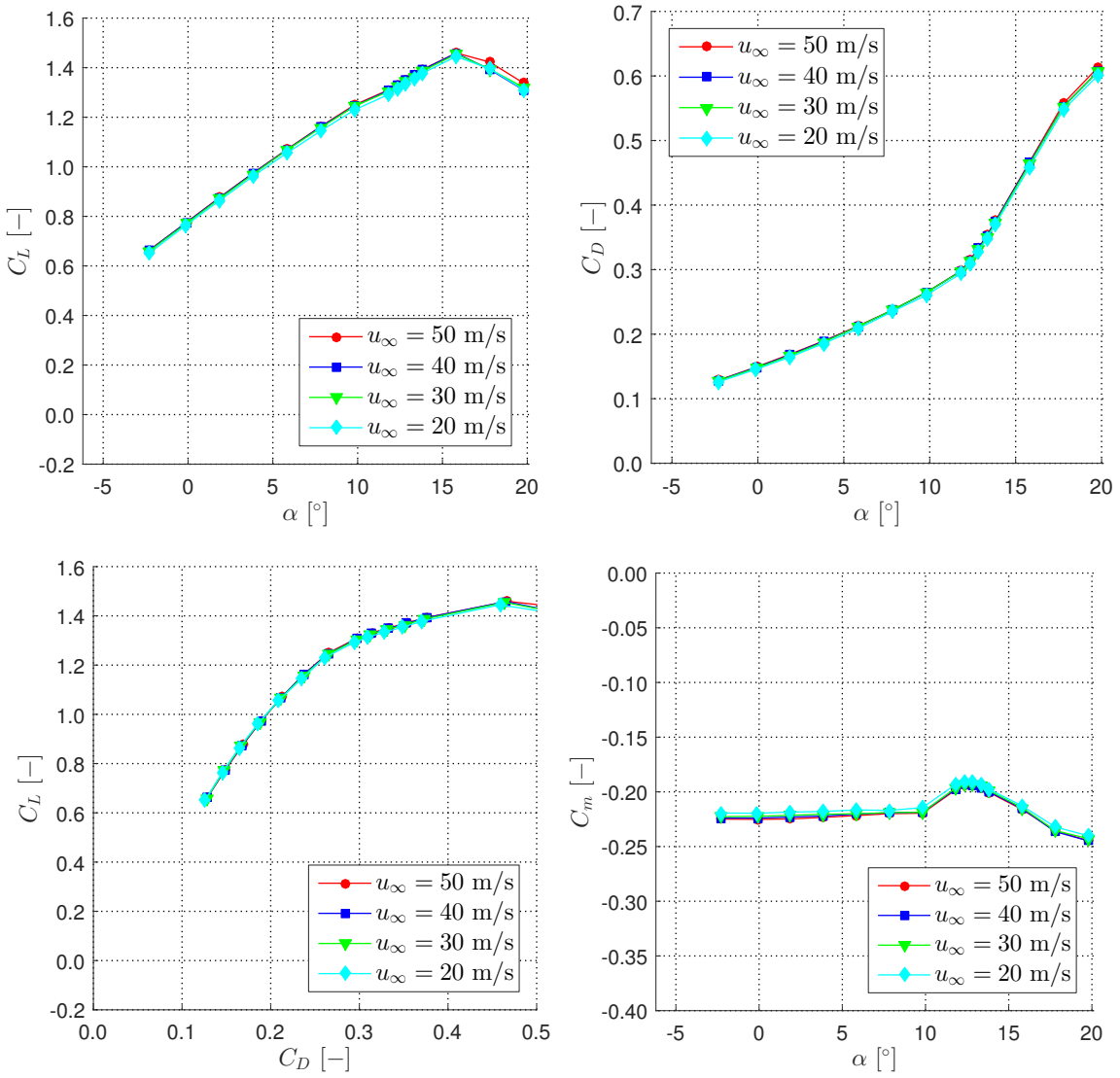

Figure 4.18: Reynolds independence for the deflected flap $\delta_F = 45°$.

The pressure coefficient C_p plots in Figs. 4.20 to 4.22 confirm the previous statement that there is no effect when blowing is applied. The pressures of a blown slot (solid line) and the baseline (dashed line) lie exactly on top of each other, except right at the slot exit. However, the little increase in suction pressure diminishes so quickly that it has no effect on the actual lift. Once separation starts to occur, the corresponding pressure (see Fig. 4.22) also shows the deleterious effect of the blowing with increasing angle of attack α.

In Figs. 4.23 and 4.24 the effects of slot blowing over the wing are visualized by tufts. Each tuft image compares a baseline (no blowing) and a blown case. The differences between these cases are illustrated by color: black indicates no change, magenta stands for the baseline configuration, and

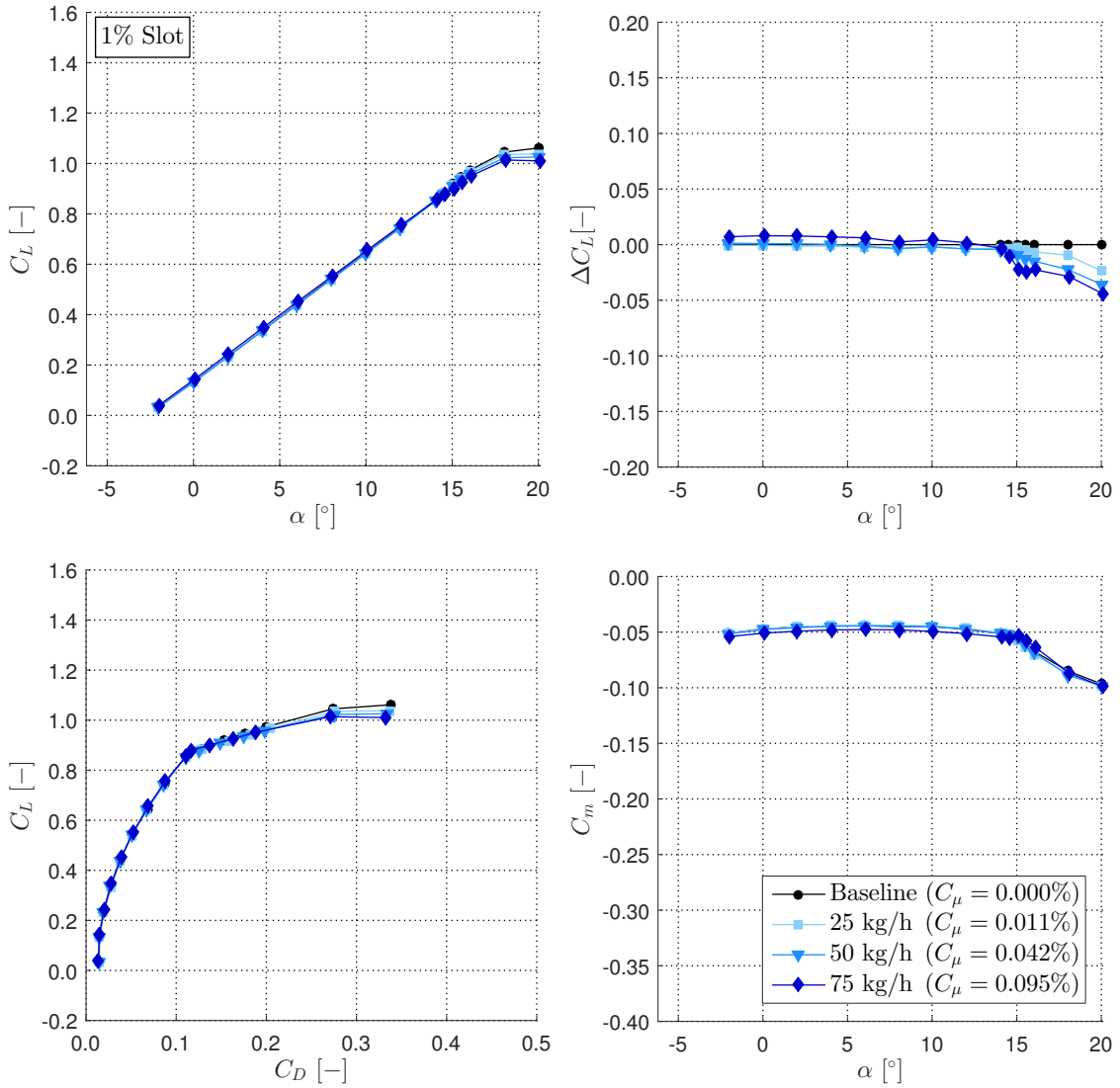

Figure 4.19: Impact of steady blowing with $\delta_F = 0°$ at the 1% slot with increasing mass flow rates compared to the baseline case (no blowing).

green represents the position of the tufts in the blown configuration. In other words, if one focuses on the parts with a lot of green and magenta, that's where blowing changes the flow regime. In Fig. 4.23 one can see that 1% blowing doesn't change anything, which is kind of what one would expect based on the force balance and pressure data. However, for $\alpha = 14.5°$ (Fig. 4.24), which is slightly after the separation started to occur, the effect of blowing at the 1% slot seems to have a high impact. In absence of blowing, a leading edge vortex is formed around $\alpha = 14°$ due to the small radius of curvature of the leading edge. The leading edge vortex (virtual chamber) develops quickly and at $\alpha = 14.5°$ it occupies almost 50% of the span and 30% of the chord. Although the leading edge suction pressure peak drops due to the bubble presence, there is still lift generated that is often

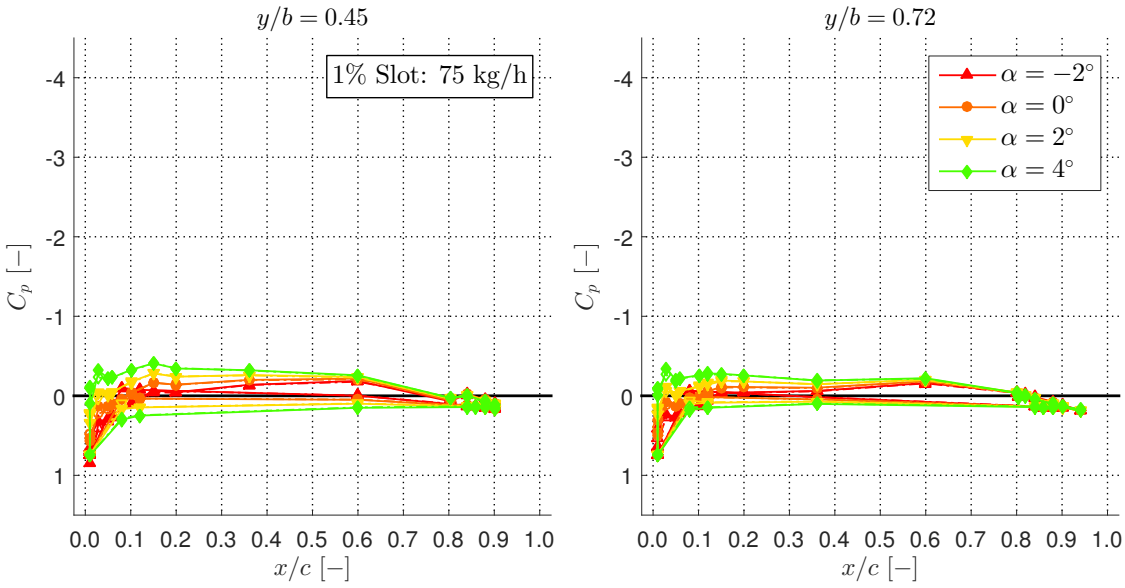

Figure 4.20: Comparison of pressure distribution C_p for $\delta_F = 0°$ with steady blowing from the 1% slot at a mass flow rate of 75 kg/h. Baseline (no blowing) is a dashed line, while the solid line represents the blowing case. Angles: -2°, 0°, 2°, 4°.

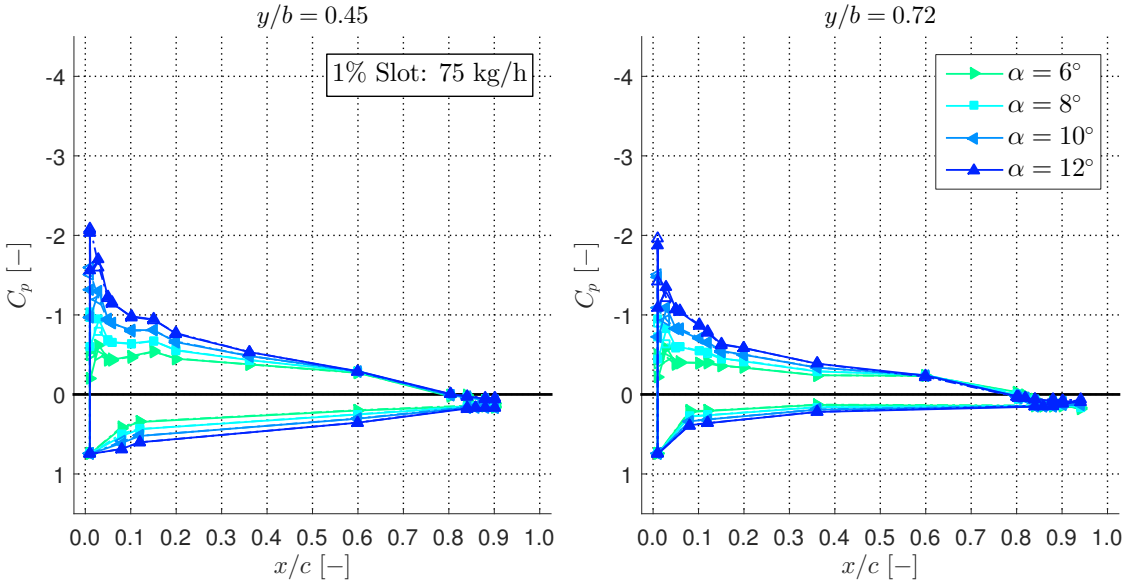

Figure 4.21: Comparison of pressure distribution C_p for $\delta_F = 0°$ with steady blowing from the 1% slot at a mass flow rate of 75 kg/h. Baseline (no blowing) is a dashed line, while the solid line represents the blowing case. Angles: 6°, 8°, 10°, 12°.

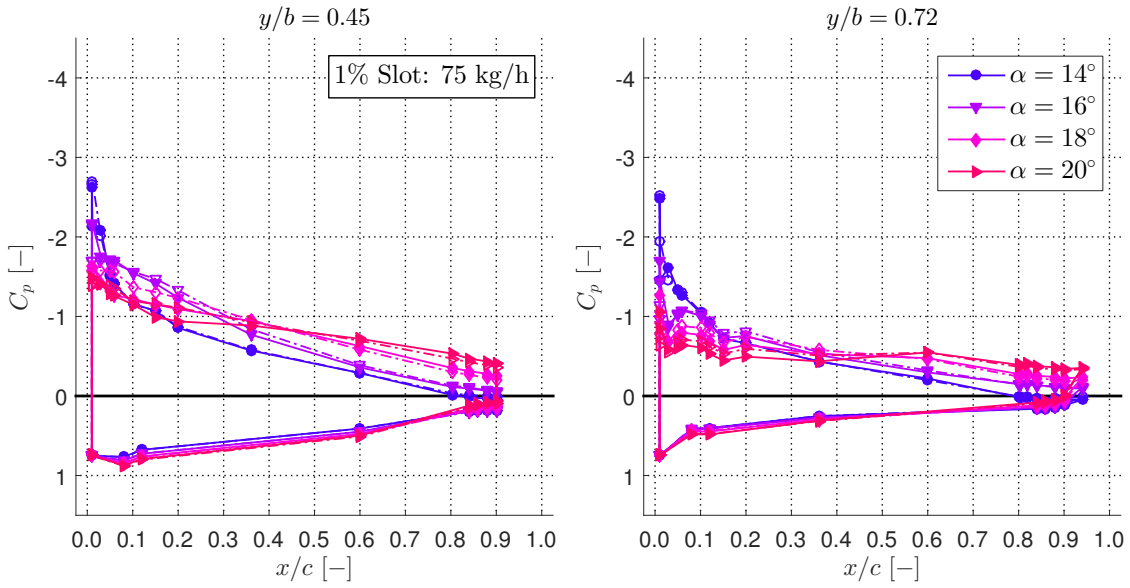

Figure 4.22: Comparison of pressure distribution C_p for $\delta_F = 0°$ with steady blowing from the 1% slot at a mass flow rate of 75 kg/h. Baseline (no blowing) is a dashed line, while the solid line represents the blowing case. Angles: 14°, 16°, 18°, 20°.

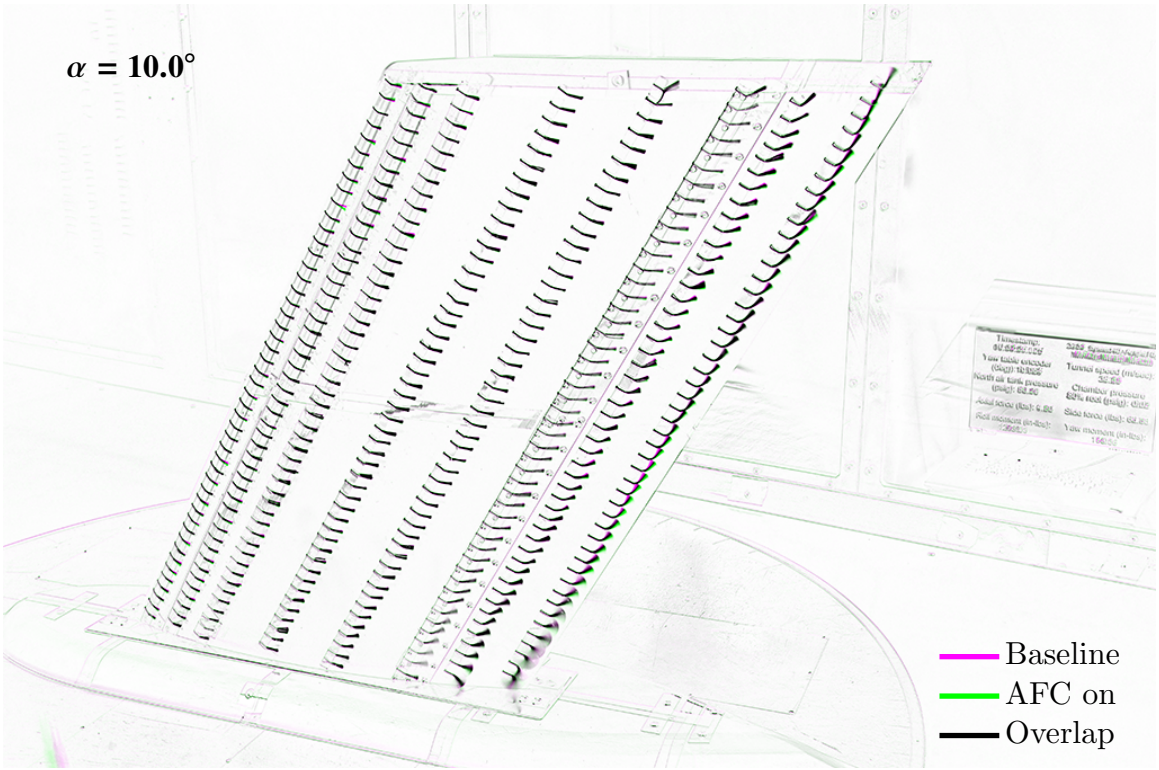

Figure 4.23: Tuft visualization for $\delta_F = 0°$ with steady blowing from the 1% slot at a mass flow rate of 75 kg/h and $\alpha = 10°$.

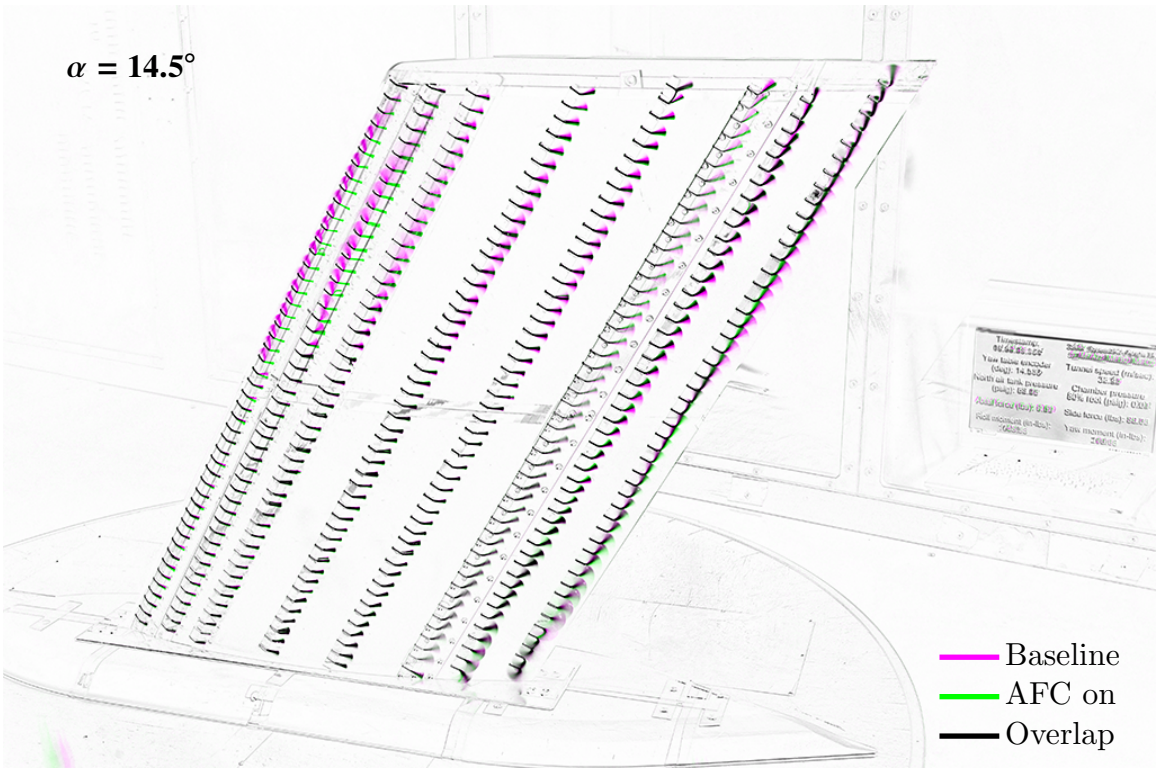

Figure 4.24: Tuft visualization for $\delta_F = 0°$ with steady blowing from the 1% slot at a mass flow rate of 75 kg/h and $\alpha = 14.5°$.

referred to as vortex lift. Blowing is able to control the separation bubble by reattaching nearly the entire separated region. The question now is why this visibly positive effect does not change the lift in a positive manner, but produces a negative impact. First, by eliminating the leading edge vortex, the vortex lift is eliminated as well. Second, the trailing edge of the wing seems to be important to control flow features, especially the lift, over the entire wing (more details to follow). The 1% slot blowing influences the trailing edge region as well, but instead of improving the flow environment, it actually enhances the spanwise cross-flow which is deleterious for lift. The combination of losing the vortex lift and increasing the trailing edge cross-flow are then responsible for the observed loss in lift.

Next, the 10% slot is investigated. Data was taken at the same mass flow rates as before: 0 kg/h (baseline, no blowing), 25 kg/h, 50 kg/h, and 75 kg/h. The results are shown in Fig. 4.25: like in the previous case, the steady blowing seems to have no effect on the lift. Even at a mass flow rate of 75 kg/h the benefit seems to be so minor that it could just be data noise. Also the deleterious effect after separation has occurred ($\alpha < 14°$) seems to be smaller compared to the 1% slot. The 10% slot

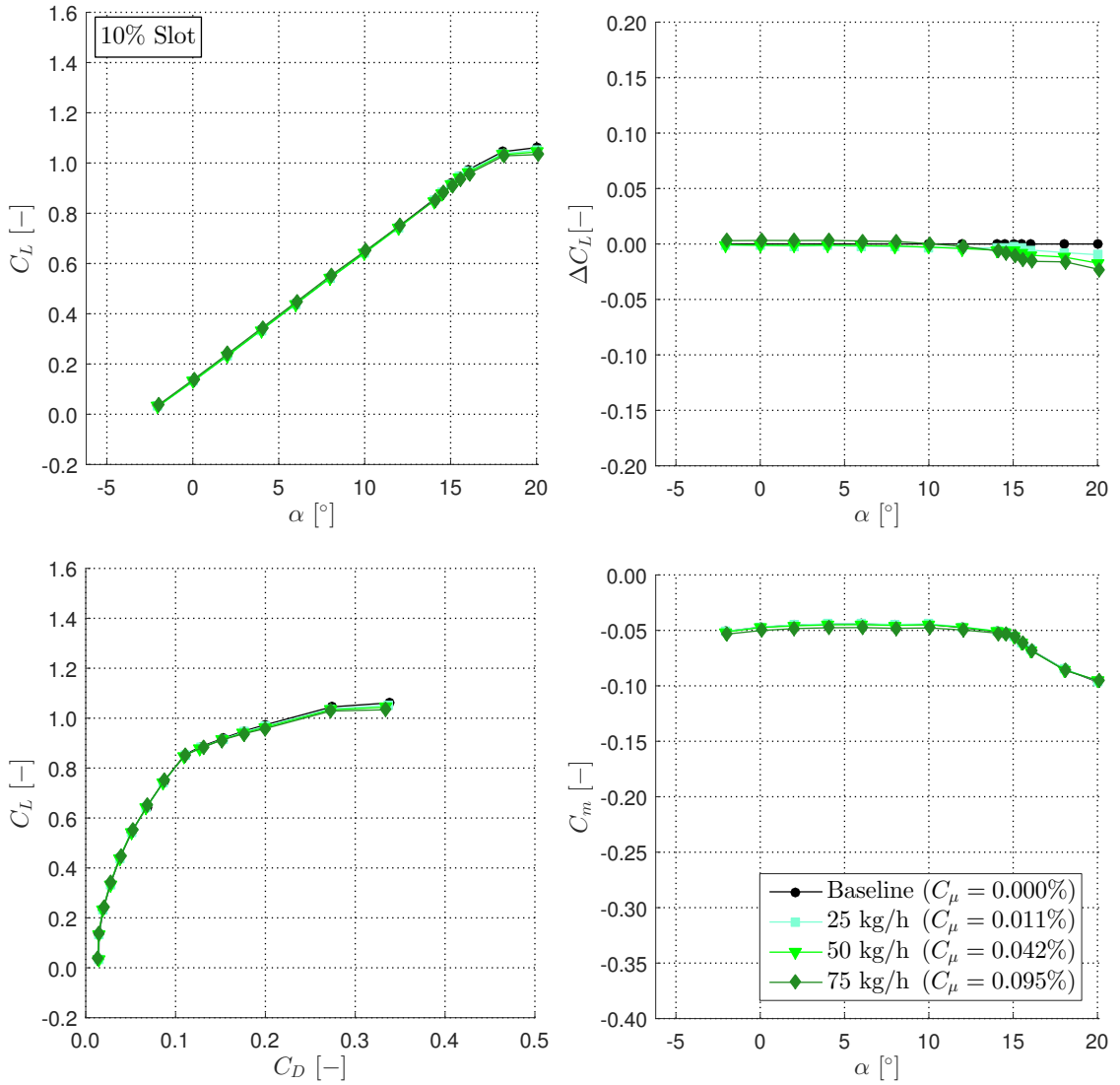

Figure 4.25: Impact of steady blowing with $\delta_F = 0°$ at the 10% slot with increasing mass flow rates compared to the baseline case (no blowing).

seems to have an even smaller effect, positively or negatively, than the 1% slot for steady blowing with no flap deflection ($\delta_F = 0°$).

A similar thing can be said about the pressure plots in Figs. 4.26 to 4.28. Again, the baseline curve (dashed) is barely visible because it is beneath the actuated curve. This means there are no pressure differences over the wing caused by steady blowing through the 10% slot. Only the pressure tap at $x/c = 0.1$ reads a small pressure difference, but that effect disappears quickly, so it doesn't lead to any noticeable lift advantage. Small deleterious differences at the leading edge in Fig. 4.28 are

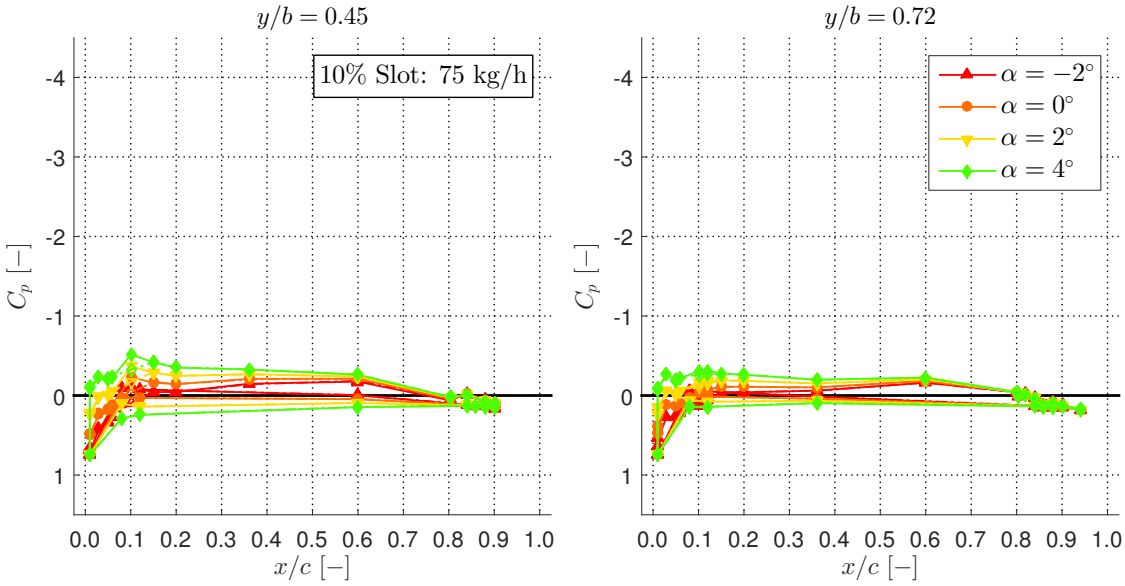

Figure 4.26: Comparison of pressure distribution C_p for $\delta_F = 0°$ with steady blowing from the 10% slot at a mass flow rate of 75 kg/h. Baseline (no blowing) is a dashed line, while the solid line represents the blowing case. Angles: -2°, 0°, 2°, 4°.

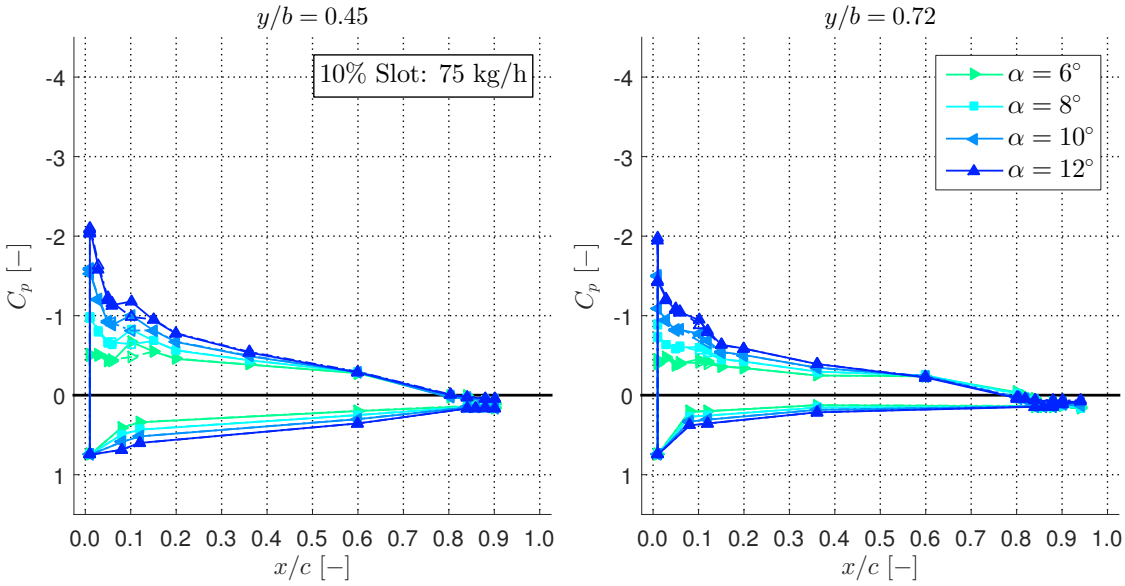

Figure 4.27: Comparison of pressure distribution C_p for $\delta_F = 0°$ with steady blowing from the 10% slot at a mass flow rate of 75 kg/h. Baseline (no blowing) is a dashed line, while the solid line represents the blowing case. Angles: 6°, 8°, 10°, 12°.

responsible for the lift reduction at higher angles of attack α. This is hinting toward vortex lift reduction.

The tuft image for $\alpha = 10°$ (Fig. 4.29) shows that there is no visible influence on the flow. At $\alpha = 14.5°$ (Fig. 4.30) there is only a partial reattachment compared to the 1% slot. Similarly, this

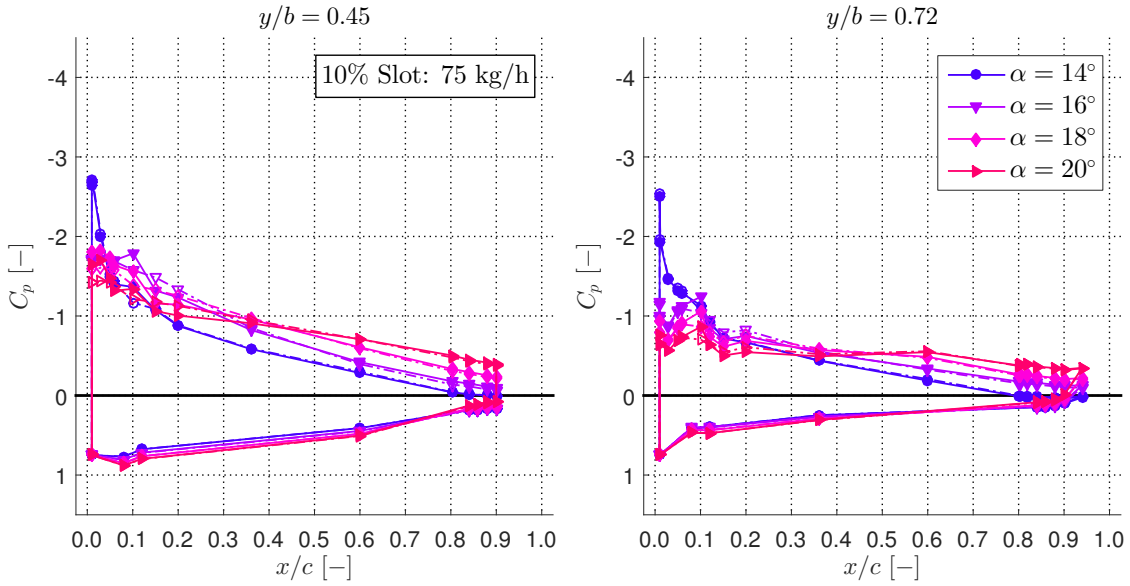

Figure 4.28: Comparison of pressure distribution C_p for $\delta_F = 0°$ with steady blowing from the 10% slot at a mass flow rate of 75 kg/h. Baseline (no blowing) is a dashed line, while the solid line represents the blowing case. Angles: 14°, 16°, 18°, 20°.

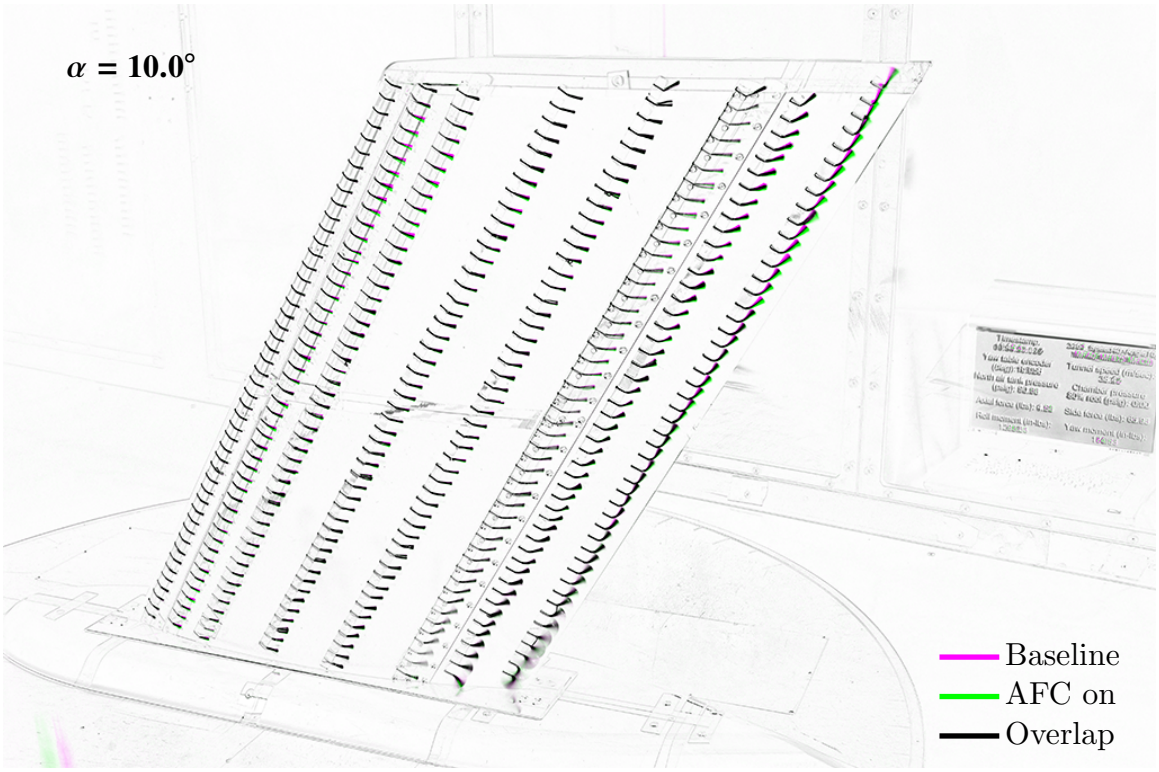

Figure 4.29: Tuft visualization for $\delta_F = 0°$ with steady blowing from the 10% slot at a mass flow rate of 75 kg/h and $\alpha = 10°$.

also influences the trailing edge (not well visible on this image), in that it increases the spanwise cross-flow. Because the influence of the 10% slot is smaller on the reattachment region (not a full

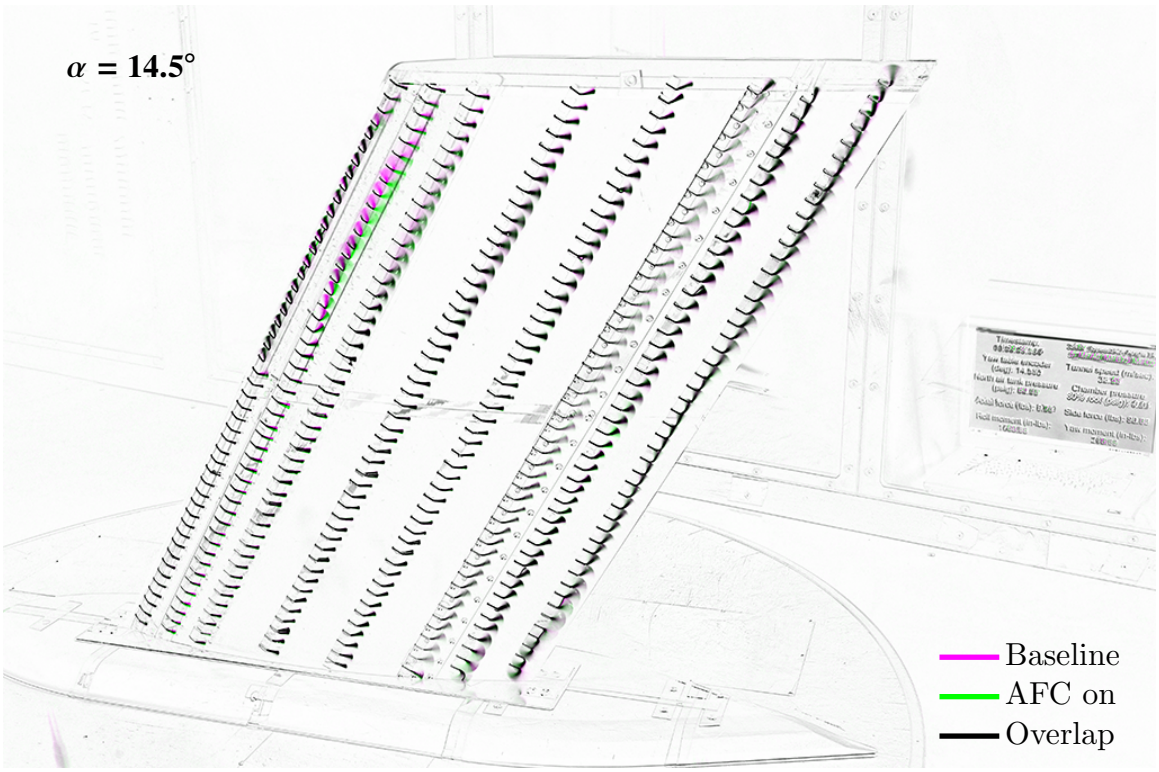

Figure 4.30: Tuft visualization for $\delta_F = 0°$ with steady blowing from the 10% slot at a mass flow rate of 75 kg/h and $\alpha = 14.5°$.

elimination of the vortex lift), it can be shown that the additional cross-flow at the trailing edge is smaller as well. As such, the deleterious effect of the blowing at the 10% slot is much weaker than at the 1% slot.

The 80% slot data is illustrated in Fig. 4.31. Again, the data consists of mass flow rates at 0 kg/h (baseline, no blowing), 25 kg/h, 50 kg/h, and 75 kg/h. The 1% slot and 10% were not actuated. The results for the 80% slots differ a little bit from the two previous cases. First, there is no deleterious effect after separation ($\alpha > 14°$). Second, there is a deleterious effect for low mass flow rates before separation occurs ($\alpha < 14°$), which turns into a "neutral" effect at 50 kg/h, and becomes a positive effect at 75 kg/h. The lift-drag curve on the bottom left side is not affected by any means. At a mass flow rate of 75 kg/h there is a small decrease of pitching moment coefficient C_m. Even though the results are still minor, this is the first slot that shows positive effects, specifically on the lift and pitching moment.

The pressure plots (Figs. 4.32 to 4.34) seem to be right on top of each other. At first, this his doesn't match with the results acquired from the force balance. However, the pressure taps only reach to

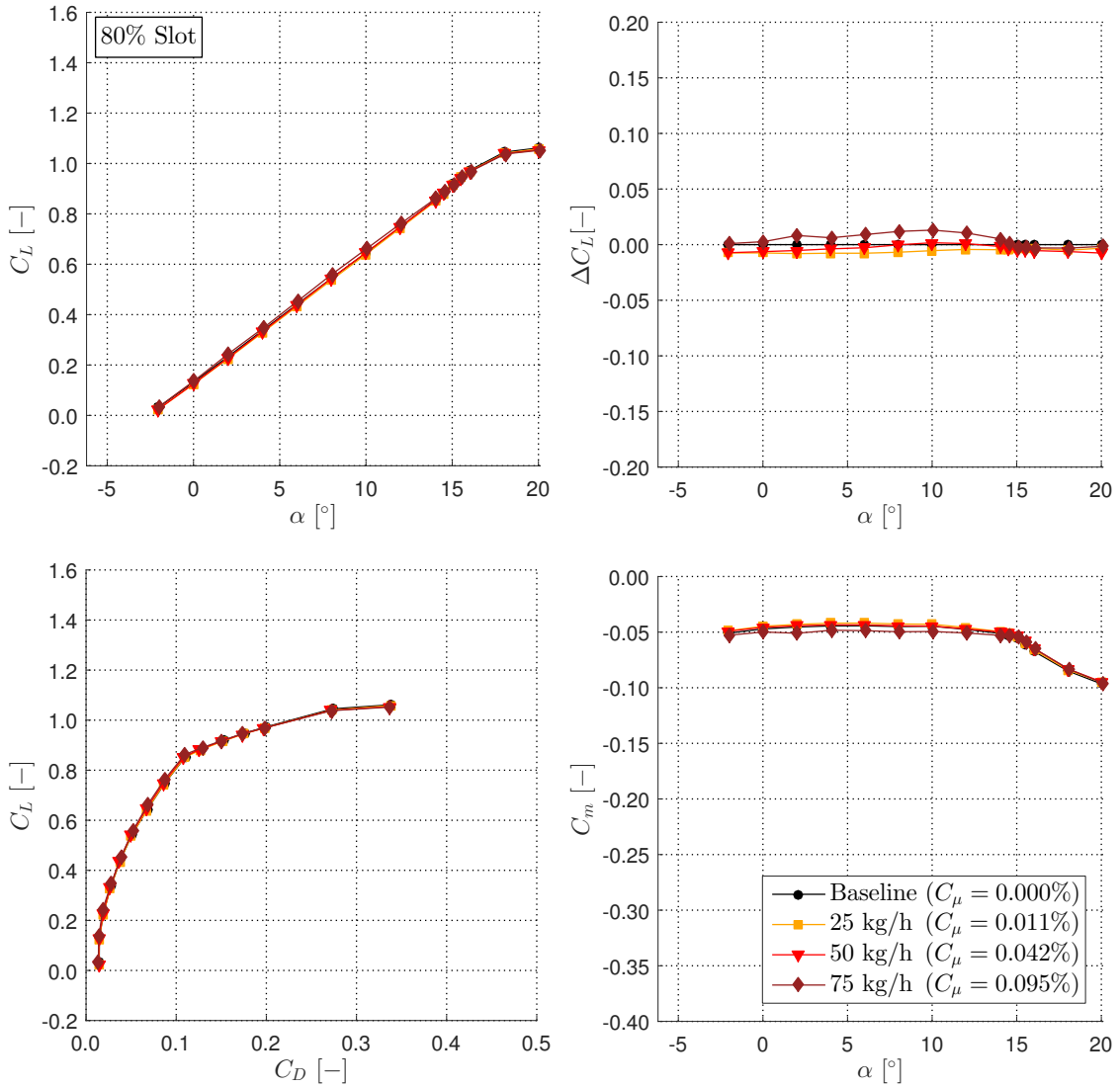

Figure 4.31: Impact of steady blowing with $\delta_F = 0°$ at the 80% slot with increasing mass flow rates compared to the baseline case (no blowing).

$x/c = 0.9$ due to space limitations and don't cover the second half of the flap. If one trusts the force balance measurements as well as the pressure tap measurements, the additional lift must have been created at the second half of the non-deflected flap. An explanation for this could be that the blowing is injected into a thick boundary layer on the verge of separation (note that $C_p = 0$ at the last point up to $\alpha = 14°$). This may thin the boundary layer and provide a positive results, defining the Kutta condition better and increasing lift. At higher angles of attack the flow separates and this effect diminishes. Interestingly, at the slot exit $x/c = 0.8$, there's a slight increase of suction pressure. This time it spans a wider range of the chord. Consequently, one would expect a slight lift benefit.

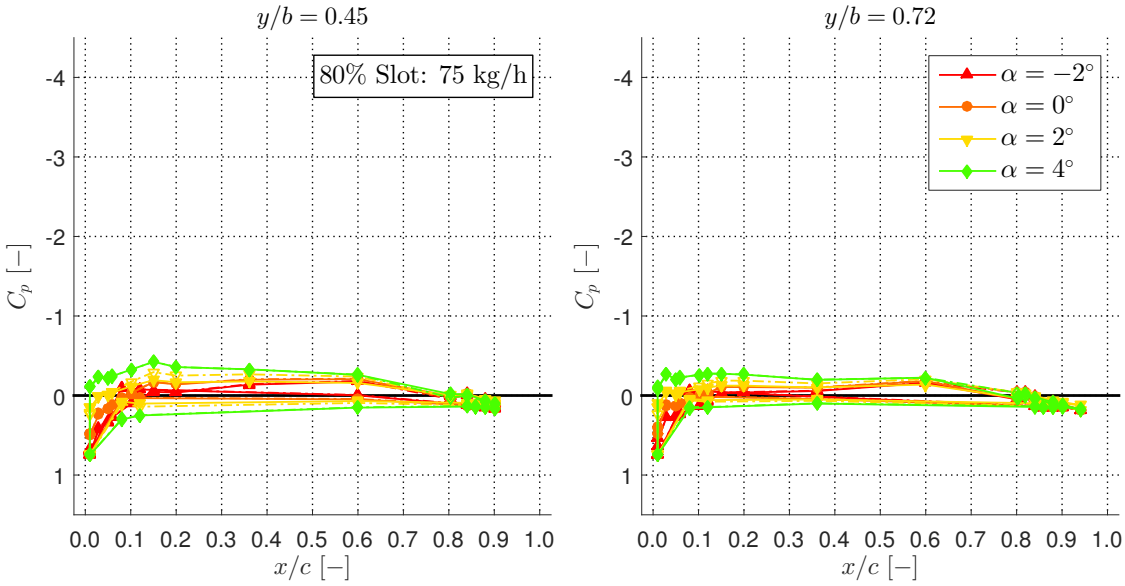

Figure 4.32: Comparison of pressure distribution C_p for $\delta_F = 0°$ with steady blowing from the 80% slot at a mass flow rate of 75 kg/h. Baseline (no blowing) is a dashed line, while the solid line represents the blowing case. Angles: -2°, 0°, 2°, 4°.

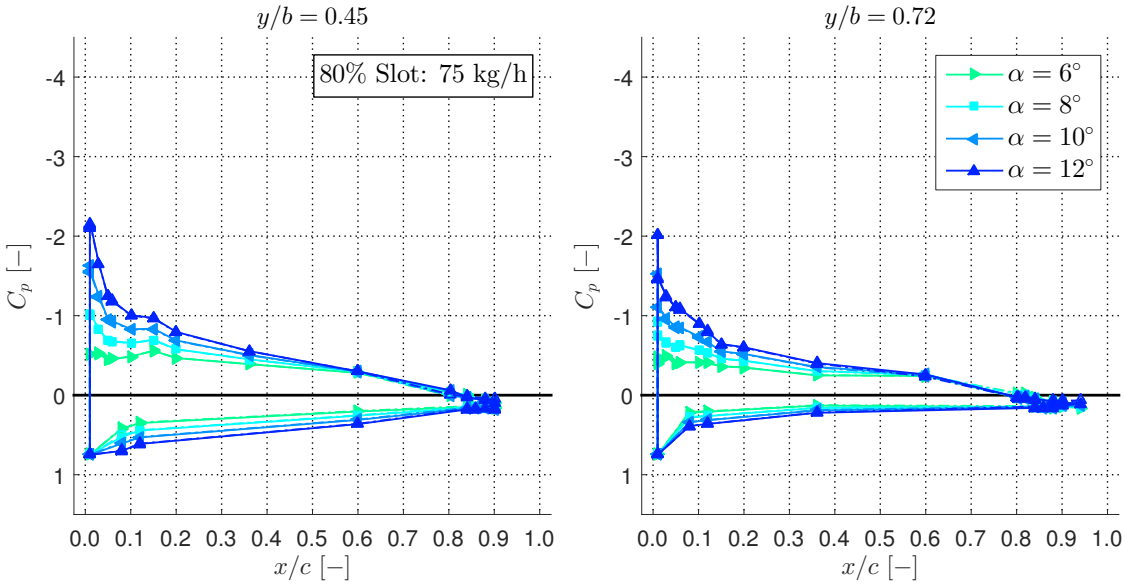

Figure 4.33: Comparison of pressure distribution C_p for $\delta_F = 0°$ with steady blowing from the 80% slot at a mass flow rate of 75 kg/h. Baseline (no blowing) is a dashed line, while the solid line represents the blowing case. Angles: 6°, 8°, 10°, 12°.

However, this benefit seems to get eaten up by the losses close to the trailing edge where no pressure taps are present.

The tuft visualization in Fig. 4.35 at $\alpha = 10°$ reveals that steady blowing at the 80% slot is capable of slightly reducing the spanwise cross-flow. This might yield the proclaimed redefinition of the

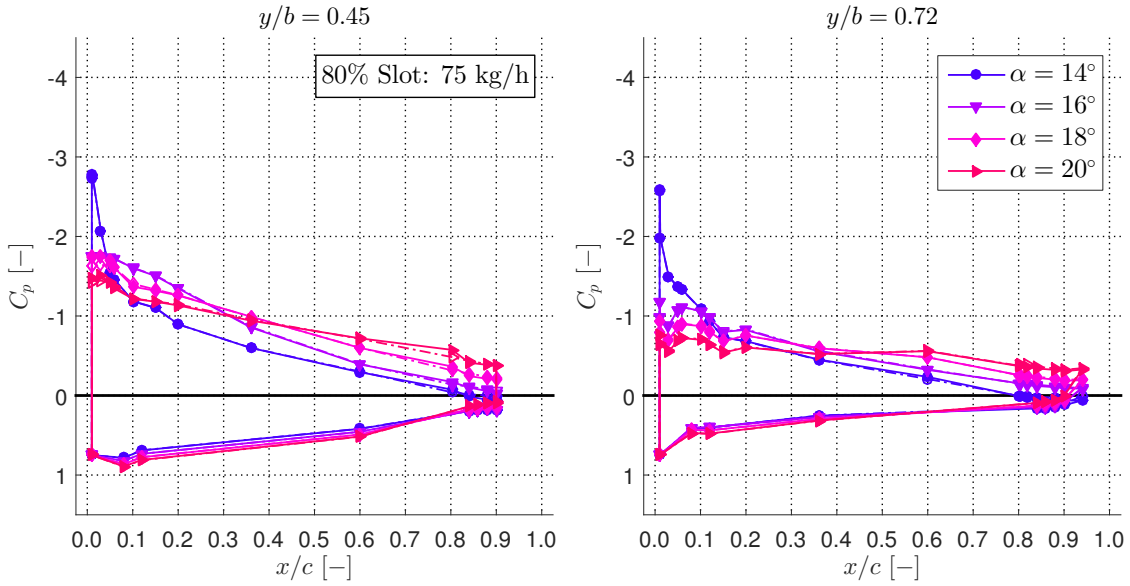

Figure 4.34: Comparison of pressure distribution C_p for $\delta_F = 0°$ with steady blowing from the 80% slot at a mass flow rate of 75 kg/h. Baseline (no blowing) is a dashed line, while the solid line represents the blowing case. Angles: 14°, 16°, 18°, 20°.

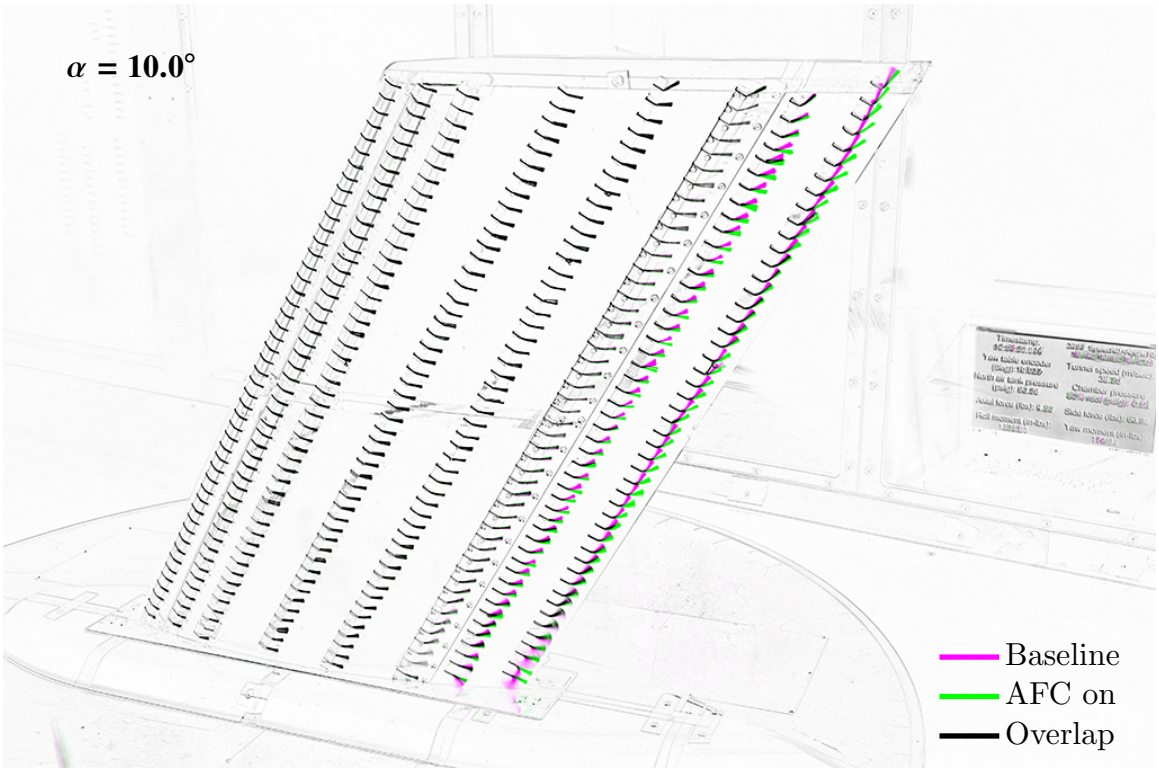

Figure 4.35: Tuft visualization for $\delta_F = 0°$ with steady blowing from the 80% slot at a mass flow rate of 75 kg/h and $\alpha = 10°$.

Kutta condition, and hence provide additional lift. On top of that, 80% blowing does not interfere with the leading edge vortex, and thus does not eliminate the vortex lift. At $\alpha = 14.5°$ (Fig. 4.36) a

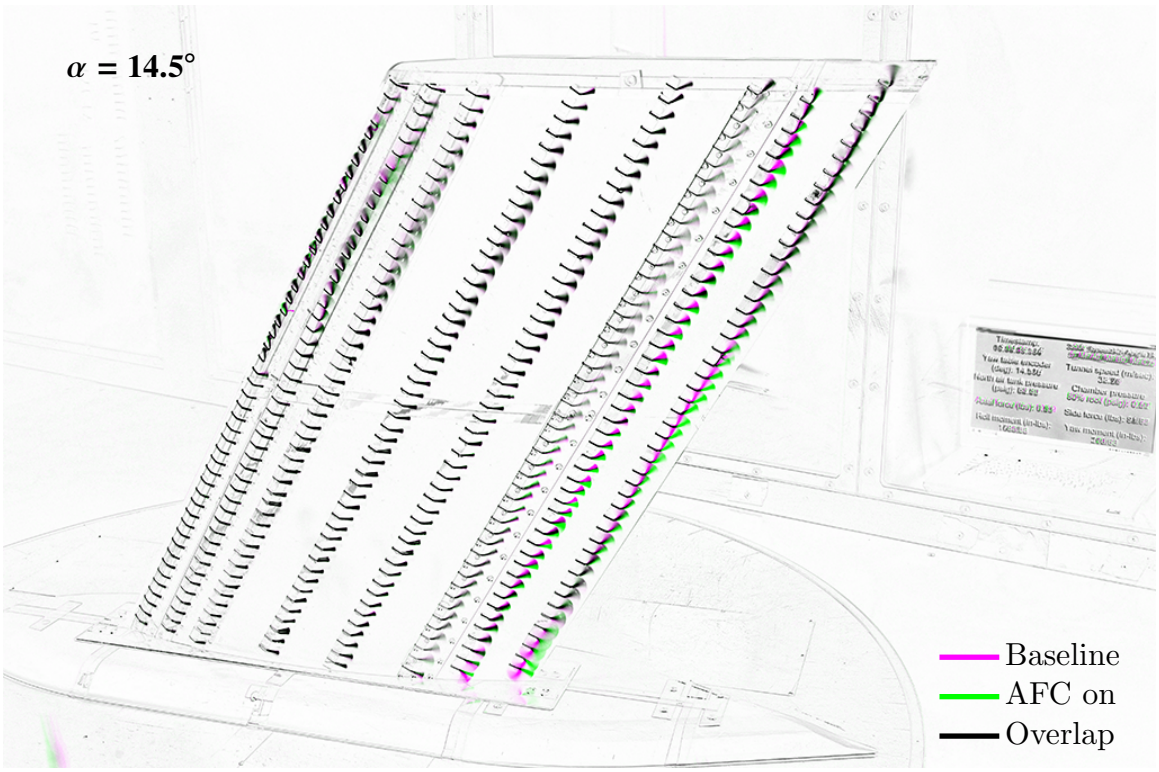

Figure 4.36: Tuft visualization for $\delta_F = 0°$ with steady blowing from the 80% slot at a mass flow rate of 75 kg/h and $\alpha = 14.5°$.

reduction of spanwise cross-flow for the lower part of the wing (roughly $y/b < 0.6$) can be observed. At higher spanwise locations, there is no correction, and the blowing seems to hurt the flow regime, which leads to an overall lift decrease at these angles compared to the baseline case.

4.3.4 Configuration 2: Steady Blowing with $\delta_F = 45°$

Configuration 2 was defined as steady blowing for all slots at 1%, 10%, and 80% with the deflected flap $\delta_F = 45°$. Again, all possible combinations of mass flow rates of 0 kg/h, 25 kg/h, and 50 kg were tested at every slot (total of 27 combinations). Additionally, every slot was tested at a mass flow rate of 75 kg/h while the other two slots were turned off.

Like the previous section, let's look at the impact of every single slot as no combinatory effects could be observed. A steady-blown 1% slot is presented in Fig. 4.37. To make this easily comparable to the previous cases, the mass flow rates are exactly the same: 0 kg/h (baseline, no blowing), 25 kg/h, 50 kg/h, and 75 kg/h. The scale of the plots was kept the same as well. Due to the fact that the slots are not influenced by adding the flap, the C_μ values haven't changed as well, which means they stay comparably low. The lift coefficient C_L vs. angle of attack α plot shows the same results as

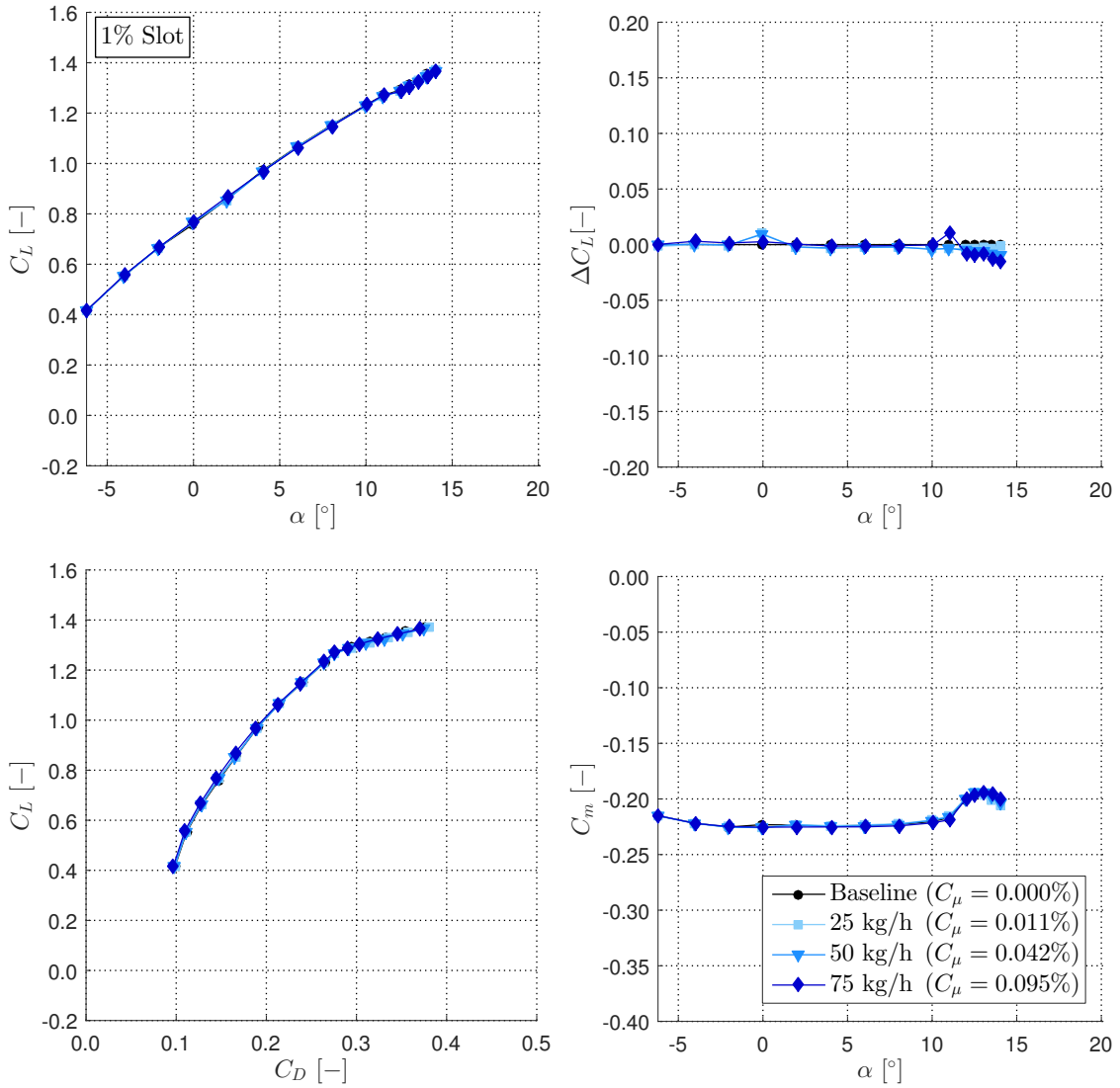

Figure 4.37: Impact of steady blowing with $\delta_F = 45°$ at the 1% slot with increasing mass flow rates compared to the baseline case (no blowing).

the non-deflected flap: the curves are on top of each other and steady blowing has no effect in the attached region ($\alpha < 12°$). Once the flow separates ($\alpha > 12°$), the effect of blowing is deleterious. The ΔC_L plot reveals tiny differences in the attached region, but these seem to exist due to a small measurement error rather than an actual flow effect. In other words, steady blowing from the 1% slot over a flap at $\delta_F = 45°$ seems to have no effect on lift. Also the drag is neither reduced nor increased. The same applies for the the pitching moment coefficient C_m.

Figs. 4.38 to 4.40 show the pressure plots for a mass flow rate of 75 kg/h. As expected, there is no difference between the baseline (dashed line) and the actuated case (solid line) for $\alpha < 11°$. For

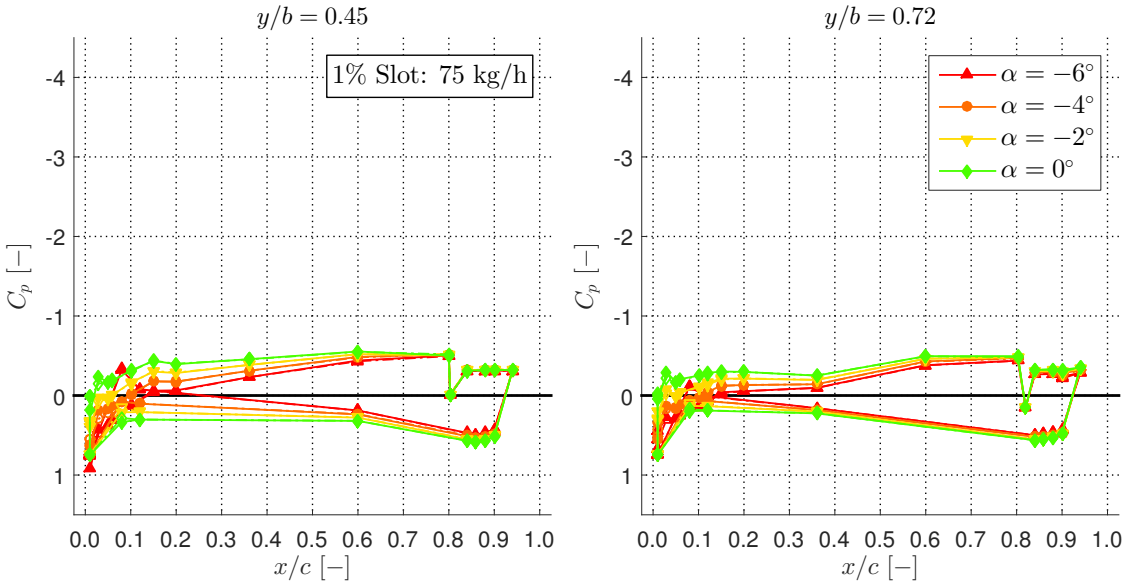

Figure 4.38: Comparison of pressure distribution C_p for $\delta_F = 45°$ with steady blowing from the 1% slot at a mass flow rate of 75 kg/h. Baseline (no blowing) is a dashed line, while the solid line represents the blowing case. Angles: -6°, -4°, -2°, 0°.

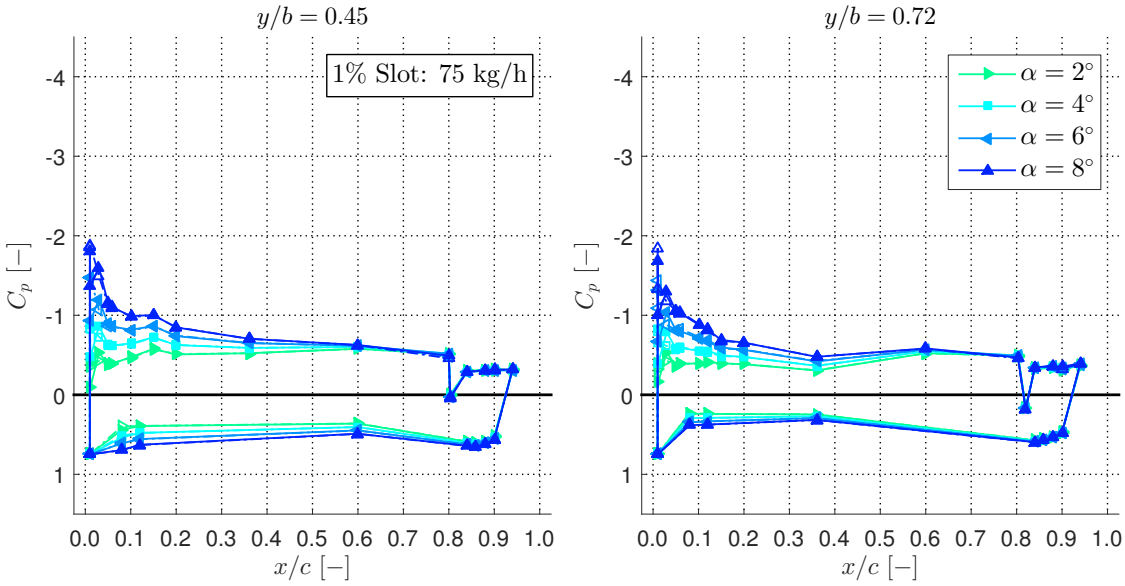

Figure 4.39: Comparison of pressure distribution C_p for $\delta_F = 45°$ with steady blowing from the 1% slot at a mass flow rate of 75 kg/h. Baseline (no blowing) is a dashed line, while the solid line represents the blowing case. Angles: 2°, 4°, 6°, 8°.

$\alpha = 12°$ and $\alpha = 14°$, the pressure is slightly reduced for $0.1 < x/c < 0.4$, which explains the deleterious effect on the lift at these angles. This is fundamentally different than the case with the non-deflected flap, where no apparent effect could be observed. Based on the results of the 80% slot

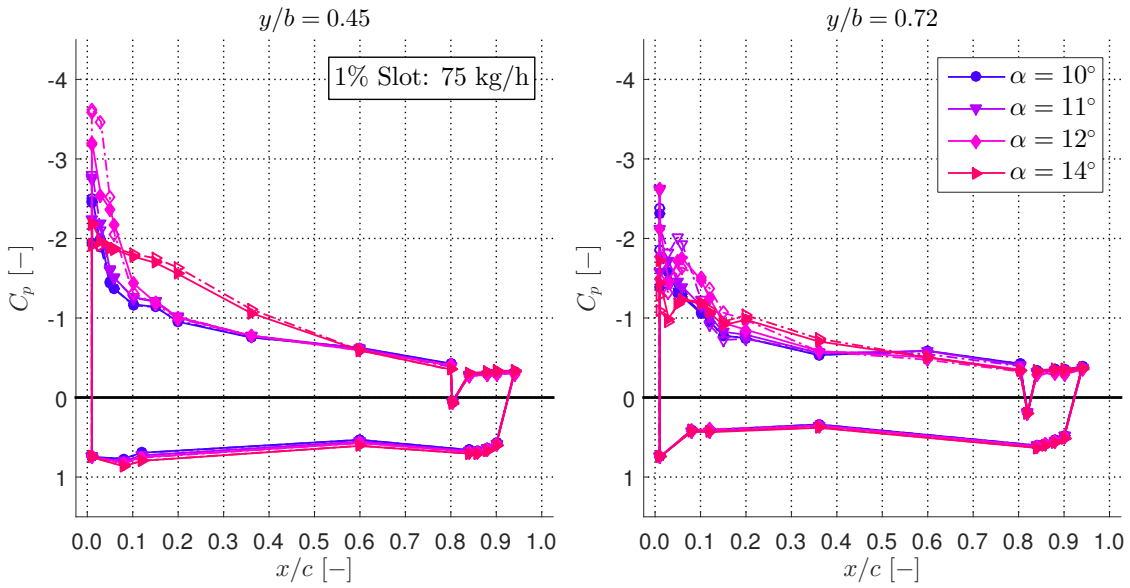

Figure 4.40: Comparison of pressure distribution C_p for $\delta_F = 45°$ with steady blowing from the 1% slot at a mass flow rate of 75 kg/h. Baseline (no blowing) is a dashed line, while the solid line represents the blowing case. Angles: 10°, 11°, 12°, 14°.

(see later), it is assumed that the lift benefit/reduction is generated close to the trailing edge. On top of that, there seems to be a loss of vortex lift.

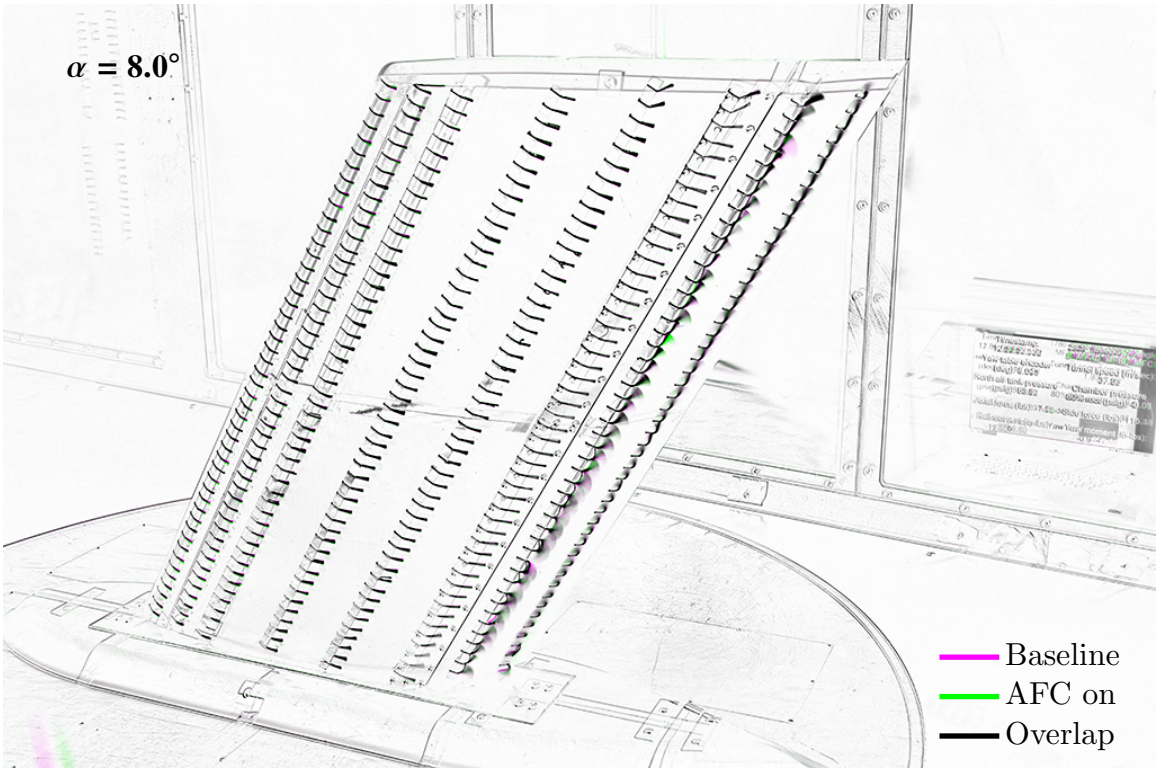

Figure 4.41: Tuft visualization for $\delta_F = 45°$ with steady blowing from the 1% slot at a mass flow rate of 75 kg/h and $\alpha = 8°$.

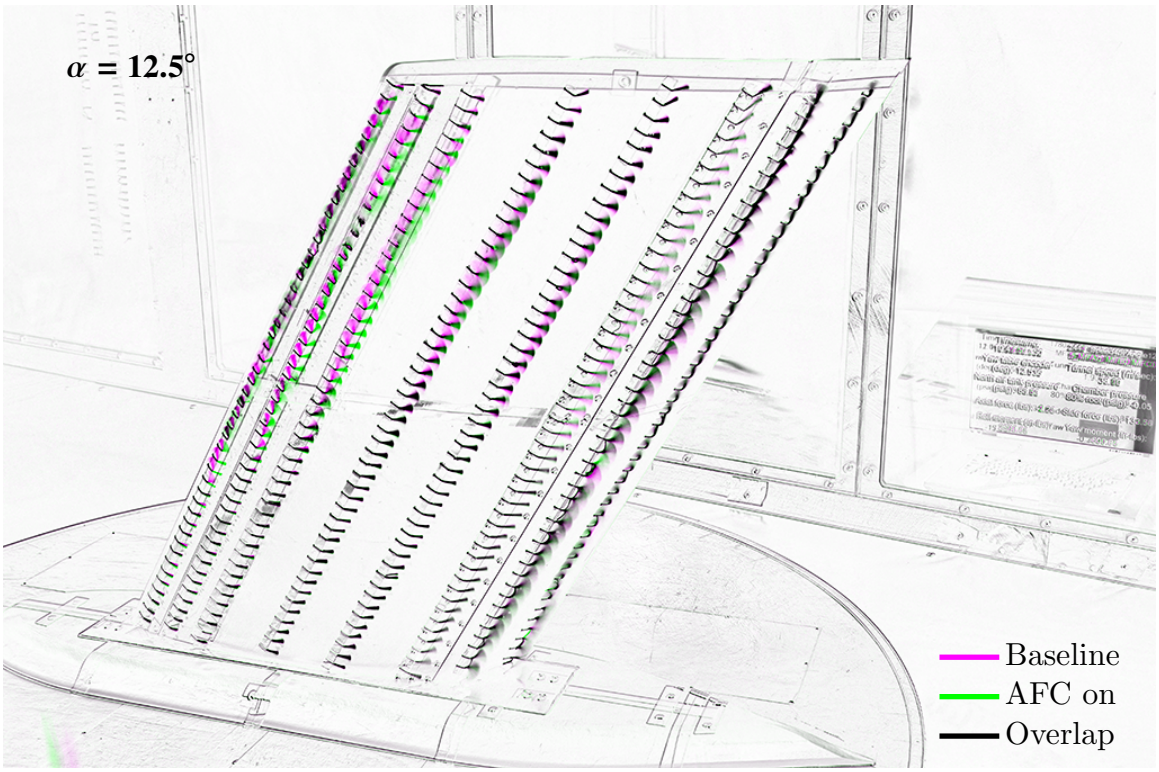

Figure 4.42: Tuft visualization for $\delta_F = 45°$ with steady blowing from the 1% slot at a mass flow rate of 75 kg/h and $\alpha = 12.5°$.

Fig. 4.41 shows the influence of 1% slot on the flow around the wing at $\alpha = 8°$ visualized by tufts. Compared to the non-deflected case, the flow near the leading edge is marginally different. The added circulation of the flap changes the location of the attachment line moving it toward the rear of the bottom surface. Thus, a vortex is created at lower incidence than in the absence of a flap deflection. There is a visible separation downstream of the flap hinge, particularly near the root of the wing (see Fig. 4.42). Similar to the previous case with a non-deflected flap ($\delta_F = 0°$), there is no visible benefit in lift, drag, or pitch moment from the 1% slot blowing. At $\alpha = 12.5°$ (Fig. 4.42), the 1% slot is able to influence a large portion of the wing by partially reattaching the flow, or at least reducing the separation effects. This is similar to the previous case ($\delta_F = 0°$) with the non-deflected flap. This time, however, there doesn't seem to be an increase of spanwise cross-flow at the trailing edge. However, even though there is no apparent increase in spanwise cross-flow, it might be still there. The deflection angle of the flap causes the flow to be separated for all angles of attack α, which then camouflages the negative effect of steady blowing at the 1% slot in the trailing edge flow regime.

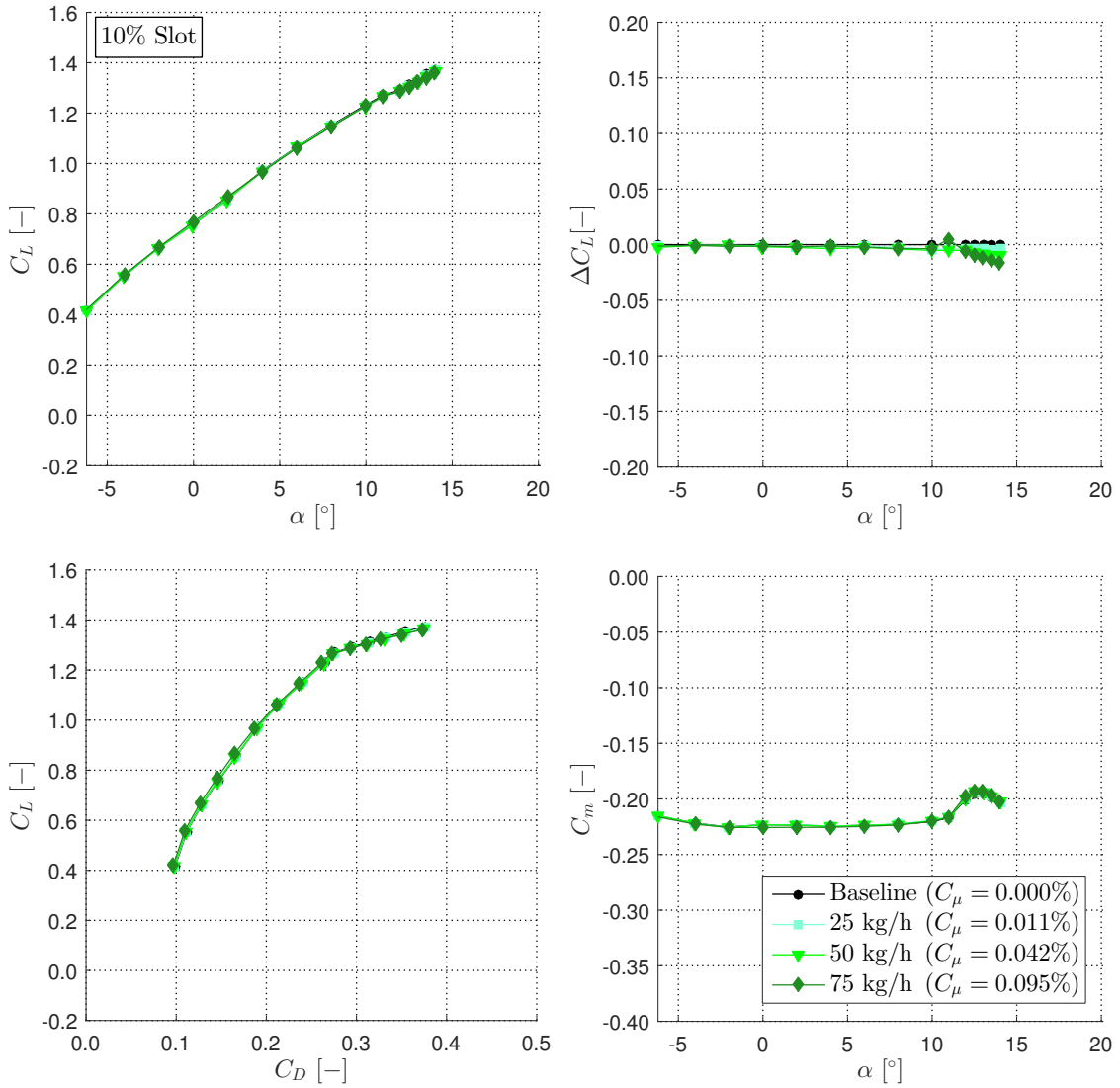

Figure 4.43: Impact of steady blowing with $\delta_F = 45°$ at the 10% slot with increasing mass flow rates compared to the baseline case (no blowing).

The data for the 10% slot presented in Fig. 4.43 highly resembles the 1% slot without the little lift increase at 0°, which confirms the suspicion that it comes from a small measurement error. As such, steady blowing from the 10% slot has no effect on lift, drag, or pitching moment when the flow is attached ($\alpha < 12°$). Once the flow separates there is a deleterious effect that increases with increasing mass flow rates and increasing C_μ's.

The pressure coefficient C_p plots (Figs. 4.44 to 4.46) follow the previous examples. There's a sharp peak right at the slot exit ($x/c = 0.1$) that diminishes so quickly that its effect on the lift coefficient is minuscule. For angles of attack $\alpha > 12°$ one can see the same phenomena described for the

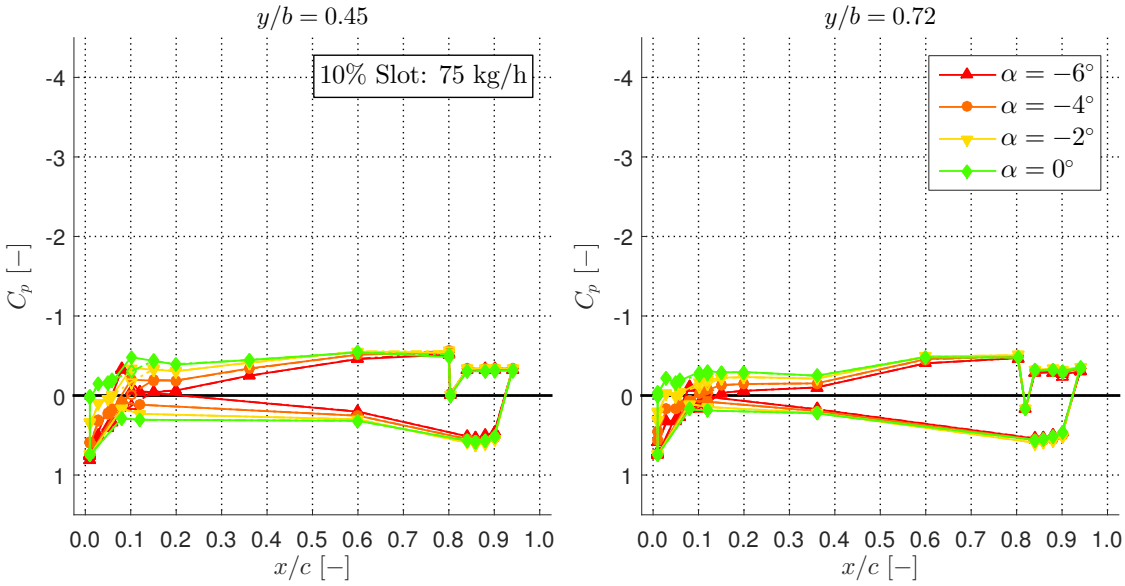

Figure 4.44: Comparison of pressure distribution C_p for $\delta_F = 45°$ with steady blowing from the 10% slot at a mass flow rate of 75 kg/h. Baseline (no blowing) is a dashed line, while the solid line represents the blowing case. Angles: -6°, -4°, -2°, 0°.

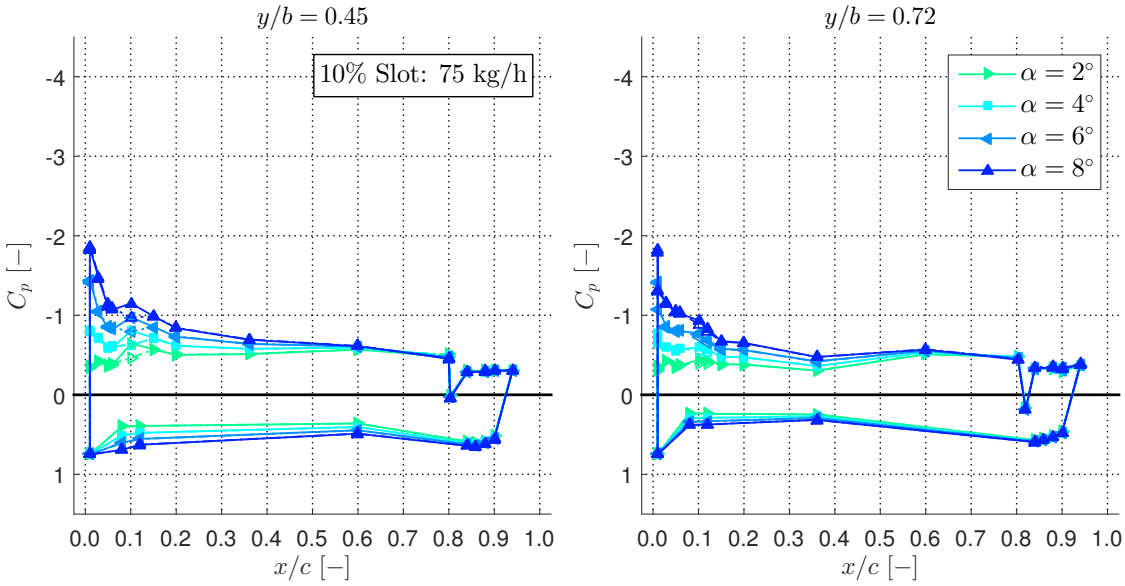

Figure 4.45: Comparison of pressure distribution C_p for $\delta_F = 45°$ with steady blowing from the 10% slot at a mass flow rate of 75 kg/h. Baseline (no blowing) is a dashed line, while the solid line represents the blowing case. Angles: 2°, 4°, 6°, 8°.

1% slot: the deleterious effect after separation originates from a decrease of suction pressure at $0.1 < x/c < 0.4$. This is due to the elimination of the vortex lift, which is consistent with the non-deflected flap case.

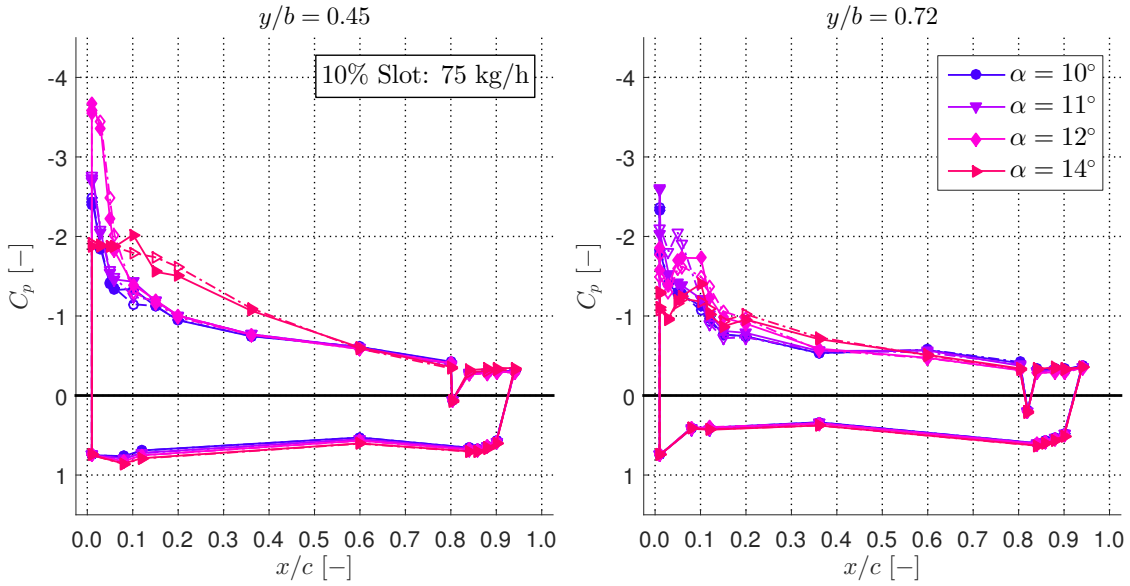

Figure 4.46: Comparison of pressure distribution C_p for $\delta_F = 45°$ with steady blowing from the 10% slot at a mass flow rate of 75 kg/h. Baseline (no blowing) is a dashed line, while the solid line represents the blowing case. Angles: 10°, 11°, 12°, 14°.

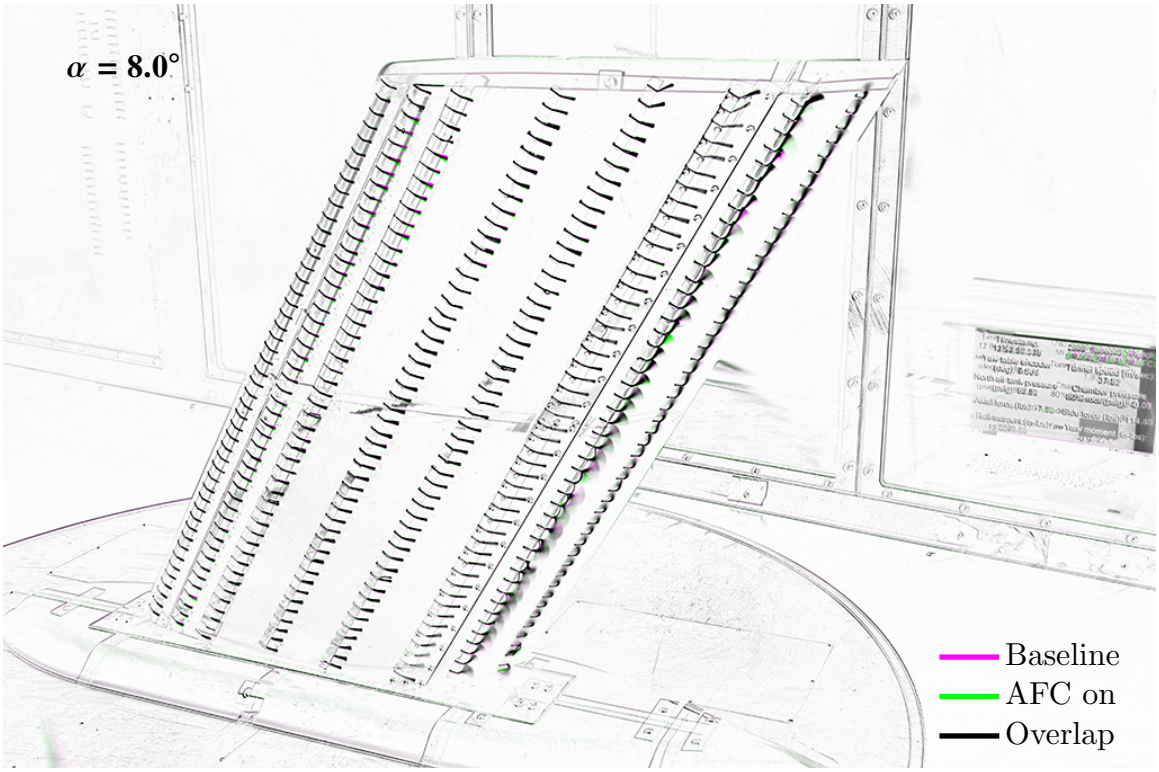

Figure 4.47: Tuft visualization for $\delta_F = 45°$ with steady blowing from the 10% slot at a mass flow rate of 75 kg/h and $\alpha = 8°$.

The tuft images (Figs. 4.47 and 4.48) highly resemble the ones from the 1% slot. This confirms the force balance measurements, as they are nearly the same as well. In summary, blowing from the

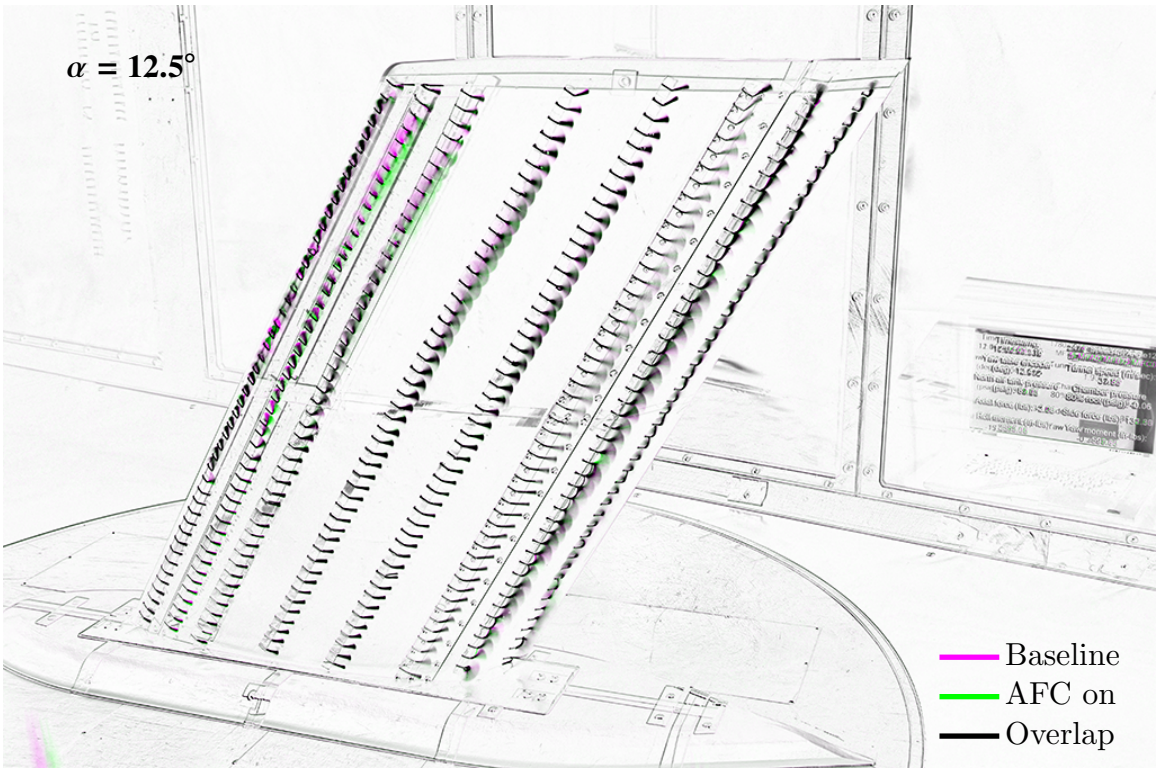

Figure 4.48: Tuft visualization for $\delta_F = 45°$ with steady blowing from the 10% slot at a mass flow rate of 75 kg/h and $\alpha = 12.5°$.

10% slot at a angle of attack $\alpha = 8°$ doesn't affect the flow at all, while at $\alpha = 12.5°$, the flow regime is considerably improved. However, it is assumed that the positive visual effects after the slot are negated by a hidden (due to the flap separation) increase of spanwise cross-flow at the trailing edge and a reduced vortex lift at the leading edge.

Just like for the non-deflected flap ($\delta_F = 0°$), the 80% slot is the most interesting case when it comes to steady blowing. Fig. 4.49 shows that steady blowing actually reduces the lift of the wing for the non-separated regions of the flow ($\alpha < 12°$). Once the flow is separated ($\alpha > 12°$), there is a benefit for the largest mass flow rate of 75 kg/h. In terms of lift, these results are opposing what has been seen so far. The drag seems to be slightly reduced, and the pitching moment is increased (less negative).

The pressure plots (Figs. 4.50 to 4.52) show that there is no specific location, where a large effect is present, but rather that the lift is lost over the whole wing suction side (the actuated solid lane is slightly under the dashed baseline). Note that the 80% slot doesn't produce a pressure peak due to the flap. It is believed that blowing at a velocity comparable to the freestream, meaning the steady

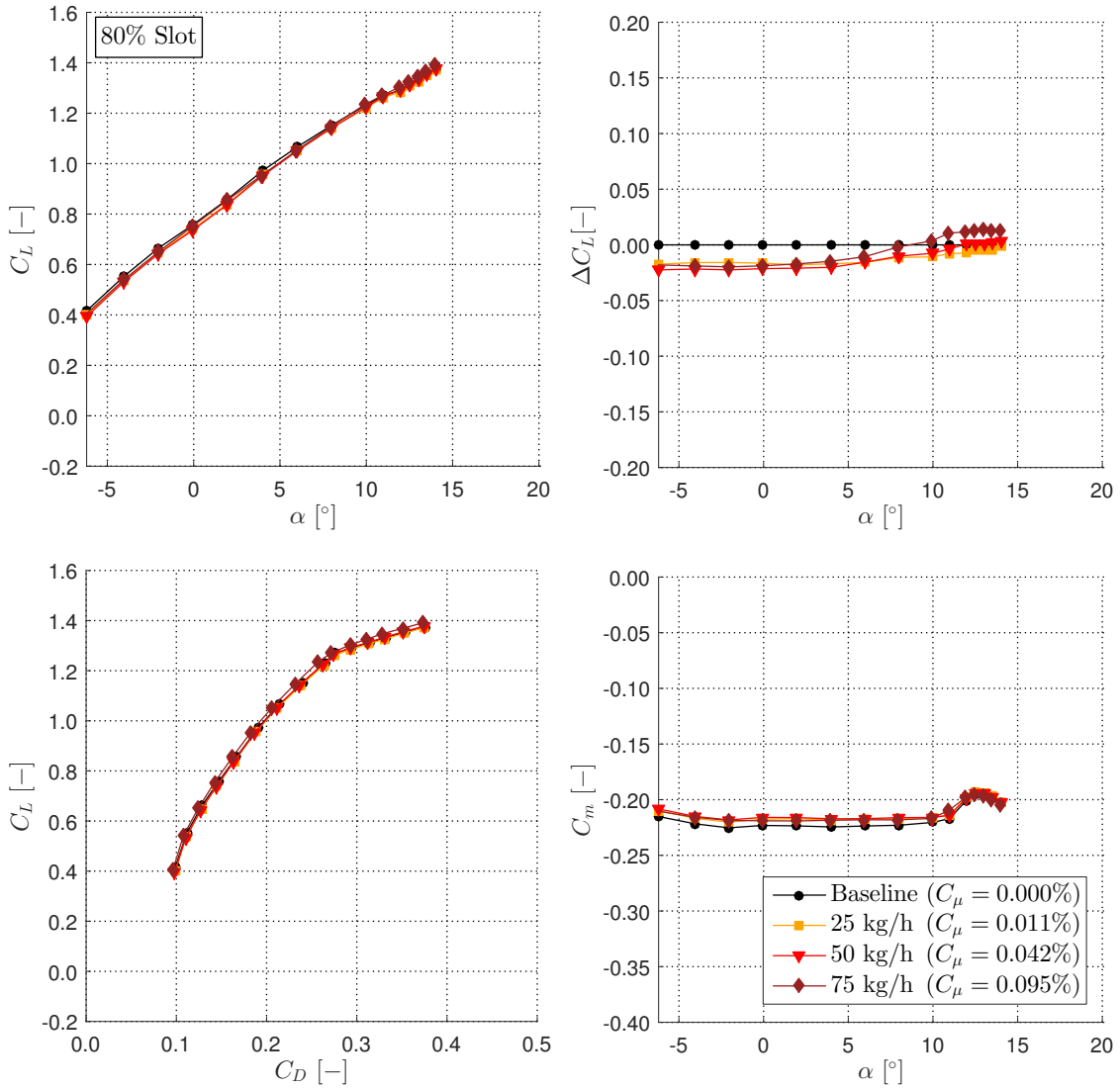

Figure 4.49: Impact of steady blowing with $\delta_F = 45°$ at the 80% slot with increasing mass flow rates compared to the baseline case (no blowing).

blowing velocity is roughly equivalent to the wind tunnel speed ($u_{jet}/u_\infty \approx 1$), does not attach the flow, and it only displaces the streamlines upward from the upper slot lip. Such a displacement is known to reduce the lift.

The tuft images (Figs. 4.53 and 4.54) support the previous explanation. There is no visible effect of 80% slot blowing for both angles of attack $\alpha = 8°$ and $\alpha = 12.5°$. Compared to the 1% and 10% slot there is also no indication of increased spanwise cross-flow. Therefore, the explanation with streamline displacement seems to be confirmed.

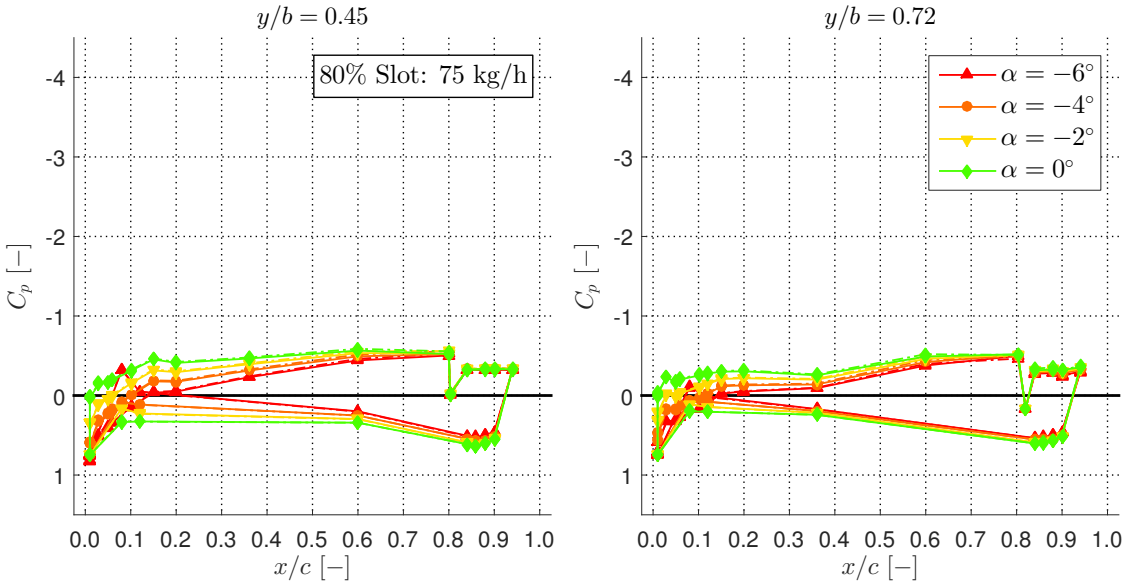

Figure 4.50: Comparison of pressure distribution C_p for $\delta_F = 45°$ with steady blowing from the 80% slot at a mass flow rate of 75 kg/h. Baseline (no blowing) is a dashed line, while the solid line represents the blowing case. Angles: -6°, -4°, -2°, 0°.

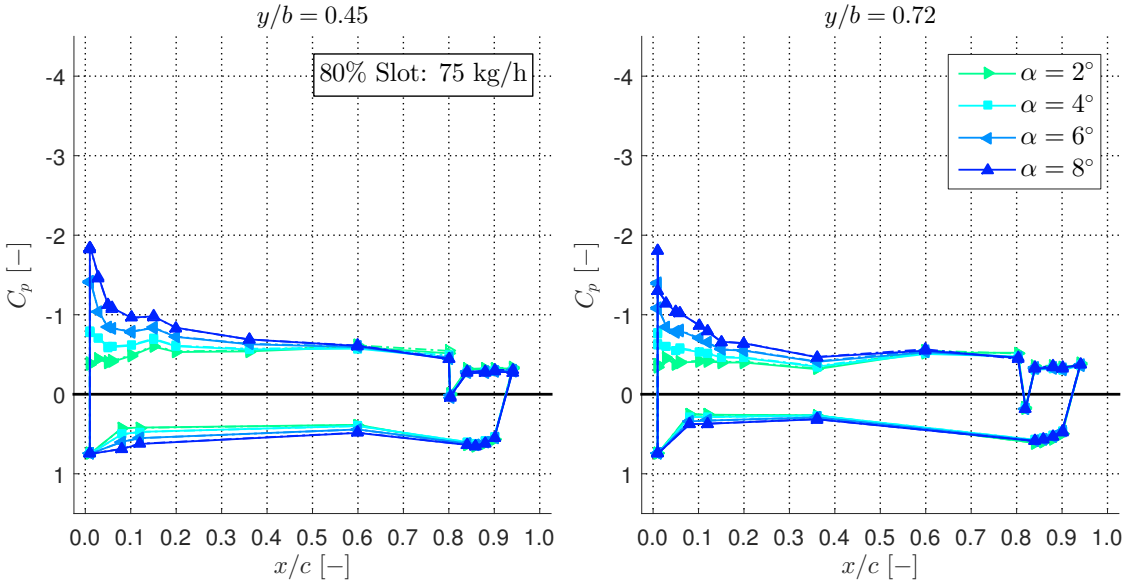

Figure 4.51: Comparison of pressure distribution C_p for $\delta_F = 45°$ with steady blowing from the 80% slot at a mass flow rate of 75 kg/h. Baseline (no blowing) is a dashed line, while the solid line represents the blowing case. Angles: 2°, 4°, 6°, 8°.

4.3.5 Configuration 3: Unsteady Blowing with $\delta_F = 0°$

After steady blowing showed to be not a very successful AFC method, configuration 3 switched to unsteady blowing (sweeping jet actuators) for all slots. The flap deflection was reduced back to $\delta_F = 0°$. The unsteady blowing was achieved by using sweeping jet actuator; the design of a single

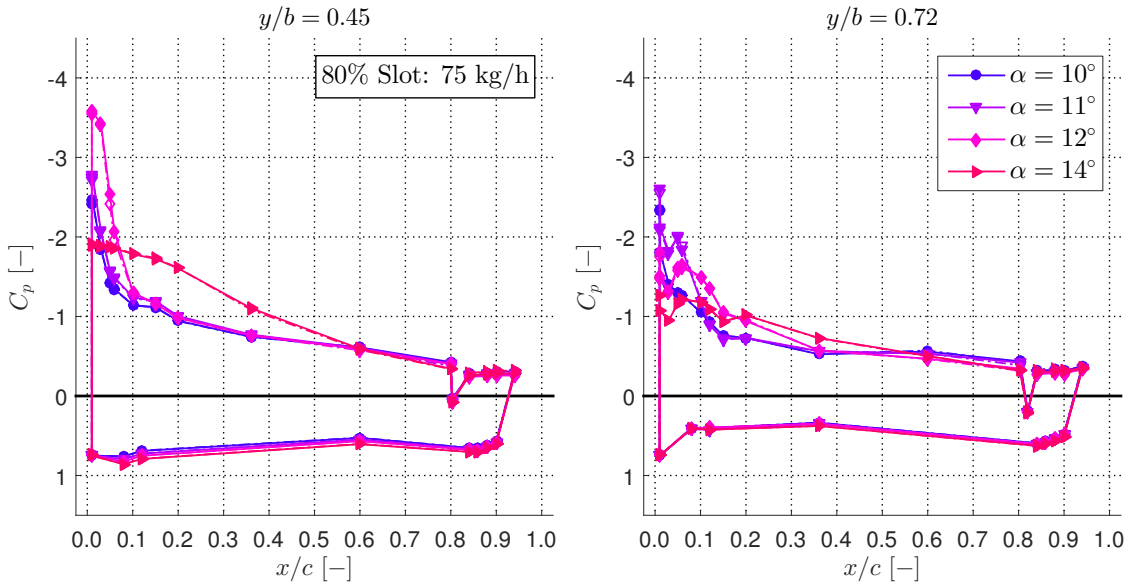

Figure 4.52: Comparison of pressure distribution C_p for $\delta_F = 45°$ with steady blowing from the 80% slot at a mass flow rate of 75 kg/h. Baseline (no blowing) is a dashed line, while the solid line represents the blowing case. Angles: 10°, 11°, 12°, 14°.

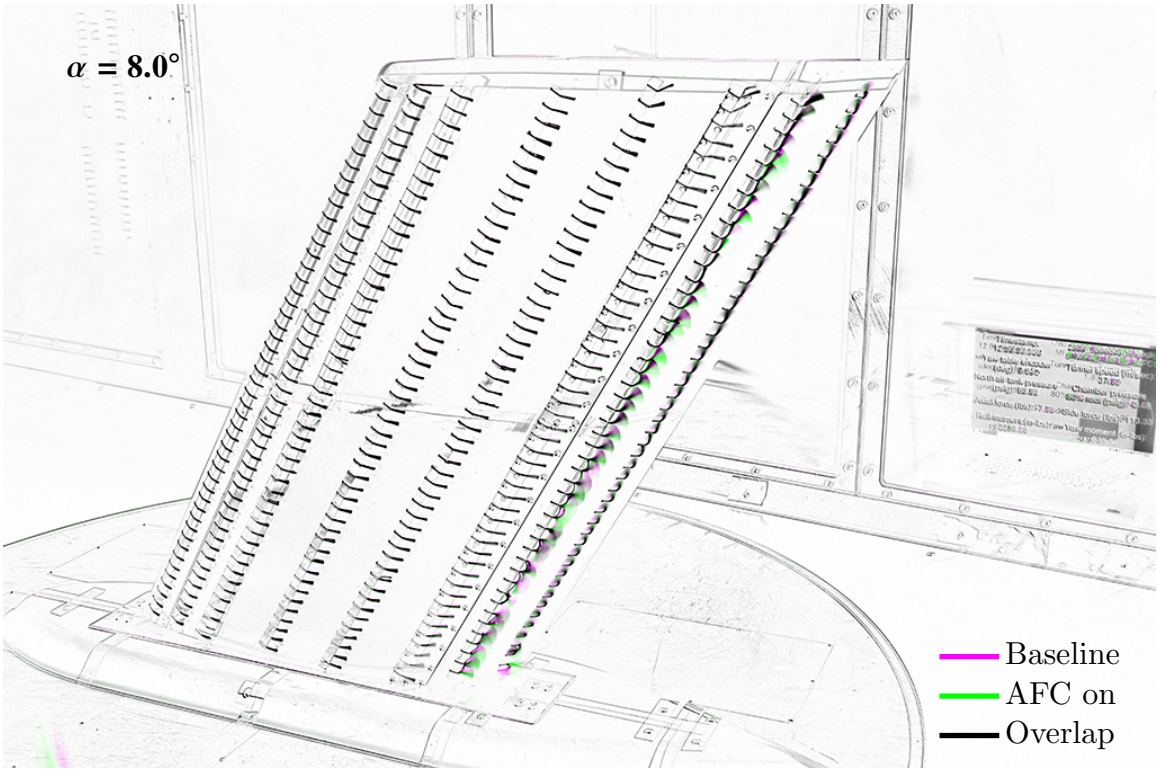

Figure 4.53: Tuft visualization for $\delta_F = 45°$ with steady blowing from the 80% slot at a mass flow rate of 75 kg/h and $\alpha = 8°$.

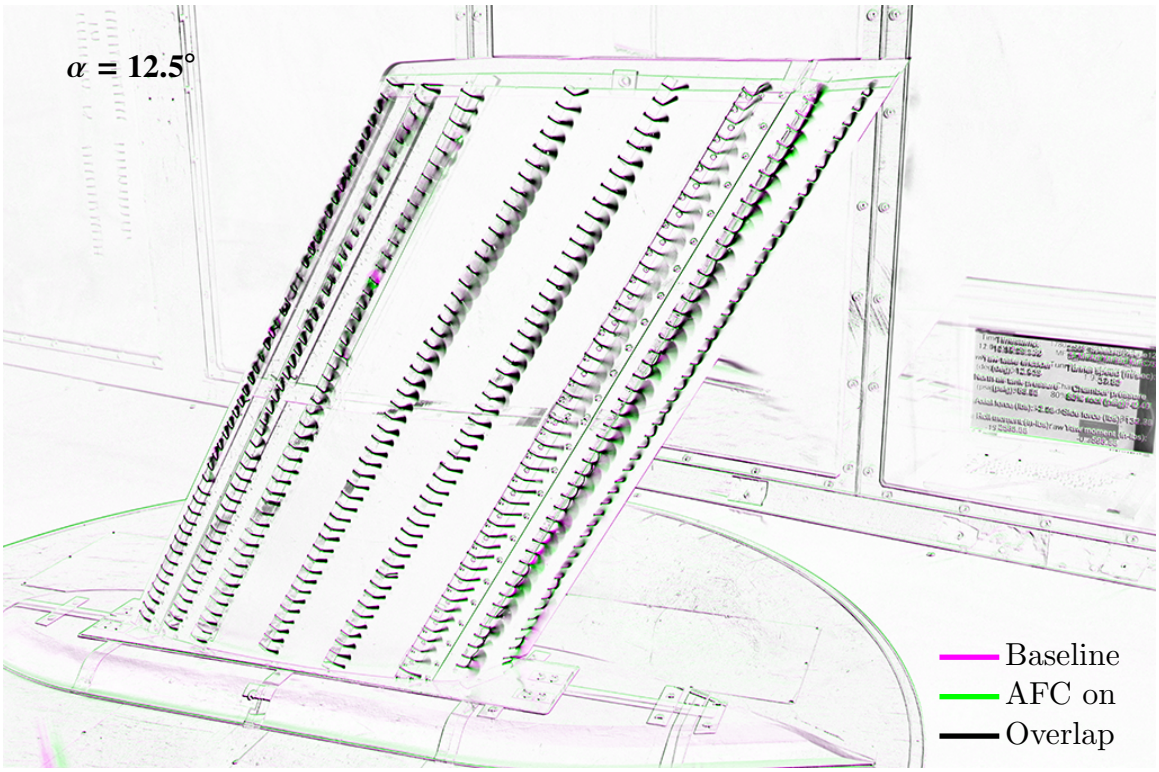

Figure 4.54: Tuft visualization for $\delta_F = 45°$ with steady blowing from the 80% slot at a mass flow rate of 75 kg/h and $\alpha = 12.5°$.

sweeping jet actuator can be found in Section 1.3. To recap: these actuators sweep without moving parts at a frequency of the order of 1000 Hz. The specific actuators used inside the wing sweep at a frequency of about 1500 Hz. Again, all possible combinations of mass flow rates of 0 kg/h, 25 kg/h, and 50 kg were tested at every slot (total of 27 combinations), as well as a mass flow rate of 75 kg/h for a single slot. Again, no combinatory effects could be observed, and these cases are omitted. Because the actuator exits are much smaller in area compared to the steady blowing slot, the achievable C_μ values are considerably higher with the same mass flow rate. While the output velocity for steady blowing was on the order of the freestream velocity, the sweeping jet actuators operated at jet velocities that were 2.5 to 6 times higher. Note that the data in this configuration was taken at a wind tunnel speed of 50 m/s.

Fig. 4.55 shows sweeping jet actuators at the 1% slot with the same mass flow rates as the steady blowing cases: 0 kg/h (baseline), 25 kg/h, 50 kg/h, and 75 kg/h. As mentioned previously, due to the fact that the reference area for the sweeping jet actuators is based on their throat area, the coefficient of momentum input C_μ is close to 1% for a mass flow rate of 75 kg/h. Looking at the data, one can

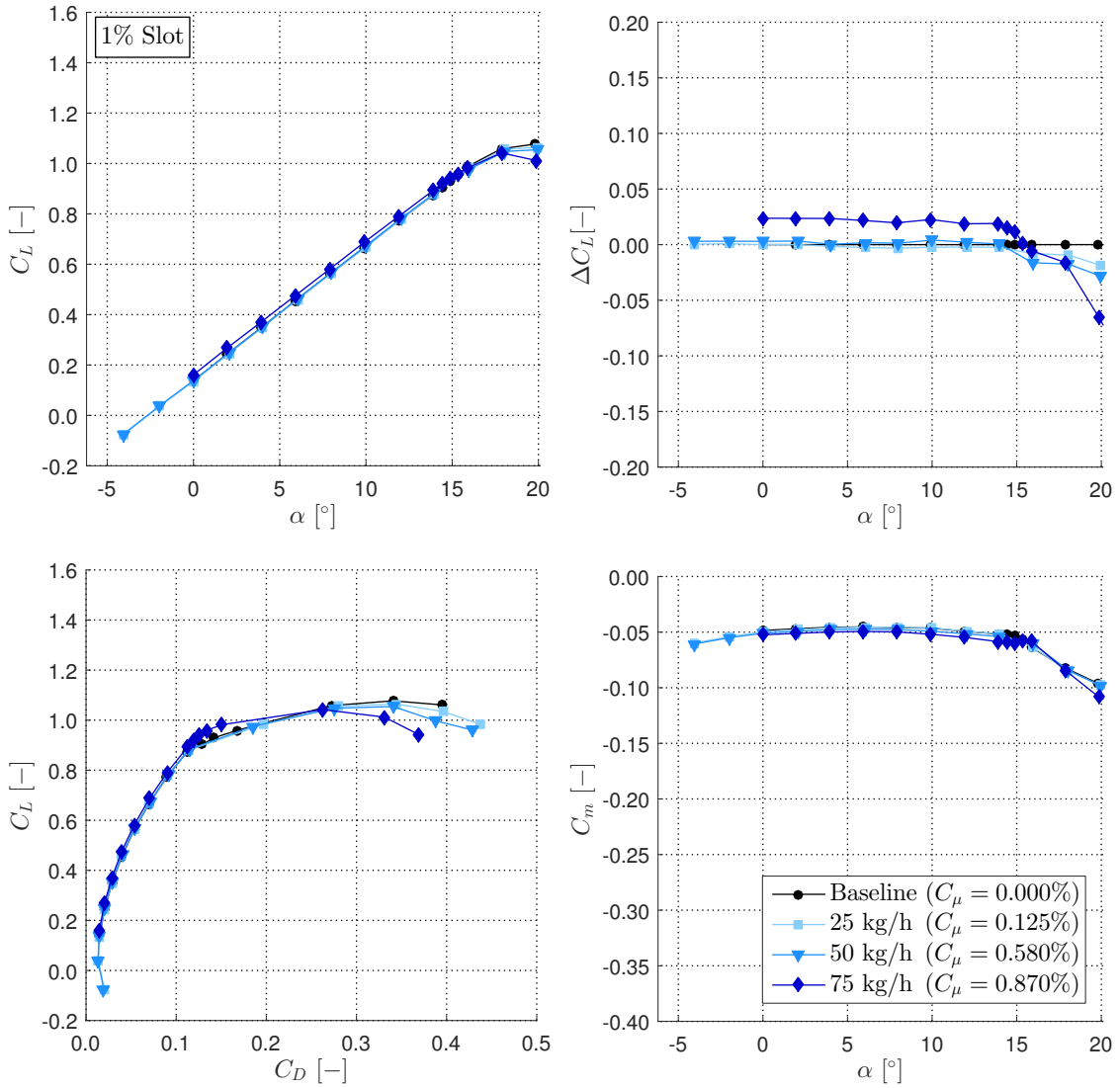

Figure 4.55: Impact of sweeping jet actuators with $\delta_F = 0°$ at the 1% slot with increasing mass flow rates compared to the baseline case (no blowing).

see that changing from steady blowing to sweeping jet actuation doesn't have a large impact except at a mass flow rate of 75 kg/h. While the other mass flow rates don't provide any additional lift at the non-separated angles ($\alpha < 14°$), there's a small increase at the highest tested mass flow rate. It seems like there is a minimum mass flow rate required before the sweeping jet actuators can take effect. It is believed that this minimum requirement is roughly $u_{jet}/u_\infty > 3$. This condition was discovered during the NASA ERA program (Seele, Graff, Lin, et al., 2013), and it seems like it plays a big role here as well. One may argue, that the jet velocities for the lower mass flows rates (25 kg/h and 50 kg/h) would fulfill this rule of thumb as well. Even though this is correct, the exit curve of the model seems to slow down the jet velocity while turning it around. It takes a minimum mass flow rate of

75 kg/h, until the jet speed is fast enough at the curve exit to fulfill the above mentioned condition, and hence show an impact on the flow regime. There's also a minor effect on on the pitch moment coefficient. However, for this input mass flow rate, the sweeping jet actuators are deleterious for the separated flow regime ($\alpha > 14°$) in terms of lift for the same reasons as steady blowing: increase of spanwise cross-flow at the trailing edge and vortex lift reduction.

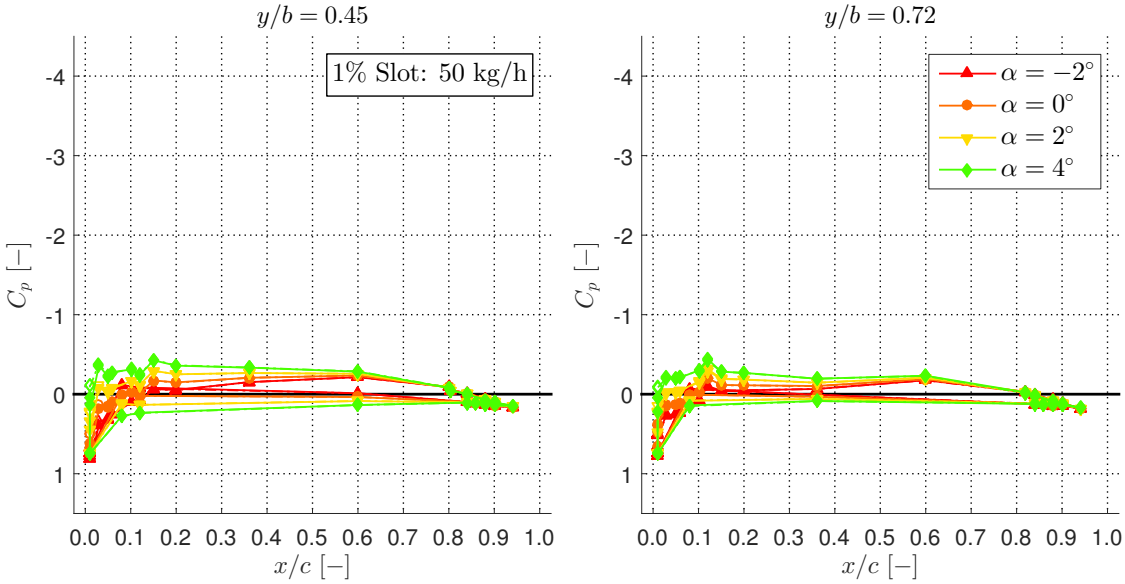

Figure 4.56: Comparison of pressure distribution C_p for $\delta_F = 0°$ with sweeping jet actuators from the 1% slot at a mass flow rate of 50 kg/h. Baseline (no blowing) is a dashed line, while the solid line represents the blowing case. Angles: -2°, 0°, 2°, 4°.

Figs. 4.56 to 4.58 show the pressure distributions over the wing. The pressure data for the highest mass flow rate couldn't be acquired during those tests due to a bug in the acquisitions software. The data for a mass flow rate of 50 kg/h is available, but unfortunately it does not reveal as much, because the critical jet velocity condition has not been reached yet. Nevertheless, it is worth taking a look at it: one can see that at the 1% slot exit, the suction pressure is slightly decreased due to the blowing in the attached flow regime ($\alpha < 14°$). However, the effect of the slot travels down the chord and increases the suction pressure. This indicates that the sweeping jet blowing is able to carry downstream and cover a larger wing area unlike the steady blowing. One can see the same effect once the flow is separated ($\alpha > 14°$): the flow regime around the whole wing is affected; the section aft of 40% of the chord ($x/c > 0.4$) seems to provide additional lift, as well as the leading edge portion of the wing ($x/c < 0.1$). The overall deleterious effect of the wing is created between $0.1 < x/c < 0.4$ of chord. Similar to the steady cases, this seems to be due to a loss of vortex lift.

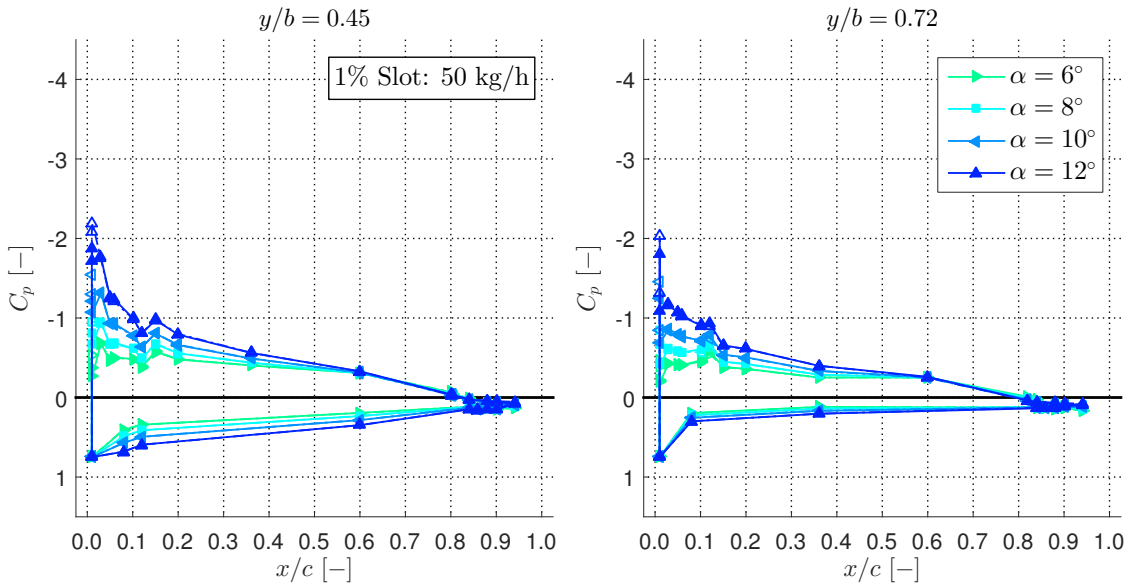

Figure 4.57: Comparison of pressure distribution C_p for $\delta_F = 0°$ with sweeping jet actuators from the 1% slot at a mass flow rate of 50 kg/h. Baseline (no blowing) is a dashed line, while the solid line represents the blowing case. Angles: 6°, 8°, 10°, 12°.

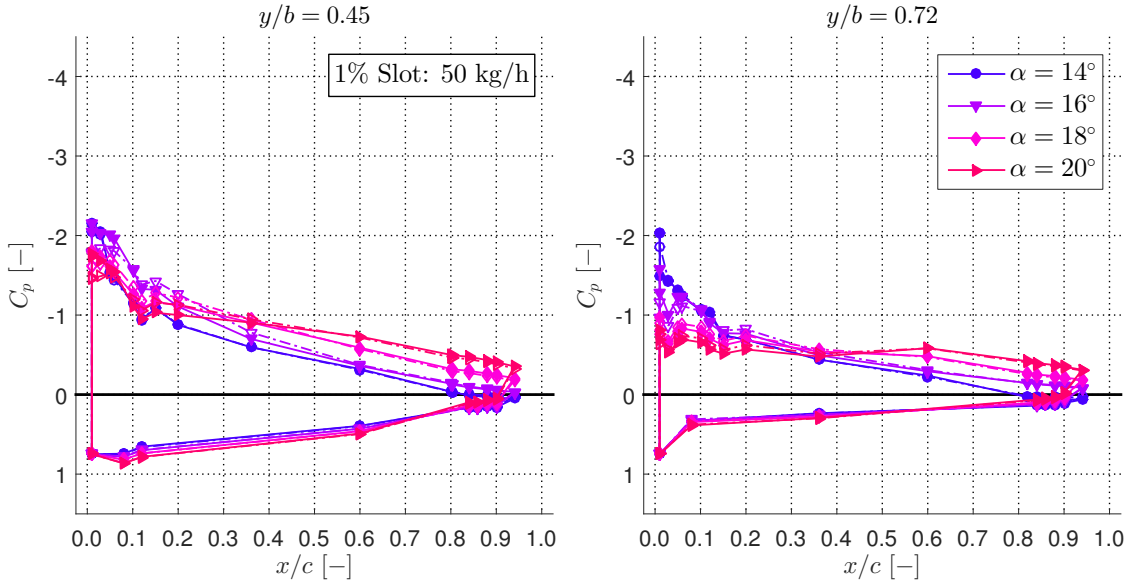

Figure 4.58: Comparison of pressure distribution C_p for $\delta_F = 0°$ with sweeping jet actuators from the 1% slot at a mass flow rate of 50 kg/h. Baseline (no blowing) is a dashed line, while the solid line represents the blowing case. Angles: 14°, 16°, 18°, 20°.

The tuft image taken at an incidence of $\alpha = 10°$ in Fig. 4.59 doesn't reveal any hints, as sweeping from the 1% slot doesn't seem to change anything. Compared to the steady blowing, there's also no effect on the spanwise cross-flow at the trailing edge. It is not exactly known where the lift benefit comes from. At $\alpha = 14.5°$ (Fig. 4.60) the 1% slot sweeping reattaches the flow from the leading

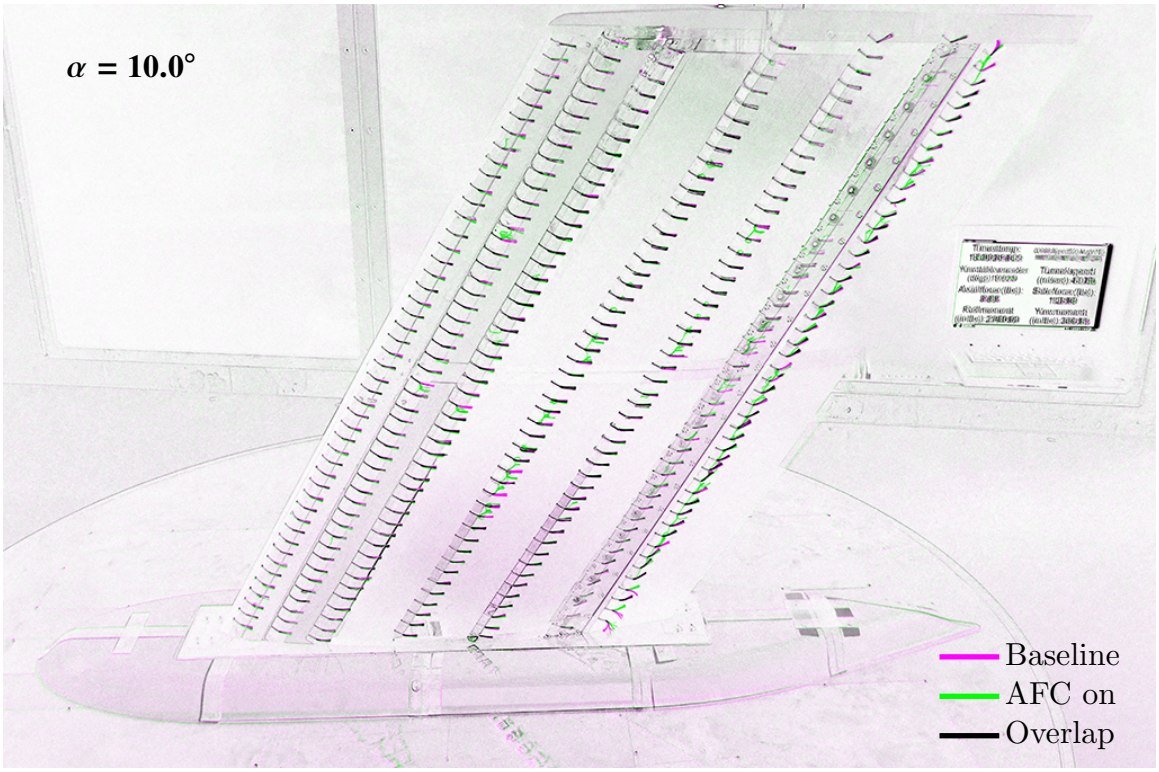

Figure 4.59: Tuft visualization for $\delta_F = 0°$ with sweeping jet actuators from the 1% slot at a mass flow rate of 75 kg/h and $\alpha = 10°$.

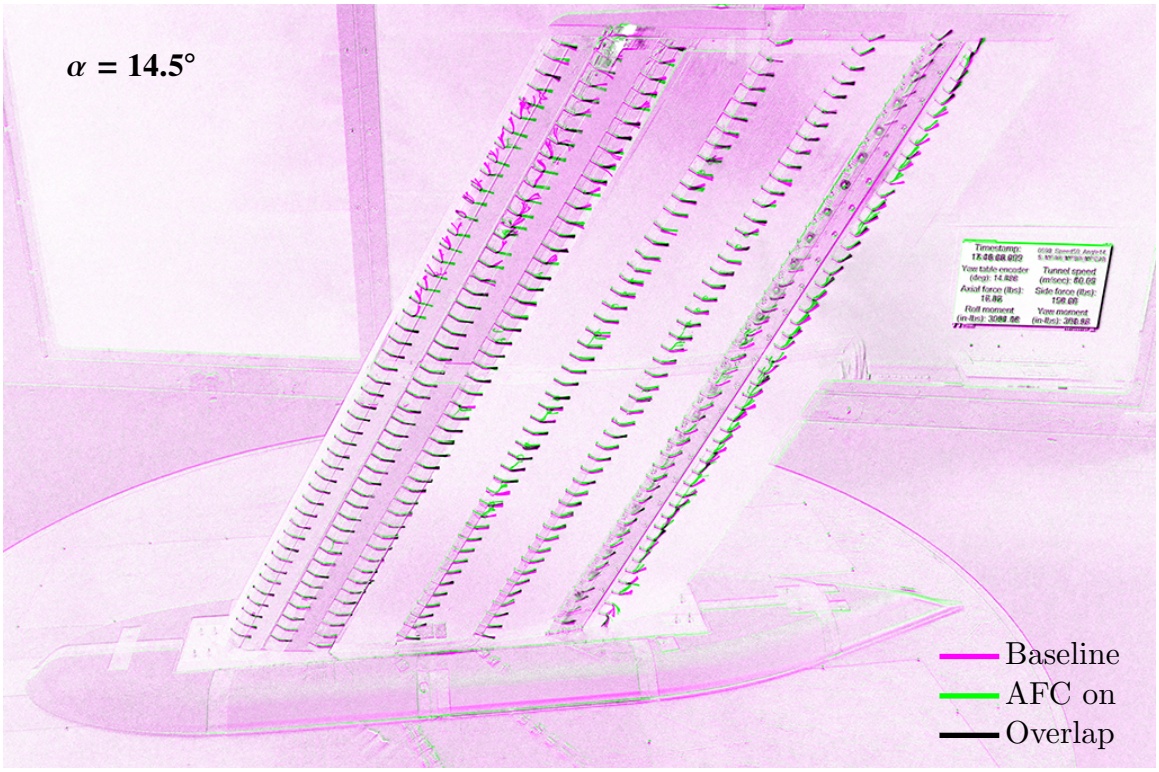

Figure 4.60: Tuft visualization for $\delta_F = 0°$ with sweeping jet actuators from the 1% slot at a mass flow rate of 75 kg/h and $\alpha = 14.5°$.

edge separation bubble (loss of vortex lift), and causes additional spanwise cross-flow at the trailing edge, which then leads to the deleterious effect on the lift. This is exactly the same effect observed for the steady blowing cases.

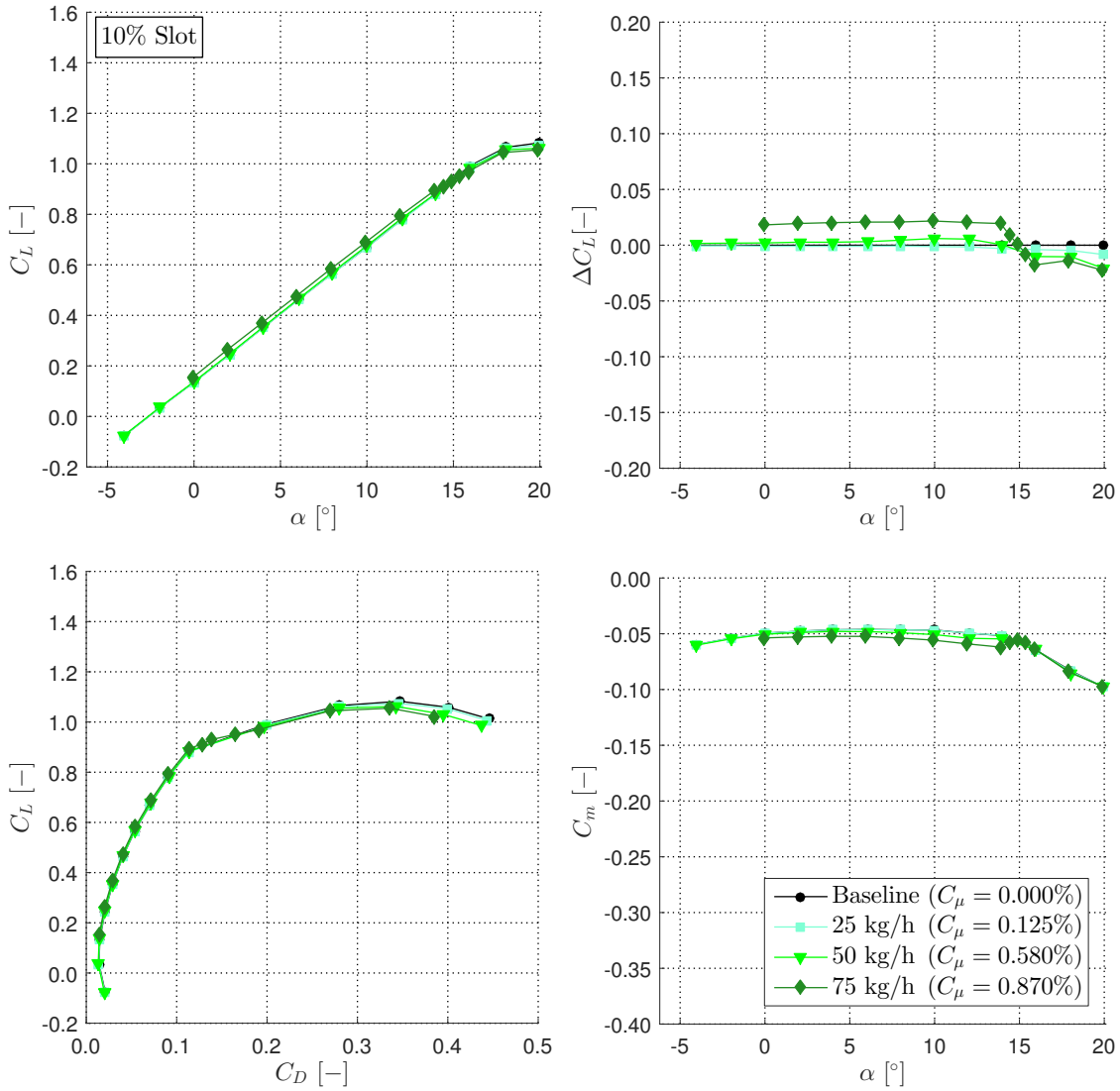

Figure 4.61: Impact of sweeping jet actuators with $\delta_F = 0°$ at the 10% slot with increasing mass flow rates compared to the baseline case (no blowing).

The force balance data for the 10% slot (Fig. 4.61) looks very similar to the 1% data. The highest mass flow rate is able to generate a slight lift increase, while the others are close to zero. A key difference is the lift-drag curve that shows no reaction to 10% sweeping. At higher angles there is a reduction of lift due to the deleterious effect of the blowing. The pitching moment behaves like the previous case: there is a small reduction of pitching moment at a mass flow rate of 75 kg/h, while the other cases don't seem to have any influence. A similar effect compared to the 1% slot is to

blame: once the critical jet speed is reached ($u_{jet}/u_\infty > 3$), one can see an immediate improvement, while otherwise there is no effect.

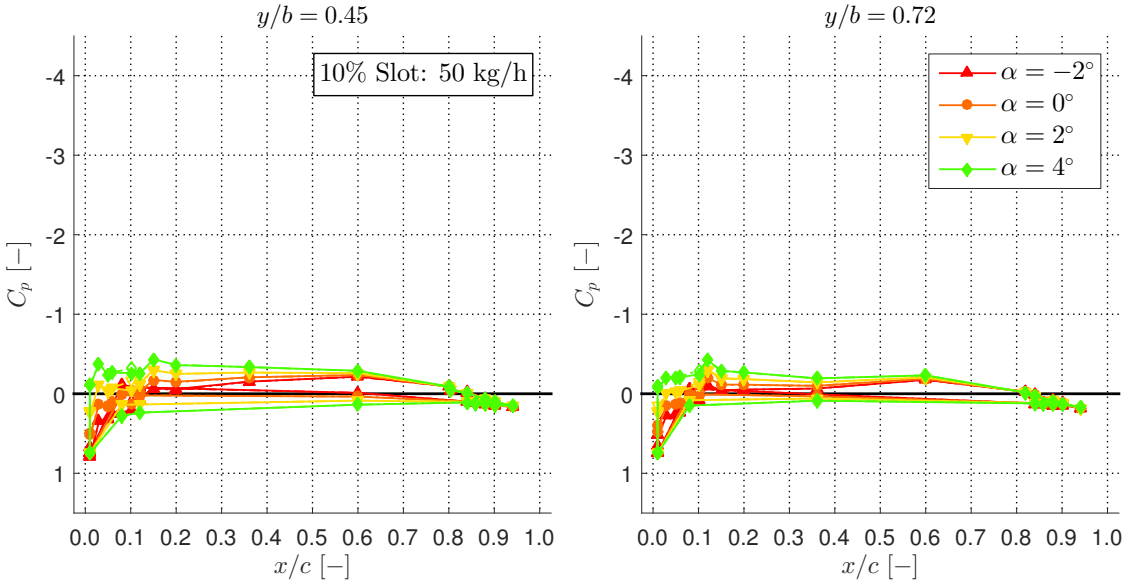

Figure 4.62: Comparison of pressure distribution C_p for $\delta_F = 0°$ with sweeping jet actuators from the 10% slot at a mass flow rate of 50 kg/h. Baseline (no blowing) is a dashed line, while the solid line represents the blowing case. Angles: -2°, 0°, 2°, 4°.

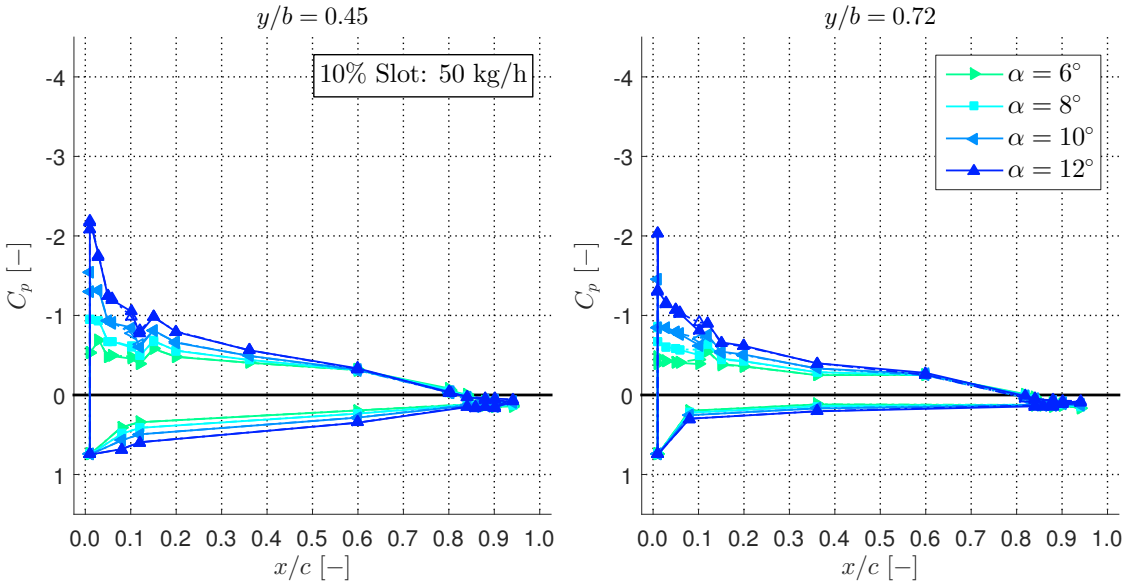

Figure 4.63: Comparison of pressure distribution C_p for $\delta_F = 0°$ with sweeping jet actuators from the 10% slot at a mass flow rate of 50 kg/h. Baseline (no blowing) is a dashed line, while the solid line represents the blowing case. Angles: 6°, 8°, 10°, 12°.

The pressure data (Figs. 4.62 to 4.64) is only available for the mass flow rate of 50 kg/h for the same reason mentioned previously. Once again, this makes any interpretation of the lift data challenging

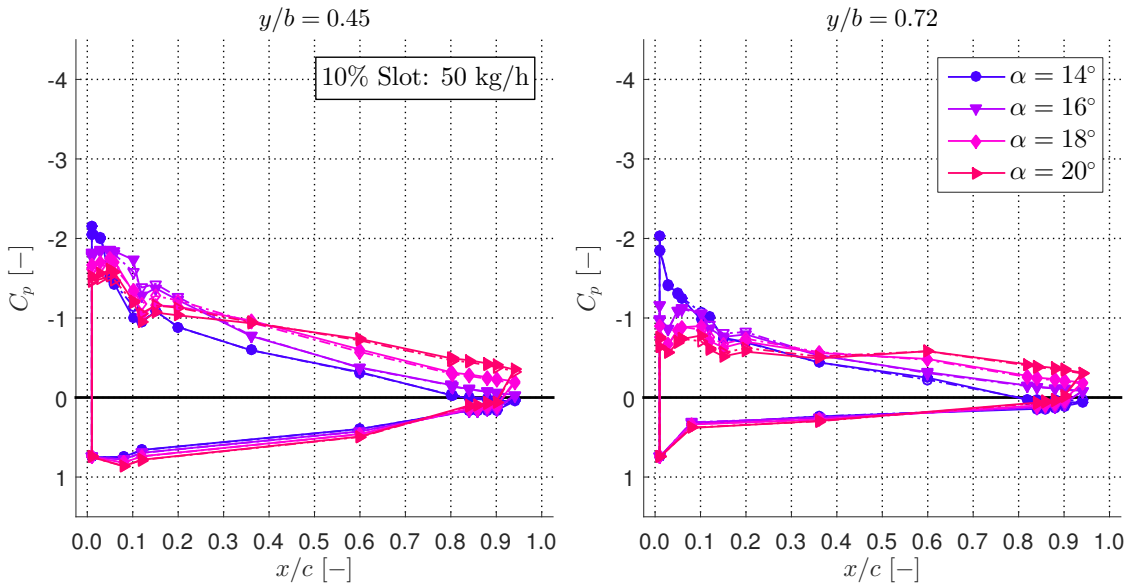

Figure 4.64: Comparison of pressure distribution C_p for $\delta_F = 0°$ with sweeping jet actuators from the 10% slot at a mass flow rate of 50 kg/h. Baseline (no blowing) is a dashed line, while the solid line represents the blowing case. Angles: 14°, 16°, 18°, 20°.

as the critical jet velocity is only reached by a mass flow rate of 75 kg/h. The effect of sweeping at $x/c = 0.1$ has a different effect depending on the spanwise position y/b. At $y/b = 0.45$ sweeping from the 10% slot increases the suction pressure, while at $y/b = 0.72$ it decreases it. The higher mass flow rate might be able to resolve this phenomena by increasing the suction pressure over the whole spanwise length, and as a consequence, increase the lift increment. When looking at the separated flow regime ($\alpha > 14°$), this assumption is supported as the wing loses its pressure benefit at $y/b = 0.45$, and hence creates a deleterious lift effect.

As expected from the previous observation, the 10% slot follows the tracks of the 1% slot. This is also true for the tuft images (Figs. 4.65 and 4.66). At $\alpha = 10°$ there is no visual effect on the tufts, and it remains questionable where the lift increase is generated. At the higher incident $\alpha = 14.5°$ the separation bubble reattaches after the slot exit at $x/c = 0.1$ (loss of vortex lift). Additionally, this increases the spanwise cross-flow at the trailing edge. Both these phenomena combined cause the observed deleterious lift effect.

The data of the 80% slot in Fig. 4.67 shows a consistent increase of lift. Increasing the mass flow rate increases the lift benefit roughly in proportion to C_μ. As previously mentioned, compared to the other two slots, the 80% slot has no curve, and the jet exits are directly blowing into the freestream.

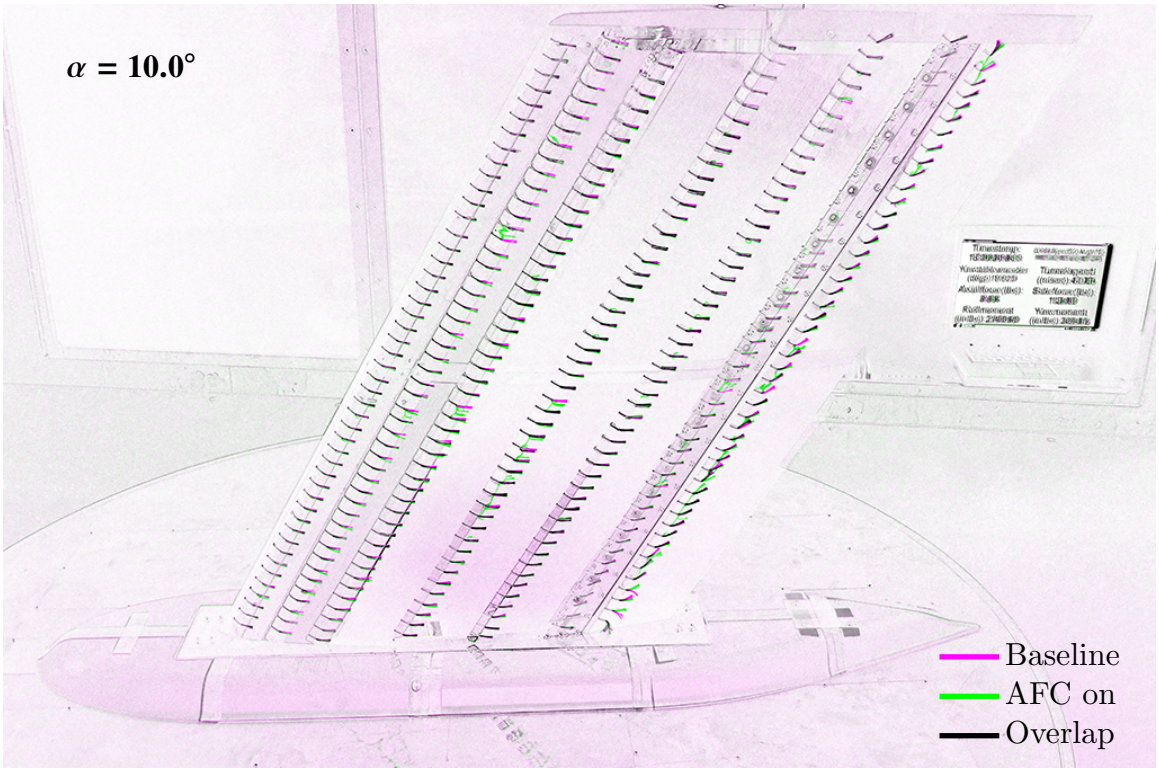

Figure 4.65: Tuft visualization for $\delta_F = 0°$ with sweeping jet actuators from the 10% slot at a mass flow rate of 75 kg/h and $\alpha = 10°$.

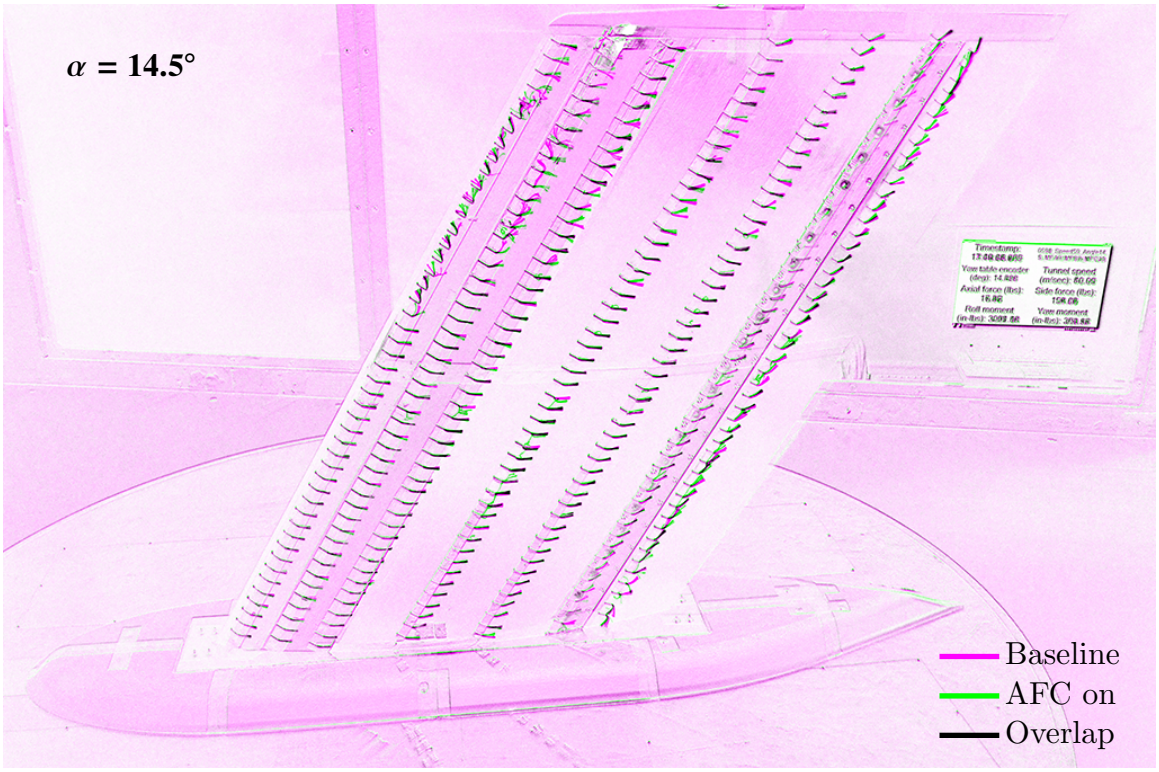

Figure 4.66: Tuft visualization for $\delta_F = 0°$ with sweeping jet actuators from the 10% slot at a mass flow rate of 75 kg/h and $\alpha = 14.5°$.

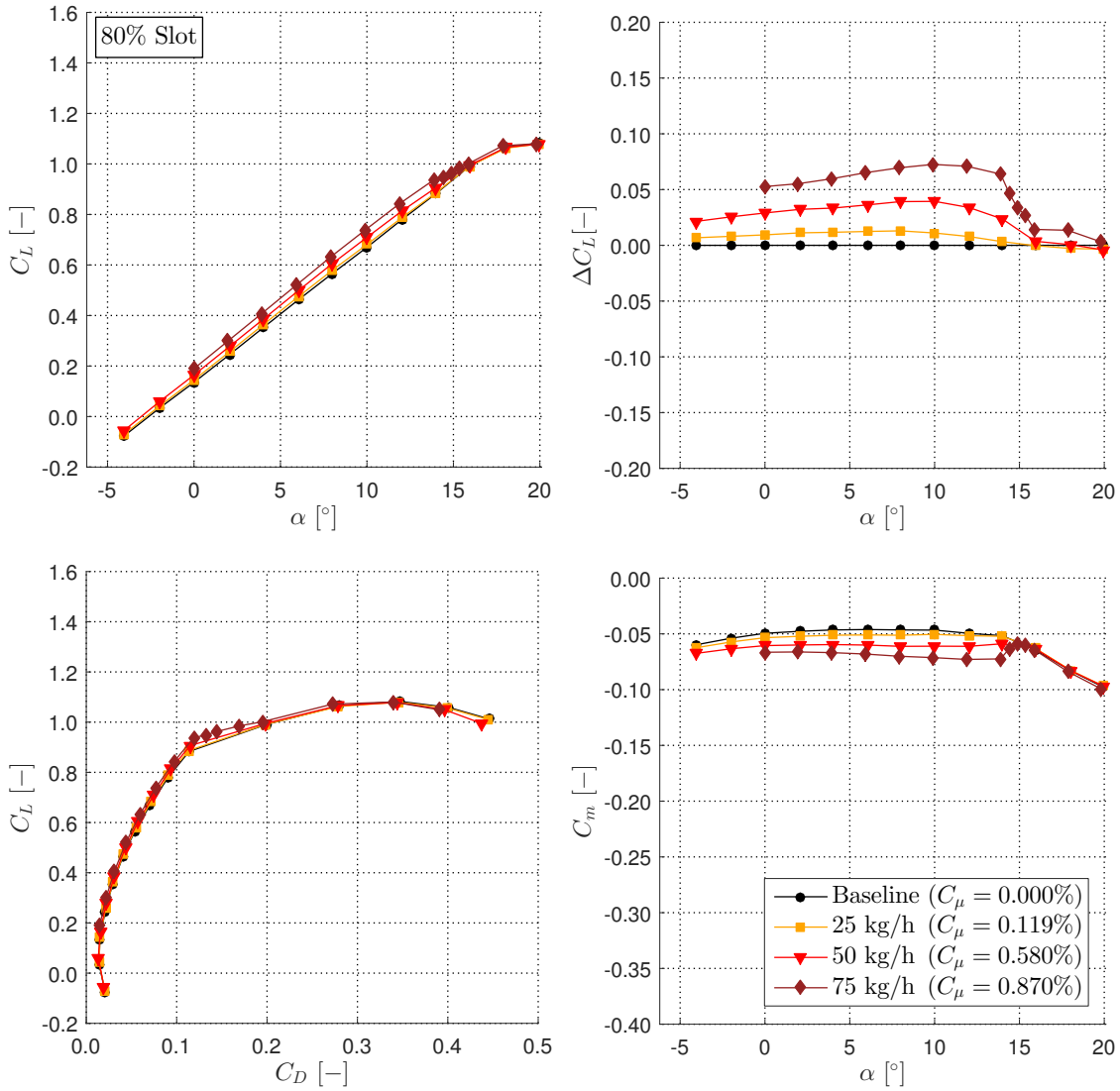

Figure 4.67: Impact of sweeping jet actuators with $\delta_F = 0°$ at the 80% slot with increasing mass flow rates compared to the baseline case (no blowing).

The previously stated condition $u_{jet}/u_\infty > 3$ is easily fulfilled by the mass flow rates of 75 kg/h and 50 kg/h, which both have their respective jet velocities at a Mach number of $M = 1$ ($u_{jet}/u_\infty \approx 6$). Even the lowest mass flow rate of 25 kg/h nearly reaches the condition by $u_{jet}/u_\infty \approx 2.6$, which is probably the reason that it shows a minor benefit. The lift-drag curve gets slightly extended by AFC, but the differences are minor. The pitching moment coefficient C_m is decreased significantly due to the sweeping at the 80% slot, but there's no indication of separation delay.

The pressure plots in Figs. 4.68 to 4.70 are taken from a mass flow rate of 50 kg/h once again. This time, there is a trend in the lift curve, and therefore one should be able to get a good idea of what's

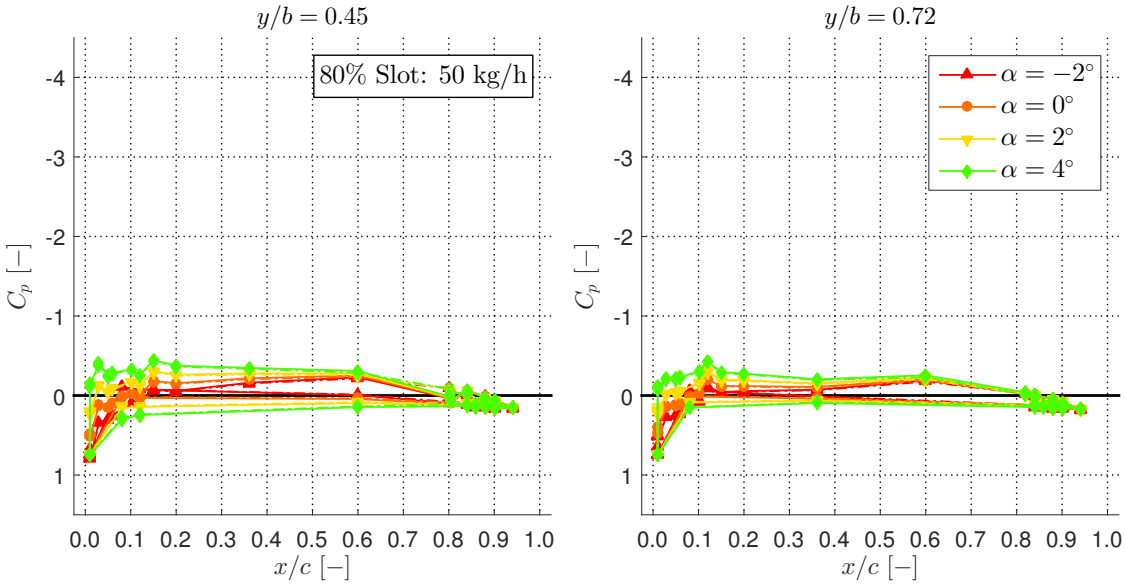

Figure 4.68: Comparison of pressure distribution C_p for $\delta_F = 0°$ with sweeping jet actuators from the 80% slot at a mass flow rate of 50 kg/h. Baseline (no blowing) is a dashed line, while the solid line represents the blowing case. Angles: -2°, 0°, 2°, 4°.

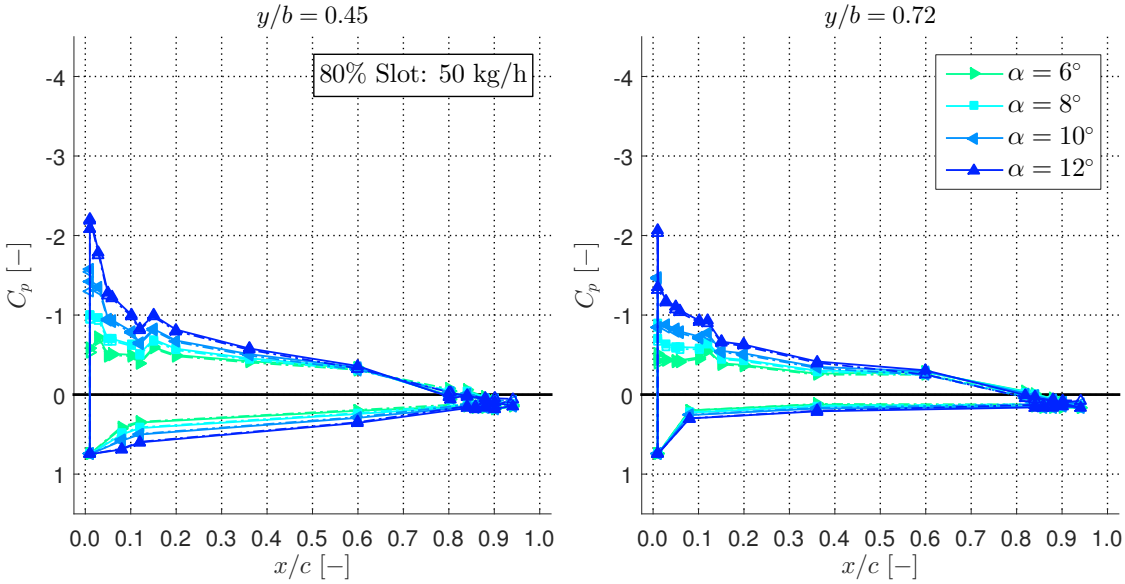

Figure 4.69: Comparison of pressure distribution C_p for $\delta_F = 0°$ with sweeping jet actuators from the 80% slot at a mass flow rate of 50 kg/h. Baseline (no blowing) is a dashed line, while the solid line represents the blowing case. Angles: 6°, 8°, 10°, 12°.

going on. It is evident that the sweeping causes a slight reduction of pressure on the suction side, and a slight pressure increase on the pressure side. In other words, the additional lift increment that is generated through the 80% slot sweeping jet actuators is based on small benefits across the whole chord of the wing on the pressure as well as the suction side. The 80% slot using sweeping jet

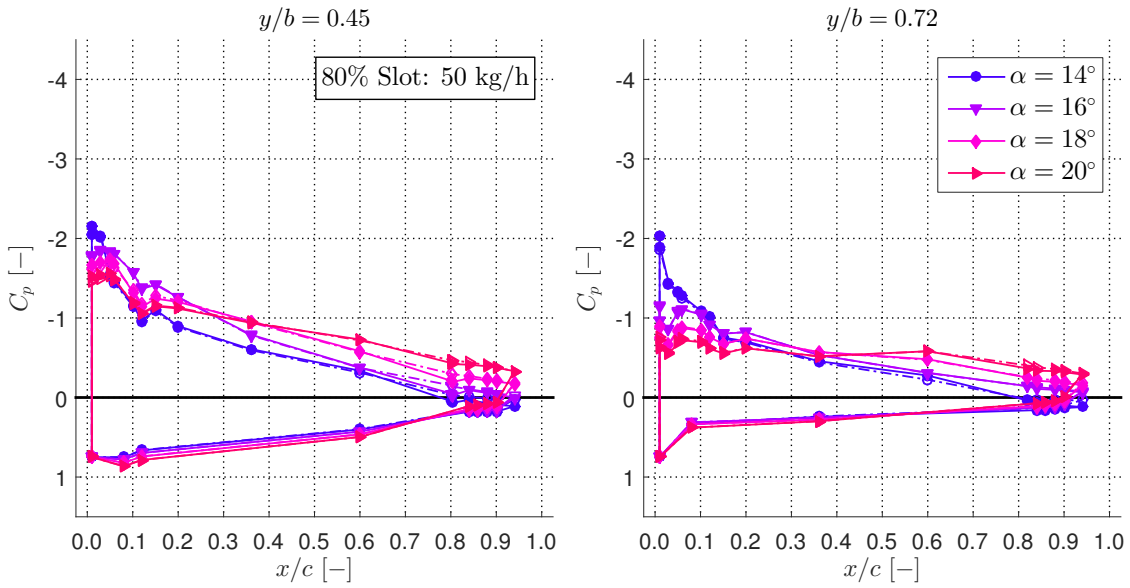

Figure 4.70: Comparison of pressure distribution C_p for $\delta_F = 0°$ with sweeping jet actuators from the 80% slot at a mass flow rate of 50 kg/h. Baseline (no blowing) is a dashed line, while the solid line represents the blowing case. Angles: 14°, 16°, 18°, 20°.

actuators is able to change the whole flow regime around the wing and influences not only the whole chord on the suction side, but reaches all the way around the wing to the pressure side. There are also no visible peaks due to the sweeping at $x/c = 0.8$, which supports the previous statement, that it does not only influence the flow locally, but on a global scale. Once the flow separates ($\alpha > 14°$), the benefit of sweeping disappears, but doesn't go into a deleterious effect like many other cases.

Figs. 4.71 to 4.73 show the tuft images for the 80% slot. For $\alpha = 10°$ there is no change except at the very last tuft column, where the spanwise cross-flow is reduced by the sweeping from the 80% slot. This reduction of spanwise cross-flow is believed to be the reason for the large lift benefit that is created. At a larger angle of attack $\alpha = 14.5°$, the leading edge separation bubble starts to grow, and the spanwise cross-flow increases again despite the sweeping. The additional spanwise cross-flow seems to be the reason for the reduction of the lift benefit with increasing angle of attack after the separation bubble starts to form ($\alpha > 14°$). However, at $\alpha = 16°$ there is still a visible spanwise cross-flow reduction especially at the root, despite the high incidence angle and the large separation at the leading edge. Consequently, the C_L vs. α plot shows a small lift benefit, until the sweeping has no more effect at $\alpha = 20°$.

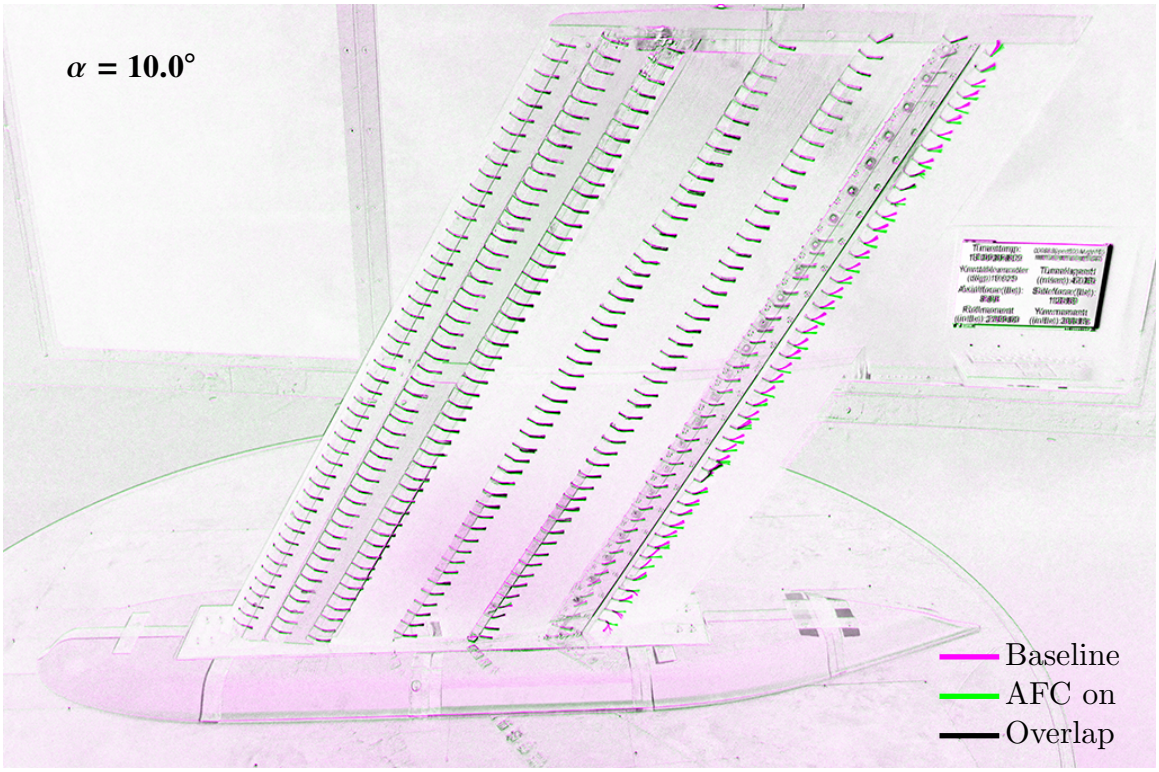

Figure 4.71: Tuft visualization for $\delta_F = 0°$ with sweeping jet actuators from the 80% slot at a mass flow rate of 75 kg/h and $\alpha = 10°$.

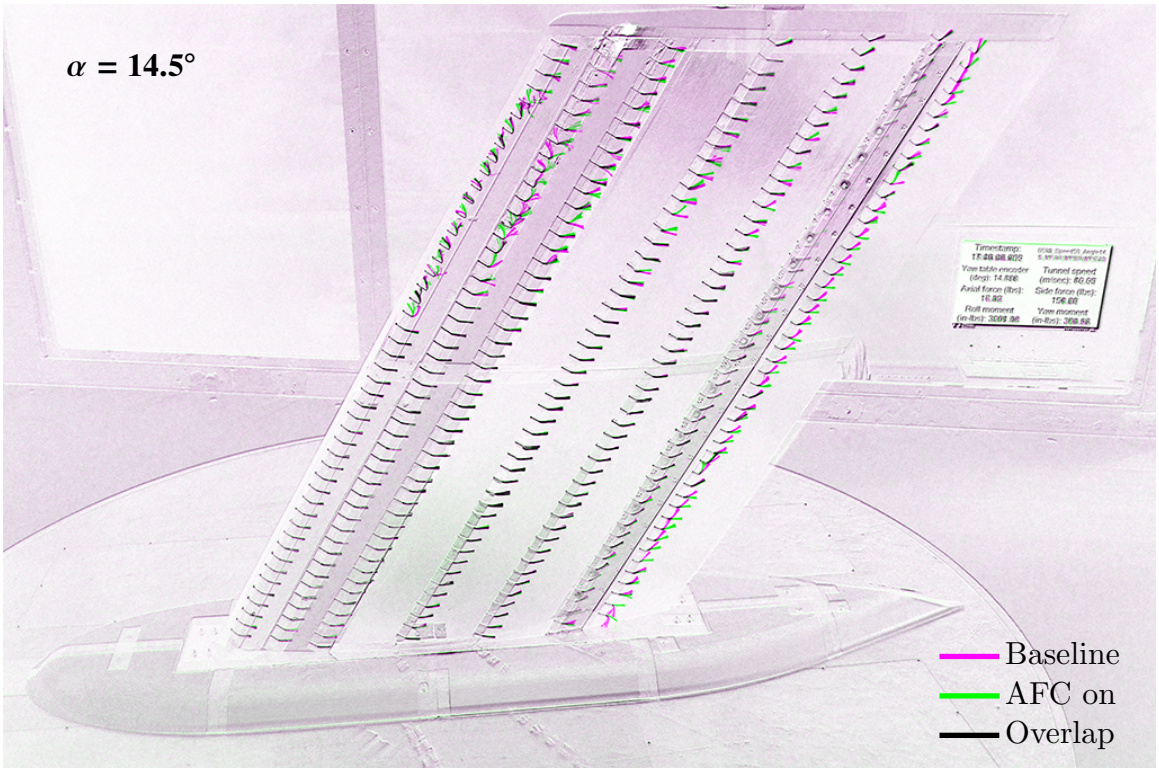

Figure 4.72: Tuft visualization for $\delta_F = 0°$ with sweeping jet actuators from the 80% slot at a mass flow rate of 75 kg/h and $\alpha = 14.5°$.

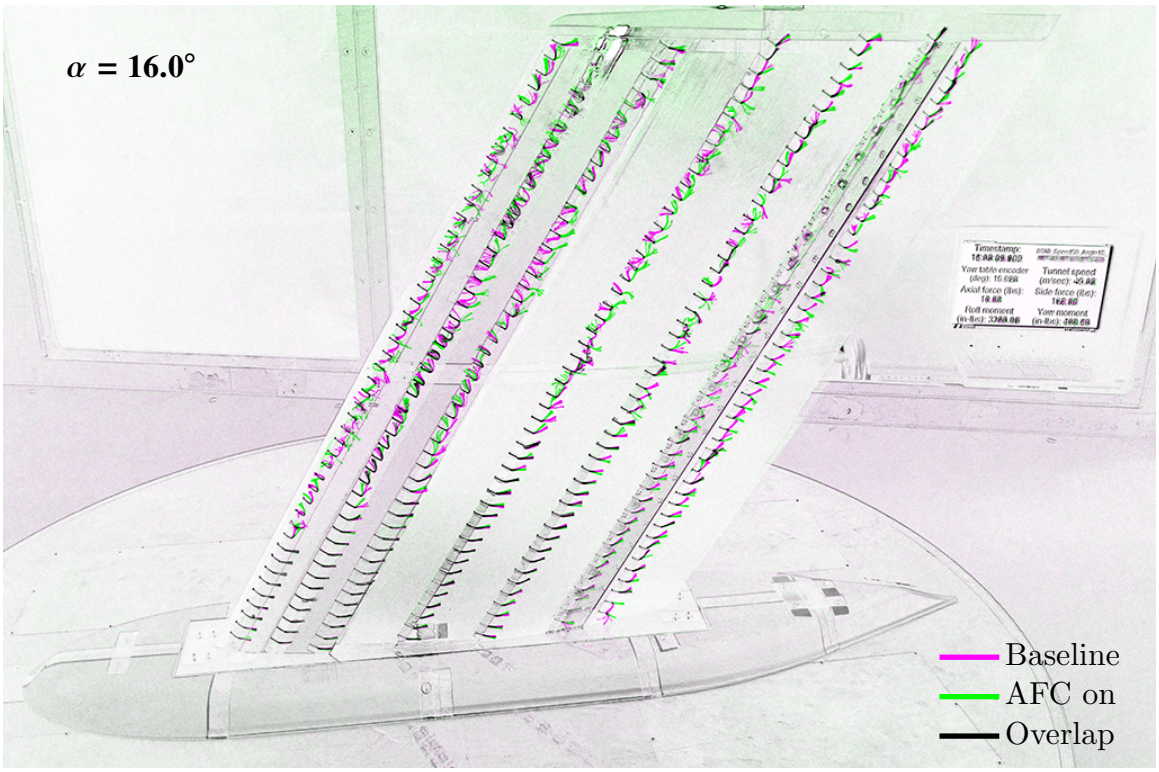

Figure 4.73: Tuft visualization for $\delta_F = 0°$ with sweeping jet actuators from the 80% slot at a mass flow rate of 75 kg/h and $\alpha = 16°$.

4.3.6 Configuration 4: Unsteady Blowing with $\delta_F = 45°$

The last configuration used the deflected flap ($\delta_F = 45°$) along with sweeping jet actuators. The data was taken at a wind tunnel speed of 40 m/s, which yields the highest coefficients of momentum input C_μ compared to the previous cases. To be consistent, the mass flow rates were the same again: 0 kg/h, 25 kg/h, and 50 kg/h for every slot, yielding 27 different combinations. For every slot location a mass flow rate of 75 kg/h was added to extend the C_μ values for the given experimental setup analogous to the previous cases. Due to the reduction of the wind tunnel speed the ratio u_{jet}/u_∞ reached values from 3 (25 kg/h) up to 8 (50 kg/h and 75 kg/h). The combinatory cases are omitted again due to the lack of additional benefits.

Fig. 4.74 summarizes the force balance data for the 1% slot. Taking a closer look at the lift differences ΔC_L compared to the baseline (no blowing), there is a small lift increase for the highest mass flow rate. C_μ is considerably large, and thus one would expect a much larger benefit. An explanation for this could be the curved exit, which causes the sweeping jet to expand and mix. During this process the effective jet velocity is significantly reduced at the slot exit and leads to disappointing results.

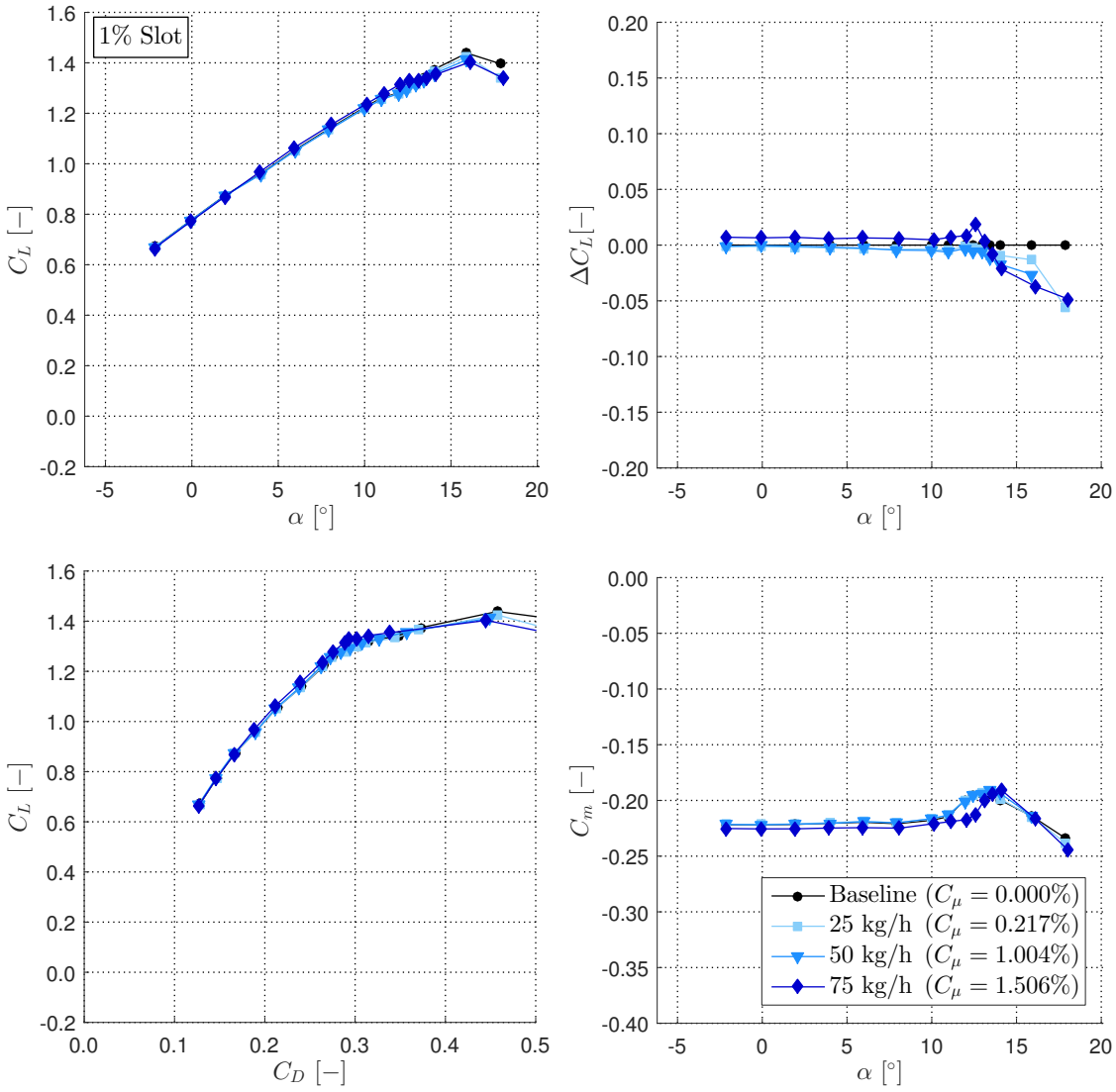

Figure 4.74: Impact of sweeping jet actuators with $\delta_F = 45°$ at the 1% slot with increasing mass flow rates compared to the baseline case (no blowing).

However, there is a little lift peak at $\alpha = 12.5°$. This is interesting, because one can see that the pitching moment has a little shift to the right exactly at the same angle of attack. In other words, even though the 1% slot with sweeping jet actuators doesn't seem to be very beneficial for the lift, it seems to be the first "solution" so far that is able to delay separation. In this case, the separation is delayed by about $\alpha = 1-2°$. The 1% slot hasn't shown a lot of promising results during the previous experiments, but it might be capable of effectively delaying separation.

The pressure distribution is plotted in Figs. 4.75 to 4.77. At the lower angles of attack (Fig. 4.75) there is nothing special going on, except that the sweeping causes the suction pressure to slightly

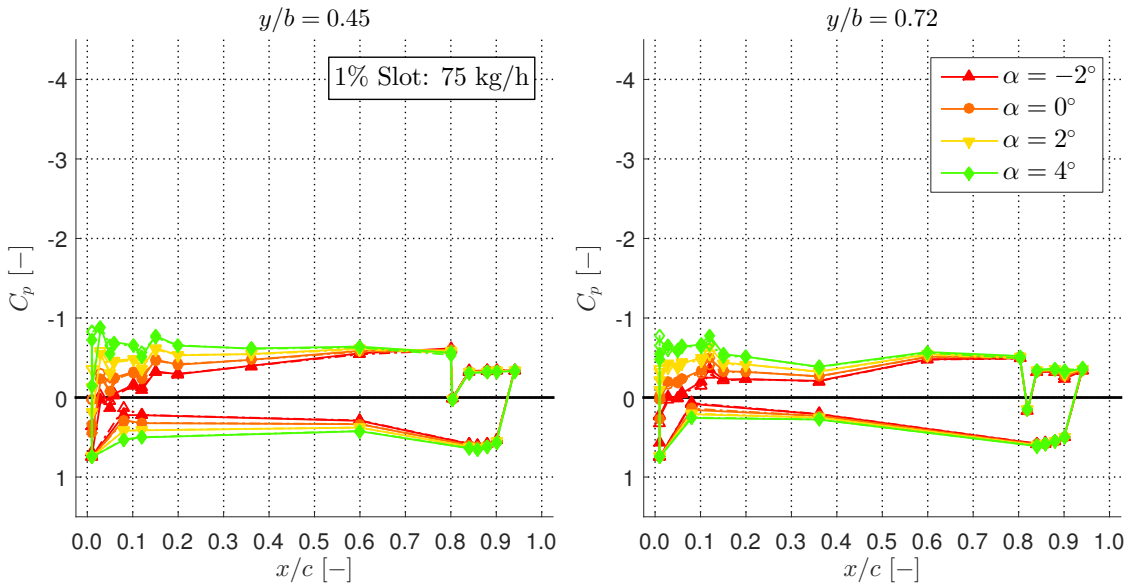

Figure 4.75: Comparison of pressure distribution C_p for $\delta_F = 45°$ with sweeping jet actuators from the 1% slot at a mass flow rate of 75 kg/h. Baseline (no blowing) is a dashed line, while the solid line represents the blowing case. Angles: -2°, 0°, 2°, 4°.

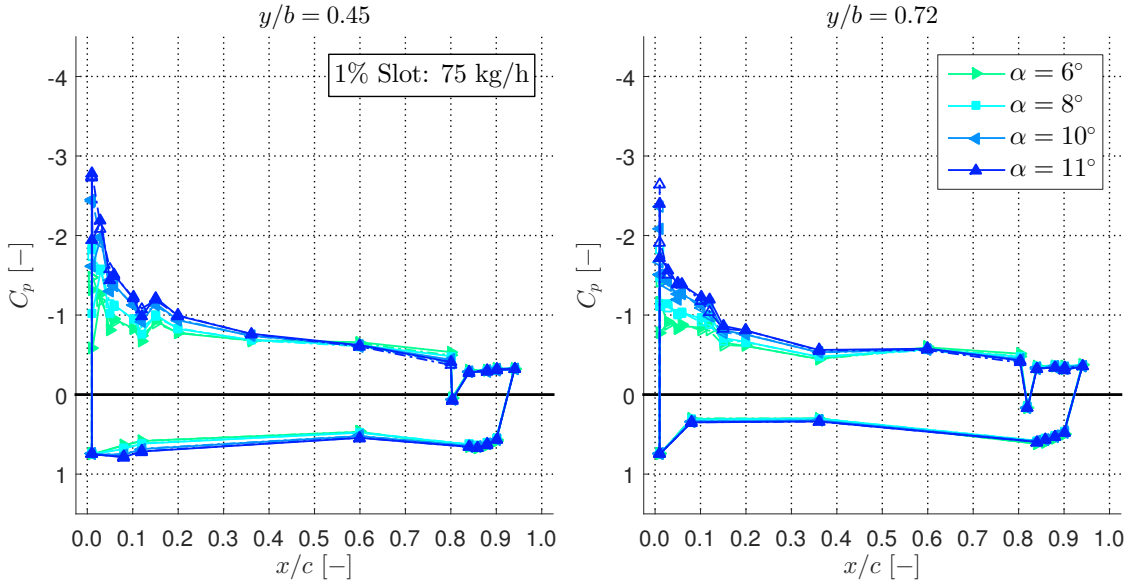

Figure 4.76: Comparison of pressure distribution C_p for $\delta_F = 45°$ with sweeping jet actuators from the 1% slot at a mass flow rate of 75 kg/h. Baseline (no blowing) is a dashed line, while the solid line represents the blowing case. Angles: 6°, 8°, 10°, 11°.

decrease right around the 1% slot. For the next set of incidence angles, there's an apparent difference between $y/b = 0.45$ and $y/b = 0.72$. While at a lower spanwise location, sweeping now actually improves the suction pressure around the 1% slot, at $y/b = 0.72$ it gets decreased. This is an indication that the sweeping jet actuators are changing the flow regime at these angles. The effect of

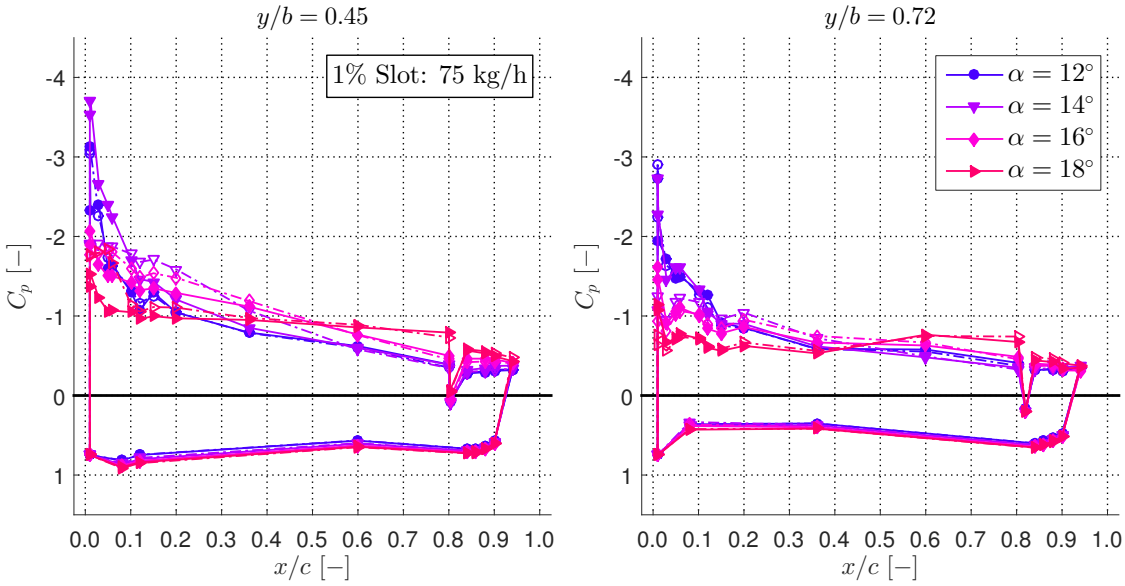

Figure 4.77: Comparison of pressure distribution C_p for $\delta_F = 45°$ with sweeping jet actuators from the 1% slot at a mass flow rate of 75 kg/h. Baseline (no blowing) is a dashed line, while the solid line represents the blowing case. Angles: 12°, 14°, 16°, 18°.

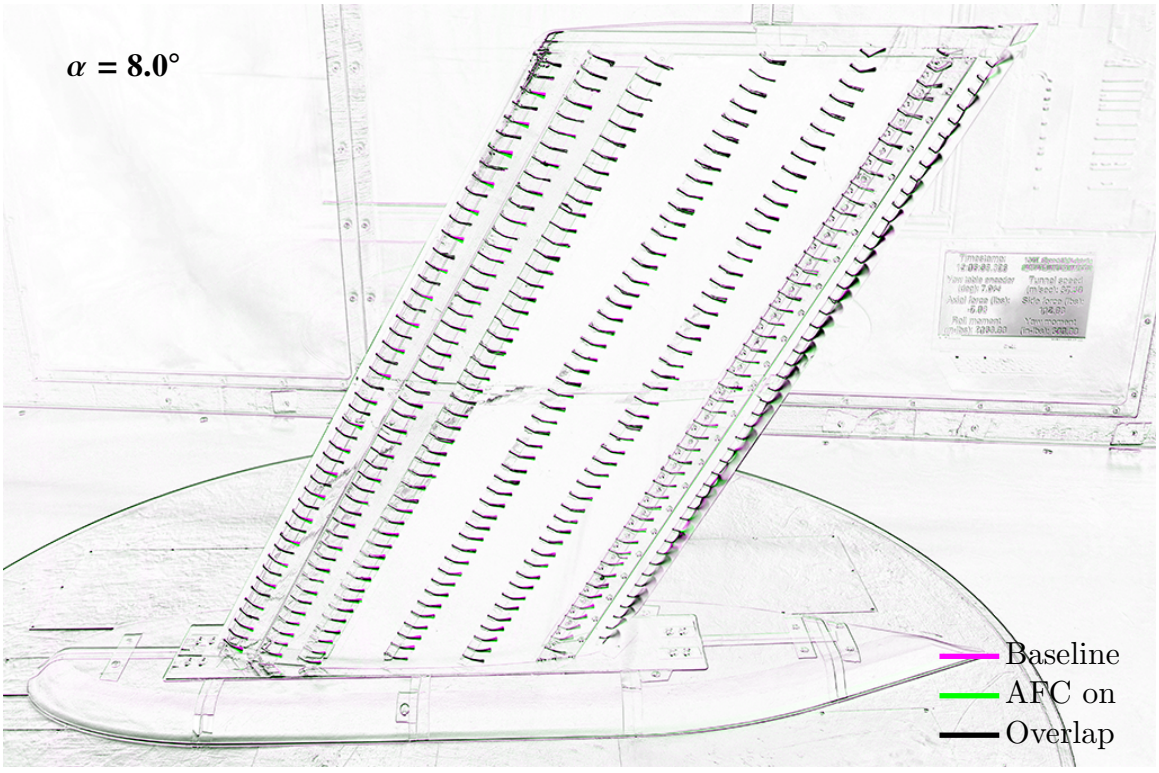

Figure 4.78: Tuft visualization for $\delta_F = 45°$ with sweeping jet actuators from the 1% slot at a mass flow rate of 75 kg/h and $\alpha = 8°$.

it is visible at a angle of attack $\alpha = 14°$, where the flow around the 1% slot is able to achieve much

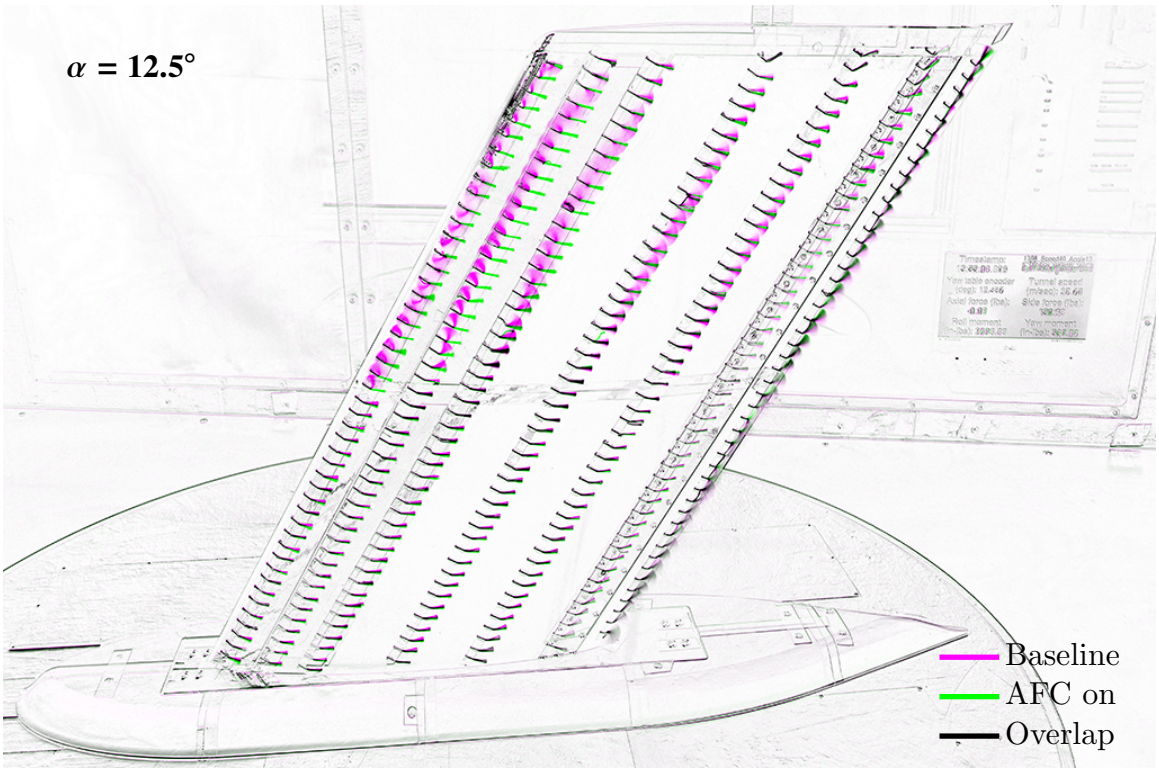

Figure 4.79: Tuft visualization for $\delta_F = 45°$ with sweeping jet actuators from the 1% slot at a mass flow rate of 75 kg/h and $\alpha = 12.5°$.

higher suction pressures, and therefore generate extra lift. As stated before, this is not due to a lift benefit, but rather the consequence of a separation at leading edge of the wing.

Similarly to the case with the non-deflected flap ($\delta_F = 0°$), the tuft image in Fig. 4.78 doesn't reveal anything that could explain the small additional lift that gets created. Note that the tufts right after the 1% slot point perpendicularly downwards with reference to the slot exit of the wing. In the unblown case, the tufts are slightly influenced by the free stream, and hence are shifted a bit upwards. However, it is not known if that is the reason for the slight lift increase, as the previous configurations would suggest otherwise. This is more evident when comparing the previous data to Fig. 4.79 with $\alpha = 12.5°$, where the 1% slot is again capable of reattaching the leading edge separation bubble, but this time without causing any additional spanwise cross-flow at the trailing edge. This might serve as a good explanation for the pitching moment delay that was observed. It seems that if one can reattach the separation bubble without causing additional spanwise cross-flow at the trailing edge, then the destabilization of the pitching moment can be delayed for a limited

range of angles of attack. The loss of vortex lift that is created by the separation bubble might be the reason why it hardly has any effect on C_L.

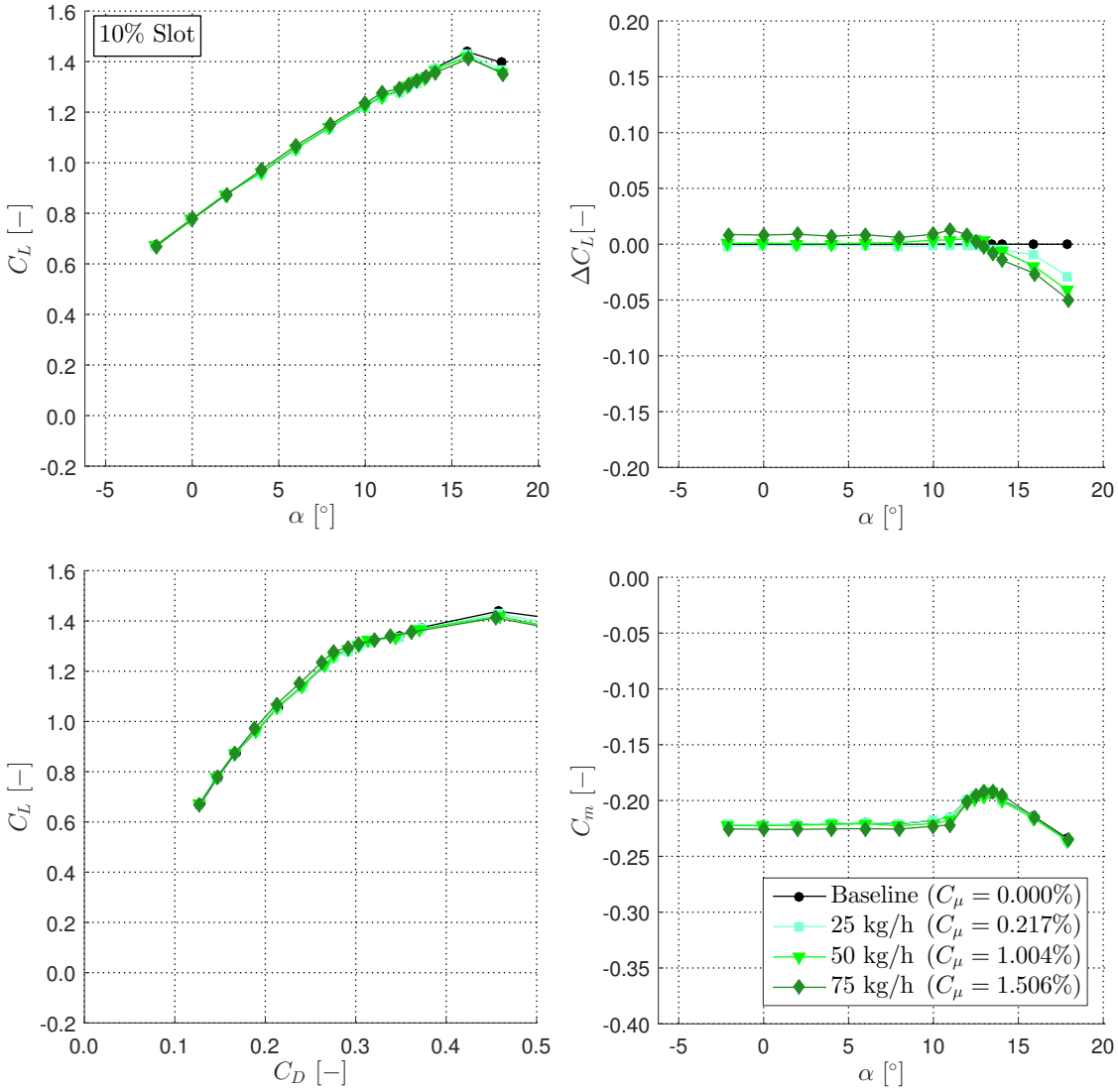

Figure 4.80: Impact of sweeping jet actuators with $\delta_F = 45°$ at the 10% slot with increasing mass flow rates compared to the baseline case (no blowing).

The 10% slot using sweeping jet actuators with a flap at 45° shows only minor changes (see Fig. 4.80). The 75 kg/h mass flow rate shows a slim improvement in lift, while the other mass flow rates follow the baseline. Compared to the 1% slot, there is no separation delay visible. The lift-drag curve and the pitching moment don't seem to be influenced by any means while the flow is attached ($\alpha < 12°$). At higher incidence, sweeping from the 10% slot is deleterious for lift, but still has only minor effects on the lift-drag curve and the pitching moment coefficient.

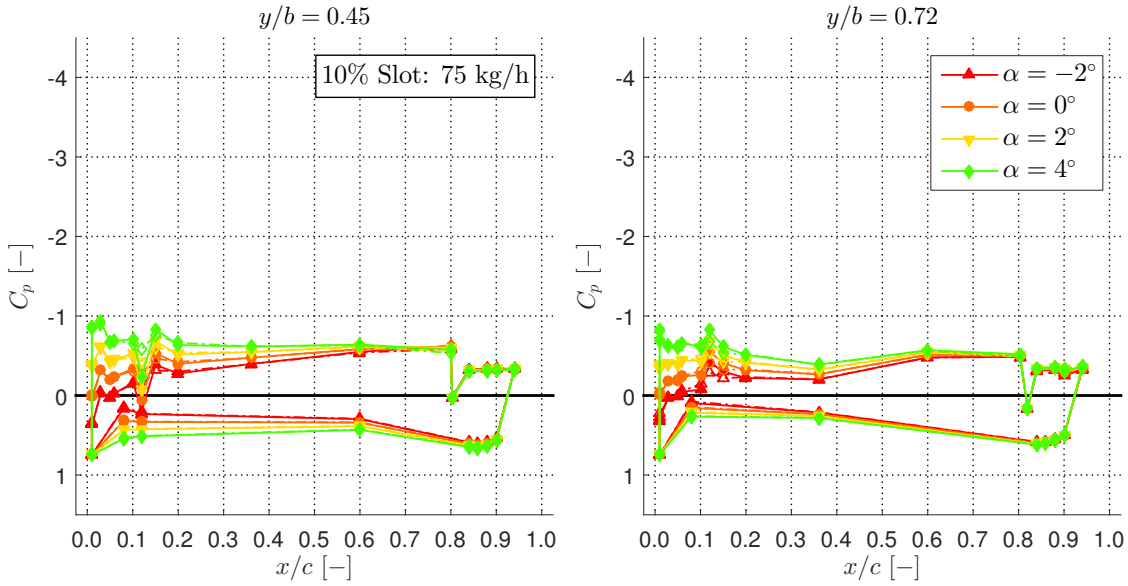

Figure 4.81: Comparison of pressure distribution C_p for $\delta_F = 45°$ with sweeping jet actuators from the 10% slot at a mass flow rate of 75 kg/h. Baseline (no blowing) is a dashed line, while the solid line represents the blowing case. Angles: -2°, 0°, 2°, 4°.

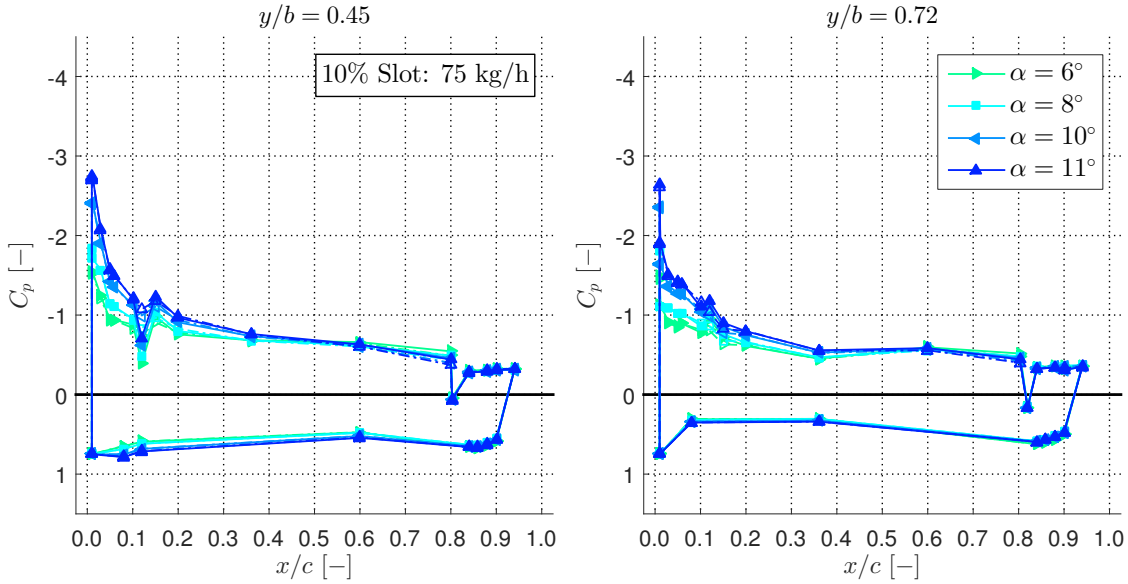

Figure 4.82: Comparison of pressure distribution C_p for $\delta_F = 45°$ with sweeping jet actuators from the 10% slot at a mass flow rate of 75 kg/h. Baseline (no blowing) is a dashed line, while the solid line represents the blowing case. Angles: 6°, 8°, 10°, 11°.

The pressure plots (Figs. 4.81 to 4.83) don't show big changes for the attached flow regime. The only interesting thing is the clear suction pressure valley at $x/c = 0.1$ that is a direct consequence of the jet blowing. One might notice that this only occurs at $y/b = 0.45$ and not at $y/b = 0.72$. The reason is that the pressure tap row at $y/b = 0.45$ is inline with a single jet, while the pressure tap row

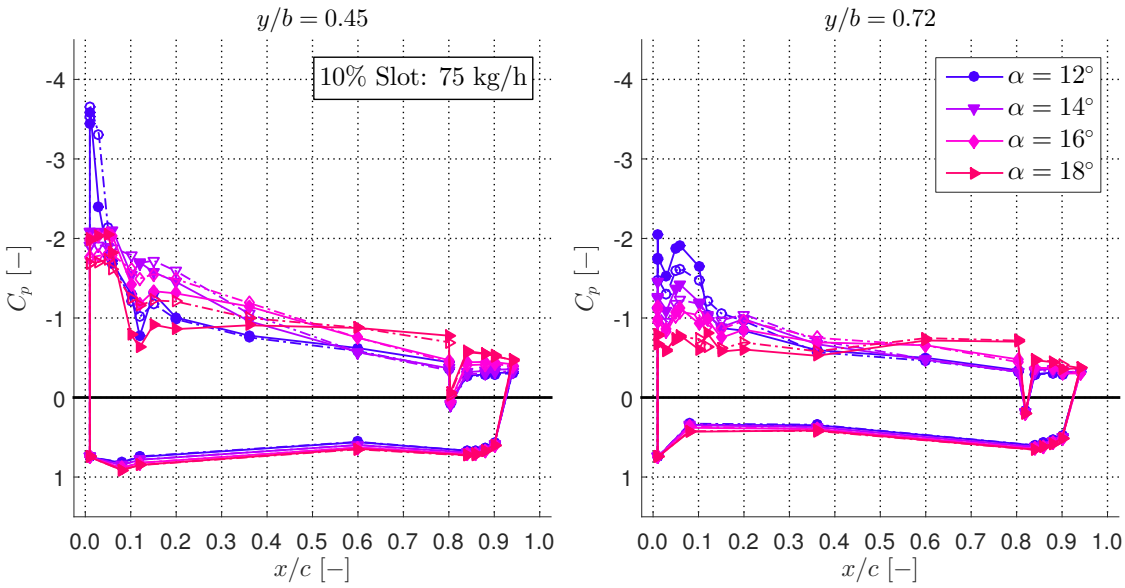

Figure 4.83: Comparison of pressure distribution C_p for $\delta_F = 45°$ with sweeping jet actuators from the 10% slot at a mass flow rate of 75 kg/h. Baseline (no blowing) is a dashed line, while the solid line represents the blowing case. Angles: 12°, 14°, 16°, 18°.

at $y/b = 0.72$ has an offset. For the angles of attack $\alpha > 12°$, one can observe that the deleterious lift effect is created at about $0.1 < x/c < 0.3$. There is actually a lift benefit for $x/c < 0.1$ but it is much smaller than the previously mentioned region with negative lift. This is a sign of loss of vortex lift once again. The 10% slot partially attaches the leading edge vortex, and as a consequence lift is lost between $0.1 < x/c < 0.3$.

The tuft images (Figs. 4.84 and 4.85) show the same effects that were observed with the steady blowing 10% slot. At angles of attack before the separation occurs ($\alpha < 12°$), blowing does basically nothing, and hence there is barely any lift benefit. The benefit is so small that it could just be a consequence of the topmost jet, reducing the exchange between the pressure and suction side of the wing (like a winglet). At incident angles larger than the separation threshold ($\alpha > 12°$), one can observe a huge change of the flow regime after the 10% slot. However, it can be assumed that the additional spanwise cross-flow created at the trailing edge (which is not visible with the tufts due to the trailing edge separation) and the loss of vortex lift have a larger deleterious effect than the benefits created around the 10% slot.

The data of the 80% slot for configuration 4 is plotted in Fig. 4.86. As one could have guessed from the same configuration with the non-deflected flap, the 80% slot shows by far the best results.

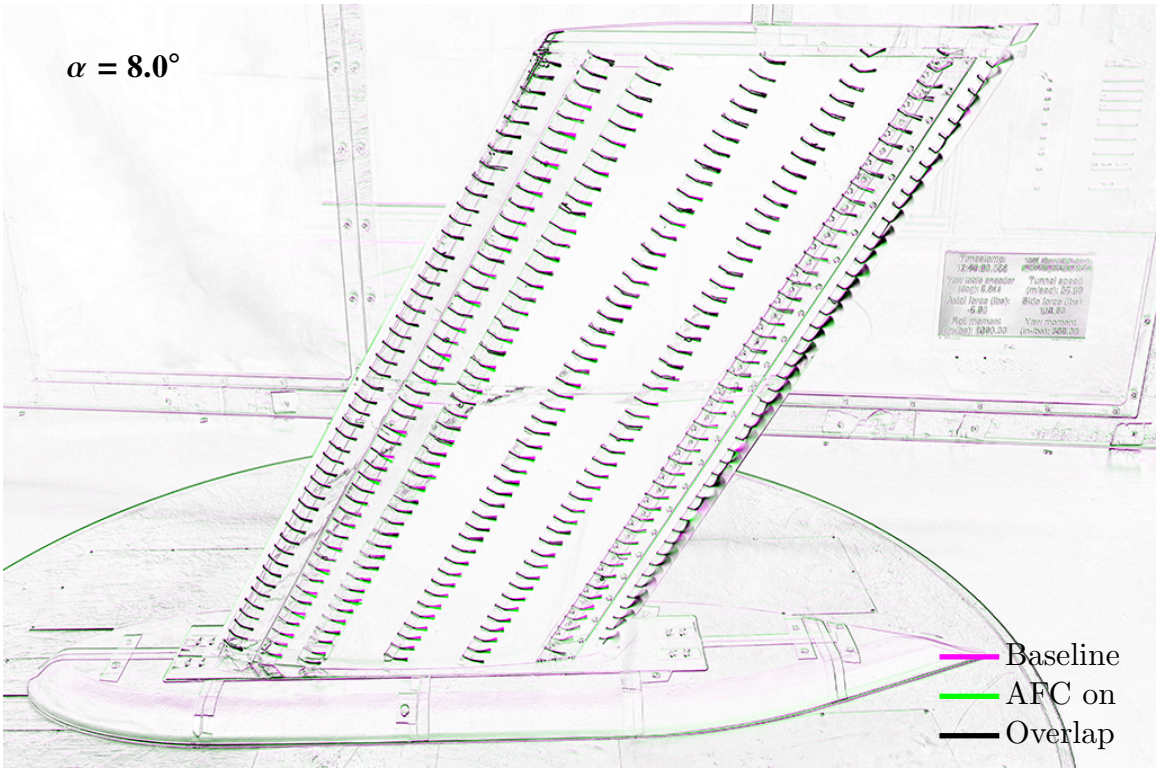

Figure 4.84: Tuft visualization for $\delta_F = 45°$ with sweeping jet actuators from the 10% slot at a mass flow rate of 75 kg/h and $\alpha = 8°$.

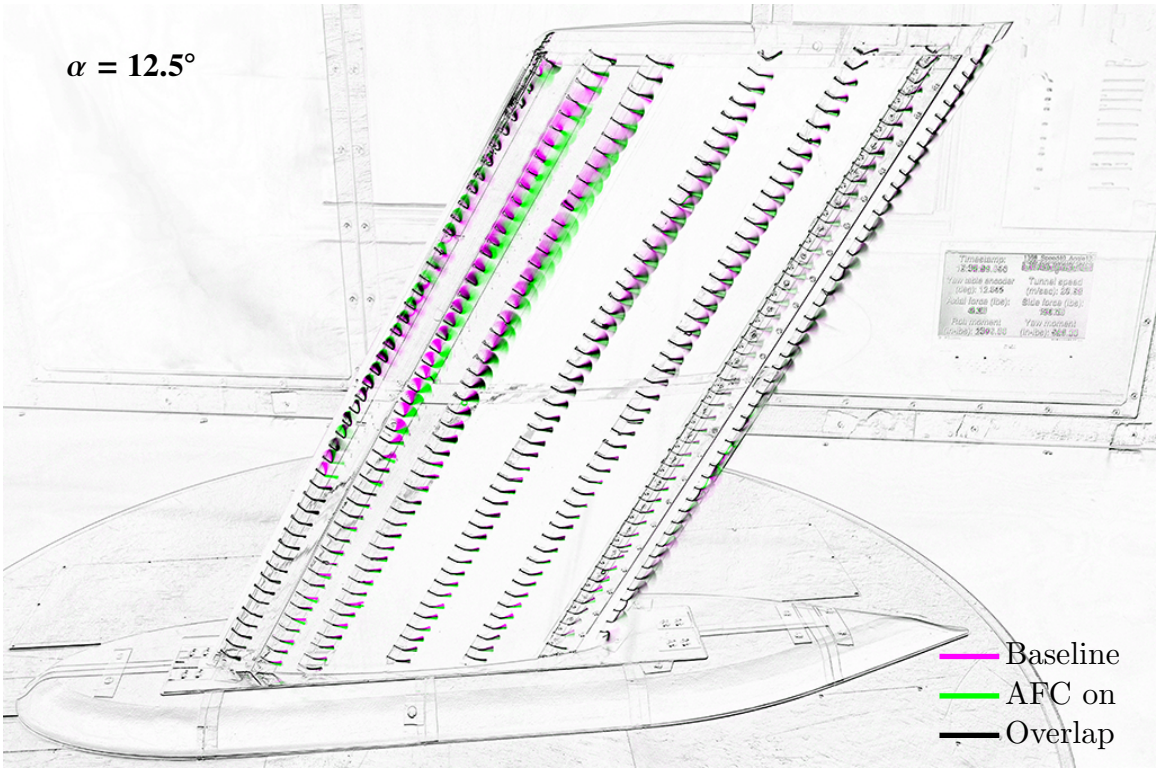

Figure 4.85: Tuft visualization for $\delta_F = 45°$ with sweeping jet actuators from the 10% slot at a mass flow rate of 75 kg/h and $\alpha = 12.5°$.

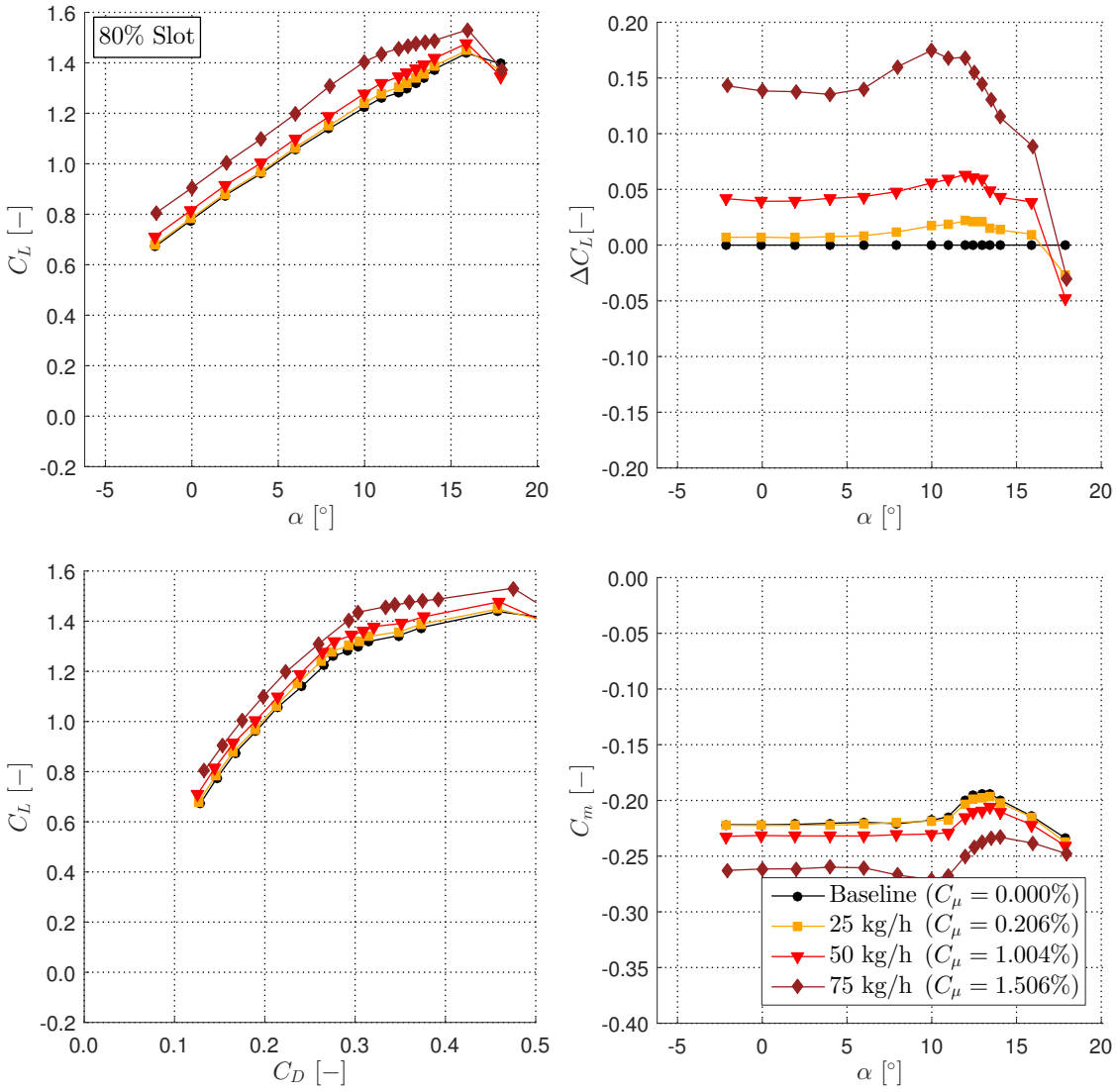

Figure 4.86: Impact of sweeping jet actuators with $\delta_F = 45°$ at the 80% slot with increasing mass flow rates compared to the baseline case (no blowing).

Because the wind tunnel speed was reduced to 40 m/s, higher C_μ values could be achieved, which makes the additional lift increments even larger. The lift increase for a coefficient of momentum input of C_μ of 1.5% (75 kg/h) is about 0.15 in C_L through all attached angles of attack ($\alpha < 12°$). This corresponds to a 10% lift benefit compared to the maximum lift coefficient $C_{L,\max}$ for a reasonable mass flow rate input. The other cases show a lower lift benefit in agreement with the lower input flow rates. However, it seems to be more beneficial to use a higher mass flow rate as the lift increase seems to grow over-proportionally. This needs further investigation (see Chapter 7). Due to the now much larger increase in lift, the lift-drag curve is able to improve significantly. On top of that, the pitching moment coefficient shifts down by about 20%. However, compared to the 1% slot, there

doesn't seem to be any separation delay. There is still a lift benefit when separation starts occurring at $12° < \alpha < 16°$, but it diminishes very quickly, and then goes into a deleterious effect.

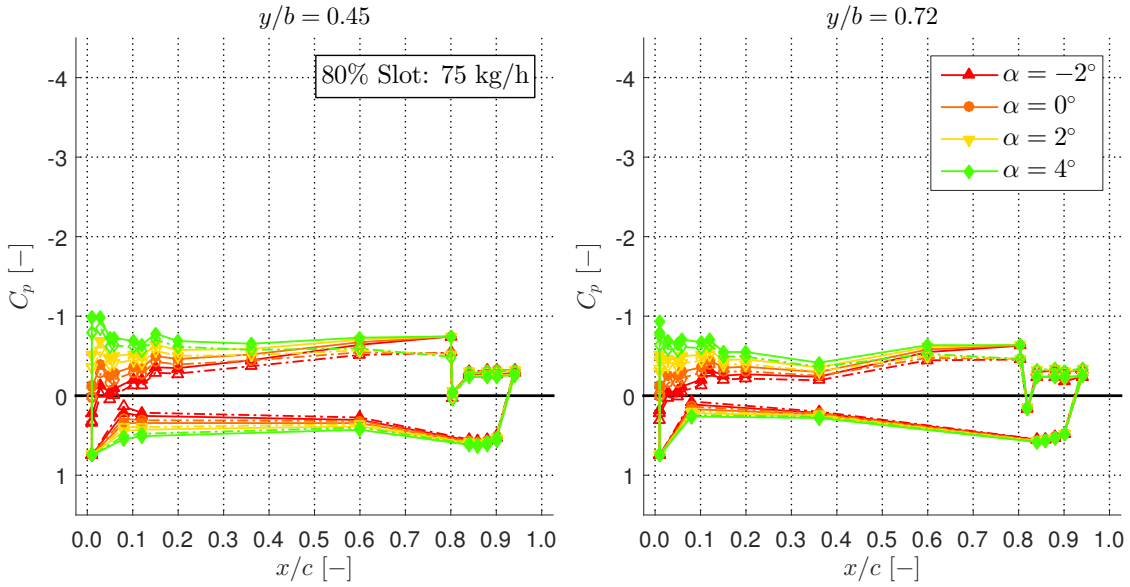

Figure 4.87: Comparison of pressure distribution C_p for $\delta_F = 45°$ with sweeping jet actuators from the 80% slot at a mass flow rate of 75 kg/h. Baseline (no blowing) is a dashed line, while the solid line represents the blowing case. Angles: -2°, 0°, 2°, 4°.

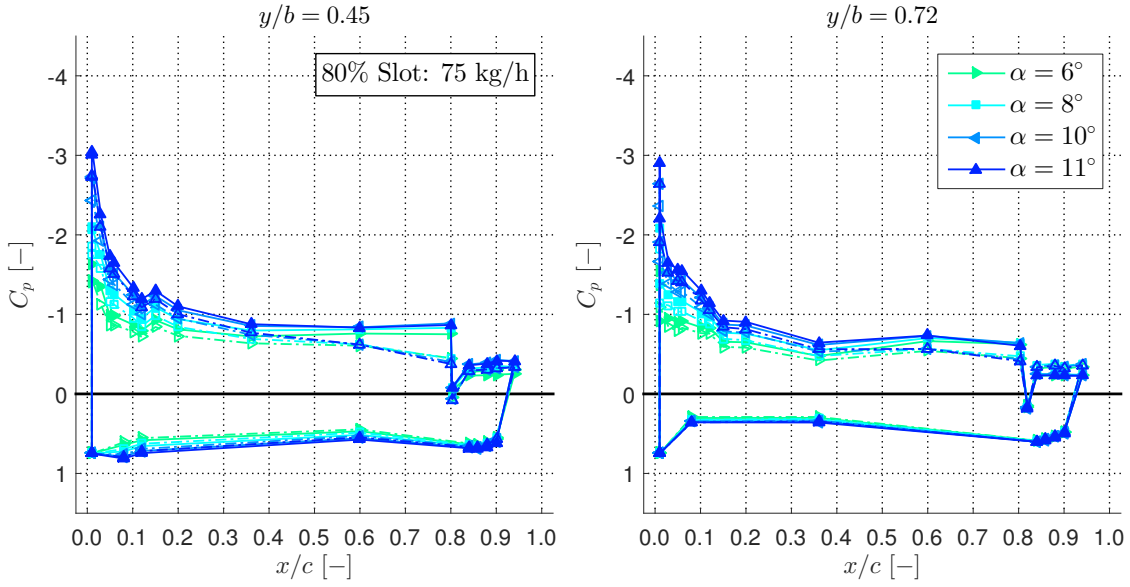

Figure 4.88: Comparison of pressure distribution C_p for $\delta_F = 45°$ with sweeping jet actuators from the 80% slot at a mass flow rate of 75 kg/h. Baseline (no blowing) is a dashed line, while the solid line represents the blowing case. Angles: 6°, 8°, 10°, 11°.

With the larger lift differences, the pressure plots (Figs. 4.87 to 4.89) are much easier to interpret. It is interesting to see that the 80% sweeping doesn't affect the trailing edge region too much, but

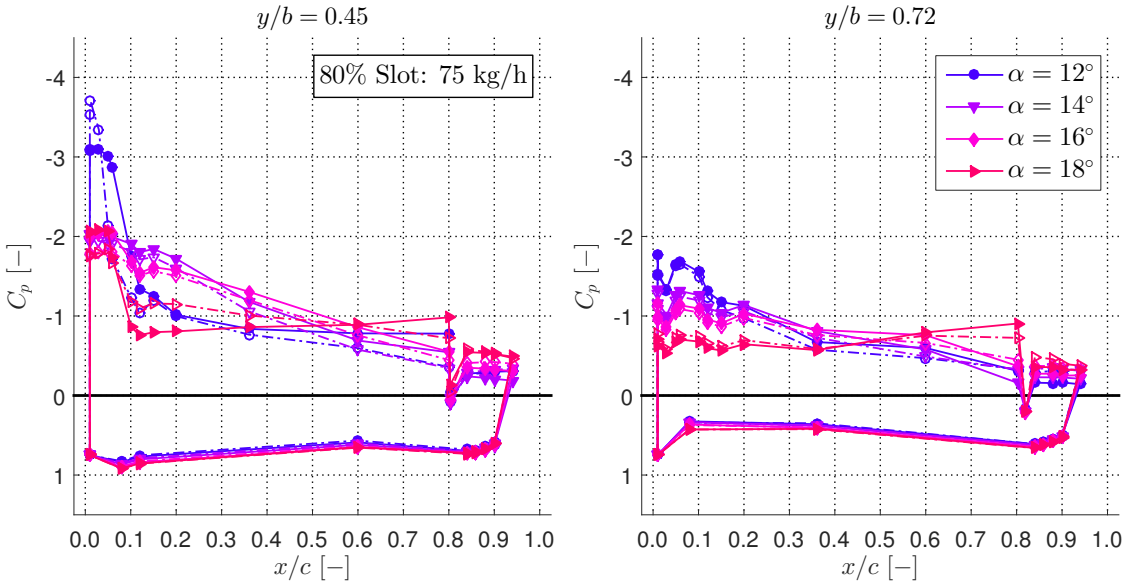

Figure 4.89: Comparison of pressure distribution C_p for $\delta_F = 45°$ with sweeping jet actuators from the 80% slot at a mass flow rate of 75 kg/h. Baseline (no blowing) is a dashed line, while the solid line represents the blowing case. Angles: 12°, 14°, 16°, 18°.

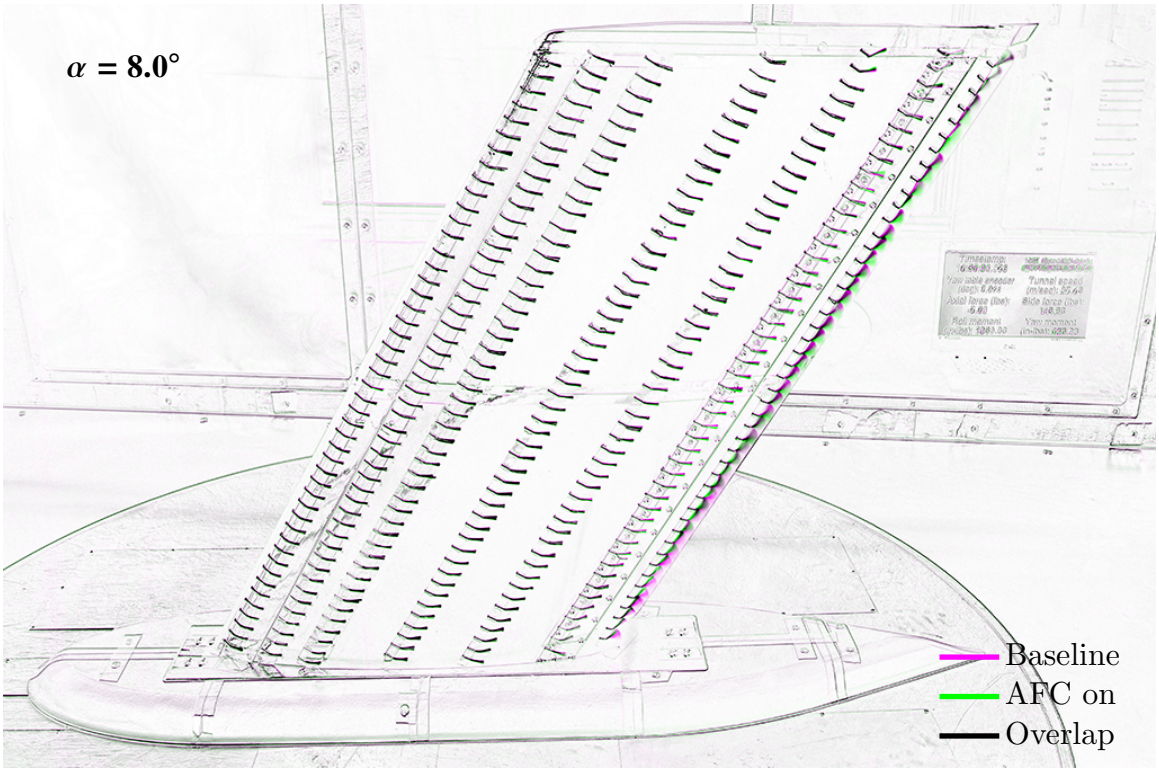

Figure 4.90: Tuft visualization for $\delta_F = 45°$ with sweeping jet actuators from the 80% slot at a mass flow rate of 75 kg/h and $\alpha = 8°$.

creates a lift benefit that spans over the whole wing. The biggest portion of lift is created right before the flap hinge between $0.6 < x/c < 0.8$. Sweeping jet actuation at the 80% slot seems to be the only

Figure 4.91: Tuft visualization for $\delta_F = 45°$ with sweeping jet actuators from the 80% slot at a mass flow rate of 75 kg/h and $\alpha = 10°$.

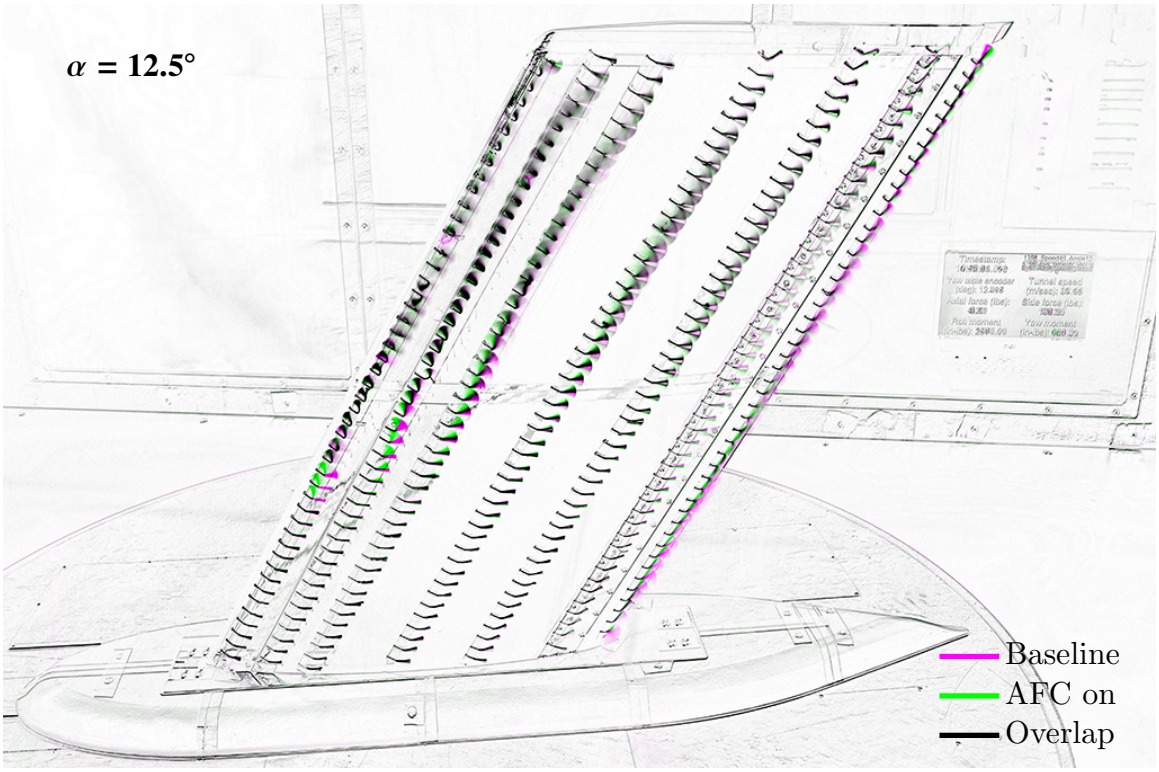

Figure 4.92: Tuft visualization for $\delta_F = 45°$ with sweeping jet actuators from the 80% slot at a mass flow rate of 75 kg/h and $\alpha = 12.5°$.

case able to influence the entire flow regime around the wing and does not only act locally. Once separation occurs at the leading edge, lift is lost but sweeping from the 80% slot is able to make up for it by creating additional lift after the separation bubble. At $\alpha = 18°$ a deleterious lift effect takes over, which is mainly caused by a large loss of lift between $0.1 < x/c < 0.3$ (loss of vortex lift).

The tuft image for $\alpha = 8°$ (Fig. 4.90) reveals that despite the large flap deflection and the present separation, the influence of the 80% sweeping is so large that it is still able to visibly influence the spanwise cross-flow. This minor change on the tuft image has a huge impact on the lift. At $\alpha = 10°$ the C_L vs. α plot shows the biggest lift benefit. The tuft image at that angle (Fig. 4.91) doesn't show anything specific. However, the break in the C_L vs. α slope at that angle might hint toward a hinge vortex and attachment over the flap. For $\alpha = 12.5°$ the shedding of the tufts that is caused by the separation was partially suppressed by the jets. At even higher incidence, the separation gets too strong and the sweeping jet actuators at the 80% slot are not able to overcome it anymore, which then causes the decline in lift. However, this result supports the suspicion that the spanwise cross-flow at the trailing edge seems to play a crucial role for the entire lift generation of a swept back wing.

4.3.7 Discussion of Results

By looking at the overall data, it becomes quite obvious that the best cases all come from the 80% slot equipped with sweeping jet actuator. It became evident through the entire project, that the 80% slot equipped with sweeping jet actuators was the only configuration that worked reliably well. The 1% and 10% slots are inferior when it comes to pure lift performance. However, when comparing these two slots directly with each other, the 1% slot seems to have a slightly higher impact, positive or negative, than the 10% slot. This makes sense; due to the fact that the 1% slot is usually able to correct the entire leading edge separation bubble (vortex lift), while the 10% slot can only correct what's after $x/c = 0.1$. On top of that, the 1% slot seems to be the only slot that has an influence on separation delay. Using sweeping jet actuators, a slight delay of about 1° to 2° could be observed. It is believed, that the 1% slot could be improved to be able to cause a much larger separation delay.

Even though the airfoil was designed so the slots would work together, no combinatory effects could be observed. Fig. 4.93 which represents the deflected flap ($\delta_F = 45°$) using sweeping jet actuators is a typical example. The results for multiple active slots at various mass flow rates can be predicted by

summing up the single slot performances. No additional benefit was observed when multiple slots were active at once. Based on these results it is suggested to focus all the available resources into a single slot, preferably the 80% slot.

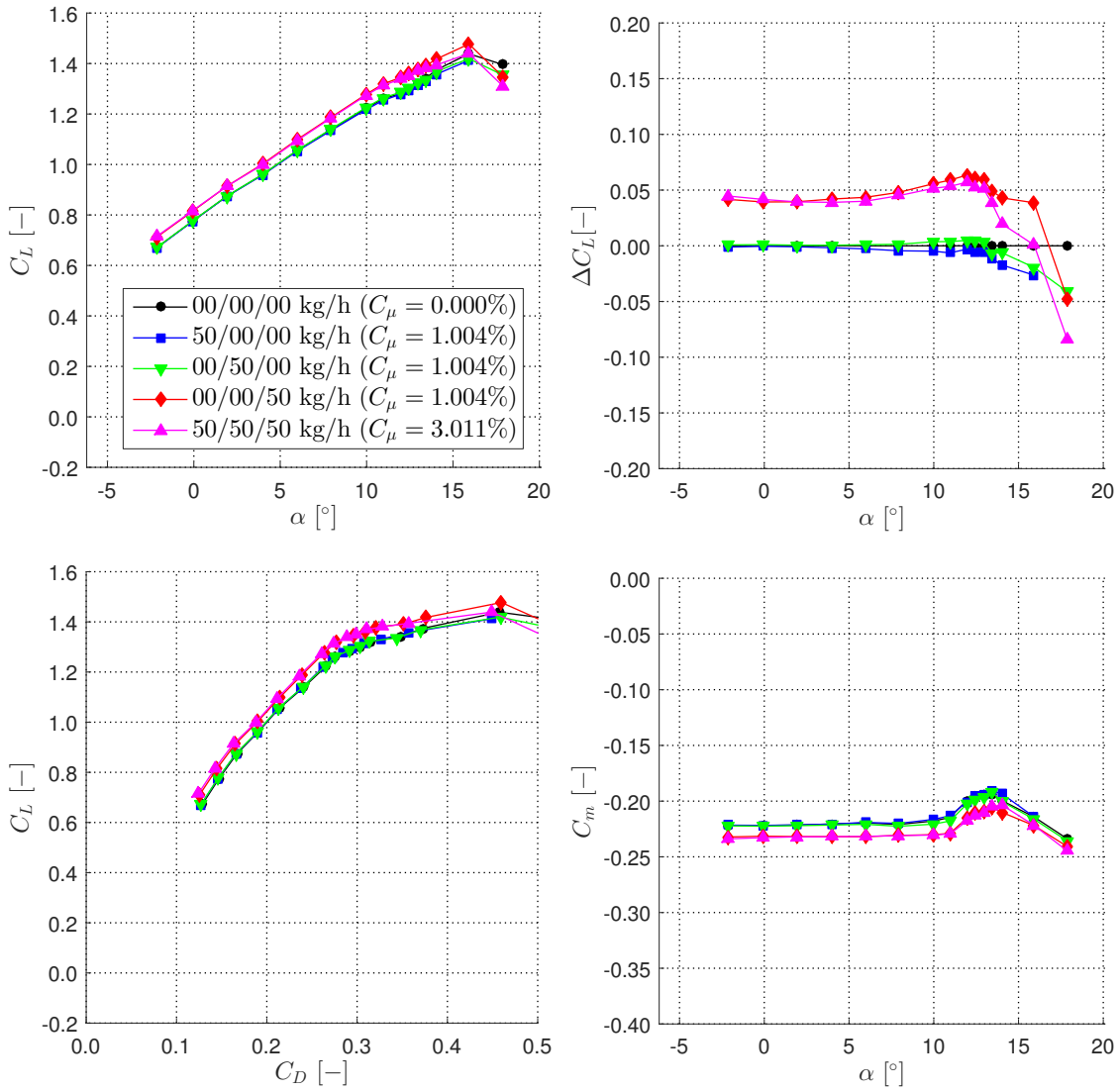

Figure 4.93: Comparison of sweeping jet actuators with $\delta_F = 45°$ at different slots including a case with all slots active. The fully active case is a combination of the single slots effects. There is no combinatory benefit.

Two other questions that pop up are the following:

1. Why does steady blowing not work?

2. Why do the 1% and 10% slot not perform as well as the 80% slot?

The answer to the first question was briefly mentioned previously: It is believed, that the ratio $u_{\text{jet}}/u_{\infty}$ is critical to make AFC work well. When the velocity ratio is of the order of one the jets act as a source while at higher velocity ratios they act like a line sink. During the NASA ERA project (Seele, Graff, Lin, et al., 2013) it was established that this ratio should roughly fulfill the following rule of thumb to ensure performance benefits:

$$u_{\text{jet}}/u_{\infty} > 3. \tag{4.1}$$

In the steady test cases, the mass flow rate was actually too low to fulfill this rule. In fact, the ratio was around 1 for the highest mass flow rates. Hence, based on previous experience, it could have been expected that these slots would never be able to work at the provided mass flow rates. It is likely that the steady blowing slots would work eventually at higher mass flow rates. The question remains if this mass flow rate is still practical, especially because the sweeping jet actuators seem to work well at the available mass flow rate. The aforementioned realizations eventually led to the experiments in Chapter 7, where these discrepancies are discussed and answered in detail.

Other indications are the C_{μ} values that are comparably low due to the large slots exit. However, it remains questionable if C_{μ} is the right parameter to compare a slot with a jet due to their large difference in exit area. It doesn't seem to be the right approach to try to equalize C_{μ} for a slot vs. jet comparison. The mass flow rates would be vastly different.

The answer for the second question can't be explained that easily. For the sweeping jet actuators, the requirement $u_{\text{jet}}/u_{\infty} > 3$ should be fulfilled, but the 1% and 10% slots still don't show a large effect compared to the 80% slot. The only difference between the 1% and 10% slots compared to the 80% slot is the additional curve before the slot exit. It was shown in experiments that the curve has an influence on the jet power. The specific design of the curve minimized this effect, however, it was still present. Even if it is assumed that the curve doesn't reduce the sweeping power of the jet at all, the jet will still spread into a larger area just because it has a longer path until it reaches an exit. If one assumes a fixed mass flow rate and divides it by a larger area, the problems gets quite obvious: the effective jet speed gets drastically reduced, and hence it doesn't fulfill the $u_{\text{jet}}/u_{\infty} > 3$ requirement anymore. The sweeping jet actuators at the 1% and 10% slots are obviously a little bit closer to fulfilling this conditions than when steady blowing is applied to an open slot, which explains the small performance benefits that could be observed. One way to solve this problem would be to

embed the sweeping jet actuators directly into the curve, so that their exits are directly at the airfoil just like the 80%. However, creating a working actuator design and making it machinable might be an extremely difficult task; 3D printing might be a viable solution in the near future. Additionally, the 1% and 10% slots seem to influence the vortex lift in a deleterious manner. It might be difficult to fix this phenomenon without drastically changing the wing or actuator exit design.

The power coefficient C_Π is another parameter of interest to compare. One might argue that steady blowing requires less power to run due to the wide open slot. This is true in theory, but during the performed experiments it became clear (see Fig. 4.94) that the benefit of an open slot is minor because of two facts: first, to evenly distribute the flow along an open slot a choke plate or something similar is necessary, which significantly increases the required pressure. This turned into a drawback for the 10% slot, which needed an insert for the steady blowing case, requiring a higher power to run compared to the sweeping jet actuators at the 10% slot without an insert. The second important factor is the plumbing itself. Due to the fact that every section of the wing has its own plumbing route, the tube diameters were comparably small. As such, the small tube diameters require a high pressure to uniformly feed the plenums. The 1% slot, which didn't have separate plenum sections, requires a smaller power to run compared to the other two slots. These claims are supported by Fig. 4.94. To summarize: the power coefficient for both blowing configurations (steady and sweeping) are of a similar scale due to the plumbing resistance and the introduction of choke plates for steady blowing. In other words, there's actually no or only a small benefit (depending on the design) of having an open slot compared to sweeping jet actuators.

4.4 Concluding Remarks

The experiments showed that sweeping jet actuators are superior to steady blowing at the given mass flow rates. The main reason was found to be that the rule of thumb $u_{\text{jet}}/u_\infty > 3$ needs to be fulfilled. The steady blowing slots can only reach up to about $u_{\text{jet}}/u_\infty \approx 1$, which makes them have no or only minor performance benefits on the wing (this topic is discussed in more detail in Chapter 7). When comparing the different slots with each other, the 80% slot clearly stands out as the one with the biggest performance benefit. It was able to improve the lift by more than 10% of the maximum lift achievable by the airfoil. The 80% slot was also able to increase the lift for both tested flap deflections of 0° and 45°. The main reason for the large lift benefit of the 80% slot seems to be its

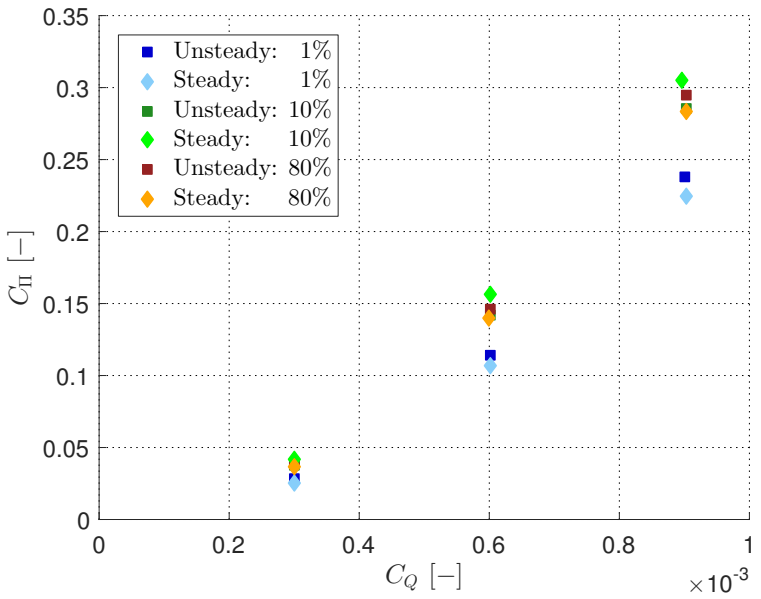

Figure 4.94: The power coefficient C_Π is plotted against the flow coefficient C_Q. It is evident that an open slot (steady blowing) does not require a much lower power to run due to the plumbing resistance and the introduction of a choke plate.

ability to control and suppress the spanwise cross-flow at the trailing edge. This doesn't seem to be possible by using the 1% and 10% slots which mostly seem to destroy the vortex lift and enhance the spanwise cross-flow. On top of that, their curved exit geometries give the sweeping jet actuators too much time to expand, which causes a reduction of jet speed, and consequently lowering the ratio u_{jet}/u_∞. However, despite these disadvantageous circumstances, the 1% slot showed the ability to delay separation to higher angles of attack. If the design can be changed to reduce the distance of the flow path of a sweeping jet, the 1% and 80% slot could be a powerful combination for controlling lift and separation over the entire wing. The effect of reduced vortex lift at higher jet velocities might remain problematic for the given airfoil design. Even though the slots were originally designed to work together, no combinatory performance benefits could be observed. One of the reasons may be that the airfoil and its slots were designed for two-dimensional configurations. Expanding it to 3D just doesn't work, as a lot of new flow phenomena, i.e. spanwise cross-flow, are introduced.

Chapter 5

The Momentum Input Coefficient C_μ

5.1 Common Calculation of C_μ

C_μ is the so called momentum input coefficient. It is an important parameter in AFC studies, and it was introduced by Poisson-Quinton, 1948. Its most common definitions is

$$C_\mu = \frac{\dot{m} u_{\text{jet}}}{\frac{1}{2}\rho_\infty u_\infty^2 S}, \tag{5.1}$$

where $\dot{m}$ is the mass flow rate, u_{jet} the jet exit velocity, ρ_∞ the freestream density, u_∞ the freestream velocity, and S a reference area. For a wing the reference area S is usually the wing planform. All these variables have to be measured with the exception of the reference area S to get an accurate representation of C_μ. While the freestream quantities are easily obtained in a wind tunnel environment, the jet-related quantities are much more difficult to acquire. The best way to measure the mass flow rate is to prescribe it as an input into the actuation system using a mass flow rate controller, or to measure it via a mass flow meter. Obtaining the jet exit velocity u_{jet} is even more challenging. The only "direct" way to acquire the velocity is by hot wire measurements. However, a hot wire probe is a brittle measurement tool which can't easily be used on a complex model. Thus, this technique sees no real use in practice.

Another technique is to measure the pressure ratio in the actuator nozzle, and then calculate the momentum input coefficient using isentropic flow relations:

$$M_{\text{jet}} = \sqrt{\frac{2}{\gamma - 1}\left[\left(\frac{p_{\text{t}}}{p_{\text{s}}}\right)_{\text{jet}}^{\frac{\gamma-1}{\gamma}} - 1\right]}, \tag{5.2}$$

$$T_s = \frac{T_t}{1 + \frac{\gamma-1}{2} M_{\text{jet}}^2}, \tag{5.3}$$

$$C_\mu = \frac{\dot{m} u_{\text{jet}}}{\frac{1}{2}\rho_\infty u_\infty^2 S} = \frac{\dot{m} a M_{\text{jet}}}{\frac{1}{2}\rho_\infty u_\infty^2 S} = \frac{\dot{m}\sqrt{\gamma R T_s} M_{\text{jet}}}{\frac{1}{2}\rho_\infty u_\infty^2 S}. \tag{5.4}$$

While this approach is theoretically exact with the assumption of isentropy, practically it encounters several issues similar to hot wire measurements. To measure the correct nozzle pressure ratio a probe, for example a pitot tube, needs to be stuck into the usually tiny nozzles. Due to model

complexity the probe is often hand-held, and the measurements have to be repeated for every mass flow rate, jet design, and for every jet location (non-constant pressure along wing-span). The latter problem can be solved by a jig, but is then only able to compare uniformity among many nozzles. In summary, this method is tedious, unreliable, and impractical to use on an actual wing model but finds widespread acceptance due to the lack of "exact" alternatives. Examples in the literature employing this technique can be found in Bauer, Grund, and Nitsche, 2014 or Clemons and Wlezien, 2016.

A third approach is to assume incompressibility. This method has the obvious advantage that it doesn't require a pressure measurement, and C_μ can be calculated based on the mass flow rate once the freestream quantities are known. The incompressible flow assumption works well in water, but for wind tunnel measurements the working fluid is air. Treating air as an incompressible fluid leads to large errors with increasing Mach number. Nevertheless, the ease of this approach still convinces people to use it, and live with the errors as seen in Seele, Tewes, et al., 2009 or Schmidt et al., 2015.

5.2 Common Misconceptions

The most common misconception is the one that was just mentioned: an incompressible approach is taken in air for AFC devices that clearly do not reside in the regime with a low Mach number. Adding to the problem is that most "mass" flow meters actually measure the volume flow rate $\dot{Q}$ and not the mass flow rate itself. The following equations apply:

$$\dot{m} = \rho\dot{Q} = \rho u_{\text{jet}} n A_{\text{act}}, \tag{5.5}$$

$$u_{\text{jet}} = \frac{\dot{Q}}{n A_{\text{act}}}, \tag{5.6}$$

where $\dot{Q}$ is the volume flow rate, n the number of actuators, and A_{act} the exit area of a single actuator. Inserting this into Eq. (5.1) and using an incompressible assumption yields

$$C_\mu = 2\frac{A_{\text{act}} n}{S}\left(\frac{u_{\text{jet}}}{u_\infty}\right)^2 = 2\frac{1}{A_{\text{act}} n S}\left(\frac{\dot{Q}}{u_\infty}\right)^2. \tag{5.7}$$

This approach seems fairly simple and straightforward. However, there are several pitfalls associated with measuring the volume flow rate $\dot{Q}$. First, the volume flow rate is not an invariant variable like the mass flow rate and changes along a flow path with different pressures and temperatures. Second, for many volume flow rate meters, especially older ones without an internal processor, the measured

volume flow rate has to be corrected to the flow meter's calibration conditions:

$$\dot{Q}_\mathrm{e} = \dot{Q}_\mathrm{m}\sqrt{\frac{p_\mathrm{e}T_\mathrm{c}}{p_\mathrm{c}T_\mathrm{e}}}, \tag{5.8}$$

where the subscript (e) stands for the effective, (m) for the measured, and (c) for the calibrated value. The pressure and temperature values need to be in absolute units, which is another pitfall in this context. It doesn't end here. Typically, volume flow rate meters in the United States measure in "Standard Cubic Feet per Minute" or "SCFM". The unit itself is extremely confusing: it is a volumetric flow rate corrected to a set of "standardized" conditions of pressure, temperature, and sometimes humidity. The standard condition can be defined in various ways and are mainly depending on the manufacturer. The definition of the "standard" condition makes the volume flow rate technically a mass flow rate, because the conversion at a known density is simple. Unfortunately, the formulation of Eq. (5.7) doesn't encourage this. Instead, it creates another pitfall where calculations are based on a volume flow rate, which should be defined at the jet exit and not at the volume flow rate meter. In this case, another conversion is necessary, and can be derived from the combined gas law

$$\dot{Q}_\mathrm{e,jet} = \dot{Q}_\mathrm{m,jet}\left(\frac{p_\mathrm{atm}}{p_\mathrm{e,jet}}\right)\left(\frac{T_\mathrm{e,jet}}{T_\mathrm{atm}}\right). \tag{5.9}$$

It is not uncommon that additionally the pressure and temperature quantities at the exit are assumed to be equal to the atmospheric conditions, which introduces another error on top of the incompressible assumption. One can imagine that the error gets specifically large when the jet throat is choked and the only way to increase the mass flow rate is to increase the pressure and density based on the standard formulation

$$\dot{m} = A_\mathrm{act}n\sqrt{\gamma\rho_t p_t\left(\frac{2}{\gamma+1}\right)^{\frac{\gamma+1}{\gamma-1}}}. \tag{5.10}$$

The induced error by assuming incompressibility and atmospheric conditions at the jet exit is compared with the "correct" solution in Section 5.4.

5.3 New Approach to Calculate C_μ

Due to the fact that neither the incompressible assumption (huge errors) nor measuring the pressure ratio in the nozzles (tedious and inaccurate) are satisfying methods for the calculation of C_μ, a new approach is proposed. This approach tries to combine the advantages of both methods (incompressible approach: easiness, pressure ratio: correctness) but still avoids their drawbacks.

Given that the mass flow rate and pressure ratio across drive the whole actuation system, there is no way around measuring at least one of them. The mass flow rate holds the benefit of being a conserved variable. Based on the continuity equation the following equation holds anywhere in the actuation system:

$$\dot{m} = \rho u A, \tag{5.11}$$

where ρ is the gas density, u the velocity, and A the cross-sectional area. At the actuator throat Eq. (5.11) can be written as

$$\dot{m} = \rho u_{\text{jet}} A_{\text{act}} n, \tag{5.12}$$

where n is the number of actuators and u_{jet} is the velocity at the jet's throat. In contrast to the incompressible approach, compressibility is now taken into account for further calculations. Thus, the density in the mass flow rate calculations needs to be specified as the static density

$$\dot{m} = \rho_s u_{\text{jet}} A_{\text{act}} n. \tag{5.13}$$

Further, the isentropic assumption relates the static and total density as

$$\frac{\rho_t}{\rho_s} = \left(1 + \frac{\gamma - 1}{2} M^2\right)^{\frac{1}{\gamma - 1}}, \tag{5.14}$$

where ρ_t represents the total density, γ the specific heat capacity ratio, and M the Mach number. Eq. (5.13) can be rewritten as

$$\frac{\dot{m}}{u_{\text{jet}} A_{\text{act}} n} = \frac{\rho_t}{\left(1 + \frac{\gamma-1}{2} M_{\text{jet}}^2\right)^{\frac{1}{\gamma-1}}}. \tag{5.15}$$

By using the Mach relation

$$u = Ma = M\sqrt{\gamma R T_s}, \tag{5.16}$$

where a is the speed of sound, R the specific gas constant, and T_s the static temperature, one then gets the extended formula

$$\frac{\dot{m}}{\sqrt{\gamma R T_s} M_{\text{jet}} A_{\text{act}} n} = \frac{\rho_t}{\left(1 + \frac{\gamma-1}{2} M_{\text{jet}}^2\right)^{\frac{1}{\gamma-1}}}. \tag{5.17}$$

As a final step the isentropic temperature relation

$$\frac{T_t}{T_s} = \left(1 + \frac{\gamma - 1}{2} M^2\right) \tag{5.18}$$

can be used to arrive at

$$\frac{\dot{m}}{\sqrt{\frac{\gamma R T_t}{1+\frac{\gamma-1}{2}M_{\text{jet}}^2}}M_{\text{jet}}A_{\text{act}}n} = \frac{\rho_t}{\left(1+\frac{\gamma-1}{2}M_{\text{jet}}^2\right)^{\frac{1}{\gamma-1}}}. \tag{5.19}$$

Eq. (5.19) looks fairly complicated, especially when considering it is only an extended continuity equation. However, the equation now holds a lot of variables that are known, which includes the mass flow rate $\dot{m}$, the heat capacity ratio γ, the specific gas constant R, the cross-sectional area of an actuator A_{act}, and the number of actuators n. The total temperature T_t can be assumed to be constant because there is no heat addition or removal within the actuation system. This leaves two unknowns, namely the jet Mach number at the throat M_{jet} and the total density ρ_t. Two unknowns and one equation can usually not be uniquely solved. So what makes Eq. (5.19) useful? In fact, M_{jet} and ρ_t are a special combination that complements itself very well. If one assumes the jet nozzle will choke at the throat there are two distinctive cases: the jet Mach number $M_{\text{jet}} < 1$ or $M_{\text{jet}} = 1$ (the case $M_{\text{jet}} > 1$ obviously doesn't exist at the throat). The total density ρ_t also changes within these exact two cases: for $M_{\text{jet}} < 1$ the total density can be assumed to be equal to the atmospheric density (neglecting friction losses inside the plumbing) $\rho_t = \rho_{\text{atm}}$, and for $M_{\text{jet}} = 1$ it will be compressed to accommodate higher mass flow rates. One can see now that in every case one of the two variables is known and thus it is possible to calculate the other one using Eq. (5.19). Because it is not known a priori in which of the cases applies, a two-step iterative approach is applied. First, one assumes that $\rho_t = \rho_{\text{atm}}$ and uses Eq. (5.19) to solve for M_{jet}. If $M_{\text{jet}} > 1$, then a choked regime with $M_{\text{jet}} = 1$ is present, and in a second iteration the correct ρ_t can be calculated. If $M_{\text{jet}} < 1$ then the original assumption $\rho_t = \rho_{\text{atm}}$ was correct and no further iteration is necessary.

The advantages of this approach are quite evident: like with an incompressible approach only the mass flow rate is needed to calculate the jet velocity, but at the same time it "conserves" the compressibility of the flow by using isentropic calculations. However, there are also disadvantages to it. First, the approach assumes that there is no driving pressure needed until the choking point is reached. This is not correct in practice and causes an error in the estimation of total density, which would not be equal to the atmospheric density but slightly higher. This problem cannot be solved that easily, because it would differ between different experimental setups (plumbing, actuator type, actuator size, etc.). The second drawback is that everything is based on the throat of a jet. Depending on the jet design, the differences between throat area and jet exit area can be quite large;

one example is the sweeping jet actuators where there is a large exit trapezoid. To accommodate for that, a discharge coefficient C_d can be introduced that has to be established experimentally:

$$C_{\mu,\mathrm{e}} = C_d \cdot C_{\mu,\mathrm{calc}}. \tag{5.20}$$

An example of how to acquire the discharge coefficient for a sweeping jet actuator is given in Section 6.3.

5.4 Comparison to Incompressible Approach

A comparison between this new approach with the simple incompressible approach is of particular interest to see if it is even worth doing the more complicated approach, or if the errors are within an acceptable level. Because for the calculation of C_μ the freestream conditions and actuator size need to be known, the following calculations assume some generic values from the vertical tail experiments (Seele, Graff, Lin, et al., 2013).

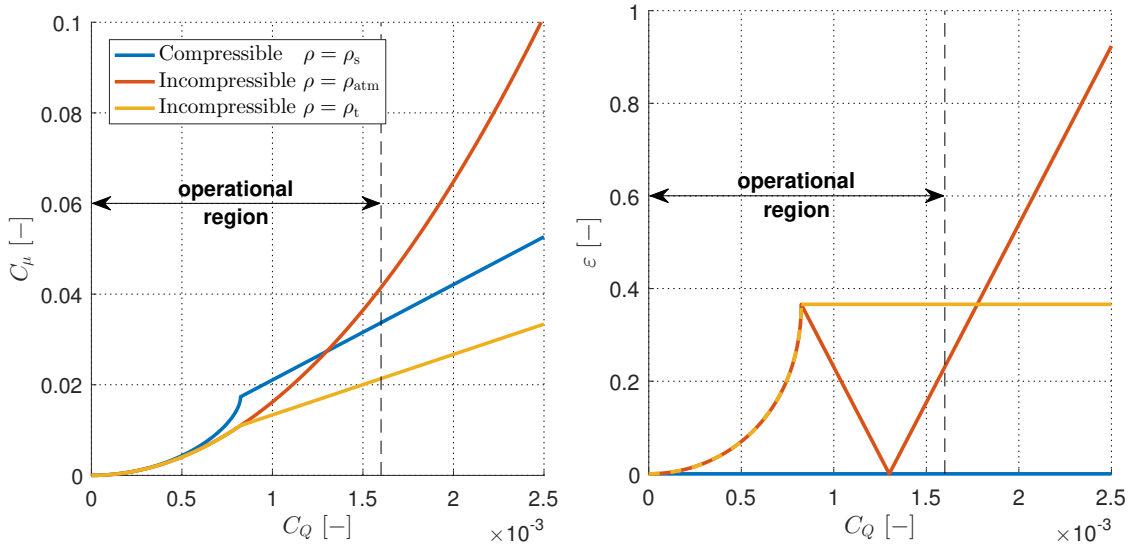

(a) Comparison **(b)** Error

Figure 5.1: Comparison between the different C_μ calculations and their errors compared to a compressible approach. The operational region represents typical mass flow rate values that were used in actual experiments.

Fig. 5.1 compares the different C_μ calculation approaches: the compressible approach, that was presented in the previous section, with $\rho = \rho_s$, the incompressible approach with no density correction at the throat $\rho = \rho_{\mathrm{atm}}$, and an incompressible approach with a density correction $\rho = \rho_t$.

The error ε is defined as the normalized deviation from the compressible approach, defined as:

$$\varepsilon = \left| \frac{C_\mu - C_{\mu,\text{compressible}}}{C_{\mu,\text{compressible}}} \right|. \tag{5.21}$$

As expected, the values of the different approaches are close to each other at low flow inputs C_Q, where the Mach number is comparably low. However, closer to $M = 1$ (at the kink) and beyond this point (choked nozzle increase of C_Q through compression of air) the results start to strongly deviate. At really high mass flow rates the non-corrected incompressible approach's errors can reach multiples of the actual value (for this scale only up to about 90%). The corrected incompressible approach's error grows until $M = 1$ is reached, and then stays there for increased mass flow rates. Interestingly, when one looks at typical operational values for input mass flows C_Q, the non-corrected incompressible approach actually outperforms the corrected incompressible approach.

5.5 Implications of the Model

The model does not only simplify the calculation of C_μ in actual experiments but also establishes a direct relation between the mass flow rate and the momentum input coefficient. This allows one to understand the relationship between these two quantities at a much higher level than previously possible. The same generic values are used as in the previous section. Fig. 5.2 illustrates the relation between C_μ and C_Q. One can distinguish three "flow states" that can also be observed in the Schlieren images of sweeping jet actuators (Fig. 5.3). However, this relation holds for all jets and is not limited to sweeping jet actuators.

State 1 describes a low subsonic conditions, where compressibility effects play only a minor role and the scaling of the two variables follows approximately $C_\mu \sim C_Q^2$. State 2 describes the transition zone up to the kink in the plot that marks $M = 1$. The corresponding Schlieren image (Fig. 5.3b) shows the appearance of first shocks. In this region the input momentum coefficient grows faster than the square of the mass flow rate $C_\mu \gtrsim C_Q^2$ due to the fact that compressibility effects matter now (specifically the reduction of the static density due to the increased jet velocity). The linear part in the plot ($C_\mu \sim C_Q$) describes the choked flow condition, where the only increase in C_Q is based on compressing the air leading to a higher total density. As a consequence, an underexpanded jet emerges which can be seen in Fig. 5.3c.

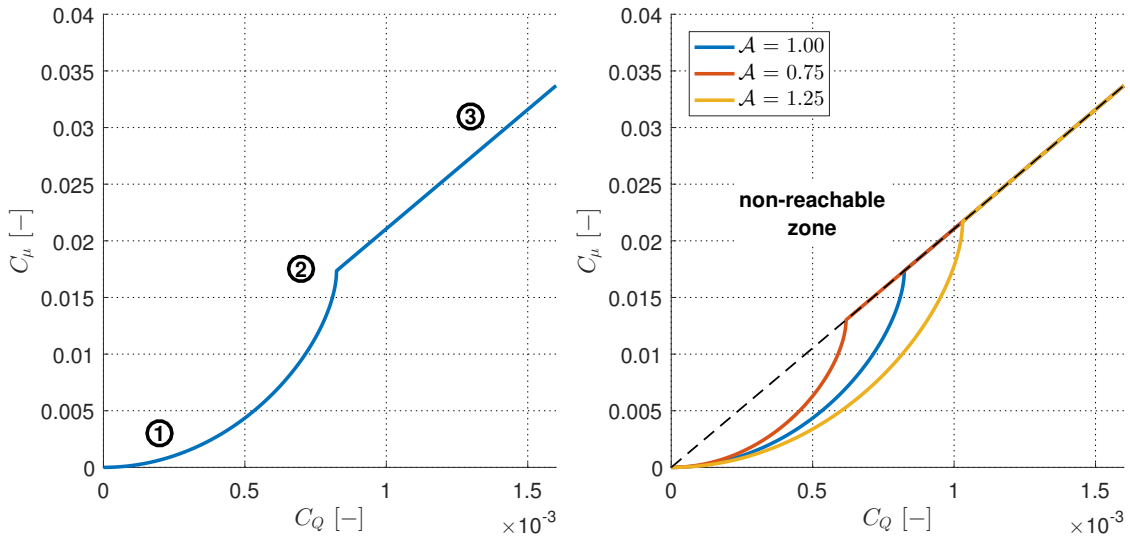

(a) Flow states **(b)** Non-reachable zone

Figure 5.2: The relation between C_μ and C_Q shows three different flow states (left), and reveals a physical limitation of values that can be achieved at fixed freestream conditions (right).

The model can yield even another interesting result that is not necessarily intuitive. Fig. 5.2b shows the model's plots for different actuator sizes at the same freestream conditions. It is evident that independent of the actuator size, eventually all values collapse onto a line that is related to the sonic speed. This barrier (dashed line in the plot) can't be penetrated by any jet designs at the given freestream conditions. Below that line, every point can be reached by a different actuator size, but the zone above this line is not-reachable. Assuming C_μ is a driving factor for AFC and is directly related to the lift coefficient C_L (which is challenged in Chapter 7), this indicates that there are situations where AFC fails to achieve performance goals, because they would violate this physical barrier. Section 6.3 describes a way to break this barrier by introducing temperature as another adjustable variable.

5.6 Concluding Remarks

This chapter introduces the momentum input coefficient C_μ as the traditional similarity parameter in AFC. The difficulties of acquiring the variables for its calculation are shown, and three different calculations methods are presented: a direct hotwire measurement of the jet exit velocity, an incompressible approach, and an isentropic approach using the nozzle pressure ratio of a jet. Common errors and misconceptions in the calculation of C_μ are explained. Due to the fact that none of the current calculation techniques are satisfactory, a new way is presented by combining the ease of an

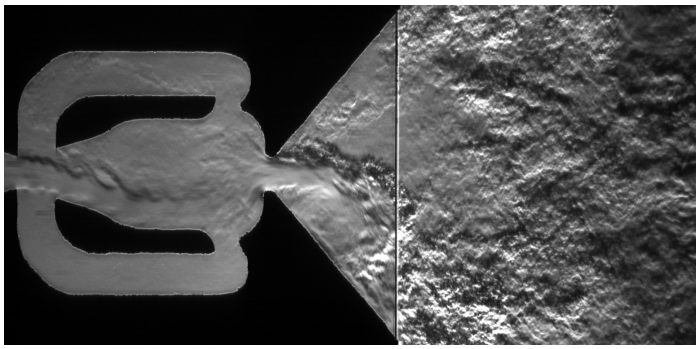

(a) Flow state 1: $C_\mu \sim C_Q^2$

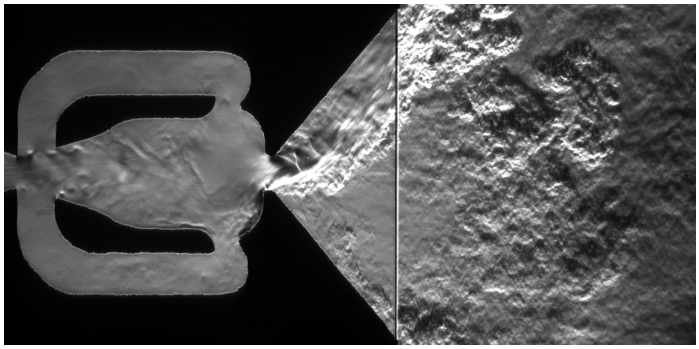

(b) Flow state 2: $C_\mu \gtrsim C_Q^2$

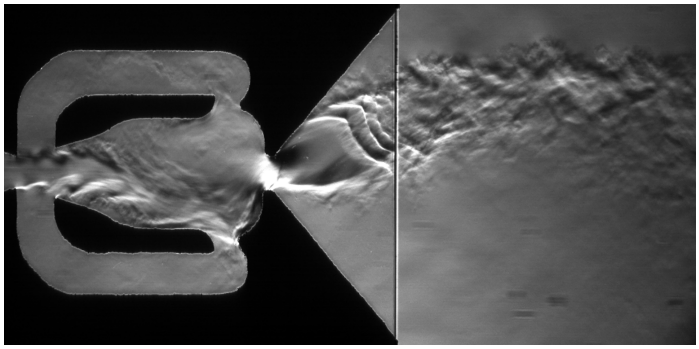

(c) Flow state 3: $C_\mu \sim C_Q$

Figure 5.3: The three different flow states can be observed in the Schlieren images as well.

incompressible approach and the correctness of the tedious nozzle pressure ratio calculation. The new approach is then compared to the incompressible assumption, exemplifying the large errors that can occur. The new method of calculation also allows for new insight into the physics of AFC. It is shown that there exists a physical limit of what AFC can achieve (this is later revoked by introducing thermal active flow control), and that the different flow regimes that are predicted by this calculation method/model can be found experimentally as well.

Chapter 6

Thermal Active Flow Control

6.1 Introduction

Active flow control demonstrated on many occasions the potential to expand aircraft capabilities. However, the input requirements are often the limiting factor, and need to be reduced to within available resources on board while maintaining performance goals. Therefore, the key requirement for a successful and practical design is the use of low power input to achieve design targets. As a result, the Boeing Company started a new project to augment actuator efficiency via thermal control. Derivations from gas-dynamics principles indicate that increased supply temperature at constant pressure results in a reduced mass flow rate with no degradation in flow effectiveness. Thermal active flow control acts as a "knob" that enables dialing down inputs to lower levels. While Boeing was able to confirm this in CFD simulations, the experimental confirmation of the concept was done at Caltech. It was expected that the results will improve the understanding of thermal active flow control and its effects on flight efficiency. This could allow for the development of more efficient actuators, and it could enable practical integration on future commercial and military platforms.

6.2 Derivation of the Concept

The concept can be derived by starting with the momentum input coefficient

$$C_\mu = \frac{\dot{m}u_{\text{jet}}}{\frac{1}{2}\rho_\infty u_\infty^2 S}. \tag{6.1}$$

The numerator of C_μ represents the momentum flow. Using the ideal gas law

$$p = \rho RT \tag{6.2}$$

and the definition of the sonic speed of an ideal gas

$$a = \sqrt{\gamma RT}, \tag{6.3}$$

one can rewrite the momentum flow as

$$\dot{m}u = \rho u^2 A = \frac{p}{RT}\gamma RTM^2 A = p\gamma M^2 A. \tag{6.4}$$

Because of the cancellation of the two temperature terms, the momentum flow is in fact independent of the temperature. Assuming the heat capacity ratio γ and the area A remain constant for AFC purposes, it is solely dependent on the input pressure p and the Mach number M. If a similar approach is taken for the mass flow rate, one gets that

$$\dot{m} = \rho u A = \rho a M A = \frac{p}{RT}\sqrt{\gamma RT}MA = \frac{\sqrt{\gamma}p}{\sqrt{RT}}MA. \tag{6.5}$$

It is evident, that the mass flow rate stays dependent on the temperature using the same approach. The other driving variables in this case are again the input pressure p and the Mach number M. To summarize one can write

$$\dot{m} = \frac{\sqrt{\gamma}p}{\sqrt{RT}}MA \sim \frac{p}{\sqrt{T}}M = f\left(\frac{1}{\sqrt{T}}\right), \tag{6.6}$$

$$\dot{m}u = p\gamma M^2 A \sim pM^2 \neq f(T). \tag{6.7}$$

Thus, according to this concept an increase in temperature would not change the momentum of the associated flow but reduce the required mass flow rate by the square root of the temperature.

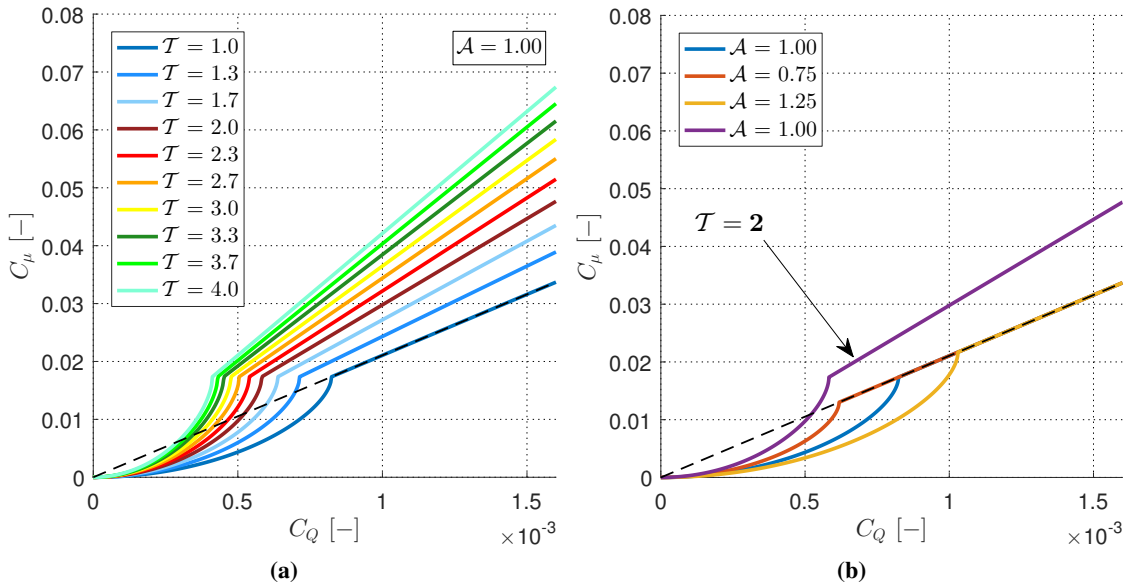

Figure 6.1: The C_μ-model introduced in Section 5.3 confirms the theoretical derivation predicting a reduced mass flow rate at higher temperatures to achieve the same momentum coefficients (left). Thermal effects also allow breaching into the "non-reachable zone" from Fig. 5.2b (right).

Using temperature as a variable for the C_μ-model that was introduced in Section 5.3, one gets the plot in Fig. 6.1a with the previously used generic values for the freestream quantities. The variable

$\mathcal{T}$ represents the temperature ratio, which is defined as

$$\mathcal{T} = \frac{T_{\text{jet}}}{T_{\text{atm}}}, \tag{6.8}$$

where T_{jet} is the active flow control temperature and T_{atm} the atmospheric temperature. Evidently, the curves follow the expected trend requiring the square root of $\mathcal{T}$ less mass flow rate for achieving the same momentum coefficient C_μ.

Other interesting correlations, especially in the linear part after choking (at the kinks), can be derived and observed in the plot. In the linear part ($M = 1$) for the same mass flow rate the momentum coefficient increases by the square root of the temperature ratio. The same is true for the pressure p and inversely for the total density ρ_t. Fig. 6.1b is equivalent to Fig. 5.2b with the only differences being that now the previously "non-reachable zone" is accessible with a higher temperature. In other words, the former physical barrier for AFC can be breached by adding heat to the flow to reach different parameter sets.

6.3 Bench-top Experiment

To verify the thermal active flow control concept a simple bench-top model was built. It was based on the previously used Schlieren visualization model (see Chapter 2) but was improved to accommodate higher temperatures. The model illustrated in Section 6.3 is assembled from machined steel parts, high-temperature optical glass to grant Schlieren access for future studies, high-temperature Kalrez o-rings, a heat shield to protect the temperature-sensitive force balance/load cell from the heat to guarantee accurate measurements, and a high-temperature RTV gasket material to bond the glass and the actuator plates. This assembly allows for a maximum temperature of around 525 K ($\mathcal{T} \approx 1.77$). For higher temperatures the Teflon tape sealing the tube connections needs to be replaced with another material. The mass flow rate and air temperature were controlled by separate self-regulating controller units. It was decided to test a straight jet design with a trapezoid exit with a 70° opening similar to that of a sweeping jet actuator. The straight jet design can be seen between the glass plates in (Section 6.3). The jet has a throat diameter of 0.2 inches and the plate is 0.1 inches thick.

As previously, C_μ is only defined within freestream conditions, which makes it difficult to use in a bench-top setting. To resolve this problem, once again, the predefined "standard" conditions are assumed ($u_\infty = 30$ m/s at standard atmospheric conditions with a reference area of roughly 0.5 m^2).

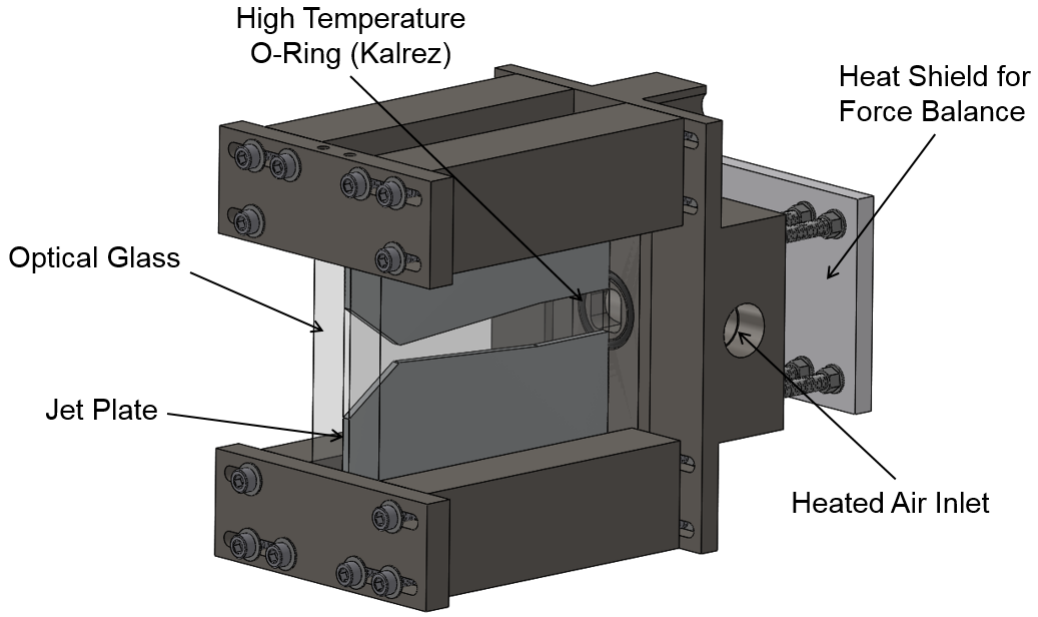

Figure 6.2: The bench-top model for the thermal active flow control concept study is designed to withstand high temperatures.

While the mass flow rate $\dot{m}$ can be measured and regulated by the mass flow rate controller, the jet velocity u_{jet} is difficult to acquire as explained in Chapter 5. Fortunately, the numerator of C_μ is in fact a momentum flow, which is simply a force

$$F = \dot{m} u_{\text{jet}}. \tag{6.9}$$

Thus, one can experimentally measure the momentum input coefficient by using a force balance or load cell. The C_μ model predicts the values in Fig. 6.3a. Unfortunately, one has to account for the fact that the jets blows into atmospheric conditions and add an additional thrust force to the model that is created due to the pressure difference between the nozzle outlet and the surrounding atmospheric air. This basically leads to the rocket thrust equation

$$F = \dot{m} u_{\text{jet}} + A_{\text{act}} \left(p_{\text{s,jet}} - p_{\text{atm}} \right), \tag{6.10}$$

where A_{act} is the actuator exit area, $p_{\text{s,jet}}$ the static jet exit pressure, and p_{atm} the atmospheric pressure. The total momentum coefficient C_J was introduced to account for these changes. It is defined as

$$C_J = \frac{\dot{m} u_{\text{jet}} + A_{\text{act}} \left(p_{\text{s,jet}} - p_{\text{atm}} \right)}{\frac{1}{2} \rho_\infty u_\infty^2 S}. \tag{6.11}$$

Fig. 6.3b exemplifies the impact of this change. Because the straight jet and the sweeping jet actuator

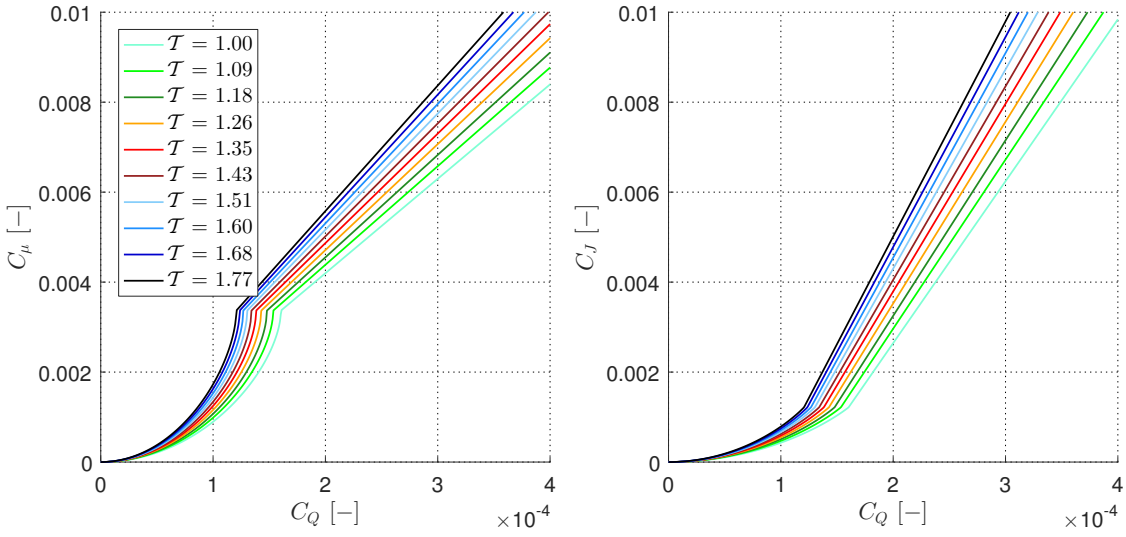

(a) C_μ **(b)** C_J

Figure 6.3: Comparison between the classic C_μ model predictions and the total momentum coefficient C_J.

have the same throat dimensions, the theoretical models looks exactly the same (Fig. 6.3). However, only a one-directional load cell was available to measure the force, which makes measurements for a sweeping motion difficult, because it would require a directional correction. Without a correction, one would expect that a sweeping jet needs a much larger discharge coefficient because its momentum flow, and thus its force, is partially distributed to the sides (see Fig. 3.10). In other words, the force is dependent on the deflection angle of the jet. Because the data taken from the load cell was averaged over several seconds, the acquired force is the integral of the force values in the direction of the centerline of the actuator. The total force measured is thus smaller than what the theoretical model would predict. In mathematical terms one can write

$$F_x = \int \dot{m} u_{\text{jet}} \cos\theta \, d\theta, \tag{6.12}$$

where F_{x} is the force in the direction of the sweeping jet's centerline. This seems to be a fairly easy correction; however, one can realize that when the jet is at an angle θ the effective throat area is reduced and thus the jet velocity increases:

$$F_x = \int \dot{m} u_{\text{jet}}(\theta) \cos\theta \, d\theta. \tag{6.13}$$

Taking a step back, one can derive the following:

$$F = \dot{m} u_{\text{jet}}(\theta) = \frac{\dot{m}^2}{\rho_s(\theta) A_{\text{act,e}}(\theta)}, \tag{6.14}$$

where $A_{\mathrm{act,e}}(\theta)$ is the effective exit area at the throat which is defined as

$$A_{\mathrm{act,e}}(\theta) = A_{\mathrm{act}} \cos\theta, \tag{6.15}$$

where A_{act} is the throat exit area. Continuing the previous equation one gets

$$F = \frac{\dot{m}^2}{\rho_s(\theta) A_{\mathrm{act}} \cos\theta} = \frac{\dot{m}^2}{\rho_t \left[1 + \frac{\gamma-1}{2} M(\theta)^2\right]^{\frac{1}{1-\gamma}} A_{\mathrm{act}} \cos\theta} \tag{6.16}$$

$$= \frac{\dot{m}^2}{\rho_t \left[1 + \frac{\gamma-1}{2} \frac{u_{\mathrm{jet}}^2}{\gamma R T_s(\theta)}\right]^{\frac{1}{1-\gamma}} A_{\mathrm{act}} \cos\theta}. \tag{6.17}$$

It is evident that the equation at this point is some form of an infinite series that can only be calculated by truncating it and using an iterative process to get the result. There's an additional complication: when reaching choked conditions the velocity is limited to the sonic speed making the equation partially independent of θ. Because this is an extremely laborious approach, it was decided to use the much simpler straight jet design. With the straight jet all these problems can be avoided and the actual force can be measured directly.

While taking the data the heater control was unfortunately limited to a minimum mass flow rate of 10 kg/h which only covers one subsonic case. However, because the actuators are operated primarily in a similar way in practice (the nozzle is choked), the experiment is still capable of reflecting important results. Fig. 6.4a compares the acquired experimental results directly with the model. Clearly, the model overestimates the actual values. This is mainly due to certain assumption that were described in Section 5.3 and led to Eq. (5.20). The discharge coefficient C_d can now be calculated by minimizing the least-square or total least-square error between the data and the model. For the straight jet this yields $C_d \approx 0.7$ depending only slightly on the minimization scheme and a bit more on the temperature of the model/experimental data. However, the differences are negligible and the simplified assumption still collapses the model onto the data (see Fig. 6.4b). There's a slight discrepancy at high mass flow rates and high air temperatures due to high thermal losses at these conditions.

Conclusively, it can be said that the concept of thermal active flow control can be confirmed based on the bench-top experiments. The values follow the model quite well when introducing a discharge

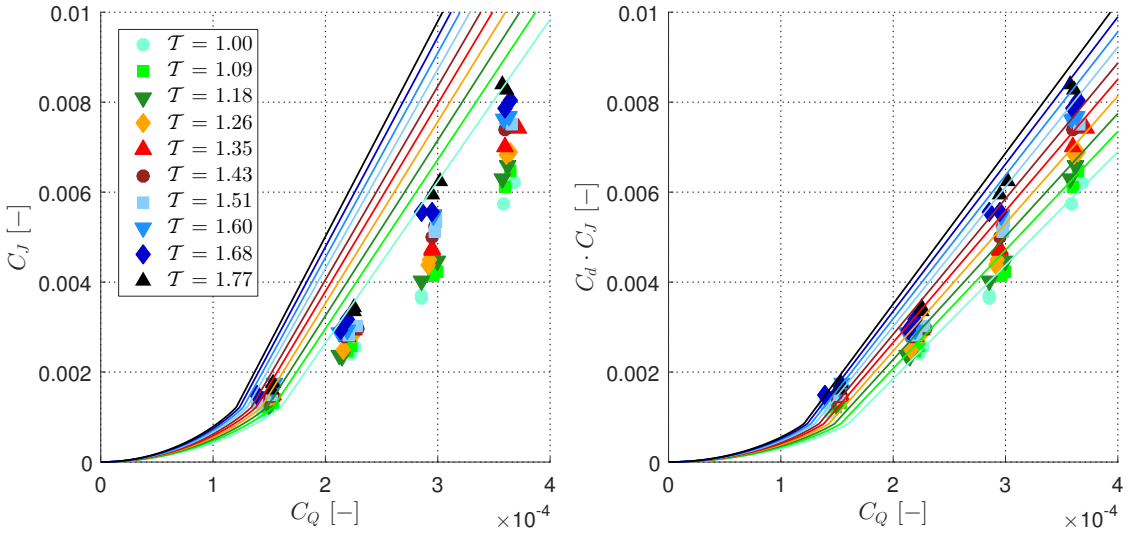

(a) The original model and the experimental data do not match very well.

(b) The introduction of a discharge coefficient collapses model and experimental data.

Figure 6.4: Comparison between the uncorrected C_J-model and the adjusted model with the discharge coefficient ($C_d \approx 0.7$) for the straight jet.

coefficient C_d to account for losses. While the C_d mainly accounts for efficiency losses, the underlying law $\dot{m} \sim \frac{1}{\sqrt{T}}$ is independent of it and is accurately fulfilled by the experimental results.

6.4 Wind Tunnel Experiment

The next and final step to prove the applicability of this concept to actual aircraft is to show that it also works in wind tunnel experiments. In a wind tunnel environment C_μ is now properly defined and should lead to improved lift coefficients C_L when increasing the temperature. The main goal is to show that a heated momentum coefficient $C_{\mu,\text{hot}}$ leads to the same lift improvements than its cold equivalent $C_{\mu,\text{cold}}$ at a higher mass flow rate.

6.4.1 Experimental Setup

The vertical stabilizer model has a NACA 0012 shape and was designed based on publicly available information. The wing is tapered and swept back by $\Lambda = 43.5°$ at the leading edge (LE), has a 35% chord flap, a 1.765 ft (0.538 m) mean aerodynamic chord (MAC), a span $b = 3.5$ ft (1.067 m) and features a dorsal fin similar to what is used on a real stabilizer to smoothen the transition between fuselage and stabilizer. The planform area of the wing, S, is 829.5 in^2 (0.5352 m^2). A fairing that roughly approximates the shape of the fuselage was installed around the model and attached to the ground plane to minimize the effect of the developing boundary layer at the wall. To

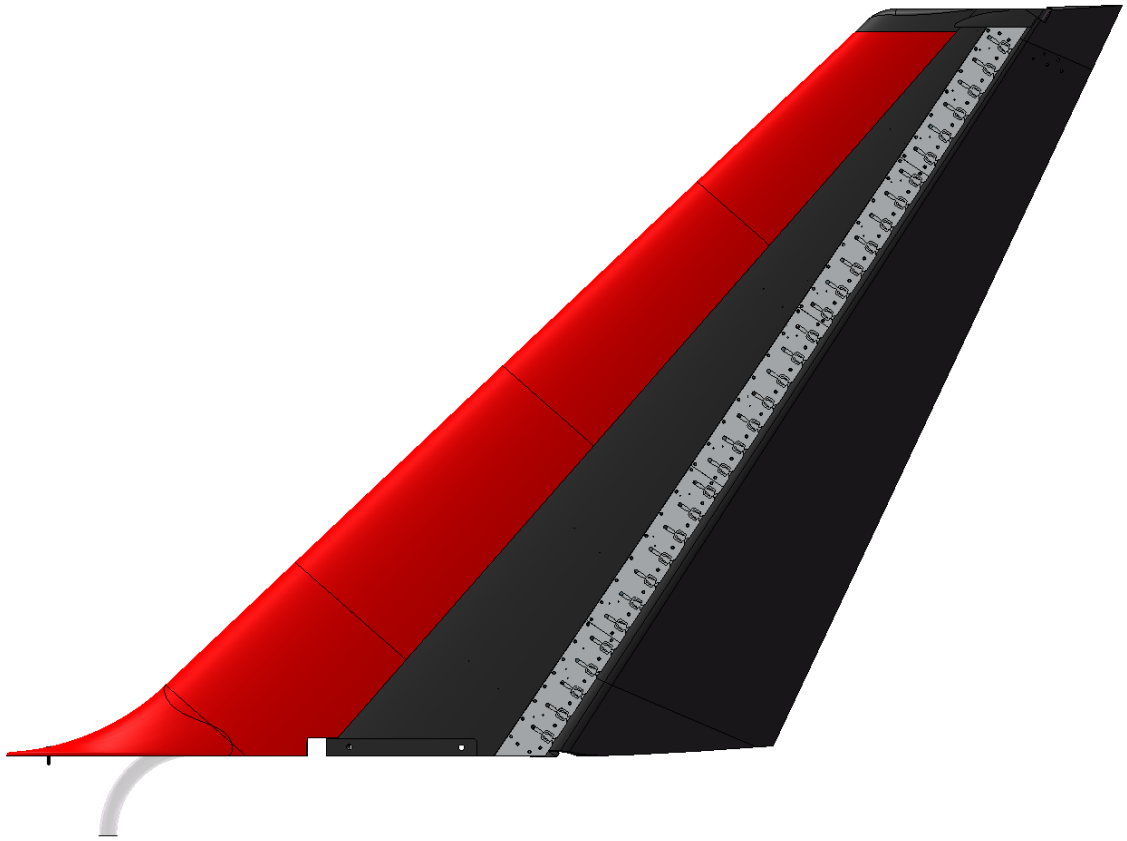

Figure 6.5: Vertical tail model seen from the suction side. The actuator covers were removed to expose the actuator array along the span.

minimize Reynolds number and transition-related effects, tripping dots were applied at $x/c = 5\%$ on the models suction side and at $x/c = 10\%$ on the pressure side (Seele, Graff, Lin, et al., 2013).

The sweeping jet actuators were supplied with compressed air through one point at the root of the model thus creating a slight negative pressure gradient along the span. Hose forces were assessed in various different arrangements and found to exert negligible loads on the model (less than 1% of the smallest measured force). The air supply was controlled, regulated, and recorded by an Omega FMA-2621A mass flow rate controller that was also used in Chapter 4. Actuation was carried out from the trailing edge (TE) of the main element normal to the hinge line.

On the main element a total of 32 actuators are available. The actuators are machined into a compact array of planar actuator planes (Raghu, 2013b). In total there are five actuator modules that can be replaced to change the actuator design (i.e. the actuator size or actuator type). The lowest of the five modules near the root features five actuators, the three modules in the center feature 7 actuators each,

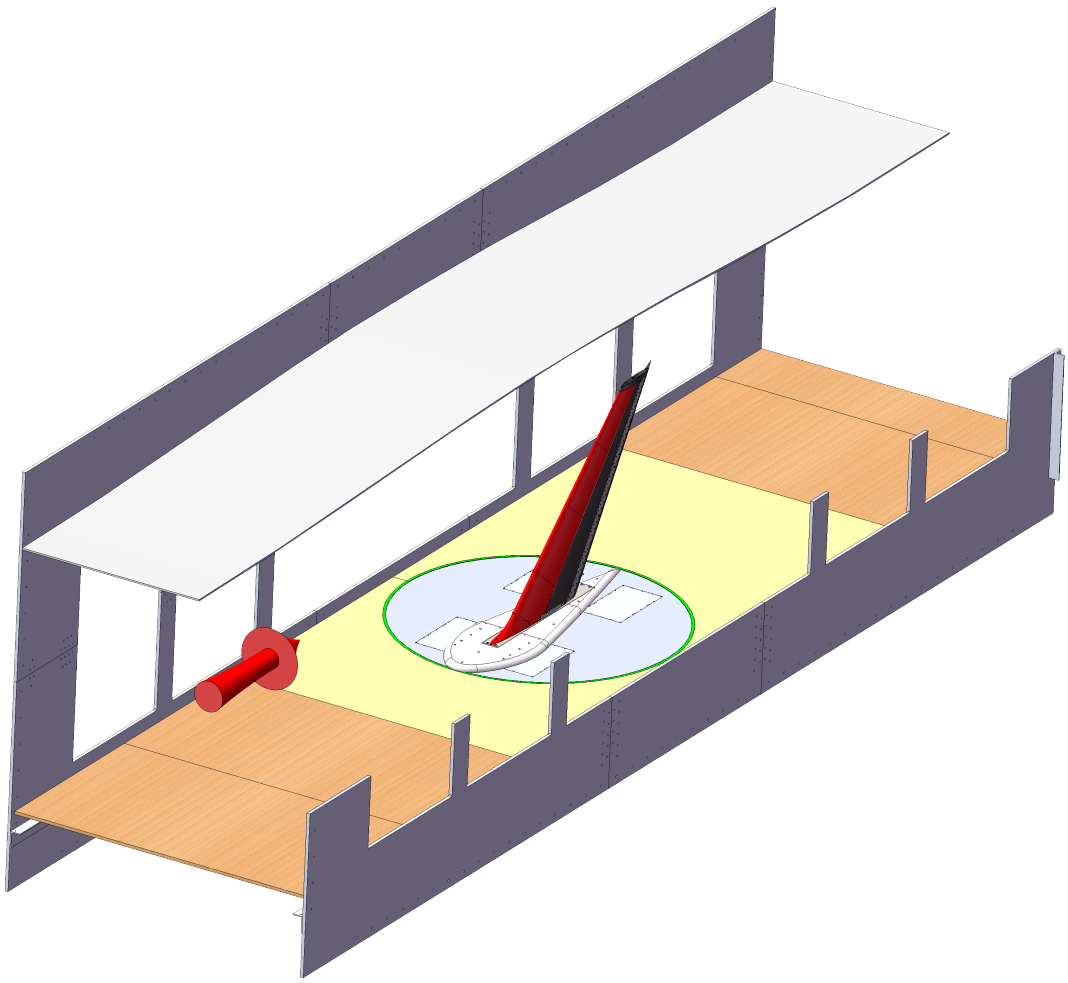

Figure 6.6: Schematic showing the model installed in the Lucas Wind Tunnel

and the highest module near the tip fits six actuators for the aforementioned total of 32 actuators. The ejection angle relative to the surface is roughly 10° (Seele, Graff, Lin, et al., 2013). The model is illustrated in Fig. 6.5. The jet covers have been removed to show the 32 jet locations along the span of the wing.

The test were conducted in the Lucas Wind Tunnel (see Section 4.2.1 for further details) at freestream speeds ranging from 15 m/s to 30 m/s. It was not possible to test at higher speed due to the roll limitations (225 Nm) of the 3161-A force balance. Sweeping jet actuators were used with a nozzle width of 0.080 inches (2.032 mm) and a height of 0.040 inches (1.016 mm). The vertical tail is not fully Reynolds independent below 25 m/s, so the results shouldn't be compared directly with each other. However, for themselves they can still answer the posed questions. As heat source a

Tutco Farnam Cool Touch 200 process heat controller was used. It's capable of regulating the air temperature within a band of 2 K. Fig. 6.6 shows a schematic of the installed model in the Lucas Wind Tunnel. The force balance, mass flow rate controller, and heat controller were all located below the test section of the wind tunnel. The flap deflection was fixed at $\delta_F = 20°$ for the entirety of these experiments.

6.4.2 Results and Discussion

Fig. 6.7 plots the lift coefficient C_L' versus the flow coefficient C_Q. The lift coefficient C_L' is a normalized lift coefficient defined as

$$C_L' = \frac{C_L - C_{L_0}}{C_{L_{0,\text{baseline}}}}, \tag{6.18}$$

where C_L is the lift coefficient, C_{L_0} the lift coefficient at zero mass flow rate input, and $C_{L_{0,\text{baseline}}}$ the lift coefficient at zero mass flow rate input of the baseline (non-heated case). Thus C_L' represents a comparison between the baseline case at zero mass flow rate and the current case. This makes the results easy to compare and has the benefit of reducing small force balance offsets.

One can see that for all freestream velocities AFC improves the lift performance, except for low mass flow rate inputs at the highest freestream velocity of 30 m/s, where a small deleterious effect can be observed. The heated cases are indeed performing better than the baseline cases, and the higher the temperature ratio the larger the benefit becomes. The overall benefit is larger for slower freestream velocities which also applies to the heated cases. However, looking at the plots more thoroughly, one can notice that the performance increase for the heated cases doesn't seem to be as high as the theory would suggest. This becomes more evident in Fig. 6.8 where the normalized lift coefficient C_L' is plotted directly against the input momentum coefficient C_μ. It is obvious that at the same input momentum coefficient C_μ the baseline performs better than the heated cases; the higher the temperature ratio, the lower is the performance improvement at the same C_μ values. In summary, the two Figs. 6.7 and 6.8 suggest that there is an overall benefit from heating the flow, but it doesn't seem to follow the laws derived from theory. However, the assumption here is that the input temperature of the heater arrives at the actuator exits. This is most likely not the case as there will be temperature losses along the plumbing and especially through the wing. Before the hot air feeds the actuators, it enters a small plenum inside the wing, thus "exposing" its temperature to the wing. Because the

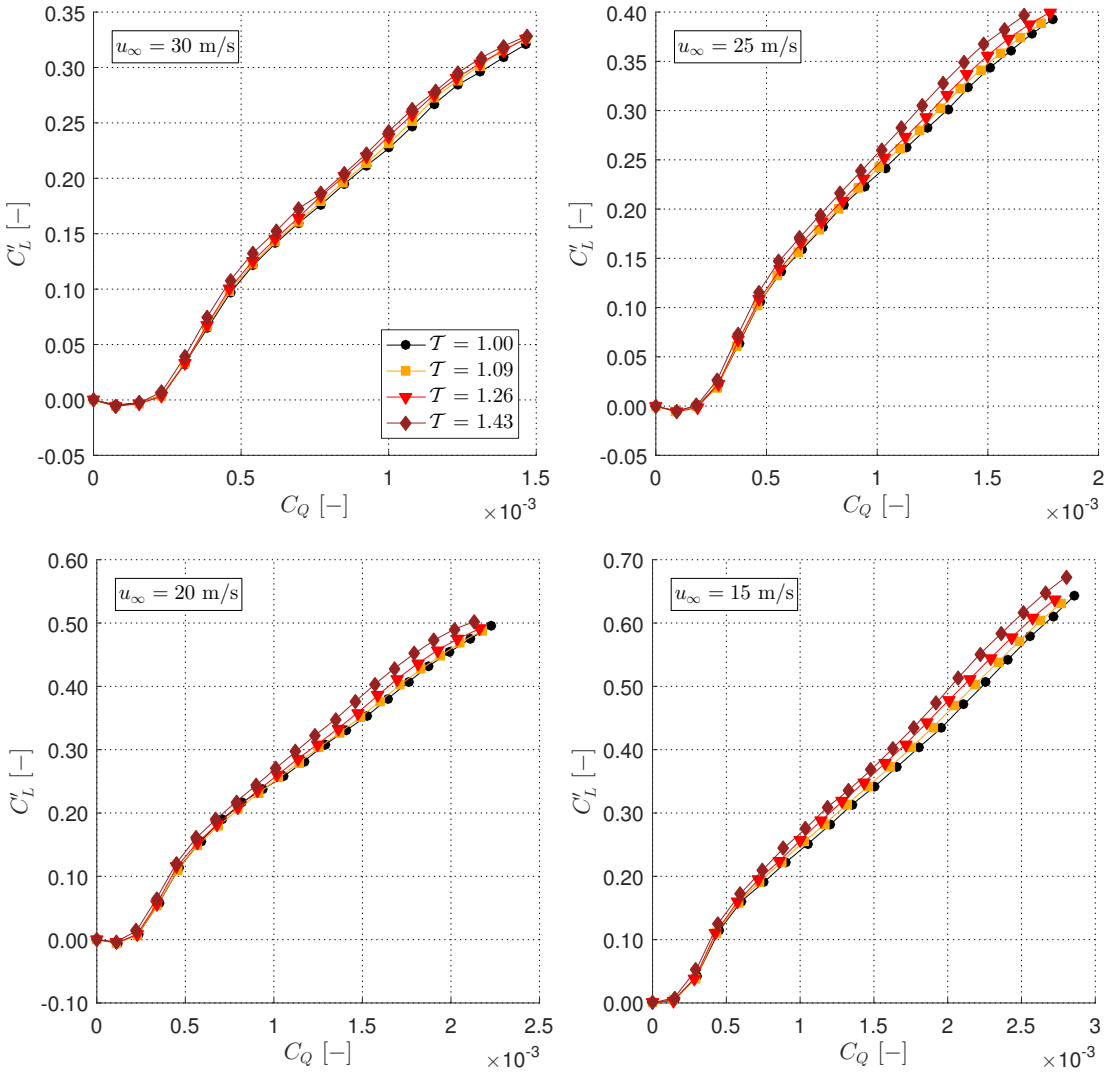

Figure 6.7: Normalized lift coefficient C_L' versus coefficient of mass flow rate input C_Q: the heated cases indeed show a higher performance benefit compared to the baseline case for all freestream velocities but seem to underperform compared to theory.

wing is made mainly from aluminum (high heat conductivity), it spreads the heat immediately along its entire wing surface. The wing itself is exposed to the freestream, and thus acts as a large heat sink draining incredible amounts of temperature from the heated air inside. This statement is supported by the plots in Fig. 6.8, where the heated cases perform worse at higher freestream velocities due to the fact that more heat can be convected. The effective temperature of the air that goes through the actuators is thus expected to be much lower. To correct the C_μ values, the effective air temperature needs to be known, which can be done by measuring the temperature directly via thermocouples or an infra-red camera. However, this way requires additional experimental investigations and introduces

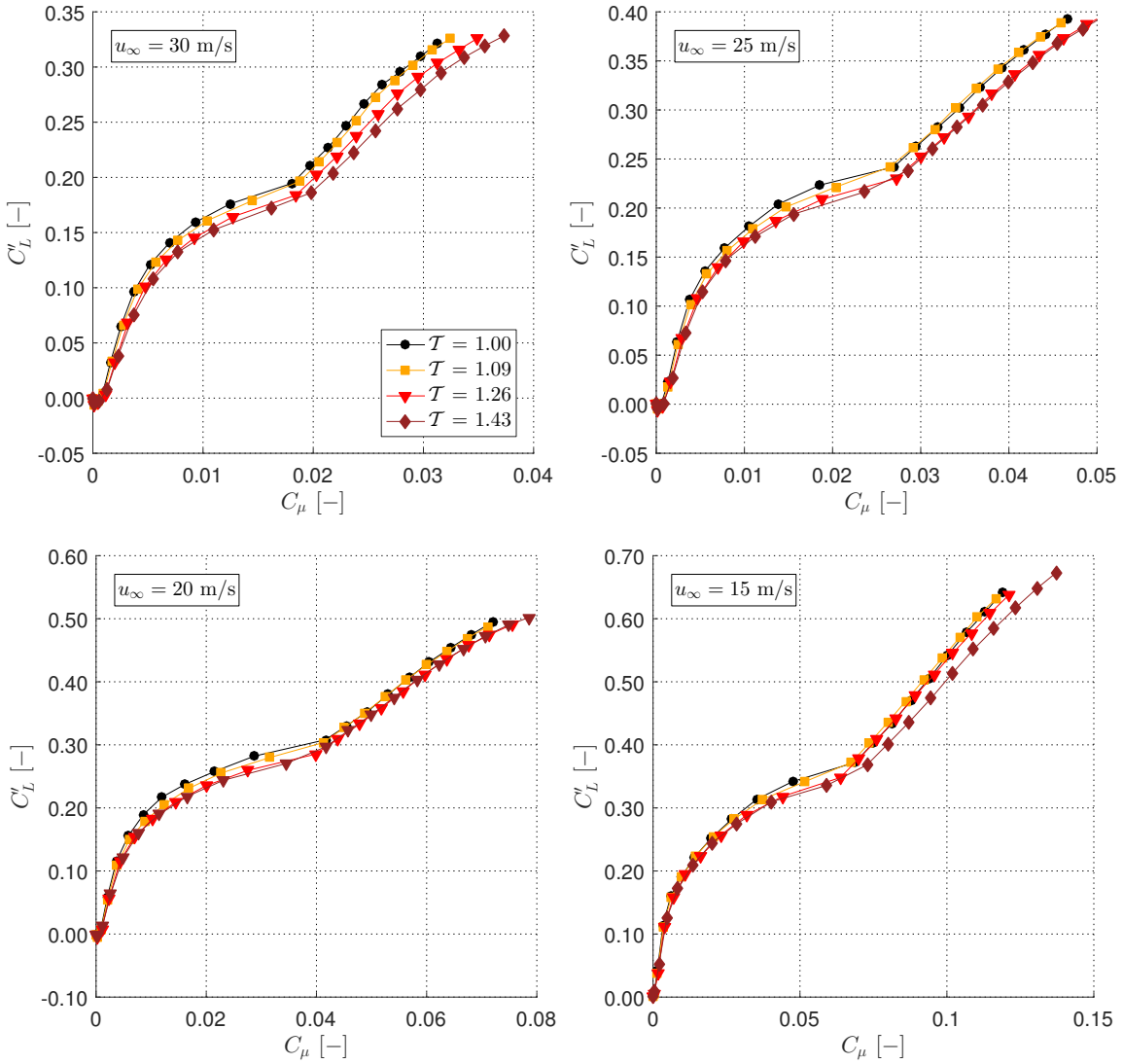

Figure 6.8: Normalized lift coefficient C_L' versus momentum coefficient C_μ: the heated input momentum coefficient C_μ shows a lower benefit compared to its cold equivalent. The equation $C_{\mu,\text{hot}} = C_{\mu,\text{cold}}$ doesn't seem to hold.

new uncertainties. Fortunately, there is a much better way to acquire the effective temperature due to the fact that the plenum pressure was measured along with the force balance data. Looking at Eq. (6.6) one can realize that if the conditions are choked ($M = 1$), then the mass flow rate $\dot{m} \sim p/\sqrt{T}$. Therefore, one can write

$$\frac{\dot{m}_1}{\dot{m}_2} = \frac{p_1\sqrt{T_2}M_1}{p_2\sqrt{T_1}M_2} = \frac{p_1\sqrt{T_2}}{p_2\sqrt{T_1}}, \tag{6.19}$$

and at the same mass flow rate

$$1 = \frac{p_1\sqrt{T_2}}{p_2\sqrt{T_1}} \Rightarrow \frac{T_2}{T_1} = \left(\frac{p_2}{p_1}\right)^2 \Rightarrow \mathcal{T} = \mathcal{P}^2, \tag{6.20}$$

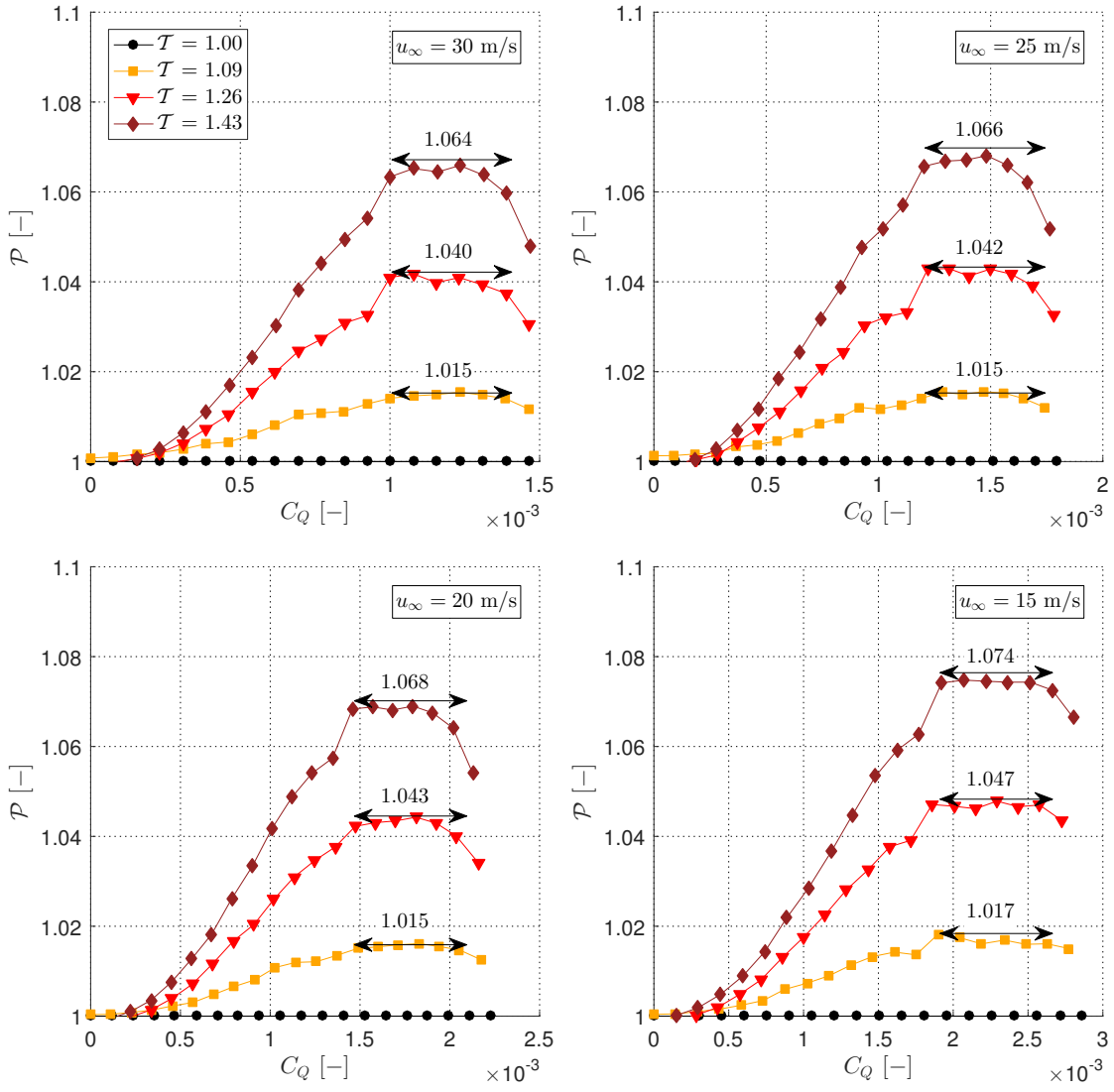

Figure 6.9: The pressure ratios $\mathcal{P}$ show a plateauing effect once the flow is choked in the jet nozzle as predicted by theory. With these values the effective temperature of the air can be calculated based on Eq. (6.20). The results of this calculation are summarized in Table 6.1.

where $\mathcal{P}$ represents the pressure ratio. For this experiment, the pressure ratio is always referenced to the baseline pressure. Looking at the actual values in Fig. 6.9, there is indeed a plateauing of the data above a certain C_Q value. The C_Q value at which choked conditions occur is negligibly higher (about one data point later) than the predicted value of the theory, mainly due to the increased pressure requirement to run the system. The highest C_Q value seems to have a large drop-off which can be explained by the fact that is was the first measured value for a sequence, and hence the model was not fully heated yet even though preheating was performed (preheating was limited to a mediocre mass flow rate due to availability limits of pressurized air). It is also worth mentioning that the pressure

Table 6.1: Calculation of the effective temperature ratios based on the pressure ratios experimentally acquired from the plenum chamber of the model.

	$\mathcal{T}_{\text{nominal}}$ [-]	$\mathcal{P}$ [-]	$\mathcal{T}_{\text{e}}$ [-]
u_∞ = 30 m/s	1.091	1.015	1.030
	1.260	1.040	1.082
	1.429	1.064	1.131
u_∞ = 25 m/s	1.091	1.015	1.030
	1.260	1.042	1.085
	1.429	1.066	1.136
u_∞ = 20 m/s	1.091	1.015	1.031
	1.260	1.043	1.087
	1.429	1.068	1.140
u_∞ = 15 m/s	1.091	1.017	1.033
	1.260	1.047	1.096
	1.429	1.074	1.154

ratio in fact decreases with higher freestream velocities because of the increased cooling effect on the wing. To calculate the effective temperature ratio, an average value of the pressure ratio plateau is taken neglecting the last value with the highest C_Q. The results are summarized in table Table 6.1.

With the new temperature ratios C_μ can be recalculated and the results can be replotted (see Fig. 6.10). Evidently, the different curves now collapse on each other. While this works perfectly for the higher freestream velocities, the two lower velocities show small offset, which is due to the relatively increased uncertainty bands (lower force values compared to a full-scale dependent error) of the force measurements. Nevertheless, this confirms the theoretical approach that the momentum coefficient C_μ can be increased by temperature alone to reduce the required mass flow rate. The heated momentum coefficient $C_{\mu,\text{hot}}$ will yield the same lift benefits than its non-heated equivalent $C_{\mu,\text{cold}}$.

6.5 Concluding Remarks

While it doesn't seem to be necessarily intuitive that thermal active flow control would work, it can be shown with a simple mathematical derivation. Assuming the main driving factor for AFC is the momentum input coefficient C_μ, it was shown that it is independent of the temperature T while the required mass flow rate is reduced with the square root of the temperature ratio. Because the mass flow rate is usually a limiting factor in real applications, i.e. onboard an airplane, this is an important finding. The concept was then later proven using a bench-top setup, and by comparing the

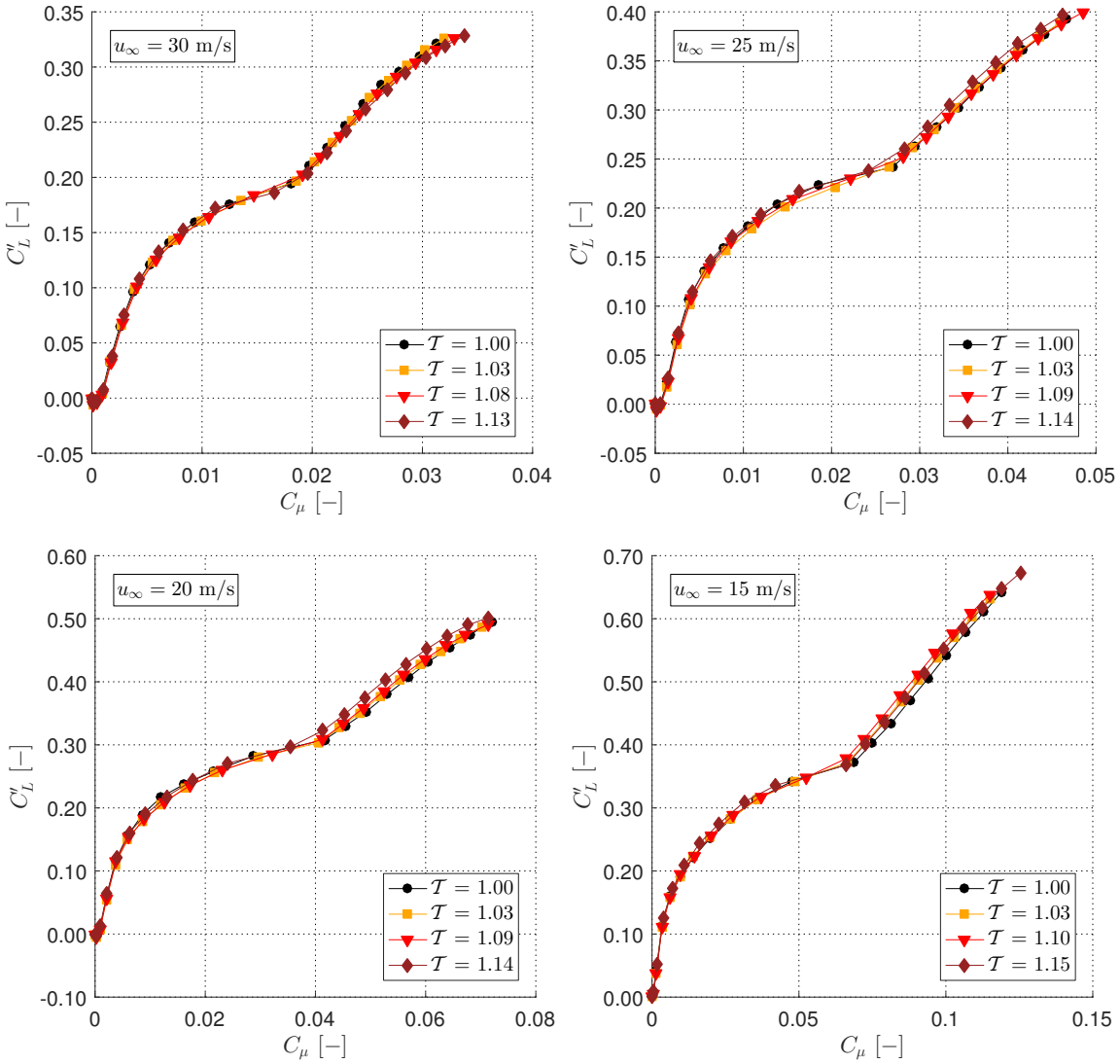

Figure 6.10: The normalized lift coefficient C_L' and the temperature-corrected momentum coefficient C_μ collapse on top of each other proving that $C_{\mu,\text{hot}}$ yields the same lift benefits at a lower mass flow rate than its cold equivalent $C_{\mu,\text{cold}}$.

theoretical with measured values from a force balance. The data points of the bench-top experiment collapse once a discharge coefficient C_d is introduced to account for losses. As a final verification a wind tunnel test on a vertical stabilizer was performed to see if a heated C_μ value at a reduced mass flow rate leads to the same lift benefit than its cold equivalent at the nominal mass flow rate. It was shown that for the wind tunnel model, it is of great importance to know the effective temperature that goes through the actuators including all the losses due to convection. This temperature might be significantly lower than the input temperature, especially if the wind tunnel model is made from aluminum acting as a large heat sink. Once the corrections were applied and the C_μ values were

recalculated, the data collapsed in all cases, proving that a given C_μ value, independent of how it was achieved (through additional mass flow rate or a higher temperature), leads to the same lift benefit. Thus, it can be stated that thermal active flow control does in fact work and can be an alternative to reduce the required mass flow rate in AFC applications at the expense of additional heat (one might use hot bleed or exhaust air from the engines).

Chapter 7

The Extended Mass Flow Coefficient $\mathcal{M}$

7.1 The Problems of C_μ

Since its introduction by Poisson-Quinton, 1948 the momentum input coefficient C_μ has dominated the area of active flow control. While in suction application the flow coefficient C_Q is prevalent, it is not often used in blowing applications. Assuming that the boundary layer controls the separation behavior, and that re-energizing it will keep it attached, using the momentum seems to make sense. However, since the day C_μ was introduced it had and still has its issues. It's by far not a perfect coefficient, but up until today no other coefficient was good enough to break its dominance. Two of its biggest flaws are shown in Fig. 7.1: on the left, C_μ fails to collapse the data against the normalized

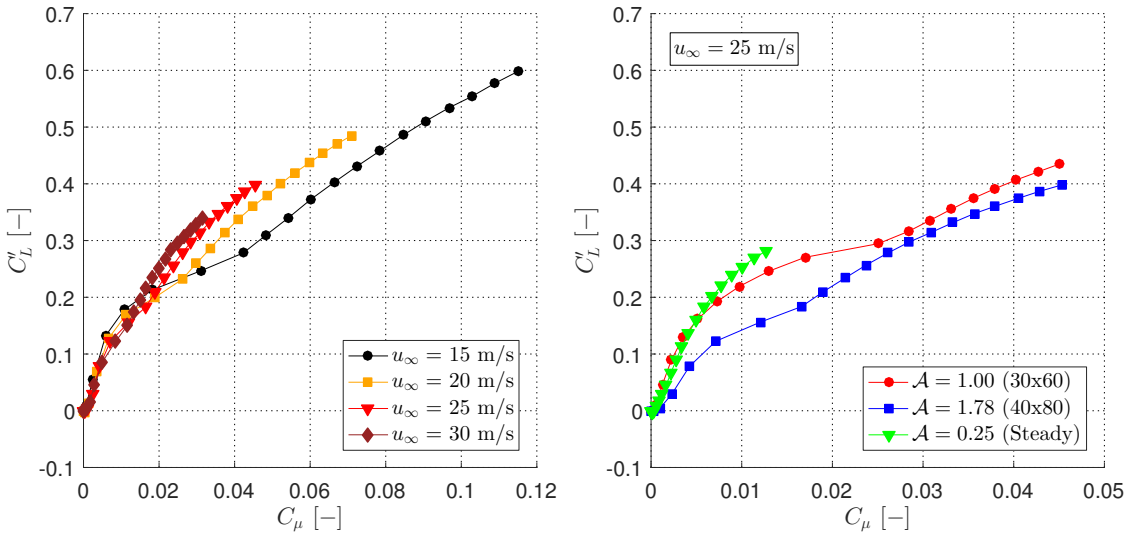

Figure 7.1: Two cases where C_μ fails to collapse the data. The first case happens when the freestream velocity u_∞ is changed (left). On the right the second case is illustrated where the actuator nozzle area differs.

lift coefficient C_L' (see Eq. (6.18) for the definition) when the freestream velocity is changed. It seems like that this case was never really considered in the past, or was purposely avoided because C_μ fails. Even in the traditional literature such as Lachmann, 1961 there is no investigation of this specific phenomenon. On the right, different actuator exit areas were used particularly two arrays ($n = 32$) of sweeping jet actuators with nozzle dimensions of 0.030 x 0.060 inches and 0.040 x 0.080

inches respectively, and a steady blowing slot with a slot height of 0.009 inches along the whole span (roughly 48 inches) of the vertical stabilizer model (see Section 6.4.1 for details). This then yields the actuator area ratios referenced by the 0.030 x 0.060 sweeping jet actuator. These results oppose older observations, such as in Attinello, 1961, where either the slot height or slot width of a steady blowing slots were changed and C_μ was still able to collapse the data. By changing the slot width and height simultaneously or by having an actuator array instead of a long steady slot, C_μ seems to struggle. This exemplifies the need for a new parameter that is able to collapse data with different freestream velocities and actuator types, but keeps the other "good" characteristics of C_μ.

The data for the following analysis was taken simultaneously with the data presented in Chapter 6. The data was acquired from the vertical tail model in the Lucas Wind Tunnel using the same acquisition tools.

7.2 Important Governing Variables

To derive a new parameter that can replace C_μ it is of upmost importance to first identify the governing variables for AFC applications. C_μ was "invented" by assuming that the boundary layer control of the separation is the only driving mechanism, and hence a momentum coefficient is the best choice. As it was shown, this is not entirely wrong, but it doesn't cover the whole spectrum of AFC. Fig. 7.2 attenuates the weakness of the momentum coefficient in an extended manner compared to the previous section. It is evident that it is not capable of catching the freestream velocity changes for the two sweeping jet cases (top images). Especially when the jet velocities approach $M = 1$, and the compressible effects start to play a larger role, the coefficient seems to completely ignore these effects. The steady blowing case at the bottom left seems to be slightly better, mainly because the compressible effects are much weaker in this case. Nevertheless, the results are still not satisfactory as they still seem to start diverging at higher flow rates which correspond to higher jet exit velocities. Putting the different jet types on top of each other on the bottom right underlines the momentum coefficient's second drawback of not being capable of collapsing jet types with different actuator exit areas.

Interestingly, when the momentum coefficient is calculated in an incompressible manner, leading to non-physical supersonic velocities at the jet throat, the data at different freestream velocities

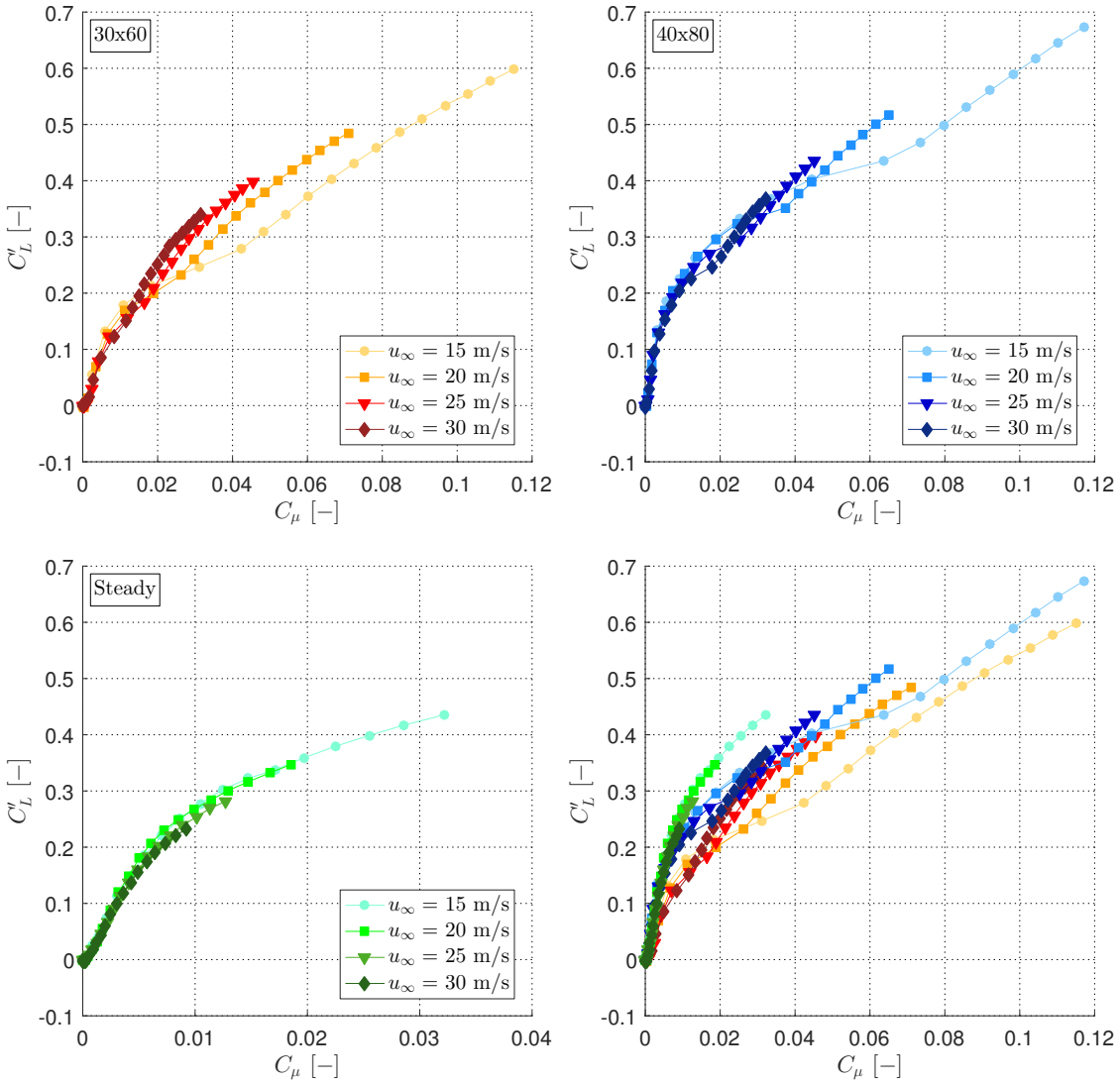

Figure 7.2: The normalized lift coefficient C_L' plotted against the input momentum coefficient C_μ for different jet types exemplify C_μ's weakness of not collapsing data at different freestream velocities. As shown in Fig. 7.1, it also fails to collapse the different actuator types even at the same freestream velocities.

collapses in a nice manner (Fig. 7.3). This might be one of the reasons why C_μ is calculated in an incompressible way in so many occasions: not because it's right, but because it works. However, this also means that the momentum doesn't seem to be the main driving factor behind AFC, and the problem with the different actuator areas is still present.

Focusing on the problem of collapsing the different freestream velocities for now, one can realize that when C_μ is calculated in an incompressible fashion (with no density correction) the following

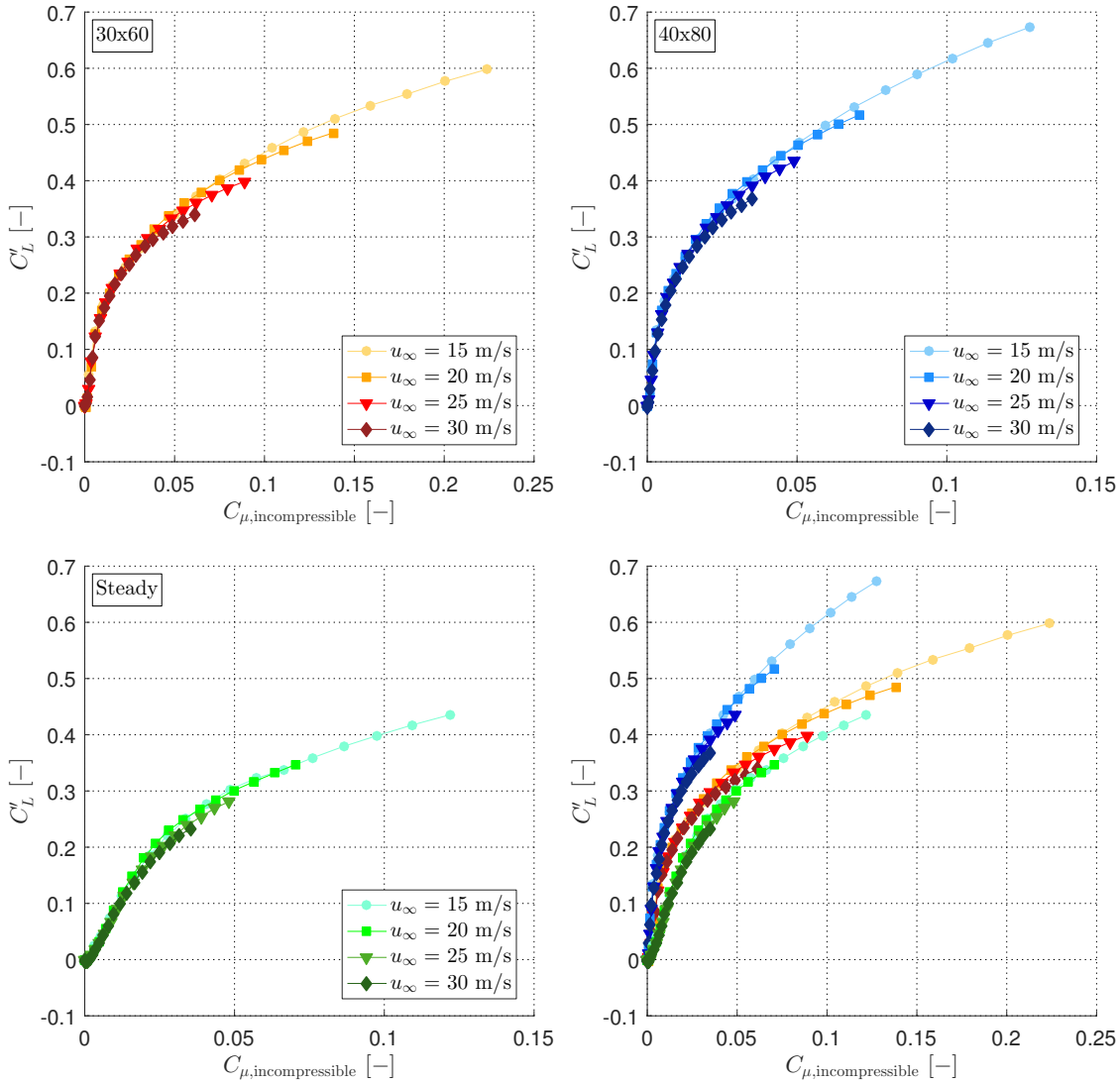

Figure 7.3: If C_μ is calculated in an incompressible fashion (which is wrong) the data collapses for different freestream velocities unlike when it's calculated the appropriate way. Nevertheless, the incompressible momentum coefficient still fails to collapse the different actuator areas.

holds:

$$C_{\mu,\text{incompressible}} = \frac{\dot{m}u_{\text{jet}}}{\frac{1}{2}\rho_\infty u_\infty^2 S} = \frac{\dot{m}^2}{\frac{1}{2}\rho_\infty^2 u_\infty^2 S A_{\text{act}} n}, \tag{7.1}$$

assuming $\rho_{\text{jet}} = \rho_\infty$. In other words, the $C_{\mu,\text{incompressible}}$ is depending on the square of the mass flow rate, or except for some "constants" on the square of the flow coefficient C_Q. Thus, it can be expected that a plot of the normalized lift coefficient C'_L against the flow coefficient C_Q would show similar results. This can indeed be observed in Fig. 7.4. While the overall curves look a bit different (due to these "constants"), the trends are exactly the same and the data is nicely collapsed. In case

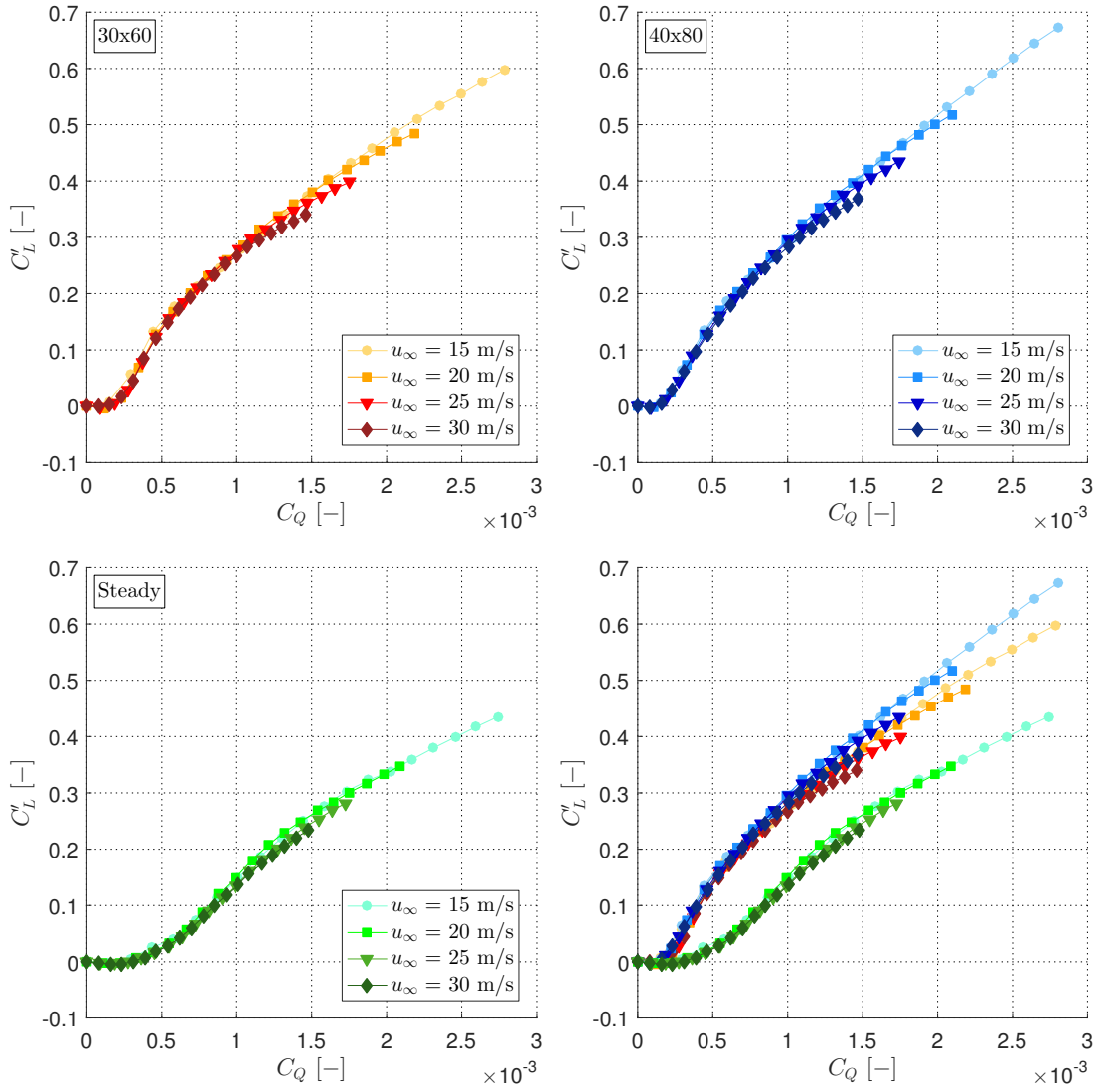

Figure 7.4: Plotting the normalized lift coefficient C_L' against the flow coefficient C_Q reveals the connection to an incompressible C_μ calculation. C_Q is able to collapse the data for different freestream velocities, but yet is still not able to collapse different actuator types.

of the different actuator types, the two sweeping jet actuators seemed to move a bit closer together, while the steady case is a little further off.

When working with different actuator designs and mass flow rates it becomes evident, that the ratio u_{jet}/u_∞ highly influences the results. Based on previous experience, and what is also mentioned in Chapter 4, the rule of thumb $u_{\text{jet}}/u_\infty > 3$ makes nearly every tested AFC design work reliably. By looking at Fig. 7.5, one realizes that this approximate relationship is actually fairly accurate. While the larger sweeping jet actuators and the steady blowing slot reach a non-zero C_L' earlier, the smaller sweeping jet actuators start picking up their pace at $u_{\text{jet}}/u_\infty \approx 2.5$. Being the smallest actuator that

was ever tested on the vertical tail, it's not surprising that $u_{\text{jet}}/u_\infty > 3$ came along as a rule of thumb. However, it is obvious that this rule of thumb is not independent of the actuator design. In the given cases it mostly overestimates the required velocity ratio, but for tiny actuators it might be set too low. Yet the velocity ratio collapses the for slow jet velocities fairly well, and only starts to diverge

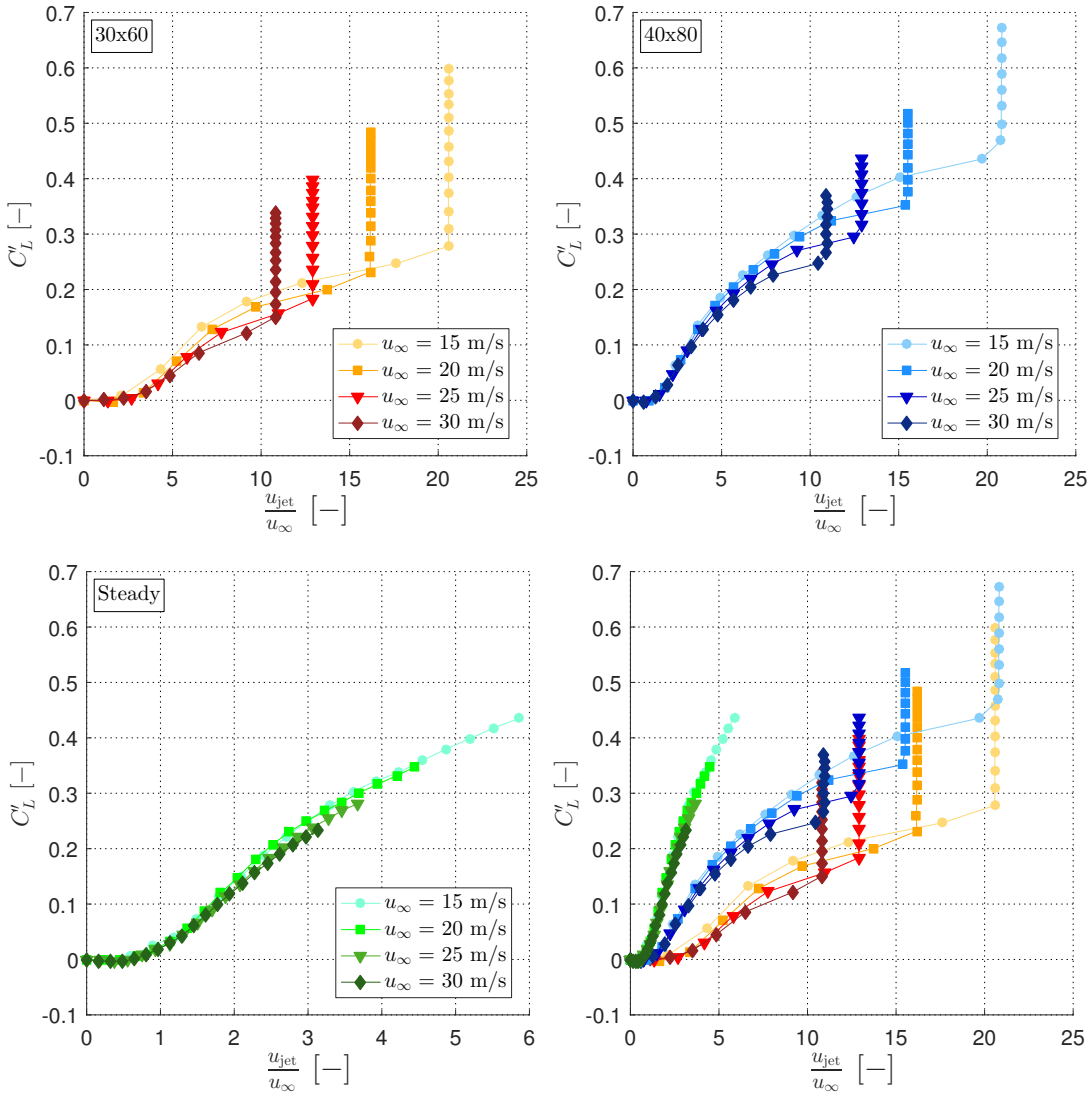

Figure 7.5: Velocity ratio for the different actuator types. A certain velocity ratio is needed before any beneficial effects start to occur. The minimum velocity ratio is independent of the freestream velocity within the same type of actuator, but different for each actuator type.

once the compressibility effects start to matter. For the steady blowing case it is able to collapse the data throughout all flow coefficients because the jet exits velocities are moderate compared to the sweeping jet actuators. For the two sweeping jet actuator cases, one can see that once they choke,

the velocity ratio creates vertical lines. Along these lines, the different actuator types can collapse again when they are exposed to the same freestream velocity.

Because the velocity ratio u_{jet}/u_∞ is already "hidden" within the flow coefficient C_Q, it's worth looking at other parts of the coefficient as well. In Fig. 7.6 the velocity ratio is multiplied with the area ratio of each actuator. For the separate cases the values are scaled while the overall appearance

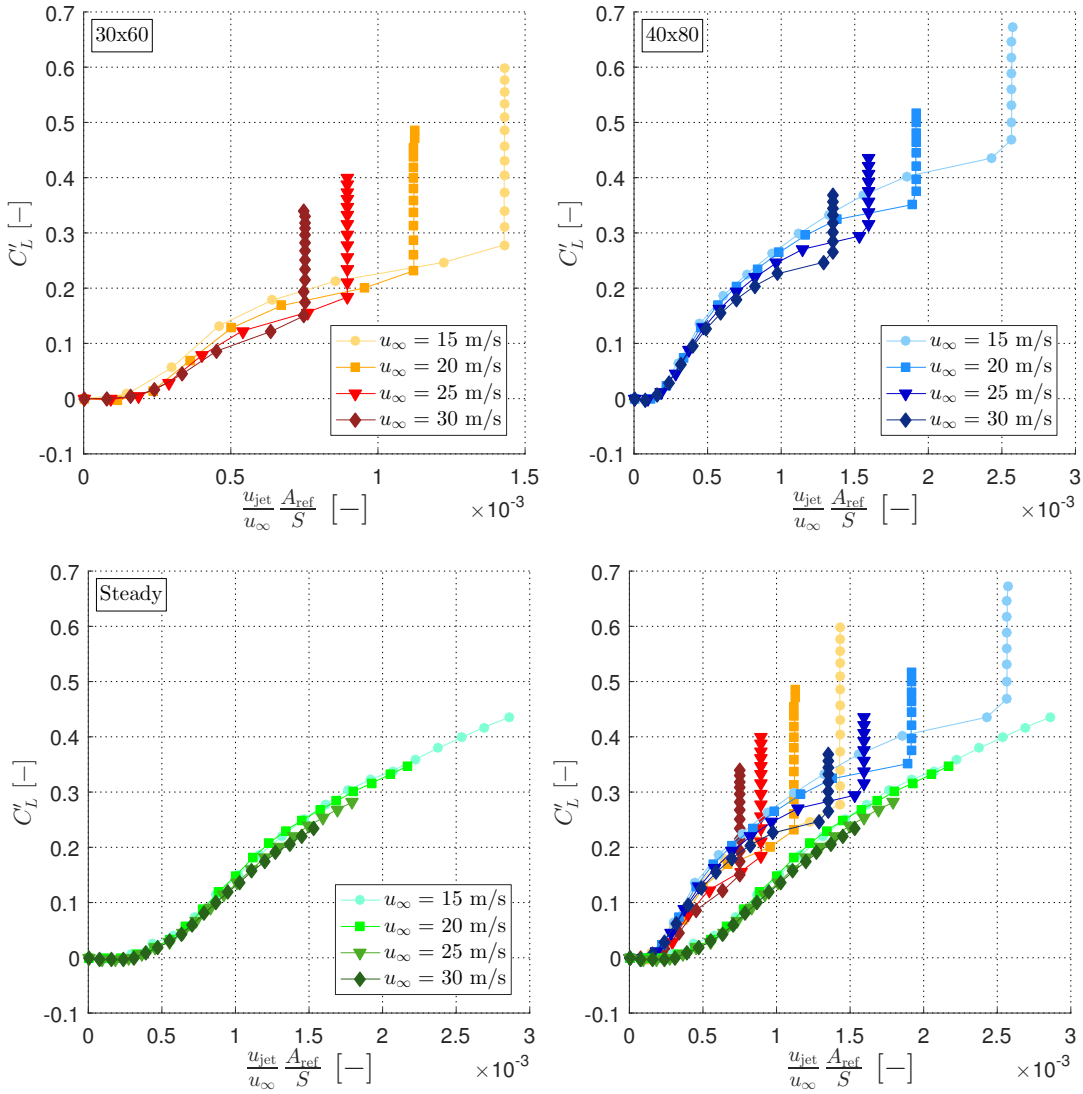

Figure 7.6: Velocity ratio multiplied by the area ratio scales the values in the separate cases compared to the pure velocity ratio. However, because the actuators all have different actuator areas the combined plot changes. The two sweeping jet actuators are now much closer to each other and the steady blowing case also reduced its difference.

stays exactly the same (that could be expected). However, the combined plot reveals some drastic changes: the two sweeping jet actuators moved much closer to each other and are collapsing in the

subsonic regime. The steady blowing case came a little closer and switched "sides" from the top to the bottom of the plot. This implies that the area ratio is an important parameter to assess the different actuator designs, as it was able to bring the different actuator types much closer together.

Plotting the density ratio will be omitted as it will just show the isentropic relation, and the same goes for the area ratio multiplied by the density ratio, which will shift the isentropic relations for the different actuator sizes apart from each other. This leaves a last combination shown in Fig. 7.7. The mass flux ratio does a great job in collapsing the data throughout all jet velocities. At lower

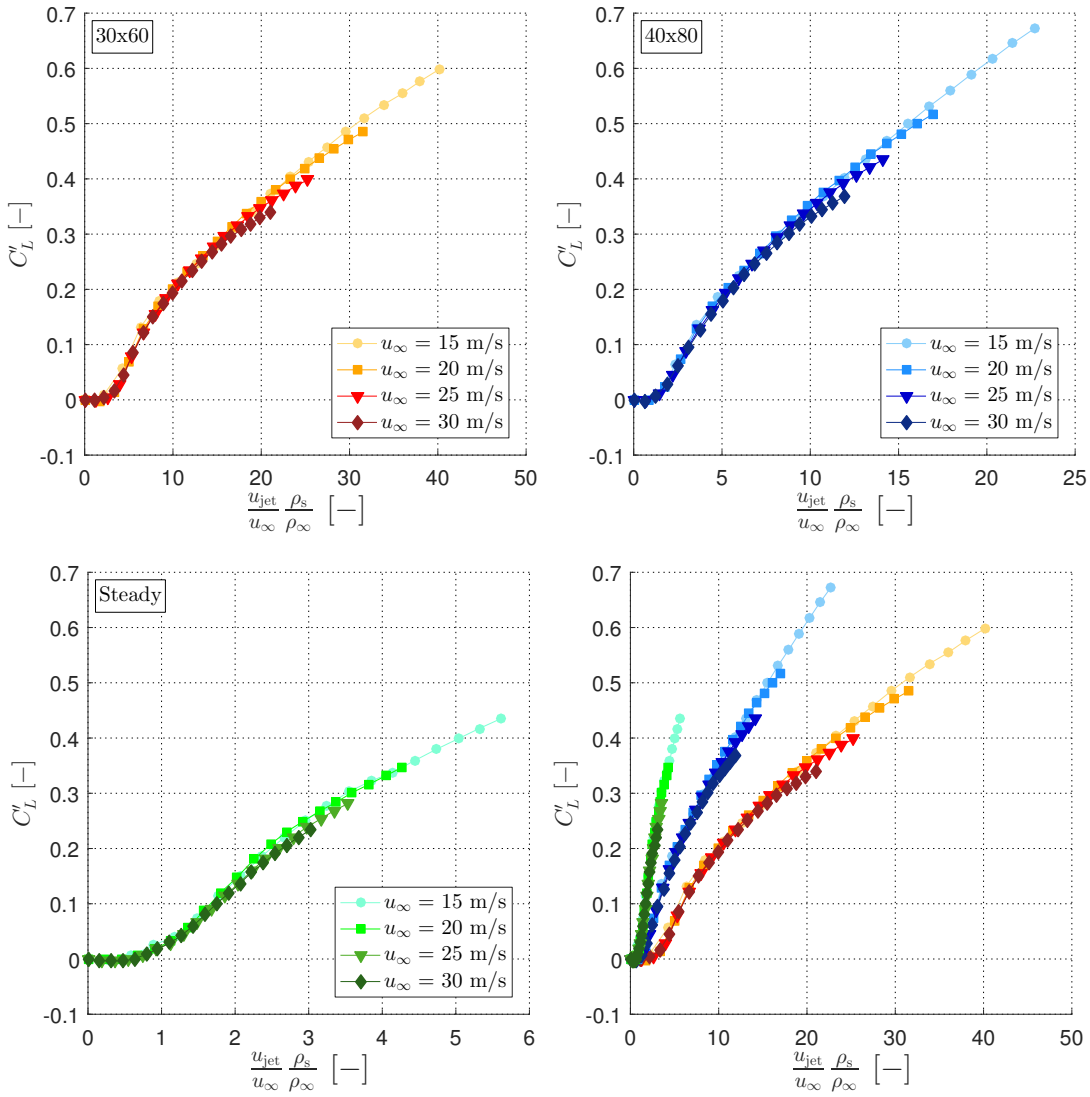

Figure 7.7: The mass flux shows an expected similarity with the velocity ratio at low jet velocities. However, at high velocities (with compressibility effects) it is able to keep the data collapsed. There is also no cut-off value anymore when the nozzle chokes. The interplay between the velocity ratio for the scaling and the density ratio to take care of the compressibility effects leads to this great result.

velocity ratios, where the flow can still be treated as incompressible, the velocity ratio takes care of the scaling to collapse the different freestream cases. When compressibility effects start to play a role the density ratio contributes by correcting the differences. Once the nozzle chokes, the density ratio will still linearly increase continuing a linear trend of the data. Based on these results, one can conclude that the mass flux is the core driver of collapsing the data in case of the flow coefficient C_Q, while the area ratio is responsible for the scaling.

7.3 Forming a New Similarity Parameter

However, the scaling doesn't seem to be quite right yet as C_Q is not capable of collapsing the complete data nicely. Kelly, Tolhurst, and Chaplin encountered a similar problem regarding some specific cases with C_μ. They concluded that for high pressure blowing systems C_μ is an acceptable, adequate, and dependable similarity parameter. For lower pressure systems, C_μ may not adequately correlate the effects of blowing.

As a correction, they introduced a further refinement of the momentum coefficient C_μ, and named it the net momentum coefficient $C_{\mu,\text{net}}$, defined as

$$C_{\mu,\text{net}} = C_\mu \left(1 - \frac{u_\infty}{u_\text{jet}}\right). \tag{7.2}$$

While this coefficient was capable of solving their similarity problems, Fig. 7.8 shows that it barely changes anything for the data, and the plots look nearly identical to the original ones in Fig. 7.2. However, the idea of introducing a correction that affects the similarity parameter in a different way depending on the actuator type is brilliant. It is easy to apply the same correction to C_Q to get the net flow coefficient

$$C_{Q,\text{net}} = C_Q \left(1 - \frac{u_\infty}{u_\text{jet}}\right). \tag{7.3}$$

Based on the previous example, one would not expect much of an influence of the net flow coefficient $C_{Q,\text{net}}$ either. However, Fig. 7.9 shows a magnificent results were all the different curves practically collapse onto each other. The differences that are remaining can now be explained by the actuator differences and their actual performance. In this case, it seems that the slightly bigger 40x80 sweeping jet actuators are better than the smaller 30x60. The 30x60 actuators are probably too small to cover the whole span of the vertical tail evenly with flow, unlike the bigger 40x80 actuators. The steady blowing case is a bit more off, which most likely has to due with the fact that there was a

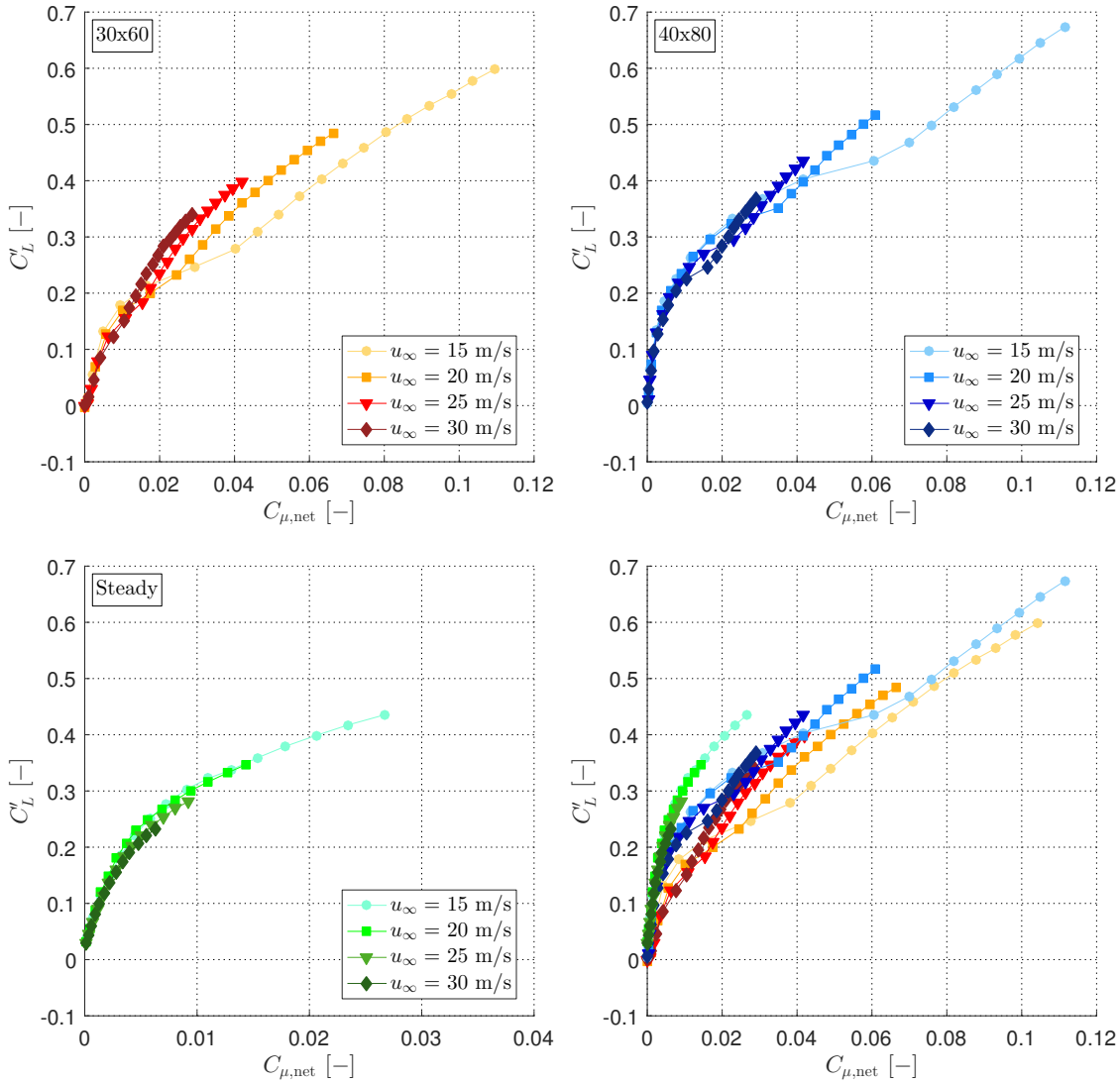

Figure 7.8: The net momentum coefficient $C_{\mu,\text{net}}$ has a vanishing effect compared to the standard momentum coefficient C_μ. The results look practically identical to Fig. 7.2

large negative pressure gradient inside the plenum from root to tip. As a consequence, the flow at the root is at different conditions (at a different net flow coefficient $C_{Q,\text{net}}$) compared to the flow at the tip. The calculated $C_{Q,\text{net}}$ represents only an average of these conditions. Because the vertical tail is tapered, the root has a much larger effect on C_L' compared to the tip, and the calculated $C_{Q,\text{net}}$ slightly underestimates the true values. This statement can be verified by reducing the slot width in the calculations, which then causes the steady blowing curve to align better with the two sweeping jet actuator curves.

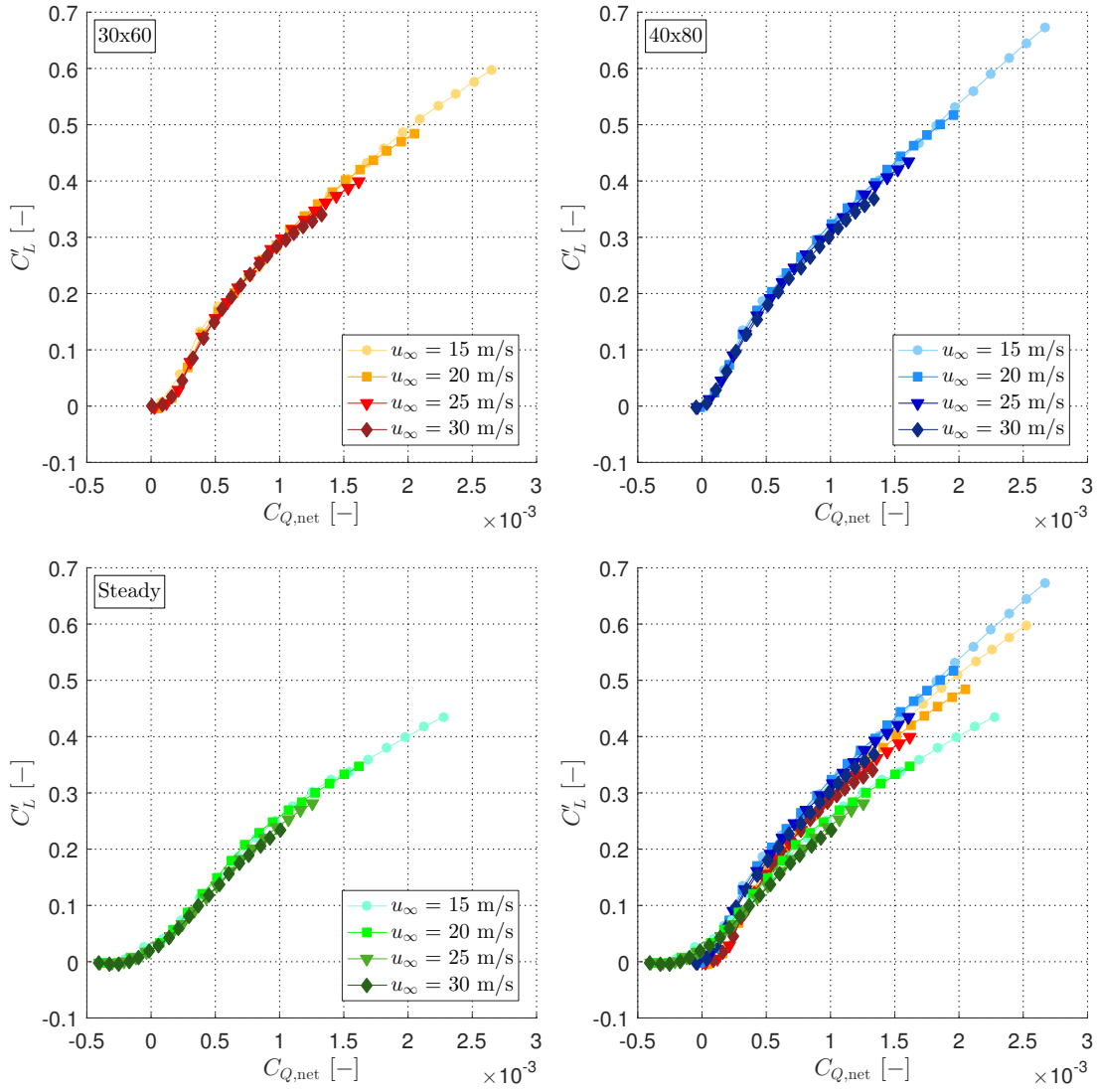

Figure 7.9: The combination of flow coefficient C_Q and velocity ratio u_{jet}/u_∞ leads to the net flow coefficient $C_{Q,\text{net}}$ that is able to collapse different freestream velocities as well as vastly different actuator designs.

In summary, it can be said that the momentum coefficient C_μ is not the driving force in AFC, and only works in specific cases. The lift benefit doesn't seem to be driven by momentum, but rather by the mass flow rate that is represented by the flow coefficient C_Q. It can be shown that another important similarity parameter in AFC is the ratio between freestream velocity u_∞ and the jet exit velocity u_{jet}. While both parameters by themselves show some flaws, their combination leads to a well-rounded similarity coefficient $C_{Q,\text{net}}$.

7.4 Extending to Thermal Active Flow Control

Chapter 6 was dedicated to thermal active flow control and all the derivations were based on the momentum input coefficient C_μ. Thus, it would be a pity if the net flow coefficient $C_{Q,\text{net}}$ would not be able to cover this case as well. Unfortunately, Fig. 7.10 shows that it is not able to cover the

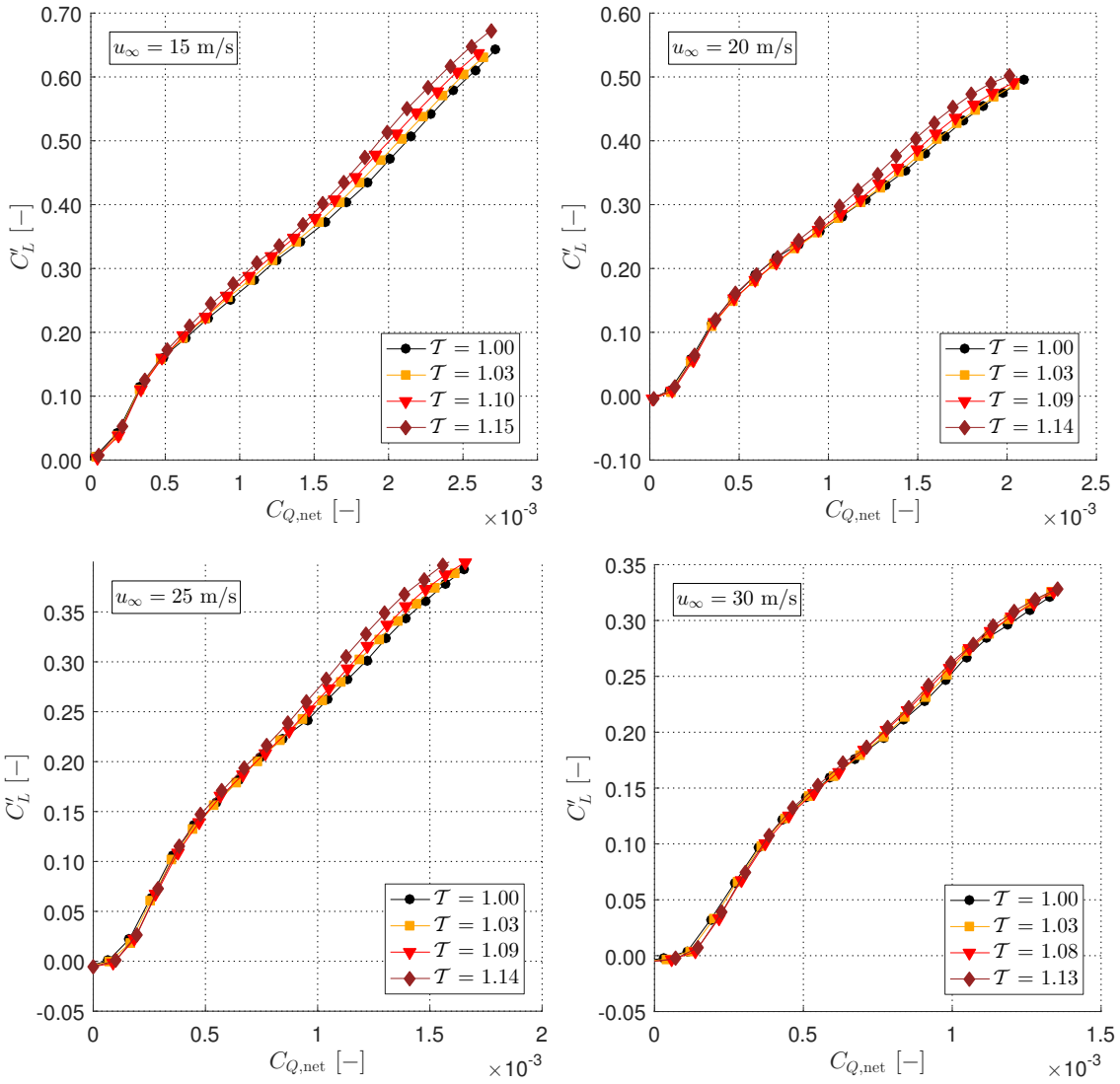

Figure 7.10: The net flow coefficient $C_{Q,\text{net}}$ is not able to account for thermal active flow control.

thermal effects. In fact, the figure looks practically identical to Fig. 6.7. This has to be expected because the velocity adjustment doesn't have a big impact in this case due to the fact that the data was taken with the same actuator type. As such, $C_{Q,\text{net}}$ is practically still a mass flow rate. In Eq. (6.6), it was shown that the mass flow rate is dependent on the temperature. Luckily, this equation contains the solution to the problem as well. If the mass flow rate is inversely dependent on the square root of

the temperature, one can simply multiply it by that factor to make it temperature-independent. This leads to the extended mass flow coefficient

$$\mathcal{M} = \frac{\dot{m}}{\rho_\infty u_\infty S}\left(1 - \frac{u_\infty}{u_{\text{jet}}}\right)\sqrt{\frac{T_{\text{jet}}}{T_\infty}} = C_{Q,\text{net}}\sqrt{\mathcal{T}}. \tag{7.4}$$

The coefficient was significantly renamed to distinguish it from the mess of current coefficients and to avoid the ill-named connection of C_Q to the volume flow rate $\dot{Q}$. Fig. 7.11 shows that the thermal data now collapses using the extended mass flow coefficient.

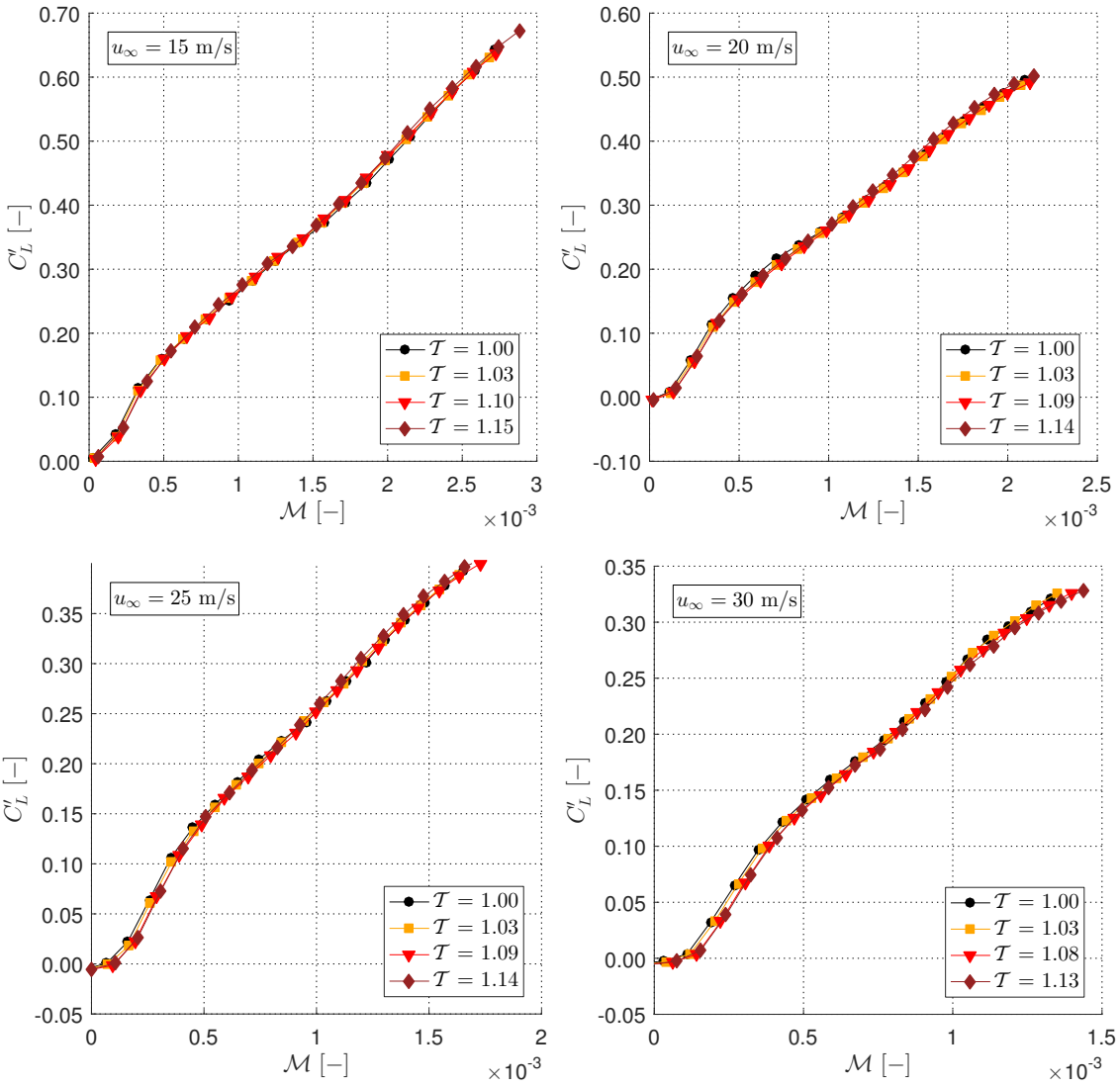

Figure 7.11: Adjusting the net flow coefficient by the square root of the temperature ratio leads to the extended mass flow coefficient $\mathcal{M}$ that is now able to collapse the thermal active flow control data.

7.5 Understanding the Extended Mass Flow Coefficient

While the momentum coefficient C_μ had its verification from the perspective of boundary layer control, the extended mass flow coefficient $\mathcal{M}$ first needs to find its meaning. Generally spoken, it is a simple mass flow coefficient, but the previous results prove that its extensions make it an extremely efficient similarity parameter. To improve its understanding, it was decided to conduct a two-dimensional DPIV experiment on the vertical tail in the Lucas Wind Tunnel for different values of the extended mass flow coefficient $\mathcal{M}$. This way, the previous results and the PIV data can be directly compared. As seeding particles small soap bubbles were used, and a 200 mJ laser at 532 nm was used as the illumination source. The seeding particles were created by pushing a highly pressurized soap mixture (1000 psi) through a small orifice, which then leads to a cavitation effect forming tiny soap bubbles between 10 to 60 μm in diameter (Gharib and Kim, 2011). The laser sheet was aimed around mid-span between actuators 17 and 18 (counted from the root). An Imperx B3420M camera was installed inside the tunnel test section directly above the model. The camera itself is fairly small which allows for enough space to the model for minimum interference. The region of interest was determined to be the region right after the flap hinge of the vertical tail. This way it is possible to observe the effects of AFC on the flap. The flap was set to deflection angle of $\delta_F = 20°$. An illustration of the laser sheet location and the region of interest is given in Fig. 7.12. The red box corresponds to the camera's field of view which coincides with the region of interest over the flap hinge as described above.

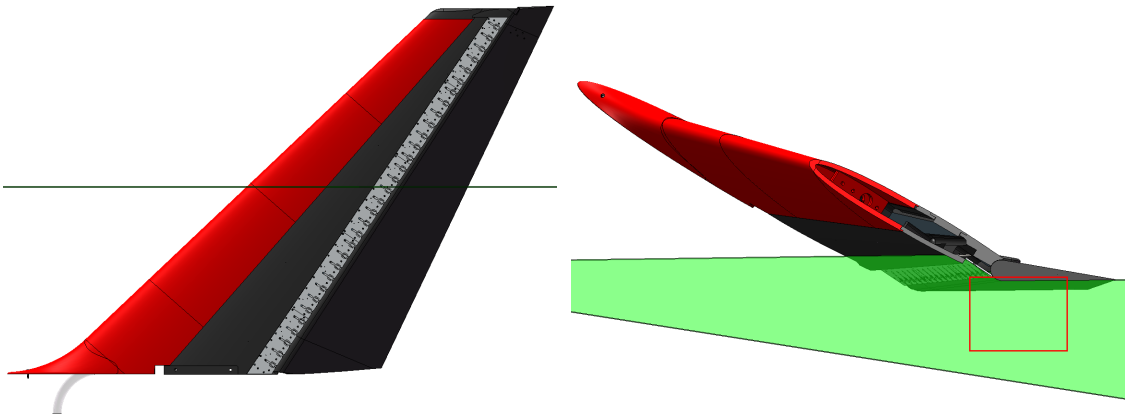

Figure 7.12: Illustration of the PIV setup on the vertical tail. On the left, one can see the spanwise location of the laser sheet between actuators 17 and 18 (counted from the root). The top view on the right shows the camera's field of view marked by the red box. This region is of particular interest as it covers the actuators on the left side and spans over the flap of the tail.

It was decided to acquire a large and dense set of data for one particular parameter set instead of a sparse data set on a variety of parameters. A standard sweeping jet actuator with a height of 0.040 inches and a nozzle diameter of 0.080 inches (40x80) was used as AFC device. The freestream velocity was set to 15 m/s to cover a large data range of extended mass flow coefficients $\mathcal{M}$. Fig. 7.13a illustrates the measurements that were acquired by the force balance for this particular case. The light blue markers correspond to the measured data points, the vertical line represents the $\mathcal{M}$ value at which the slope of the curve changes from non-linear to linear, and the colored circles correspond to the PIV data that is presented in Fig. 7.14 for the green circles and in Fig. 7.15 for the red circles. Fig. 7.13b shows the PIV results of 500 averaged image pairs for the baseline case which by the definition of $\mathcal{M}$ has no corresponding value but would be equal to a point at $\mathcal{M} = 0$ at no lift benefit $C_L' = 0$. The contour colors are defined by the measured velocity magnitude divided by the

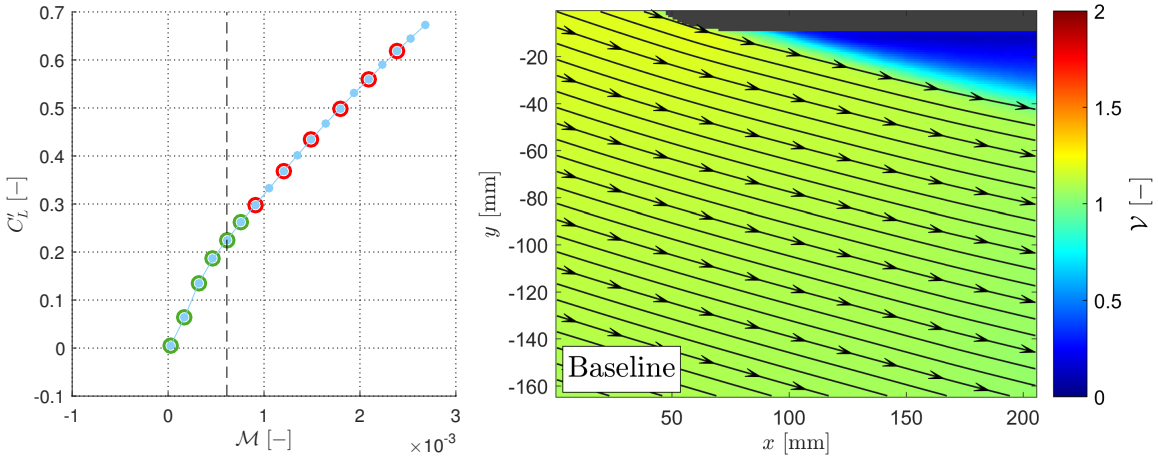

(a) Evaluated data points

(b) PIV of the baseline

Figure 7.13: On the left, the measured lift and extended mass flow coefficient values during the PIV experiment are shown. The vertical line represents a change of slope in the lift curve, and the different circle colors correspond to different data sets shown in Figs. 7.14 and 7.15. On the right, the PIV baseline (no actuation) is shown where the contour colors correspond to the velocity magnitude normalized by the freestream velocity. The black lines with arrows show the streamlines and -directions. The dark gray area corresponds to the lower part of the flap.

freestream velocity

$$\mathcal{V} = \frac{\sqrt{u^2 + v^2}}{u_\infty}. \tag{7.5}$$

The black lines correspond to streamlines and the arrows point in the flow direction. The dark gray area at the top belongs to the lower part of the flap. Because the flap is a highly reflective surface, this part of the image was covered by a mask that is slightly bigger than its real size during the PIV

calculations. A streamline that is seemingly disappearing into the flap is in fact just really close to the flap surface hiding below the mask. By looking at the baseline case in more detail, one can clearly see that there is a separation over the flap distinguishable by the low velocity magnitude inside the recirculation zone. The separation point is right at the flap hinge, which makes this case ideal for AFC. The flow magnitude in the field of view is slightly above the freestream velocity which can be explained by the presence of the vertical tail, and the acceleration of the flow on its suction side. Fig. 7.14 shows the averaged PIV results of 500 image pairs for each data point in the non-linear part of Fig. 7.13a. It is easy to see that the large increase in lift is connected to the elimination of the separation region. The separation is completely removed for an extended mass flow coefficient of $\mathcal{M} \approx 0.63 \cdot 10^{-3}$. This corresponds exactly to the value marked by the vertical line in Fig. 7.13a, where the lift increase switches from a non-linear to a linear behavior. Thus, the non-linear increase in lift is due to the removal of the separation region. One may ask why the separation is removed by AFC. A plausible answer can be found if the entrainment requirement of the shear layer between the high-velocity jets and the much slower flow in the separation bubble is considered. The shear layer is comprised of large vortices that engulf an equal amount of fluid from either side; however, the side that is exposed to the separated region can't easily provide as much as the side that is exposed to the high-speed jet. As a consequence, the separated region provides additional fluid from further downstream, causing the separation bubble to shrink and eventually to become extremely small: the separation region is practically removed, and the flow reattaches. While the result of separation removal is not surprising as it is the primary use of AFC, it is still astonishing how well the extended mass flow coefficient $\mathcal{M}$ is able to reflect this. The more interesting portion seems to be the linear increase after the separation is removed. Without the PIV images it would be difficult to guess what exactly causes the additional increase in lift, especially when knowing that there is no separation present. Fig. 7.15 shows averaged PIV results of the linear region. The images don't look much different at first glance, but there are a few highly important things to notice. First, the streamlines get pulled closer to the flap for higher values of extended mass flow coefficient. This is easiest to see, if the first and last image of the series are compared directly: the streamlines moved about 10 to 15 mm closer to the flap. Second, the additional mass flow provided by AFC causes an increased velocity magnitude at the actuator exits that then travels downstream along the flap. In the last PIV image, the velocity magnitude close to the flap is approximately twice as fast as the

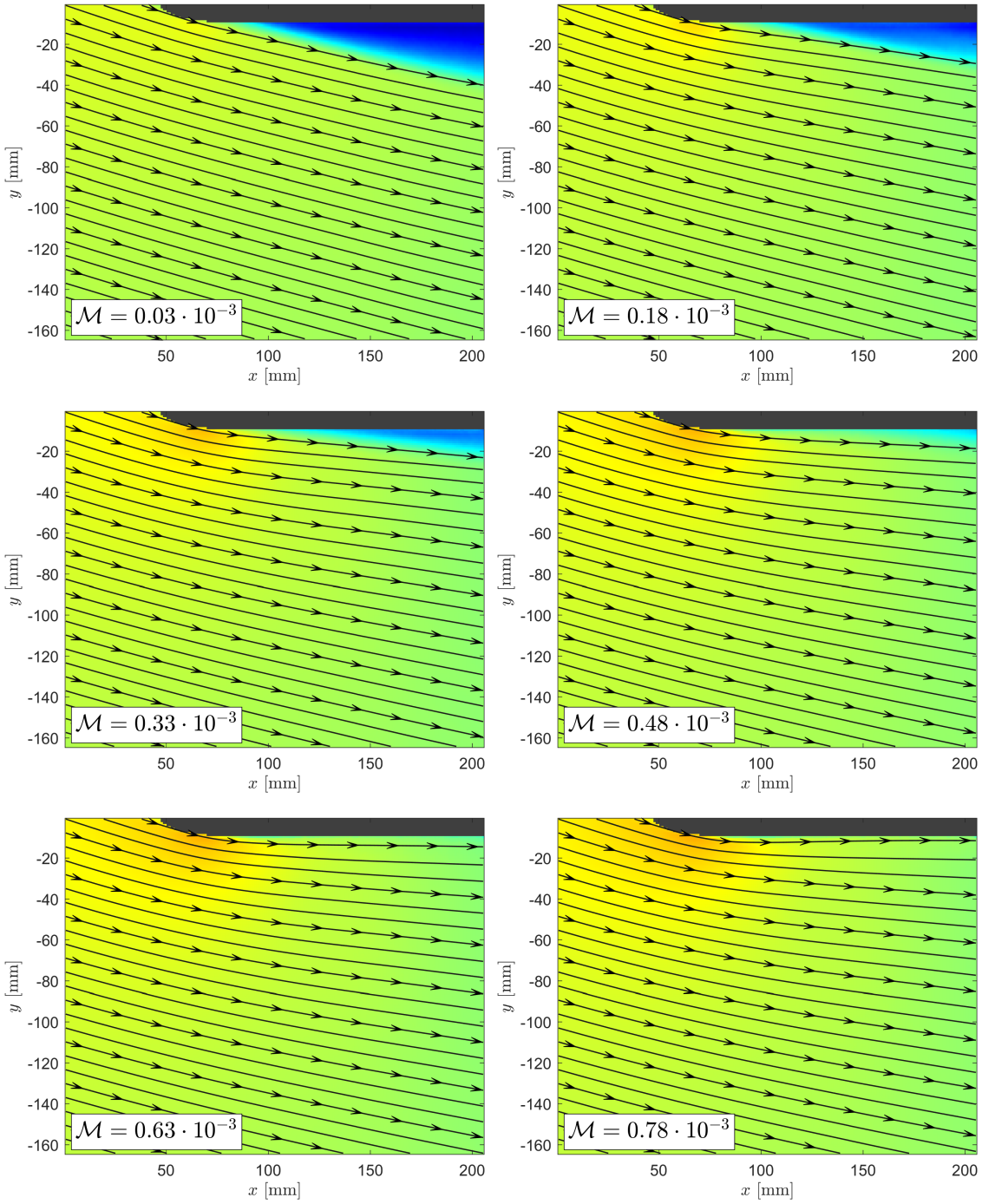

Figure 7.14: PIV images from the non-linear part of the extended mass flow coefficient $\mathcal{M}$. The strong non-linear increase is shown here to be the removal of the separation region caused by an entrainment effect of the created shear layer between the high-velocity jet and the much slower flow in the recirculation zone.

freestream velocity. Based on result acquired during the experiments published in Seele, Graff, Lin, et al., 2013, the faster fluid velocity leads to a lower pressure over the flap surface. This does not

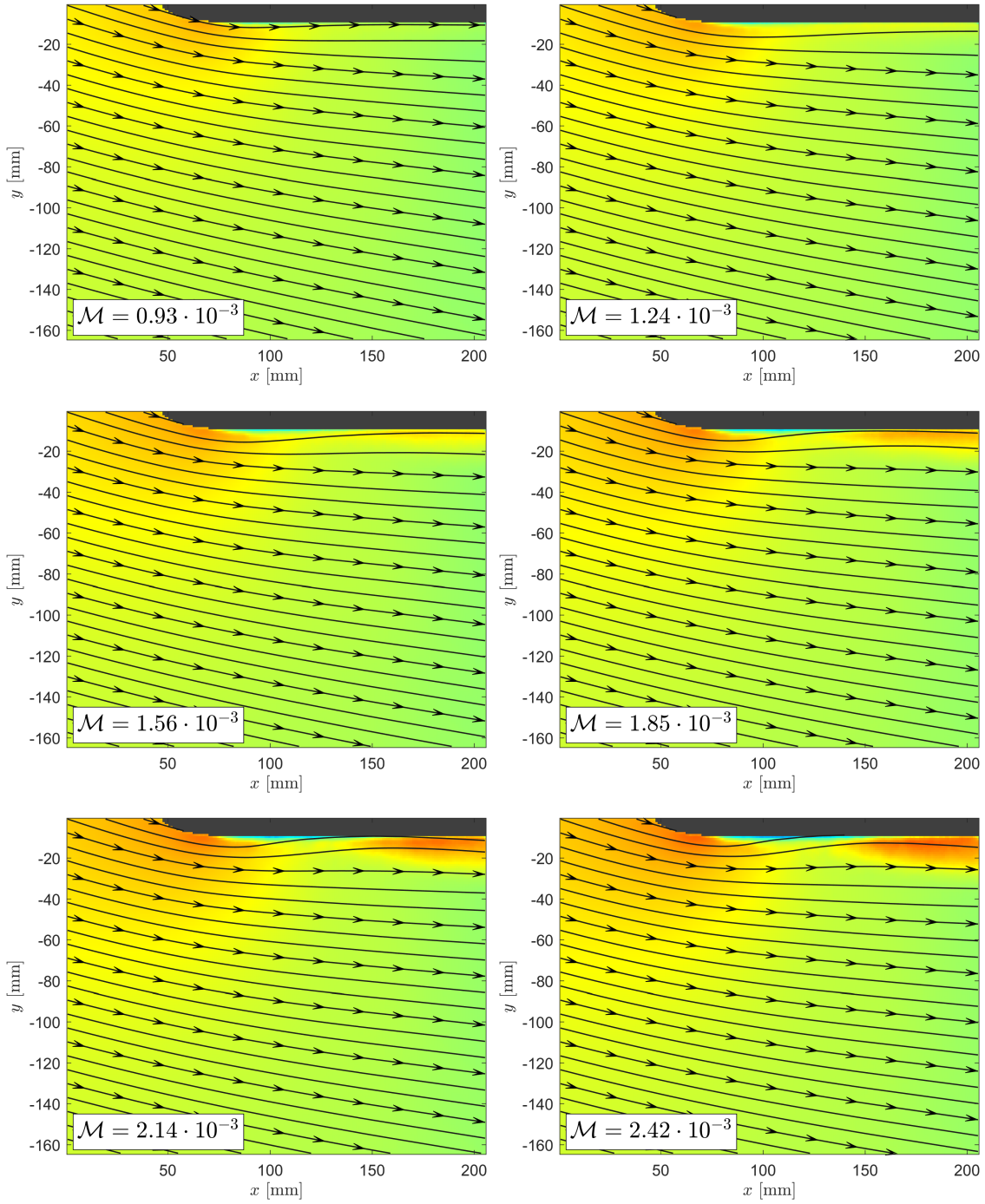

Figure 7.15: PIV images from the linear part of the extended mass flow coefficient $\mathcal{M}$ after the separation is removed. The increasing lift is generated by an increased velocity close to the flap surface due to the jet's additional mass flow in that region. The accelerated flow causes a lower overall pressure on the flap surface, pulling the streamline closer to the flap surface. This leads to an increased circulation around the entire vertical tail (supercirculation), and is essential responsible for the lift benefits.

only increases the lift, but pulls the streamlines closer to the flap surface similar to a line-sink in potential flow theory. As a consequence, this causes the circulation around the entire vertical tail to be significantly increased (which is equivalent to the statement that the lift benefit is increased), and thus this phenomenon is named supercirculation. One might observe that there seems to be a velocity magnitude deficit along the streamlines close to the flap. This is in fact not a deficit, but rather a remnant of a three-dimensional effect caused by the sweeping jet actuators. The actuators are at an angle compared to the PIV plane, which is aligned to the freestream direction (see Fig. 7.12 for more details), and thus the emitted jets cross the PIV plane in the out-of-plane direction. In other words, most of the velocity magnitude in that region is actually stored in the jet flowing in the plane's normal direction, and can't be captured by two-dimensional PIV. Three-dimensional PIV would be the technique of choice to capture this in more detail, but would make the experiment a lot more difficult and laborious. However, the acquired two-dimensional PIV results still significantly improve the understanding of the extended flow coefficient $\mathcal{M}$. It is now possible to describe the different "states" of AFC. Fig. 7.16 shows a theoretical example of these flow states which were named as boundary layer thickening, separation control, and supercirculation. Between these states are two "turning points" which are labeled as the minimum flow requirement $\mathcal{M}_{\text{min}}$ and the critical flow requirement $\mathcal{M}_{\text{crit}}$.

Boundary Layer Thickening: This "state" was observed in Chapter 4 and describes a deleterious lift effect if AFC is used with low mass flow input. Due to the fact that the jet velocity is slower than the freestream velocity, the boundary layer is displaced (thickened) which is known to impact the lift negatively. The extended mass flow coefficient $\mathcal{M}$ takes a negative value if the jet velocity is too low, and as such can "predict" the negative lift.

Mimimum Flow Requirement $\mathcal{M}_{\text{min}}$: The minimum mass flow requirement describes the minimum flow that is required to achieve $\mathcal{M} = 0$, where active flow control has no effect on the lift. Any additional mass flow will result in a lift improvement. When designing an actuation system the mass flow rate corresponding to $\mathcal{M} = 0$ needs to be surpassed.

Separation Control: This region describes the most efficient use of AFC. Active flow control reattaches separated flow resulting in a large lift benefit. It is believed that the entrainment requirement

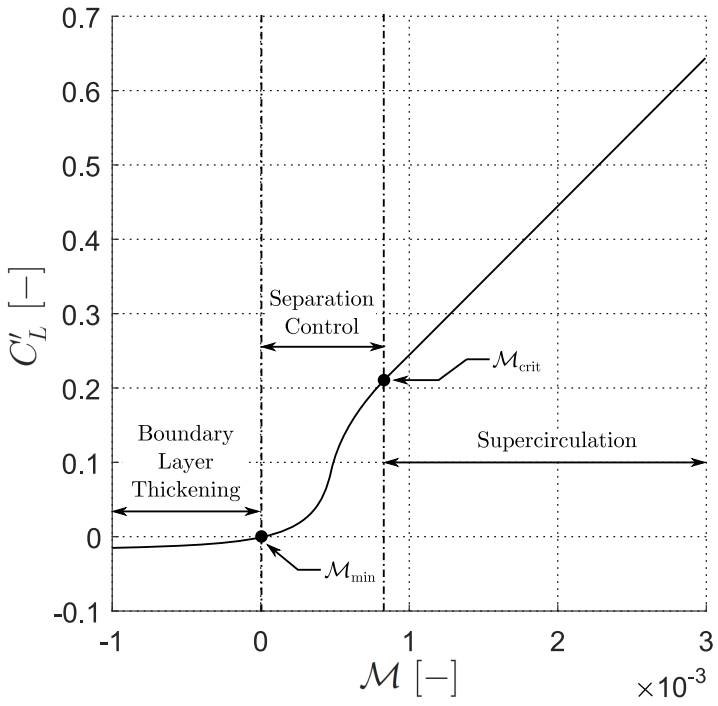

Figure 7.16: The different "states" in AFC can be described by boundary layer thickening, separation control, and supercirculation. The extended flow coefficient $\mathcal{M}$ is capable of not only distinguishing them, but also predicting them to a certain extent.

of the shear layer between the high-velocity jets and the much slower flow in the separation bubble engulfs an equal amount of fluid from either side due to its large vortices. The side that is exposed to the separated region can't easily provide as much fluid as the side that is exposed to the high-speed jet, and needs to provide additional fluid from further downstream. This causes the separation bubble to shrink and eventually to become extremely small: the separation region is practically removed, and the flow reattaches.An actuation system should cover this entire region to make the most use of its implementation. This region does not necessarily exist if there is no separation present.

Critical Flow Requirement $\mathcal{M}_{crit}$: The critical mass flow requirement describes the transition between the separation control with a large non-linear lift increase and the supercirculation region with a linearly increasing lift benefit. Compared to the minimum flow requirement $\mathcal{M}_{min}$, the critical flow requirement $\mathcal{M}_{crit}$ is not defined at a certain value, but rather depends on various parameters such as flap deflection, airfoil thickness, leading edge radius, location of maximum chamber, Reynolds number, incidence angle, etc. It is also possible that for certain combinations of variables a separation does not exist, and as such $\mathcal{M}_{crit} = \mathcal{M}_{min}$. From a design standpoint of

view, $\mathcal{M}_{\text{crit}}$ should be within the capabilities of the AFC system. Depending on the specific case, the maximum mass flow rate may go beyond this point.

Supercirculation: In this region the flow is already attached and any additional mass flow linearly improves the lift. Based on experimental results it was shown that the additional mass flow causes an increased velocity magnitude at the actuator exits that then travels downstream along the airfoil. The faster fluid velocity leads to a lower pressure over the airfoil surface, which does not only increases the lift, but also pulls the streamlines closer. As a consequence, the circulation around the entire airfoil is increased, resulting in a significant lift benefit.

While the extended mass flow coefficient works extremely well for the given experiments, it needs to be noted that the coefficient is solely derived from limited experimental data sets. It is possible that it may not work under different circumstances because it doesn't rely on any fundamental derivation, and it may miss the fundamental flow physics. Also, the distinction between boundary layer thickening, separation control, and supercirculation might not always be that clear, and assuming that they are all driven by the same parameter might be far-fetched. In general, the lift generation over an airfoil is characterized by many parameters such as incidence, flap deflection, relative flap chord, leading edge radius, airfoil thickness, camber, taper, leading edge sweep, Reynolds number, Mach number, etc. Adding AFC to the mix adds many more parameters, such as actuator type, spanwise/chordwise actuator location, actuator orientation, actuator size, wing size, jet velocity, freestream velocity, jet temperature, freestream temperature, jet pressure, freestream pressure, actuator pressure, jet density, freestream density, mass flow rate, jet momentum, etc. While a few of these parameters seem to be mainly independent of the others, such as the location or orientation of the actuators, many of them are directly or indirectly connected. If one attempts to think about variables that drive AFC, one can get the following:

$$\Delta L = f\left(\dot{m}_{\text{jet}}, u_\infty, u_{\text{jet}}, \rho_\infty, \rho_{\text{jet}}, p_\infty, p_{\text{jet}}, T_\infty, T_{\text{jet}}, S, A_{\text{jet}}\right). \tag{7.6}$$

Using the means of dimensional analysis opens several options of scaling. The following attempt uses the freestream velocity u_∞, the freestream density ρ_∞, and the wing planform S to form the dimensionless ratios:

$$\Delta C_L = f\left(C_Q, \frac{u_{\text{jet}}}{u_\infty}, \frac{\rho_{\text{jet}}}{\rho_\infty}, \frac{p_{\text{jet}}}{p_\infty}, \frac{T_{\text{jet}}}{T_\infty}, \frac{A_{\text{jet}}}{S}\right). \tag{7.7}$$

It is evident that many of the previously discussed governing variables show up in this analysis. Others, such as C_μ, can be formed by a simple multiplication:

$$C_\mu = f\left(C_Q, \frac{u_{\text{jet}}}{u_\infty}\right) = 2 \cdot C_Q \frac{u_{\text{jet}}}{u_\infty}. \tag{7.8}$$

The difficulty with these parameters and their combinations is not only their large number, but also their connections among each other. For example, the flow coefficient C_Q itself is a multiplication of density, velocity, and area ratio. The density, temperature, and pressure ratios are connected via the ideal gas law. In other words, it is not trivial to identify the important parameters based on theoretical means. A vast amount of literature exploits fundamental derivations of similar problems, for example Newman's derivation for the deflection of a two-dimensional incompressible jet by an inclined plate (Newman, 1961). While some of these problems seem to be fairly similar to an AFC application, they usually lack a key ingredient, that derails the whole concept. In Newman's example that is the two-dimensional limitation, the incompressibe flow assumption, and most importantly the absence of a freestream. The introduction of the extended mass flow coefficient based on experimental results gave yet another possibility to combine a selection of these parameters:

$$\Delta C_L \sim \mathcal{M} = f\left(C_Q, \frac{u_{\text{jet}}}{u_\infty}, \frac{T_{\text{jet}}}{T_\infty}\right) = C_Q \left(1 - \left(\frac{u_{\text{jet}}}{u_\infty}\right)^{-1}\right) \sqrt{\frac{T_{\text{jet}}}{T_\infty}}. \tag{7.9}$$

While these parameters and their specific combination works well for the presented experimental data, this may not apply to other cases, where different parameters sets, such as the pressure ratio may play a more dominant role. On top of that, parameters such as the Reynolds number (for the jet and freestream) or the Strouhal may also be added to the pool of parameters. The vast parameter space underlines the challenge of acquiring fundamentally derived coefficients. It is likely that many different parameters govern AFC, and that a subset of them may be dominant in one case, but negligible in another one.

7.6 Concluding Remarks

This chapter showed that the momentum flow coefficient C_μ as the sole parameter in AFC is not able to collapse data reliably. As a consequence, an experiment in the Lucas Wind Tunnel using a vertical tail model was performed to create a new similarity parameter based on experimental data that can overcome the weaknesses of C_μ. It was shown that the mass flow coefficient C_Q is one of

the main drivers of AFC. It was also discovered that the velocity ratio u_{jet}/u_∞ plays an important role in quantifying cases that have a largely different actuation area, such as sweeping jet actuators compared to steady blowing actuation. The combination of the flow coefficient C_Q and the velocity ratio led to a new parameter called the net flow coefficient $C_{Q,\text{net}}$ that was now able to collapse the data. $C_{Q,\text{net}}$ was further improved to accommodate for thermal active flow control (see Chapter 6), leading to the extended mass flow coefficient defined as:

$$\mathcal{M} = \frac{\dot{m}}{\rho_\infty u_\infty S}\left(1 - \frac{u_\infty}{u_{\text{jet}}}\right)\sqrt{\frac{T_{\text{jet}}}{T_\infty}} = C_{Q,\text{net}}\sqrt{\mathcal{T}}.$$

The coefficient was renamed to avoid confusion with the previous coefficients, and to give it its own existence. The implications of the extended mass flow coefficient were then explored by using PIV data taken on the vertical tail model in the Lucas Wind Tunnel. It was shown that AFC can be divided into three different "states": boundary layer thickening, separation control, and supercirculation. The extended mass flow coefficient is able to represent these states accurately, and can even predict the deleterious boundary layer thickening. The limits of this experimentally derived coefficient were also discussed, and that it probably only represents a subset of variables that drive AFC. As such, the extended mass flow coefficient may not work as reliably in other experiments. However, the large parameter space of AFC makes a fundamental derivation of such coefficients extremely difficult.

Chapter 8

Conclusion

While active flow control is a key technology to overcome future challenges in the aerospace industry, it lacks significant fundamental understanding to open the doors for commercial application. Sweeping jet actuators as promising active flow control devices were studied in detail by the means of Schlieren visualization and an in-depth analysis of their interactions. Extended tests on a high-lift airfoil showed the difficulties of applying AFC in an advanced manner. A new, much simpler calculation method for one of the most used dimensionless numbers in active flow control, the momentum input coefficient, was presented. A detailed derivation of the concept of thermal active flow control is given, and experiments were conducted to confirm its applicability in practice. The extended mass flow coefficient was introduced as a new similarity parameter in active flow control, and may play a key role in a better fundamental understanding of the technology. The results of this thesis have the potential to change the appearance and design process of future aircraft entirely.

8.1 Sweeping Jet Actuators as Part of Modern Active Flow Control

Even though sweeping jet actuators are the rising stars of active flow control, there is a shortcoming of knowledge about their working principle and basic interactions. The first goal of this thesis was to gain insight into the internal flow structure of these extraordinary active flow control devices. A Schlieren model consisting of two optical glass plates which were sandwiching an aluminum actuator plate was built to investigate the internal flow characteristics. It was shown that at the startup of a sweeping jet actuator the first sweeping motion seems to be entirely random, most likely due to tiny differences in the geometry. Once the sweeping motion has started, roll-up vortices form in the exit trapezoid due to the switching behavior of the jet. It is believed that these vortices support the superior mixing characteristics of a sweeping jet actuator and benefit its performance as an active flow control device. A further increase of the supply pressure leads to shocks at the actuator exit, and a damping effect of the sweep angle can be observed. This effect is enhanced with an increase of pressure, and eventually an underexpansion of the flow at the actuator exit becomes visible.

Furthermore, the interaction of adjacent sweeping jet actuators is studied. Schlieren images of the exit jets were taken, and the Canny edge detection method was used to track their sweeping motion. The tracking data was then analyzed with several techniques including Fast Fourier Transform, curve-fitting with a Fourier Fit, Hilbert Transform, and combinations of them. It was shown that a sweeping jet actuator cannot be influenced by any reasonable external effects; the main driver for its sweeping motion originates from its internal geometry. This is supported by the observation that small differences in supply pressure and geometry do in fact change the sweeping frequency, but strong external effects do not. The collected data also made it possible to study a sweeping jet's mass flow distribution with its large deficit in the center.

8.2 Active Flow Control Applied to a High-Lift Airfoil

This experiments applied active flow control to a high-lift airfoil at three different chord locations. The two active flow control slots close to the leading edge of the airfoil caused a deleterious lift effect by destroying the virtual leading edge of the airfoil resulting in a reduction of vortex lift. It was also shown that for limited mass flow rates, jet-like active flow control devices, such as sweeping jet actuators, are superior to steady blowing actuation. The main reason was found to be that the rule-of-thumb $u_{\text{jet}}/u_{\infty} > 3$ needs to be fulfilled. If this condition is not fulfilled, deleterious lift is generated (independent of vortex lift reduction) due to boundary layer thickening. This concept is picked up again later for the derivation of the extended mass flow coefficient. It was also shown that the main reason for the large lift benefits of the 80% slot seems to be its ability to control and suppress the spanwise cross-flow at the trailing edge, which was later found to be reduction or elimination of the flap separation and the phenomenon of supercirculation. Achieving combinatory effects by using multiple chordwise active flow control devices at the same time seemed to be unattainable for the used airfoil design. While the leading edge slots didn't provide much lift benefit, it could be shown that they might be able to play an important role for pitch moment control.

8.3 The Momentum Input Coefficient C_μ

The momentum input coefficient C_μ has been the dominant similarity parameter in active flow control since its introduction in the 1940s. It represents the momentum that is added by the active flow control devices relative to the freestream flow. The difficulties in its calculation lie in the

fact that the jet exit velocity of the active flow control devices needs to be known. Traditionally, this quantity is either measured, or calculated via an incompressible flow assumption. Due to the unsatisfactory characteristics of both methods, a novel way of its calculation is suggested, that makes use of an isentropic, semi-iterative approach. The new calculation method combines the ease of the incompressible flow assumption with the correctness of the laborious measurements at the jet exit. Employing this method, the relation between the mass flow rate and the momentum coefficient could be analyzed on the basis of isentropy, leading to new insight into the physics of active flow control. It was shown that jet-like actuators undergo several different flow states (subsonic, transitional, underexpansion), which matches the observations of the Schlieren visualizations. Additionally, it could be exemplified that for constant freestream conditions not all values of momentum input can be achieved at given mass flow rates independent of the size of the used actuators; there exists a physical limit that can't be breached by standard means.

8.4 Thermal Active Flow Control

A simple mathematical derivation was provided to justify the concept of thermal active flow control. It was shown that the required mass flow rate to achieve a certain amount of momentum input can be reduced by the square root of the ratio between the jet temperature and the ambient temperature. Next, the concept's validity for real applications was investigated in an experimental bench-top setup. The experiment was not only able to prove the concept, but also validated the theoretical C_μ model that was introduced in the previous chapter. A subsequent wind tunnel test campaign on a vertical tail was conducted to see if a heated C_μ value at a reduced mass flow rate leads to the same lift benefit than its cold equivalent at the nominal mass flow rate. It was demonstrated that thermal active flow control works on lifting aerodynamic surfaces, and that it is possible to reduce the required mass flow rate by the square root of the temperature of the jet flow without a penalty to the lift benefit.

8.5 The Extended Mass Flow Coefficient $\mathcal{M}$

The extended mass flow coefficient $\mathcal{M}$ is introduced as a consequence of the weaknesses of the momentum input coefficient C_μ. It was shown that C_μ is not capable of reliably predicting lift benefits, especially at different freestream velocities and when actuator types had a largely different actuation area, such as sweeping jet actuators versus steady blowing actuation. Experimental data

taken on a vertical tail model in the Lucas Wind Tunnel revealed that the flow coefficient C_Q is one of the main drivers for active flow control. However, previous and current experiments exemplified the importance of the velocity ratio between the jet and the freestream. The flow coefficient and the velocity ratio were then combined to form the net flow coefficient $C_{\mathrm{Q,net}}$. This coefficient showed promising features, but was not able to correctly collapse the thermal active flow control data. As a consequence, it was further adjusted, leading to the extended mass flow coefficient $\mathcal{M}$. In addition, PIV experiments were performed to get a deeper understanding of active flow control with reference to the extended mass flow coefficient. It was shown that active flow control can be divided into three different "states": boundary layer thickening, separation control, and supercirculation. Boundary layer thickening represents a deleterious lift benefit due to the displacement of the boundary layer when the freestream velocity is greater than the jet velocity. In case where separation exists, separation control describes the situation where the entrainment requirements of the shear layer between the high-velocity jet and the much slower separation bubble leads to a reattachment of the flow, and thus creates large lift benefits. Supercirculation is the linear lift increase when the flow is already attached. The fast fluid velocity of the jet accelerates the fluid close to the surface, and as such lowers the pressure on the airfoil. The result is a line-sink effect that pulls the streamlines closer to the aerodynamic surface. This causes an increased circulation around the airfoil, which essentially causes the lift benefits. The limitations of the extended mass flow coefficient as an experiment-based parameter were pointed out, and the difficulties of acquiring reliable dimensionless quantities for active flow control were underlined by a dimensional analysis that revealed the sheer amount of governing variables.

8.6 Future Work

Given the introduction of thermal active flow control and the extended mass flow coefficient, future studies should exploit these two novel concepts. The extended mass flow coefficient opens up the possibility to quantitatively compare vastly different actuator types for their performance benefits. Because the coefficient is mainly based on limited experimental data acquired at Caltech, it will be interesting to see if it will also work for different data sets. Combining these efforts with a comparison of the power coefficient should yield a clear, and distinct picture of which actuator design can be considered as the best. The same goes for chordwise and spanwise actuation location,

the actuator size and spacing. It is very likely that the results will depend on the specific situation. Other aerodynamic variables such as the airfoil thickness, leading edge radius, chamber ratio, aspect ratio, flap deflection, taper, and sweep-back profoundly influence the results of active flow control as well. These variables should be studied in depth, independent of the others to establish a hierarchy of parameters. The experiments on the high-lift airfoil have shown that changing too many variables at once does not necessarily improve the understanding and can cause additional confusion. With more caution, it would be possible to gain a more complete picture of active flow control, its underlying principles, and its possible benefits.

From an application standpoint of view, the short-term goal should be to apply thermal active flow control on current airplanes by using bleed-air from the engines. As a matter of fact, the bleed-air would already be heated up and at flight altitude the temperature ratio between the freezing ambient conditions and the hot engine air would be significantly high, allowing for large lift benefits at moderate mass flow rate requirements. This statement is supported by the fact that the ecoDemonstrator 757 tests were considered successful, even though a majority of the potential of active flow control was wasted by using a heat exchanger to cool the bleed air to protect the structural integrity of the aircraft from thermal effects. Future experiments should investigate if it is really necessary to cool down the air that much, or if it is feasible to avoid it by altering the tail design. Aerodynamic surfaces employing active flow control should be built to withstand thermal effects and reduce thermal losses to achieve the maximum effect. Ultimately, aircraft should be designed with active flow control in mind. This could lead to a revolution in aircraft design, changing the appearance and performance of airplanes tremendously.

Appendix A

Derivation of the Power Coefficient C_Π

From an engineering standpoint, it is interesting to consider how much power an AFC actuation system consumes. The power coefficient C_Π provides an estimation of the power necessary to provide a certain mass flow rate $\dot{m}$ at a certain supply pressure p_{sup}. It can be derived assuming that AFC systems work similar to a compressor system. The first step to derive the power coefficient is to look at the power consumption of a compressor system

$$\Pi = \frac{\dot{m}\,(h_2 - h_1)}{\eta}, \tag{A.1}$$

where h is the specific enthalpy and η the efficiency of the system. Assuming the system works at full efficiency $\eta = 1$, one can simplify

$$\Pi = \dot{m}\,(h_2 - h_1)\,. \tag{A.2}$$

Additionally, one can assume that air is an ideal gas, which then leads to

$$h_2 - h_1 = c_p\,(T_2 - T_1)\,. \tag{A.3}$$

Note that c_p is the heat capacity at constant pressure in this case and not the pressure coefficient. For an ideal gas it further holds that

$$\frac{c_p}{c_v} = \gamma, \tag{A.4}$$

$$c_p - c_v = R. \tag{A.5}$$

Therefore,

$$c_p = \frac{R\gamma}{\gamma - 1}, \tag{A.6}$$

and by using the ideal gas law $p = \rho RT$ at state 1 and combining the previous equations, one gets

$$h_2 - h_1 = \frac{R\gamma}{\gamma - 1}\,(T_2 - T_1) = \frac{p_1\gamma}{\rho_1 T_1\,(\gamma - 1)}\,(T_2 - T_1) = \frac{p_1\gamma}{\rho_1\,(\gamma - 1)}\left(\frac{T_2}{T_1} - 1\right). \tag{A.7}$$

By applying isentropic flow relations to the temperature ratio

$$h_2 - h_1 = \frac{p_1\gamma}{\rho_1\,(\gamma - 1)}\left[\left(\frac{p_2}{p_1}\right)^{\frac{\gamma-1}{\gamma}} - 1\right]. \tag{A.8}$$

By plugging Eq. (A.8) back into the power formulation of Eq. (A.2), and by assuming that state 1 corresponds to ambient conditions while state 2 corresponds to the supply conditions, one arrives at

$$\Pi = \frac{\dot{m} p_\infty \gamma}{\rho_\infty (\gamma - 1)} \left[\left(\frac{p_{\text{sup}}}{p_\infty} \right)^{\frac{\gamma-1}{\gamma}} - 1 \right]. \tag{A.9}$$

To get the non-dimensional power coefficient the compressor power is divided by the power of the freestream flow that could theoretically act on a wing:

$$C_\Pi = \frac{\frac{\gamma}{\gamma-1} \frac{p_\infty}{\rho_\infty} \dot{m} \left[\left(\frac{p_{\text{sup}}}{p_\infty} \right)^{\frac{\gamma-1}{\gamma}} - 1 \right]}{\frac{1}{2} \rho_\infty u_\infty^3 S} = \frac{\frac{\gamma}{\gamma-1} p_\infty \dot{m} \left[\left(\frac{p_{\text{sup}}}{p_\infty} \right)^{\frac{\gamma-1}{\gamma}} - 1 \right]}{\frac{1}{2} \rho_\infty^2 u_\infty^3 S}. \tag{A.10}$$

Appendix B

Measurement Techniques: Their Advantages and Disadvantages

This chapter introduces the different experimental measurement techniques that can be applied to study the field of AFC. Each paragraph dives into another technique listing its advantages, disadvantages, and applicability. Based on these findings, some of these techniques are used frequently while others are not (yet) practical.

Force Balance Measurements: These measurements are used for almost every single experiment. They provide hard quantifiable evidence of what works and what doesn't. It is also the technique that exactly measures the relevant parameters AFC tries to improve: lift, drag, and pitch moment. However, it can't yield any detailed insight as it is not capable of measuring any transient behavior, and the forces are always integrated over the whole model without the option of knowing where they originated from.

Hot Wire (Thermal Anemometer): This technique could provide accurate data as well as providing a decent spatial and transient resolution, yet there are two major drawbacks. First, the hot wire would need to be calibrated from low velocities in the range of 1 m/s to sonic or even supersonic velocities. There are not a lot of facilities that can provide this range of velocities for hot wire calibration. Certainly, there are none of these at Caltech. The second disadvantage is the intrusive nature of hot wire measurements. While this characteristic is negligible in a freestream environment or for stable flow conditions, the interaction of the boundary layer-freestream-jet trinity is sensitive to small deviations. Putting a hot wire next to a jet outlet might change its effect on the boundary layer and vice versa.

Pressure Taps: This technique gives a lot of insight into what is happening on the surface of a model. Compared to hot wires, its intrusive character is small. However, the technique has a limited temporal and spatial resolution, and can't provide information beyond the surface. The

limited temporal resolution is specifically a disadvantage when measuring sweeping jet actuators considering their frequency on the order of 1 kHz. Assuming the interaction of flows rapidly change near the surface, this technique won't be able to catch all the relevant flow features.

Pressure Sensitive Paint (PSP): This technique is quite new and is still in continuous development. While it has an extremely high spatial resolution (limited only by the camera's pixel resolution) the temporal resolution is still limited. Additionally, the technique currently struggles to work efficiently and reliable at low freestream velocities of less than 50 m/s. Below this velocity the accuracy drops rather quickly and the quantitative measurements become qualitative measurements. This might still be helpful in certain situations. Also, because there is so much interest and development in this technique, the accuracy at low freestream velocities will most likely increase significantly over the next few years. Thus, it is definitely worthwhile to keep an eye on this technique.

Schlieren: Visualizing the flow via Schlieren can give a lot of insight into flow motion and its interactions. Seeing an otherwise invisible flow is essential as it can make complicated things easier to understand if key features can be distinguished. However, Schlieren is a qualitative technique and can not provide qualitative data in a simple manner. Nevertheless, it's detailed visualization of the internal flow structures of a sweeping jet actuator helped a lot to understand its functionality (see Chapter 2). Unfortunately, Schlieren has a limited scalability. The observation volume is directly linked to the lens (or mirror) diameter due to the need for collimated light. Large diameter lenses (and mirrors) have an exponential growing cost to a point, where there are not affordable anymore except for a space telescope with billions of dollars of funding. This is one of the reasons why Schlieren is rarely used in a large wind tunnel setup. An additional problem is the need for a straight, unobstructed optical path through the test section, which sometimes is difficult to achieve without the use of mirrors inside the test section (which then obstruct the flow). Additionally, the windows through which the Schlieren observes the test section would need to be at optical quality as well to not negatively affect the image.

Digital Particle Image Velocimetry (DPIV): Nowadays, DPIV is the state of the art for quantitative fluid measurements. Its temporal and spatial resolution depend mainly on the laser and camera setup. Highly temporal-resolved data can be achieved with a continuous laser source and

a high-speed camera. However, while this works well in water, doing these measurements in air is much more challenging. First, the particles required for seeding can't be solid in air and are usually a liquid-gas-combination such as a helium or a soap bubble. These particles are much more likely to be destroyed during the experimental process than the solid particles used in water. As a consequence, a continuous supply of particles is required that needs to be tuned based on the experiment. Second, due to the fact that the particles in air are normally much smaller than comparable ones in air, the laser power required is much higher. In most setups this prohibits the use of continuous lasers, and therefore limits the temporal resolution because a pulsed laser is necessary. Also DPIV is a two-dimensional technique and can't reliably capture three-dimensional phenomena. However, compared to pressure taps and pressure sensitive paints it has the advantage that it is not bound to the wing surface and the interrogation plane can freely be chosen in space.

Defocusing Digital Particle Image Velocimetry (DDPIV): DDPIV is very similar to DPIV. But instead of being a two-dimensional technique, it uses additional cameras to extend into the third dimension preserving the high spatial resolution. In theory this is a simple opto-mathematical exercise, but in reality the problems of DPIV are intensified: the technique requires an illuminated volume instead of a mere sheet, asking for even more laser power, to a point where the cost of the laser is unaffordable. The large velocity differences between boundary layer, freestream, and jet velocity pose another problem that is more severe than in DPIV. Multiple laser shots are now needed to account for the differences, requiring not only a powerful, but also a multi-shot laser or multiple laser that can be synchronized. Cameras with multi-frame readout, such as high-speed cameras are scarce or expensive. Additionally, if the jet itself has no seeding particles, meaning it does not have its separate seeding supply, it will create "holes" in the flow that can't be quantified during the analysis. This obviously applies to DPIV as well but to a much lesser extent. The seeding density of the flow is even more critical and needs to be adjusted with great care. The sum of these problems make it near impossible to do three-dimensional DPIV inside a large scale wind tunnel on an AFC wing model. However, the mentioned issues should resolve themselves within a few years with more powerful and cheaper lasers with multi-shot capabilities to come. The created need for appropriate cameras will make them available as well.

Appendix C

Selection of CAD Drawings

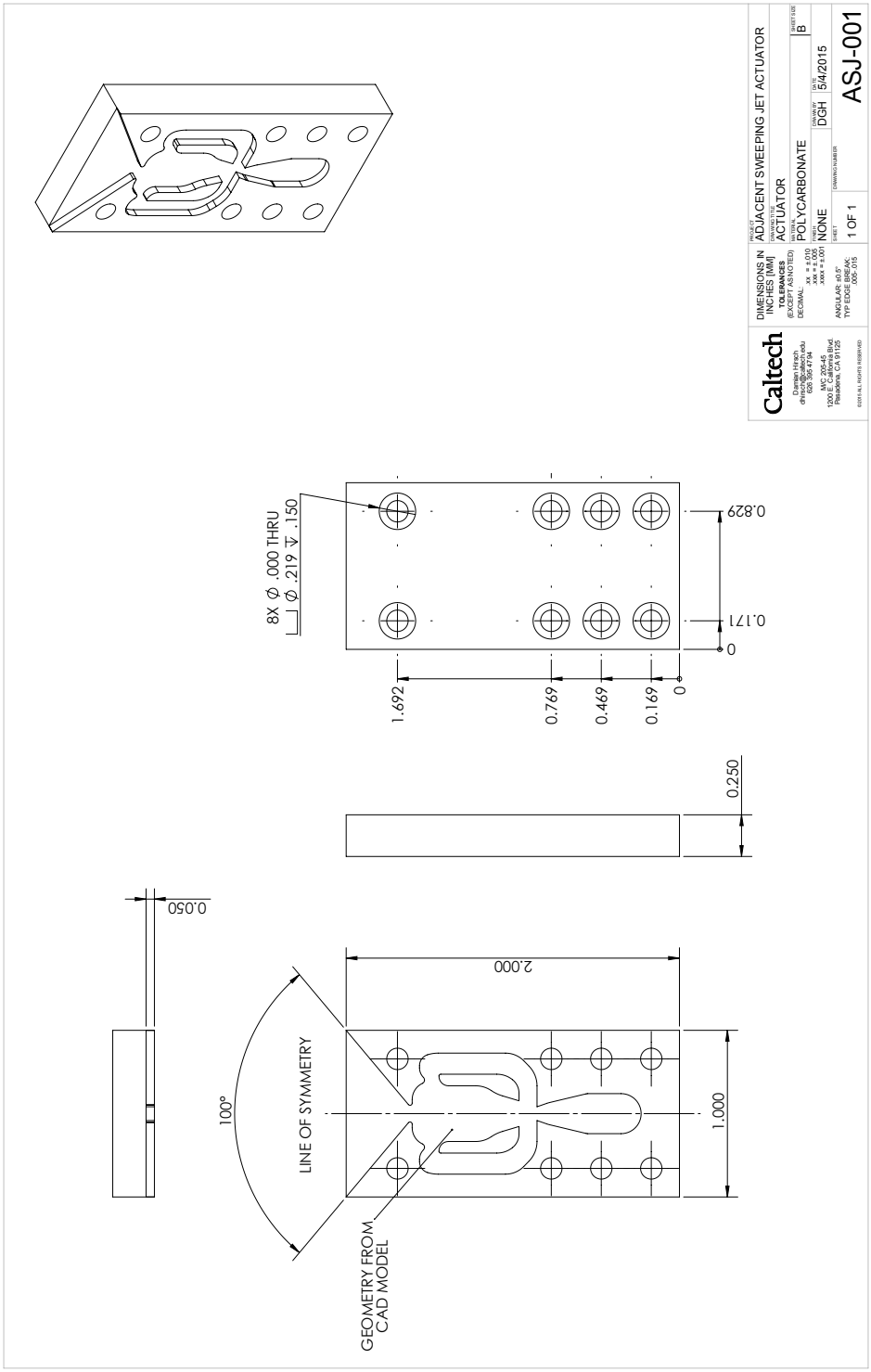

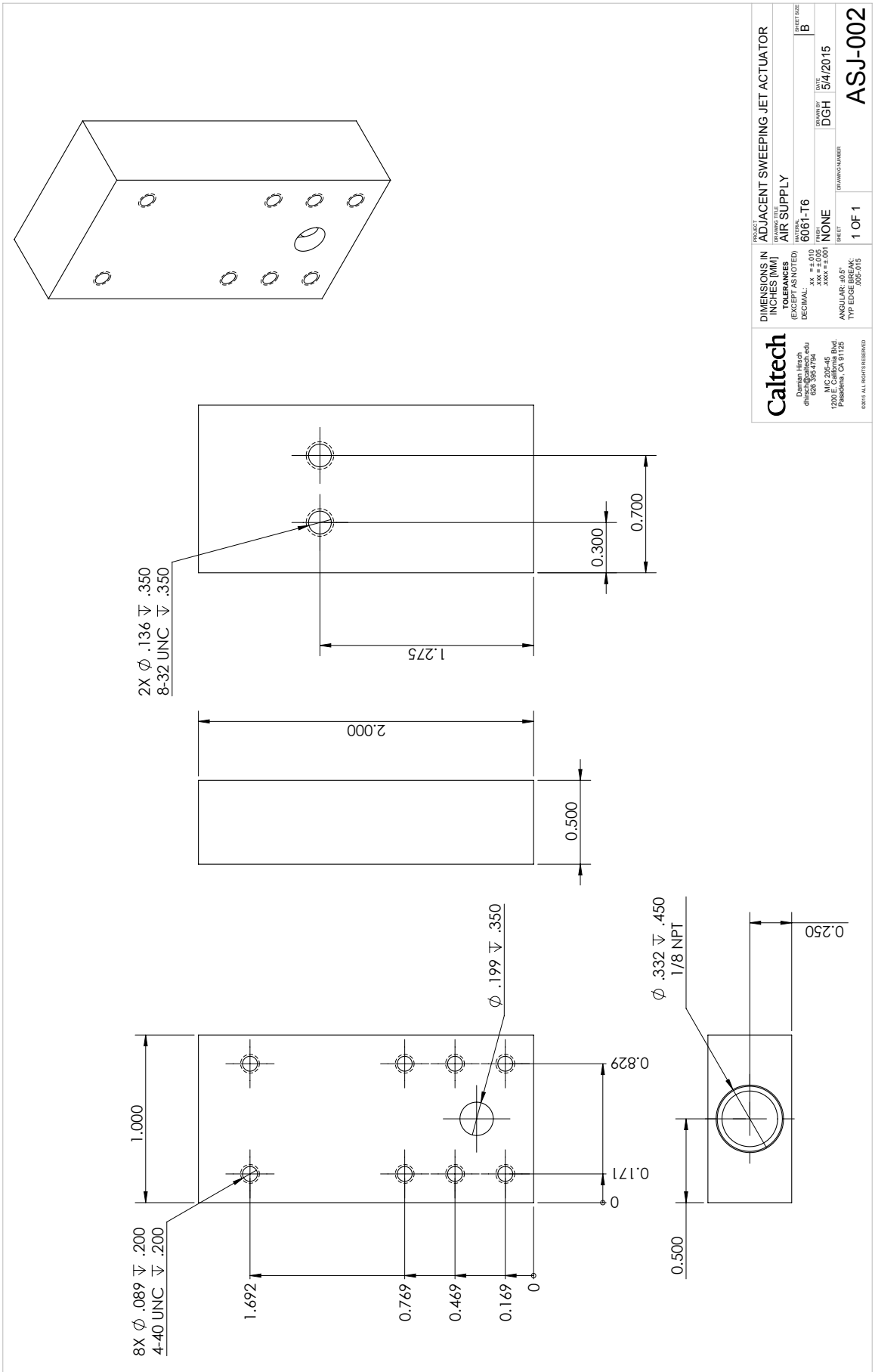
PROJECT
ADJACENT SWEEPING JET ACTUATOR
DRAWING TITLE
AIR SUPPLY
SHEET SIZE
B
MATERIAL
6061-T6
FINISH
NONE
DRAWN BY
DGH
DATE
5/4/2015
SHEET
1 OF 1
DRAWING NUMBER
ASJ-002
DIMENSIONS IN INCHES [MM]
TOLERANCES
(EXCEPT AS NOTED)
DECIMAL:
XX = ± .010
XXX = ± .005
XXXX = ± .001
ANGULAR: ±0.5°
TYP EDGE BREAK:
.005-.015
Caltech
Damian Hinch
dhinch@caltech.edu
626 395 4794
MC 205-45
1200 E. California Blvd.
Pasadena , CA 91125
©2015 ALL RIGHTS RESERVED
2X ∅ .136 ∓ .350
8-32 UNC ∓ .350
0.700
0.300
1.275
2.000
0.500
∅ .199 ∓ .350
1.000
0.829
0.171
0
8X ∅ .089 ∓ .200
4-40 UNC ∓ .200
1.692
0.769
0.469
0.169
0
∅ .332 ∓ .450
1/8 NPT
0.250
0.500

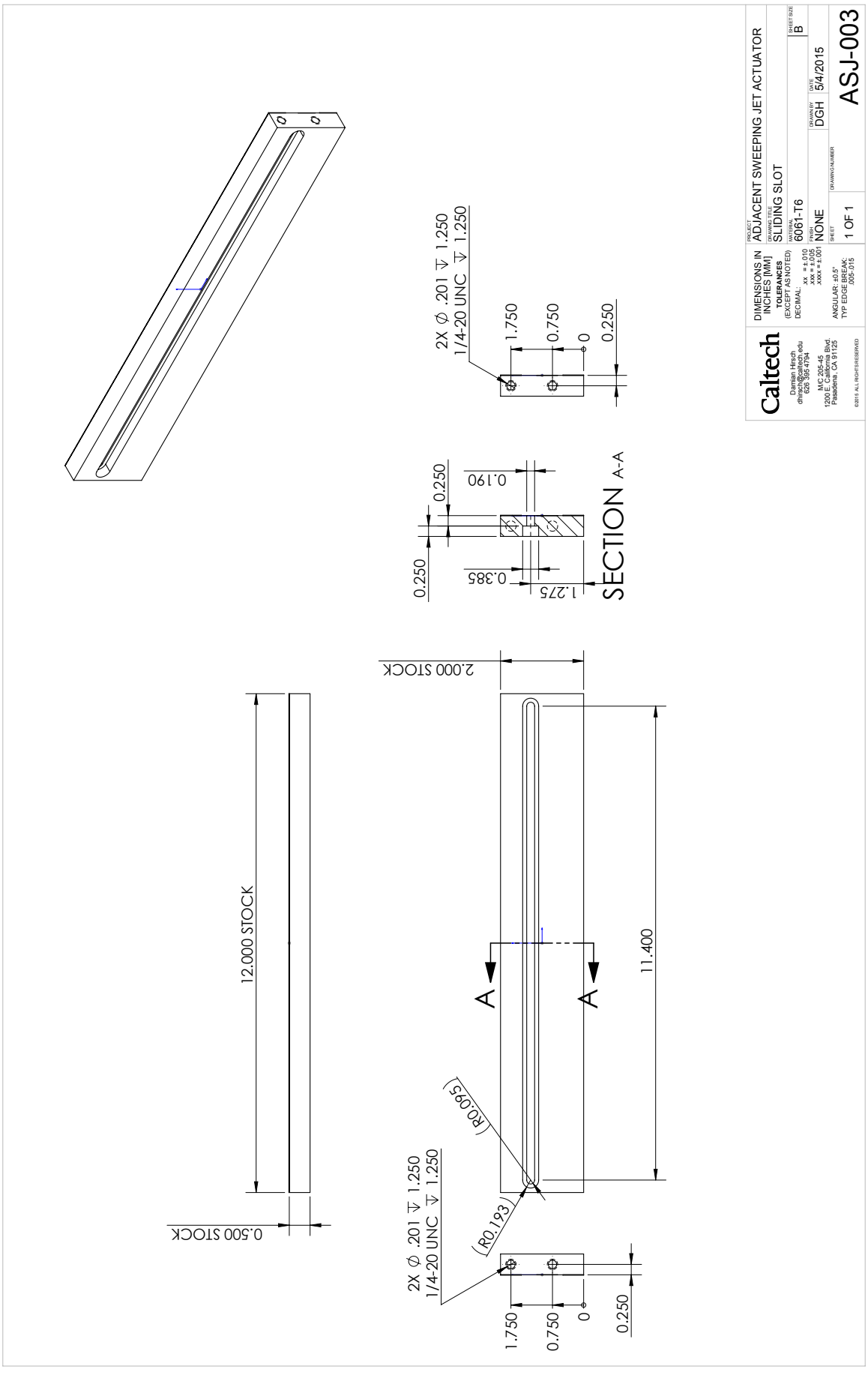
Caltech
Damian Hinsch
dhinsch@caltech.edu
626 395 4794
MC 205-45
1200 E. California Blvd.
Pasadena, CA 91125
©2015 ALL RIGHTS RESERVED
DIMENSIONS IN INCHES [MM]
TOLERANCES
(EXCEPT AS NOTED)
DECIMAL: .x = ±.010
.xx = ±.005
.xxx = ±.001
ANGULAR: ±0.5°
TYP EDGE BREAK: .005-.015
PROJECT
ADJACENT SWEEPING JET ACTUATOR
DRAWING TITLE
SLIDING SLOT
MATERIAL
6061-T6
FINISH
NONE
SHEET
1 OF 1
DRAWING NUMBER
ASJ-003
DRAWN BY
DGH
DATE
5/4/2015
SHEET SIZE
B
12.000 STOCK
0.500 STOCK
2.000 STOCK
11.400
A
A
R0.095
R0.193
2X ∅ .201 ↧ 1.250
1/4-20 UNC ↧ 1.250
1.750
0.750
0
0.250
SECTION A-A
0.190
0.385
1.275

TAG	X LOC	Y LOC	SIZE
A1	7.937	0.705	⌀ 0.129 THRU ALL ⌵ ⌀ 0.179 X 90.00°, NEAR SIDE
A2	7.929	1.519	
A3	7.797	0.156	
A4	7.406	1.889	
A5	6.597	0.156	
A6	5.906	1.874	
A7	5.397	0.156	
A8	4.406	1.860	
A9	4.397	0.156	
A10	3.471	0.156	
A11	2.906	1.845	
A12	2.546	0.156	
A13	1.406	1.830	
A14	1.346	0.156	
A15	0.148	1.818	
A16	0.148	0.220	
B1	6.172	0.608	⌀ 0.070 ↧ 0.226 2-56 UNC ↧ 0.172
B2	5.797	0.983	
B3	3.297	0.968	
B4	2.922	0.593	
B5	1.422	0.772	

TAG	X LOC	Y LOC	SIZE
1	0.666	0.834	⌀ 0.219 THRU ALL
2	2.166	0.849	
3	3.666	0.864	
4	5.166	0.879	
5	6.666	0.894	

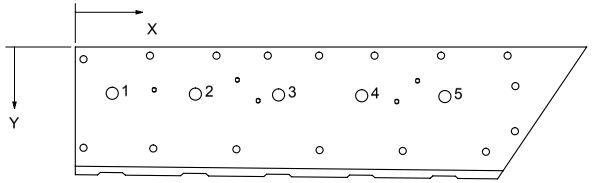

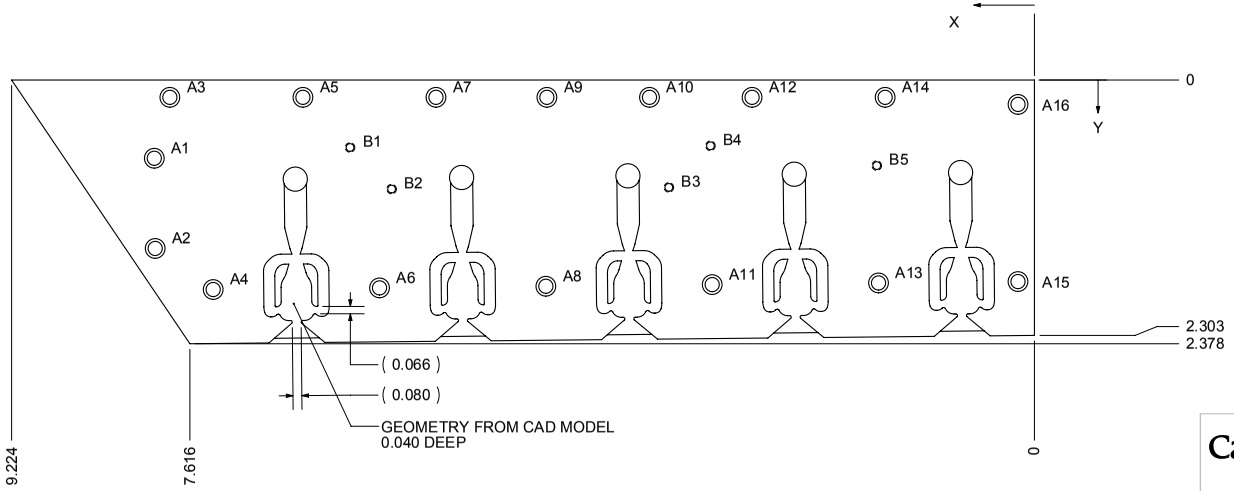

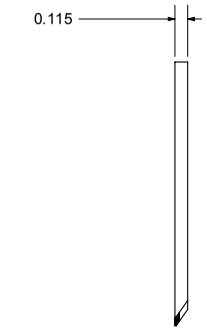

REV.	DESCRIPTION	DATE
A	INITIAL RELEASE	01/23/2012

Caltech
Emilio Graff
Lucas AWWT
ecg@caltech.edu
626 395 4795
M/C 205-45
1200 E. California Blvd.
Pasadena, CA 91125

DIMENSIONS IN INCHES [MM]
TOLERANCES (EXCEPT AS NOTED)
DECIMAL:
xx = ±.010
.xxx = ±.005
.xxxx = ±.001
ANGULAR: ±0.5°
TYP EDGE BREAK: .005-.015

PROJECT: TRAILING EDGE MODULES
DRAWING TITLE: ROOT MODULE ACTUATOR INSERT, 40x80
MATERIAL: 6061
SHEET SIZE: B
FINISH: TYPE II ANODIZE
DRAWN BY: ECG
DATE: 1/23/2012
SHEET: 1 OF 1
DRAWING NUMBER: TEM-01-002-A

TAG	X LOC	Y LOC	SIZE
A1	0.187	1.627	∅ 0.129 THRU ALL ⌵ ∅ 0.179 X 90.00°, NEAR SIDE
A2	0.187	0.218	
A3	1.310	0.156	
A4	1.591	1.800	
A5	2.810	0.156	
A6	3.091	1.785	
A7	4.310	0.156	
A8	4.591	1.771	
A9	5.810	0.156	
A10	6.091	1.756	
A11	7.310	0.156	
A12	7.591	1.741	
A13	8.810	0.156	
A14	9.091	1.726	
A15	10.310	0.156	
A16	10.321	1.526	
B1	1.501	0.557	∅ 0.070 THRU ALL 2-56 UNC THRU ALL
B2	1.876	0.932	
B3	5.626	0.874	
B4	6.001	0.499	
B5	8.751	0.455	
B6	9.126	0.830	

TAG	X LOC	Y LOC	SIZE
1	9.831	0.731	∅ 0.219 THRU ALL
2	8.331	0.745	
3	6.831	0.760	
4	5.331	0.775	
5	3.831	0.790	
6	2.331	0.805	
7	0.832	0.820	

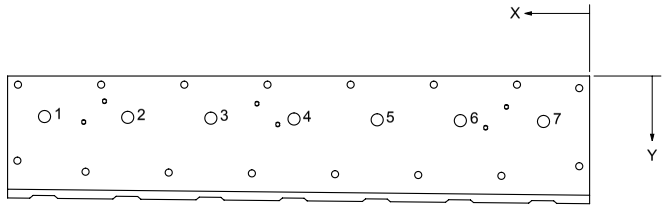

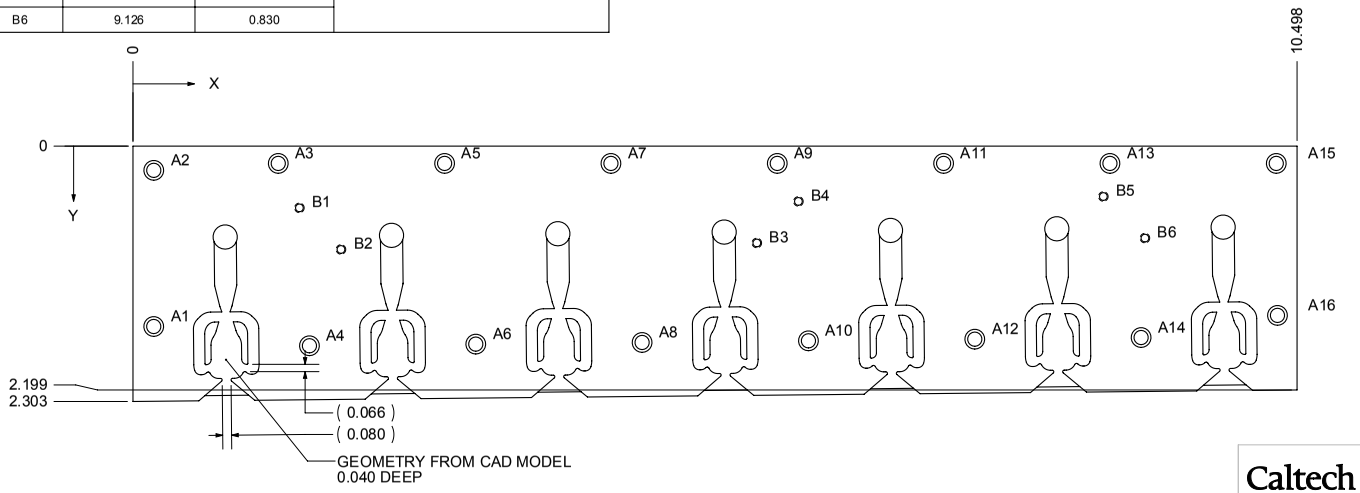

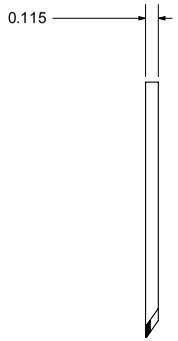

REV.	DESCRIPTION	DATE
A	INITIAL RELEASE	01/23/2012

Caltech

Emilio Graff
Lucas AWWT
ecg@caltech.edu
626 395 4795

M/C 205-45
1200 E. California Blvd.
Pasadena, CA 91125

DIMENSIONS IN INCHES [MM]
TOLERANCES (EXCEPT AS NOTED)
DECIMAL:
.xx = ±.010
.xxx = ±.005
.xxxx = ±.001
ANGULAR: ±0.5°
TYP EDGE BREAK: .005-.015

PROJECT: TRAILING EDGE MODULES
DRAWING TITLE: SECOND MODULE ACTUATOR INSERT, 40x80
MATERIAL: 6061
SHEET SIZE: B
FINISH: TYPE II ANODIZE
DRAWN BY: ECG
DATE: 1/23/2012
SHEET: 1 OF 1
DRAWING NUMBER: TEM-02-002-A

TAG	X LOC	Y LOC	SIZE
A1	0.187	1.523	Ø 0.129 THRU ALL ⌵ Ø 0.179 X 90.00°, NEAR SIDE
A2	0.187	0.156	
A3	1.560	0.156	
A4	1.591	1.696	
A5	3.060	0.156	
A6	3.091	1.682	
A7	4.560	0.156	
A8	4.591	1.667	
A9	6.060	0.156	
A10	6.091	1.652	
A11	7.560	0.156	
A12	7.590	1.637	
A13	9.060	0.156	
A14	9.090	1.622	
A15	10.560	0.156	
A16	10.561	1.483	
B1	1.501	0.519	Ø 0.070 THRU ALL 2-56 UNC THRU ALL
B2	1.876	0.894	
B3	4.626	0.880	
B4	5.001	0.505	
B5	9.001	0.486	
B6	9.376	0.861	

TAG	X LOC	Y LOC	SIZE
1	9.831	0.627	Ø 0.219 THRU ALL
2	8.331	0.642	
3	6.831	0.656	
4	5.331	0.671	
5	3.831	0.686	
6	2.331	0.701	
7	0.831	0.716	

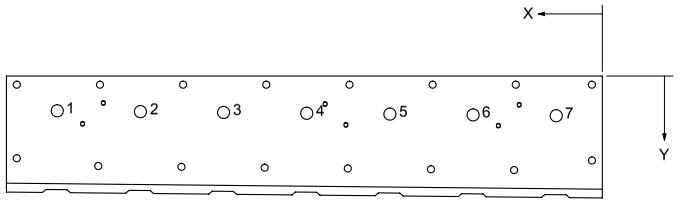

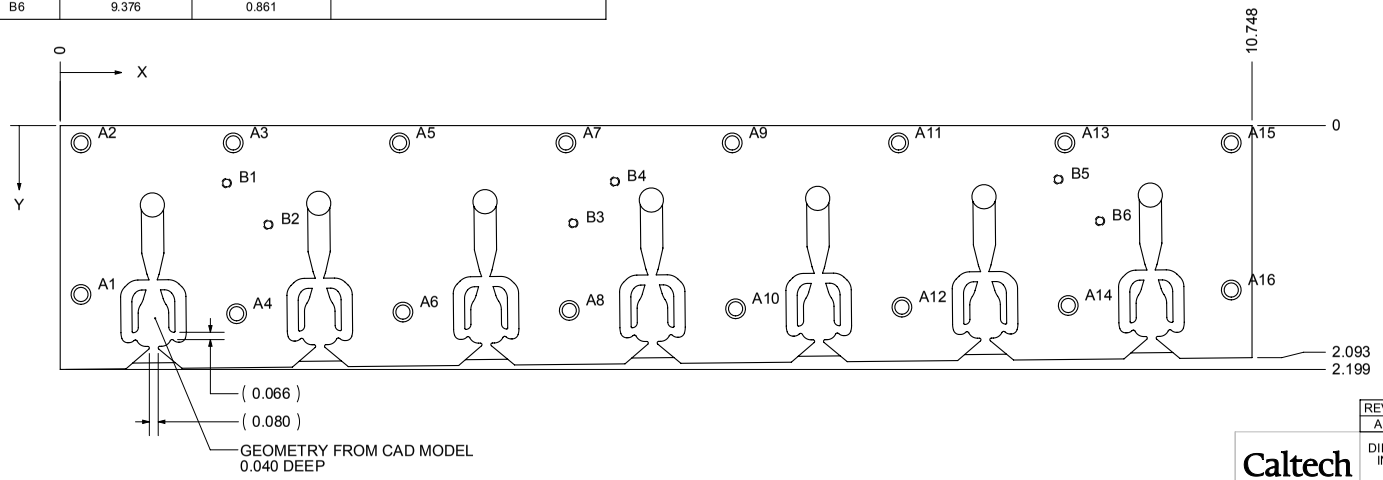

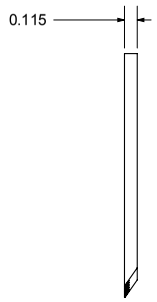

REV.	DESCRIPTION	DATE
A	INITIAL RELEASE	01/23/2012

Caltech
Emilio Graff
Lucas AWWT
ecg@caltech.edu
626 395 4795
M/C 205-45
1200 E. California Blvd.
Pasadena, CA 91125

DIMENSIONS IN INCHES [MM]
TOLERANCES (EXCEPT AS NOTED)
DECIMAL:
xx = ±.010
.xxx = ±.005
.xxxx = ±.001
ANGULAR: ±0.5°
TYP EDGE BREAK: .005-.015

PROJECT: TRAILING EDGE MODULES
DRAWING TITLE: THIRD MODULE ACTUATOR INSERT, 40x80
MATERIAL: 6061
SHEET SIZE: B
FINISH: TYPE II ANODIZE
DRAWN BY: ECG
DATE: 1/23/2012
SHEET: 1 OF 1
DRAWING NUMBER: TEM-03-002-A

TAG	X LOC	Y LOC	SIZE
A1	0.150	1.604	⌀ 0.129 THRU ALL ⌵ ⌀ 0.179 X 90.00°, NEAR SIDE
A2	0.150	0.154	
A3	1.330	0.154	
A4	1.340	1.593	
A5	2.830	0.154	
A6	2.840	1.578	
A7	4.330	0.154	
A8	4.340	1.563	
A9	5.830	0.155	
A10	5.840	1.548	
A11	7.330	0.155	
A12	7.340	1.533	
A13	8.830	0.155	
A14	8.840	1.518	
A15	10.010	0.155	
A16	10.048	1.506	
B1	1.250	0.466	⌀ 0.070 THRU ALL 2-56 UNC THRU ALL
B2	1.624	0.841	
B3	5.374	0.822	
B4	5.750	0.447	
B5	8.750	0.431	
B6	9.125	0.806	

TAG	X LOC	Y LOC	SIZE
1	9.580	0.523	⌀ 0.219 THRU ALL
2	8.080	0.538	
3	6.580	0.553	
4	5.080	0.567	
5	3.580	0.582	
6	2.080	0.597	
7	0.580	0.612	

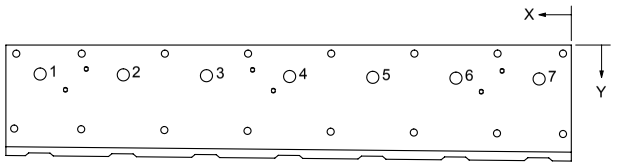

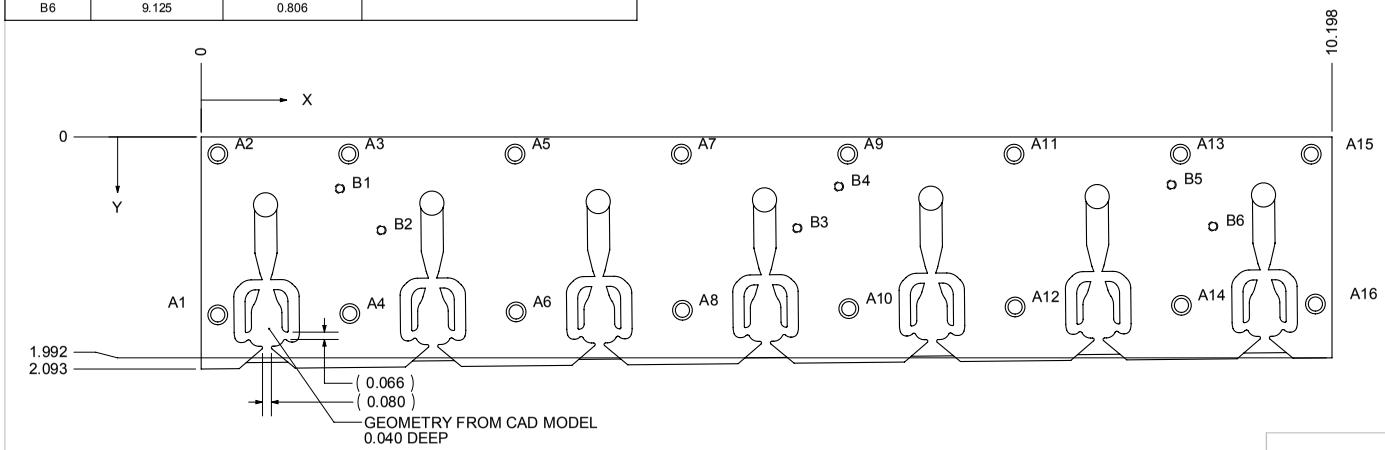

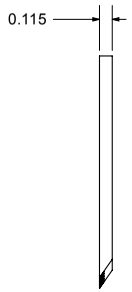

REV.	DESCRIPTION	DATE
A	INITIAL RELEASE	01/23/2012

Caltech

Emilio Graff
Lucas AWWT
ecg@caltech.edu
626 395 4795

M/C 205-45
1200 E. California Blvd.
Pasadena, CA 91125

DIMENSIONS IN INCHES [MM]
TOLERANCES (EXCEPT AS NOTED)
DECIMAL:
.xx = ±.010
.xxx = ±.005
.xxxx = ±.001
ANGULAR: ±0.5°
TYP EDGE BREAK: .005-.015

PROJECT: TRAILING EDGE MODULES
DRAWING TITLE: FOURTH MODULE ACTUATOR INSERT, 40x80
MATERIAL: 6061
SHEET SIZE: B
FINISH: TYPE II ANODIZE
DRAWN BY: ECG
DATE: 1/23/2012
SHEET: 1 OF 1
DRAWING NUMBER: TEM-04-002-A

TAG	X LOC	Y LOC	SIZE
A1	0.187	0.209	∅ 0.129 THRU ALL ⌵ ∅ 0.179 X 90.00°, NEAR SIDE
A2	0.312	1.502	
A3	1.423	0.156	
A4	1.640	1.489	
A5	2.923	0.156	
A6	3.140	1.474	
A7	4.523	0.156	
A8	4.640	1.459	
A9	5.923	0.156	
A10	6.139	1.444	
A11	7.423	0.156	
A12	7.639	1.429	
A13	8.658	0.156	
A14	8.871	1.417	
A15	8.890	0.785	
B1	1.500	0.415	∅ 0.070 THRU ALL 2-56 UNC THRU ALL
B2	1.875	0.790	
B3	4.375	0.776	
B4	4.750	0.401	
B5	7.500	0.386	
B6	7.875	0.761	

TAG	X LOC	Y LOC	SIZE
1	8.380	0.434	∅ 0.219 ↧ 1.525
2	6.880	0.449	
3	5.380	0.464	
4	3.880	0.478	
5	2.380	0.493	
6	0.880	0.508	

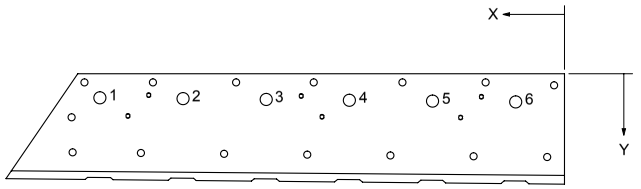

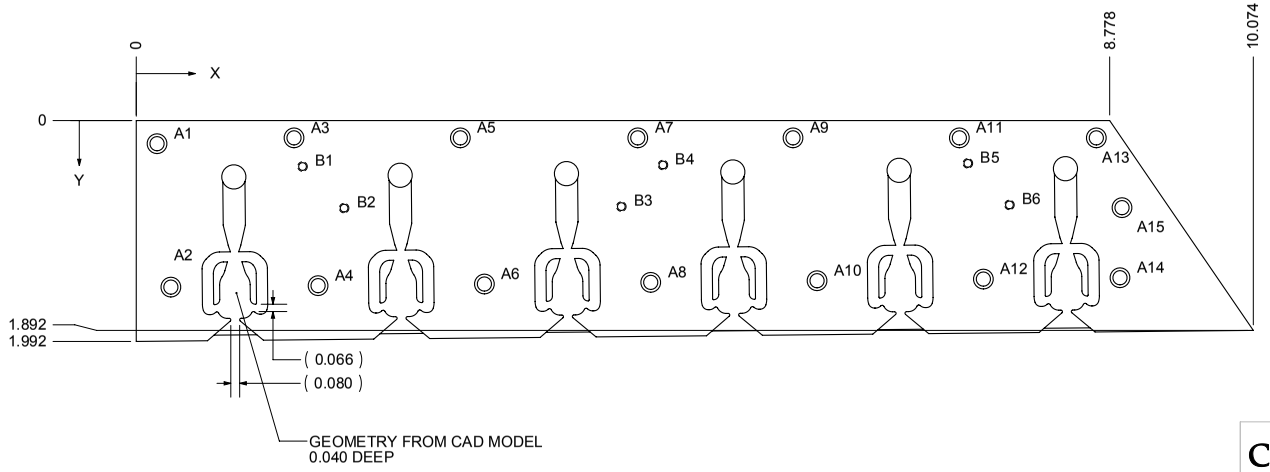

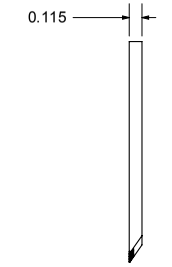

REV.	DESCRIPTION	DATE
A	INITIAL RELEASE	01/23/2012
B	CORRECTED DRAWING TITLE	02/12/2012

Caltech
Emilio Graff
Lucas AWWT
ecg@caltech.edu
626 395 4795
M/C 205-45
1200 E. California Blvd.
Pasadena, CA 91125

DIMENSIONS IN INCHES [MM]
TOLERANCES (EXCEPT AS NOTED)
DECIMAL:
xx = ±.010
.xxx = ±.005
.xxxx = ±.001
ANGULAR: ±0.5°
TYP EDGE BREAK: .005-.015

PROJECT: TRAILING EDGE MODULES
DRAWING TITLE: TIP MODULE ACTUATOR INSERT, 40x80
MATERIAL: 6061
SHEET SIZE: B
FINISH: TYPE II ANODIZE
DRAWN BY: ECG
DATE: 1/23/2012
SHEET: 1 OF 1
DRAWING NUMBER: TEM-05-002-B

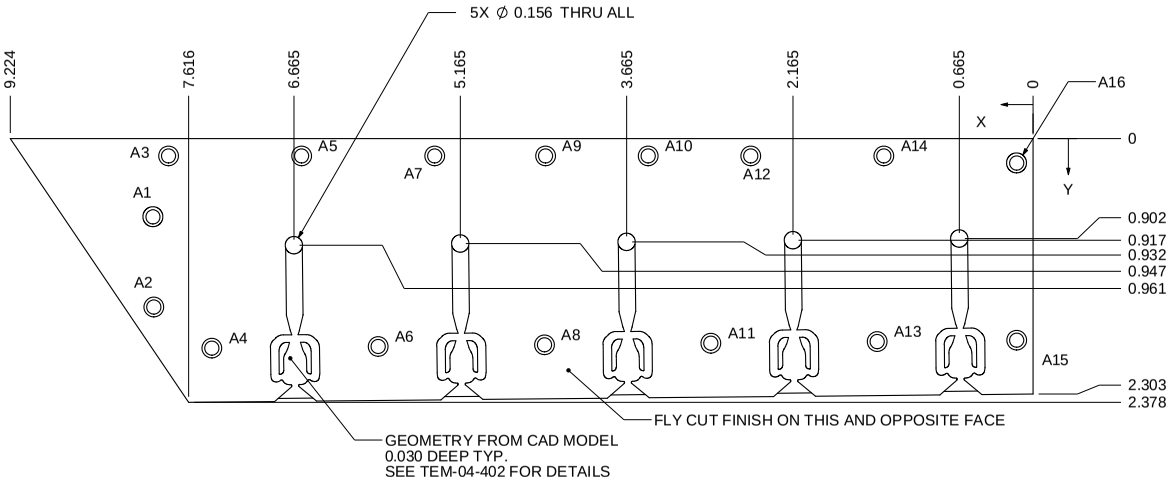

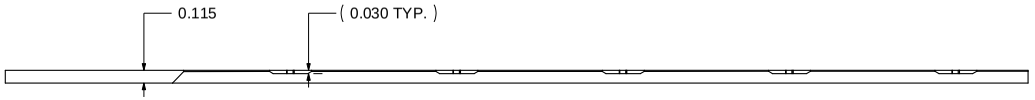

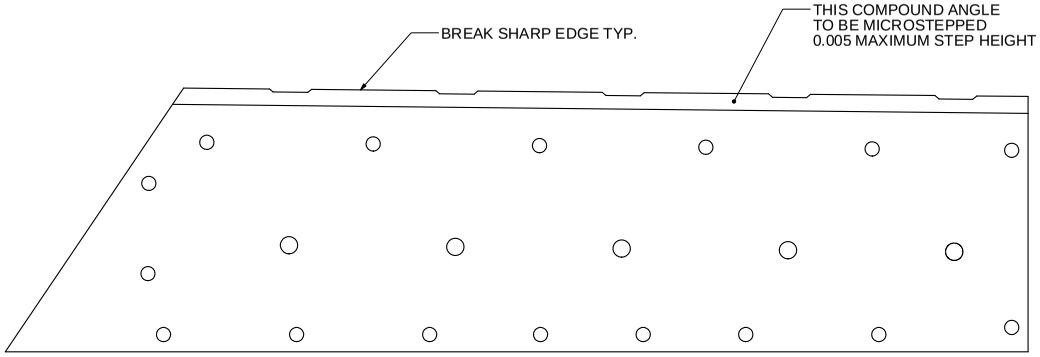

TAG	X LOC	Y LOC	SIZE
A1	7.937	0.705	∅ 0.129 THRU ALL ⌵ ∅ 0.179 X 90.000°, NEAR SIDE
A2	7.929	1.519	
A3	7.797	0.156	
A4	7.406	1.889	
A5	6.597	0.156	
A6	5.906	1.874	
A7	5.397	0.156	
A8	4.406	1.860	
A9	4.397	0.156	
A10	3.471	0.156	
A11	2.906	1.845	
A12	2.546	0.156	
A13	1.406	1.830	
A14	1.346	0.156	
A15	0.148	1.818	
A16	0.148	0.220	

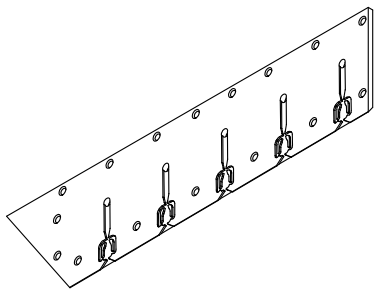

REV.	DESCRIPTION	DATE
A	INITIAL RELEASE	08/14/2012

Caltech

Emilio Graff
Lucas AWWT
ecg@caltech.edu
626 395 4795

M/C 205-45
1200 E. California Blvd.
Pasadena, CA 91125

DIMENSIONS IN INCHES [MM]
TOLERANCES
(EXCEPT AS NOTED)
DECIMAL:
.xx = ±.010
.xxx = ±.005
.xxxx = ±.001
ANGULAR: ±0.5°
TYP EDGE BREAK: .005-.015

PROJECT: TRAILING EDGE MODULES
DRAWING TITLE: ROOT MODULE INSERT, 30x60
MATERIAL: 6061
SHEET SIZE: B
FINISH: NONE
DRAWN BY: ECG
DATE: 08/14/2012
SHEET: 1 OF 1
DRAWING NUMBER: TEM-01-402-A

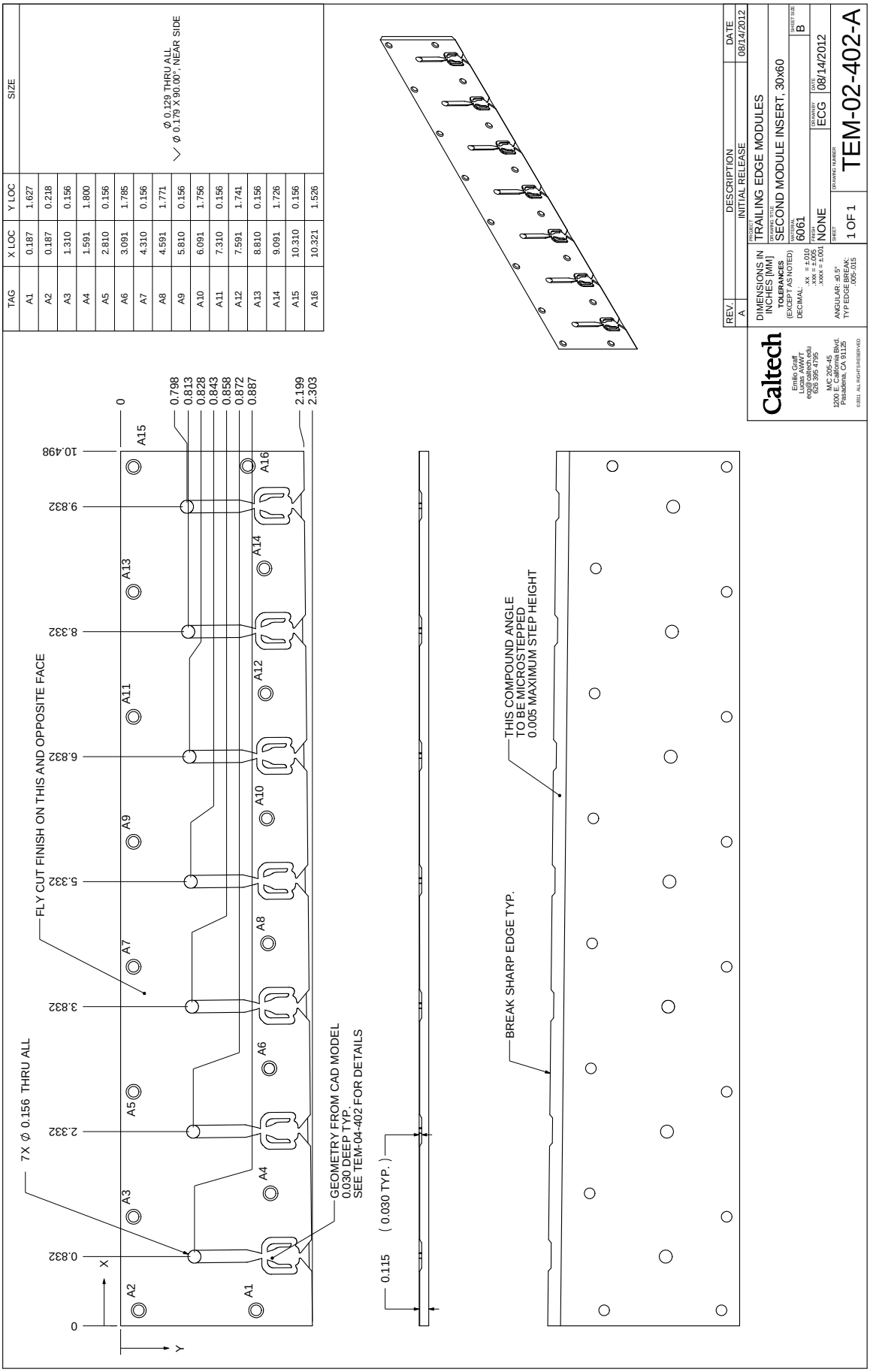
TAG | X LOC | Y LOC | SIZE
A1 | 0.187 | 1.627
A2 | 0.187 | 0.218
A3 | 1.310 | 0.156
A4 | 1.591 | 1.800
A5 | 2.810 | 0.156
A6 | 3.091 | 1.785
A7 | 4.310 | 0.156
A8 | 4.591 | 1.771
A9 | 5.810 | 0.156
A10 | 6.091 | 1.756
A11 | 7.310 | 0.156
A12 | 7.591 | 1.741
A13 | 8.810 | 0.156
A14 | 9.091 | 1.726
A15 | 10.310 | 0.156
A16 | 10.321 | 1.526
Ø 0.129 THRU ALL
Ø 0.179 X 90.00°, NEAR SIDE
REV. | DESCRIPTION | DATE
A | INITIAL RELEASE | 08/14/2012
Caltech
Emilio Graff
Lucas AWVI
egg@caltech.edu
626 395 4795
1200 MC 205-45
E. California Blvd.
Pasadena, CA 91125
©2011 ALL RIGHTS RESERVED
DIMENSIONS IN INCHES [MM]
TOLERANCES
(EXCEPT AS NOTED)
DECIMAL:
XX = ±.010
XXX = ±.005
XXXX = ±.001
ANGULAR: ±0.5°
TYP EDGE BREAK:
.005-.015
PROJECT: TRAILING EDGE MODULES
DRAWING TITLE: SECOND MODULE INSERT, 30x60
MATERIAL: 6061
FINISH: NONE
SHEET: 1 OF 1
DRAWN BY: ECG
DATE: 08/14/2012
SHEET SIZE: B
DRAWING NUMBER: TEM-02-402-A
7X Ø 0.156 THRU ALL
FLY CUT FINISH ON THIS AND OPPOSITE FACE
GEOMETRY FROM CAD MODEL
0.030 DEEP TYP.
SEE TEM-04-402 FOR DETAILS
(0.030 TYP.)
0.115
BREAK SHARP EDGE TYP.
THIS COMPOUND ANGLE
TO BE MICROSTEPPED
0.005 MAXIMUM STEP HEIGHT
X
Y
0
0.832
2.332
3.832
5.332
6.832
8.332
9.832
10.498
0.798
0.813
0.828
0.843
0.858
0.872
0.887
2.199
2.303
A1
A2
A3
A4
A5
A6
A7
A8
A9
A10
A11
A12
A13
A14
A15
A16

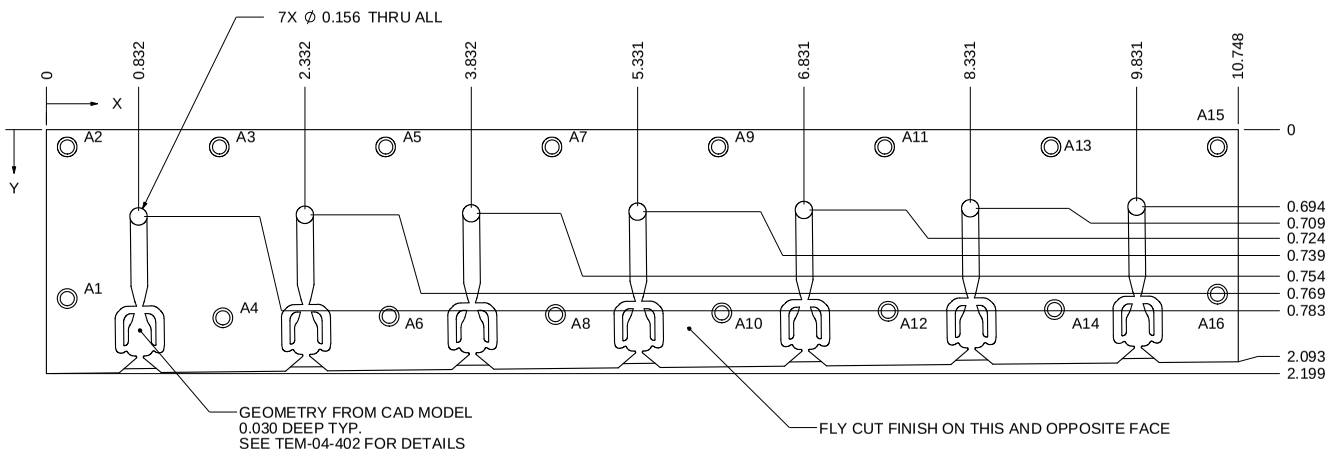

TAG	X LOC	Y LOC	SIZE
A1	0.187	1.523	∅ 0.129 THRU ALL ⌵ ∅ 0.179 X 90.000°, NEAR SIDE
A2	0.187	0.156	
A3	1.560	0.156	
A4	1.591	1.696	
A5	3.060	0.156	
A6	3.091	1.682	
A7	4.560	0.156	
A8	4.591	1.667	
A9	6.060	0.156	
A10	6.091	1.652	
A11	7.560	0.156	
A12	7.590	1.637	
A13	9.060	0.156	
A14	9.090	1.622	
A15	10.560	0.156	
A16	10.561	1.483	

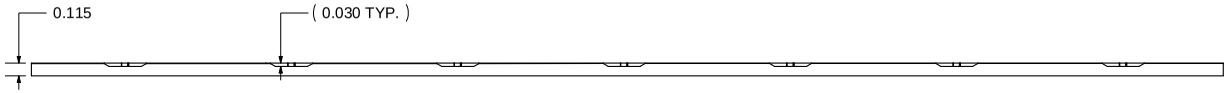

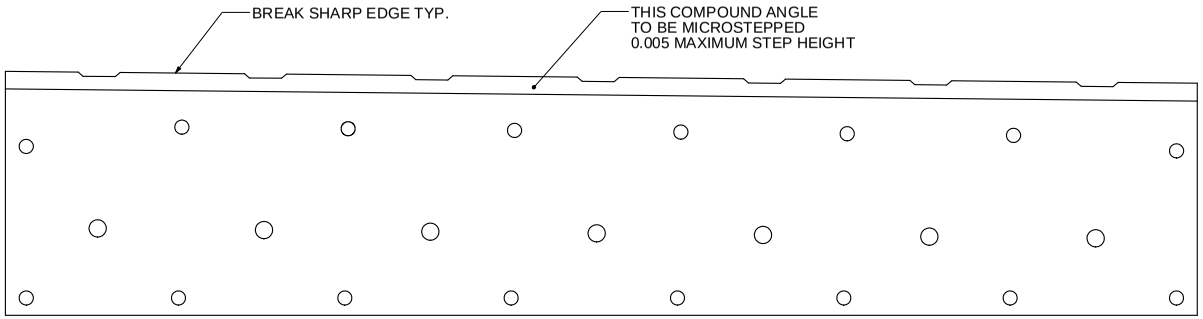

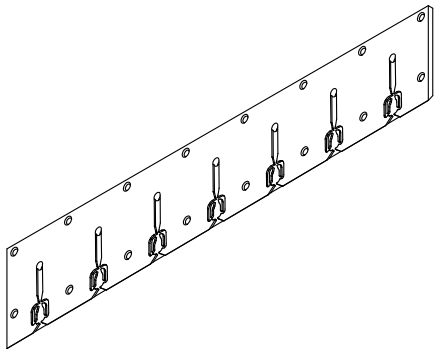

REV.	DESCRIPTION	DATE
A	INITIAL RELEASE	08/14/2012

Caltech
Emilio Graff
Lucas AWWT
ecg@caltech.edu
626 395 4795
M/C 205-45
1200 E. California Blvd.
Pasadena, CA 91125

DIMENSIONS IN INCHES [MM]
TOLERANCES
(EXCEPT AS NOTED)
DECIMAL:
.xx = ±.010
.xxx = ±.005
.xxxx = ±.001
ANGULAR: ±0.5°
TYP EDGE BREAK: .005-.015

PROJECT: TRAILING EDGE MODULES
DRAWING TITLE: THIRD MODULE INSERT, 30x60
MATERIAL: 6061
SHEET SIZE: B
FINISH: NONE
DRAWN BY: ECG
DATE: 08/14/2012
SHEET: 1 OF 1
DRAWING NUMBER: TEM-03-402-A

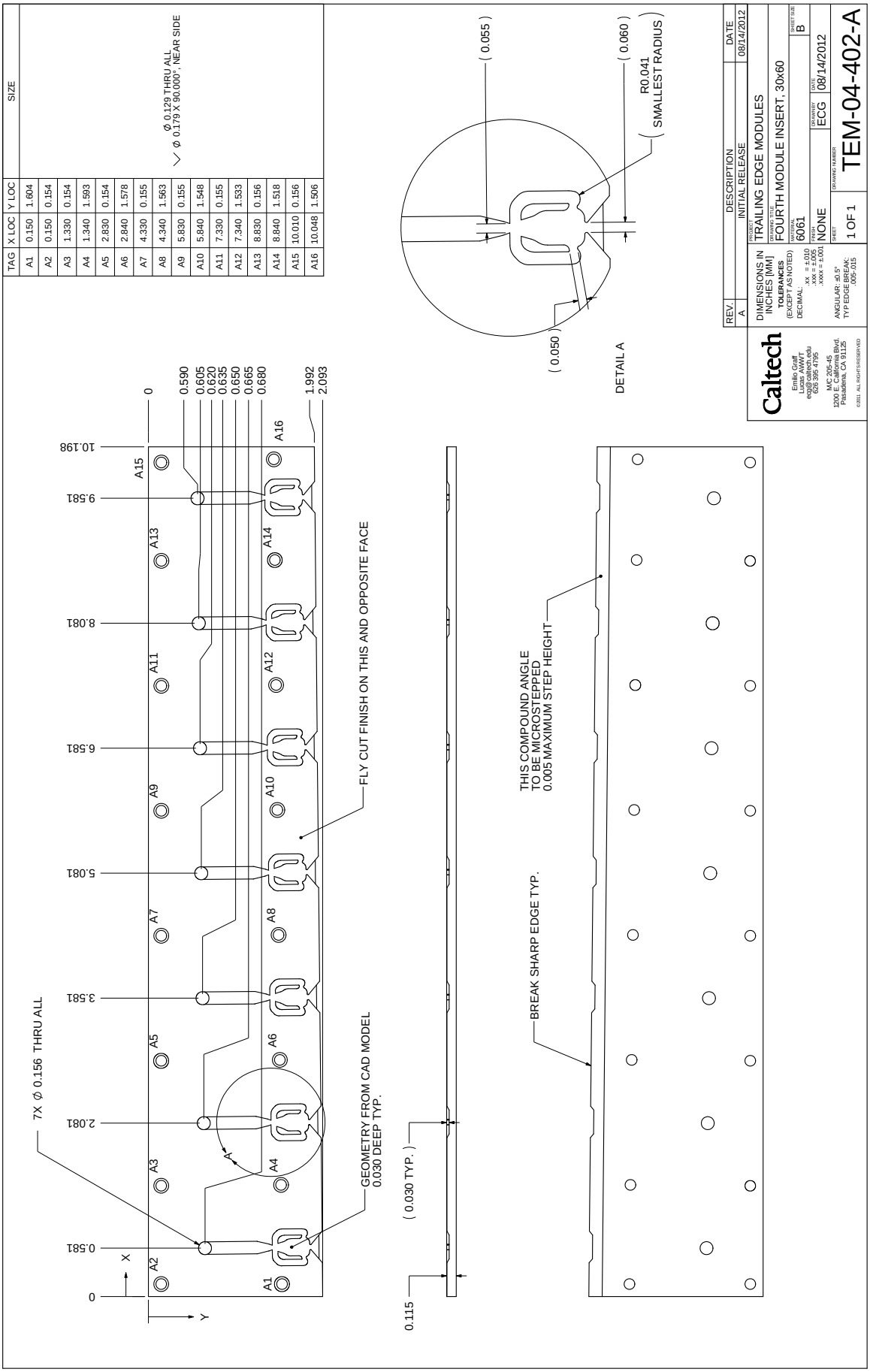
TAG | X LOC | Y LOC | SIZE
A1 | 0.150 | 1.604
A2 | 0.150 | 0.154
A3 | 1.330 | 0.154
A4 | 1.340 | 1.593
A5 | 2.830 | 0.154
A6 | 2.840 | 1.578
A7 | 4.330 | 0.155
A8 | 4.340 | 1.563
A9 | 5.830 | 0.155
A10 | 5.840 | 1.548
A11 | 7.330 | 0.155
A12 | 7.340 | 1.533
A13 | 8.830 | 0.156
A14 | 8.840 | 1.518
A15 | 10.010 | 0.156
A16 | 10.048 | 1.506
Ø 0.129 THRU ALL
⌵ Ø 0.179 X 90.000°, NEAR SIDE
7X Ø 0.156 THRU ALL
GEOMETRY FROM CAD MODEL
0.030 DEEP TYP.
FLY CUT FINISH ON THIS AND OPPOSITE FACE
(0.030 TYP.)
0.115
BREAK SHARP EDGE TYP.
THIS COMPOUND ANGLE
TO BE MICROSTEPPED
0.005 MAXIMUM STEP HEIGHT
DETAIL A
(0.055)
(0.060)
R0.041
(SMALLEST RADIUS)
(0.050)
REV. | DESCRIPTION | DATE
A | INITIAL RELEASE | 08/14/2012
Caltech
Emilio Graff
Lucas AWVI
egg@caltech.edu
626.395.4795
1200 E. California Blvd.
Pasadena, CA 91125
©2011 ALL RIGHTS RESERVED
DIMENSIONS IN INCHES [MM]
TOLERANCES
(EXCEPT AS NOTED)
DECIMAL:
XX. = ±.010
XXX. = ±.005
XXXX = ±.001
ANGULAR: ±0.5°
TYP EDGE BREAK:
.005-.015
PROJECT: TRAILING EDGE MODULES
DRAWING TITLE: FOURTH MODULE INSERT, 30x60
MATERIAL: 6061
FINISH: NONE
DRAWN BY: ECG
DATE: 08/14/2012
SHEET SIZE: B
SHEET: 1 OF 1
DRAWING NUMBER: TEM-04-402-A

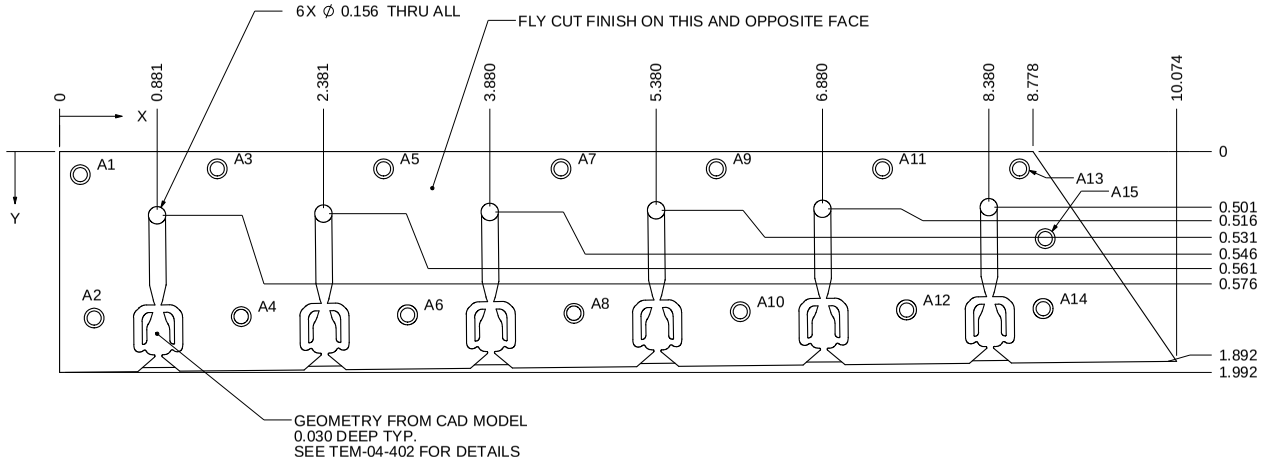

TAG	X LOC	Y LOC	SIZE
A1	0.187	0.209	∅ 0.129 THRU ALL ⌵ ∅ 0.179 X 90.000°, NEAR SIDE
A2	0.312	1.502	
A3	1.423	0.156	
A4	1.640	1.489	
A5	2.923	0.156	
A6	3.140	1.474	
A7	4.523	0.156	
A8	4.640	1.459	
A9	5.923	0.156	
A10	6.139	1.444	
A11	7.423	0.156	
A12	7.639	1.429	
A13	8.658	0.156	
A14	8.871	1.417	
A15	8.890	0.785	

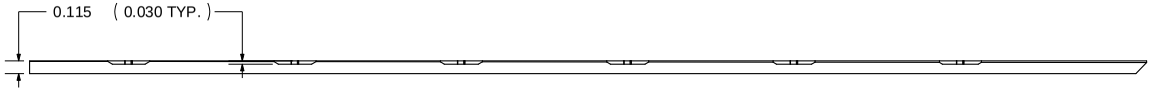

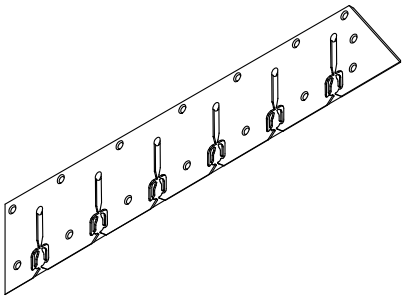

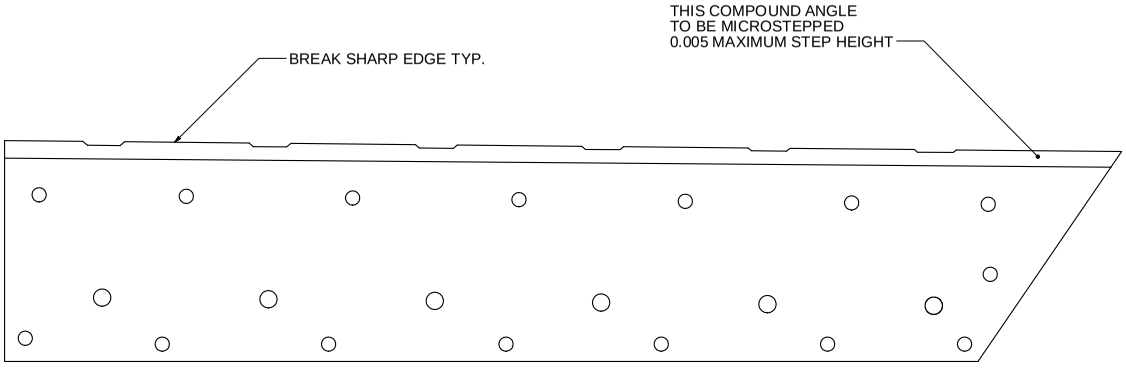

REV.	DESCRIPTION	DATE
A	INITIAL RELEASE	08/14/2012

Caltech
Emilio Graff
Lucas AWWT
ecg@caltech.edu
626 395 4795
M/C 205-45
1200 E. California Blvd.
Pasadena, CA 91125

DIMENSIONS IN INCHES [MM]
TOLERANCES (EXCEPT AS NOTED)
DECIMAL:
.xx = ±.010
.xxx = ±.005
.xxxx = ±.001
ANGULAR: ±0.5°
TYP EDGE BREAK: .005-.015

PROJECT: TRAILING EDGE MODULES
DRAWING TITLE: TIP MODULE INSERT, 30x60
MATERIAL: 6061
SHEET SIZE: B
FINISH: NONE
DRAWN BY: ECG
DATE: 08/14/2012
SHEET: 1 OF 1
DRAWING NUMBER: TEM-05-402-A

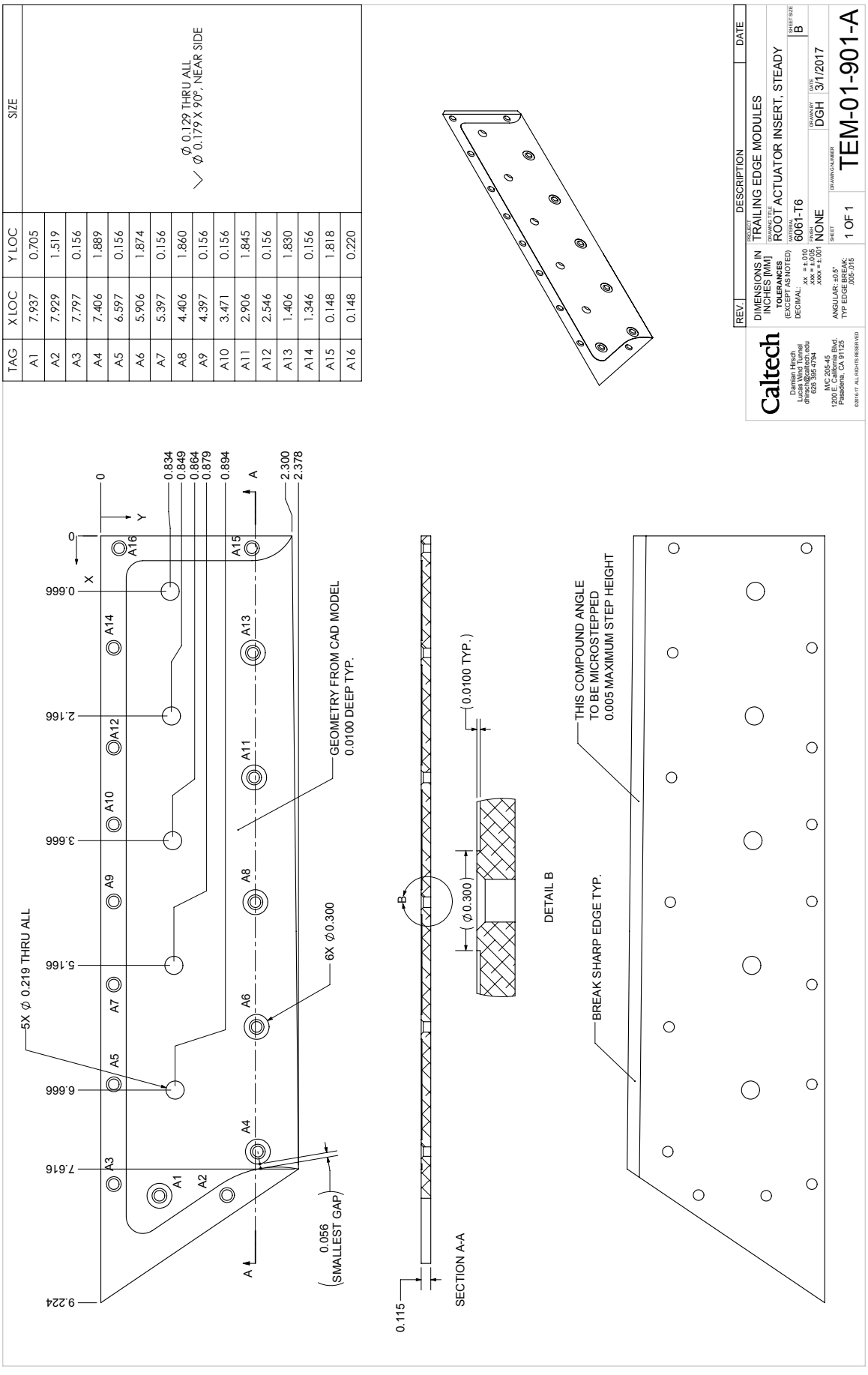
TAG | X LOC | Y LOC | SIZE
A1 | 7.937 | 0.705 | Ø 0.129 THRU ALL
A2 | 7.929 | 1.519 | Ø 0.179 X 90°, NEAR SIDE
A3 | 7.797 | 0.156
A4 | 7.406 | 1.889
A5 | 6.597 | 0.156
A6 | 5.906 | 1.874
A7 | 5.397 | 0.156
A8 | 4.406 | 1.860
A9 | 4.397 | 0.156
A10 | 3.471 | 0.156
A11 | 2.906 | 1.845
A12 | 2.546 | 0.156
A13 | 1.406 | 1.830
A14 | 1.346 | 0.156
A15 | 0.148 | 1.818
A16 | 0.148 | 0.220
5X Ø 0.219 THRU ALL
6X Ø0.300
GEOMETRY FROM CAD MODEL
0.0100 DEEP TYP.
0.056
(SMALLEST GAP)
0.115
SECTION A-A
(0.0100 TYP.)
(Ø0.300)
DETAIL B
THIS COMPOUND ANGLE
TO BE MICROSTEPPED
0.005 MAXIMUM STEP HEIGHT
BREAK SHARP EDGE TYP.
REV. | DESCRIPTION | DATE
DIMENSIONS IN INCHES [MM]
TOLERANCES (EXCEPT AS NOTED)
DECIMAL: XX = ±.010 XXX = ±.005 XXXX = ±.001
ANGULAR: ±0.5°
TYP EDGE BREAK: .005-.015
PROJECT: TRAILING EDGE MODULES
DRAWING TITLE: ROOT ACTUATOR INSERT, STEADY
MATERIAL: 6061-T6
FINISH: NONE
SHEET: 1 OF 1
DRAWING NUMBER: TEM-01-901-A
SHEET SIZE: B
DRAWN BY: DGH
DATE: 3/1/2017
Caltech
Damian Hinch
Lucas West Tunnel
dhinch@caltech.edu
626 395 4794
1200 E. California Blvd.
MC 205-45
Pasadena, CA 91125
©2016-17 ALL RIGHTS RESERVED

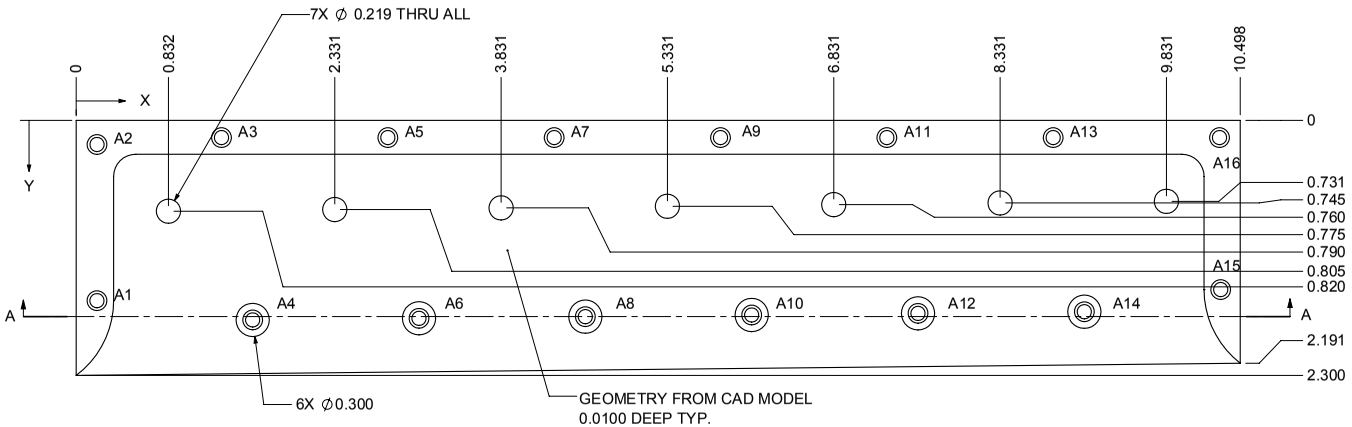

TAG	X LOC	Y LOC	SIZE
A1	0.187	1.627	∅ 0.129 THRU ALL ⌵ ∅ 0.179 X 90°, NEAR SIDE
A2	0.187	0.218	
A3	1.310	0.156	
A4	1.591	1.800	
A5	2.810	0.156	
A6	3.091	1.785	
A7	4.310	0.156	
A8	4.591	1.771	
A9	5.810	0.156	
A10	6.091	1.756	
A11	7.310	0.156	
A12	7.591	1.741	
A13	8.810	0.156	
A14	9.091	1.726	
A15	10.321	1.526	
A16	10.310	0.156	

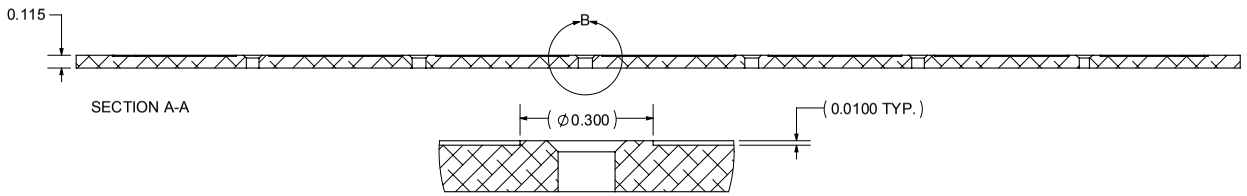

DETAIL B

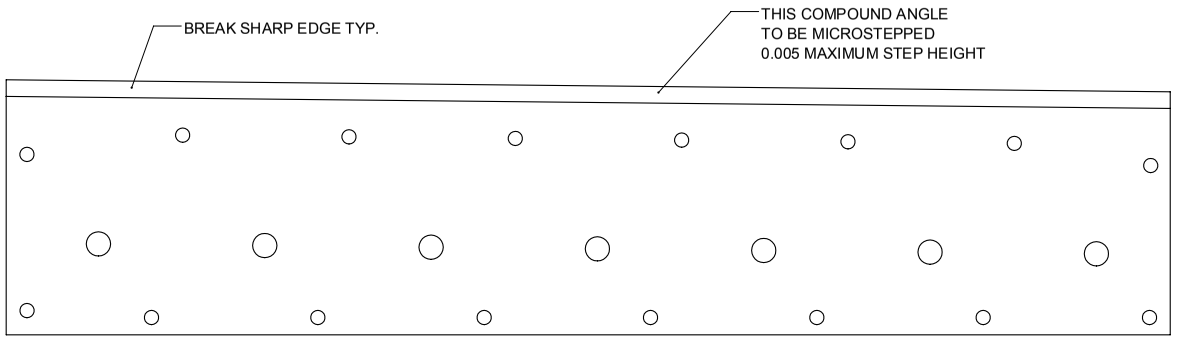

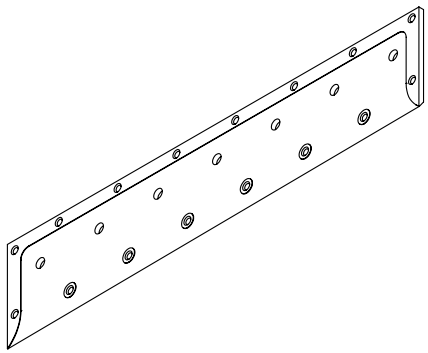

REV.	DESCRIPTION	DATE

Caltech
Damian Hirsch
Lucas Wind Tunnel
dhirsch@caltech.edu
626 395 4794
M/C 205-45
1200 E. California Blvd.
Pasadena, CA 91125

DIMENSIONS IN INCHES [MM]
TOLERANCES (EXCEPT AS NOTED)
DECIMAL:
.xx = ±.010
.xxx = ±.005
.xxxx = ±.001
ANGULAR: ±0.5°
TYP EDGE BREAK: .005-.015

PROJECT: TRAILING EDGE MODULES
DRAWING TITLE: SECOND ACTUATOR INSERT, STEADY
MATERIAL: 6061-T6
SHEET SIZE: B
FINISH: NONE
DRAWN BY: DGH
DATE: 3/1/2017
SHEET: 1 OF 1
DRAWING NUMBER: TEM-02-901-A

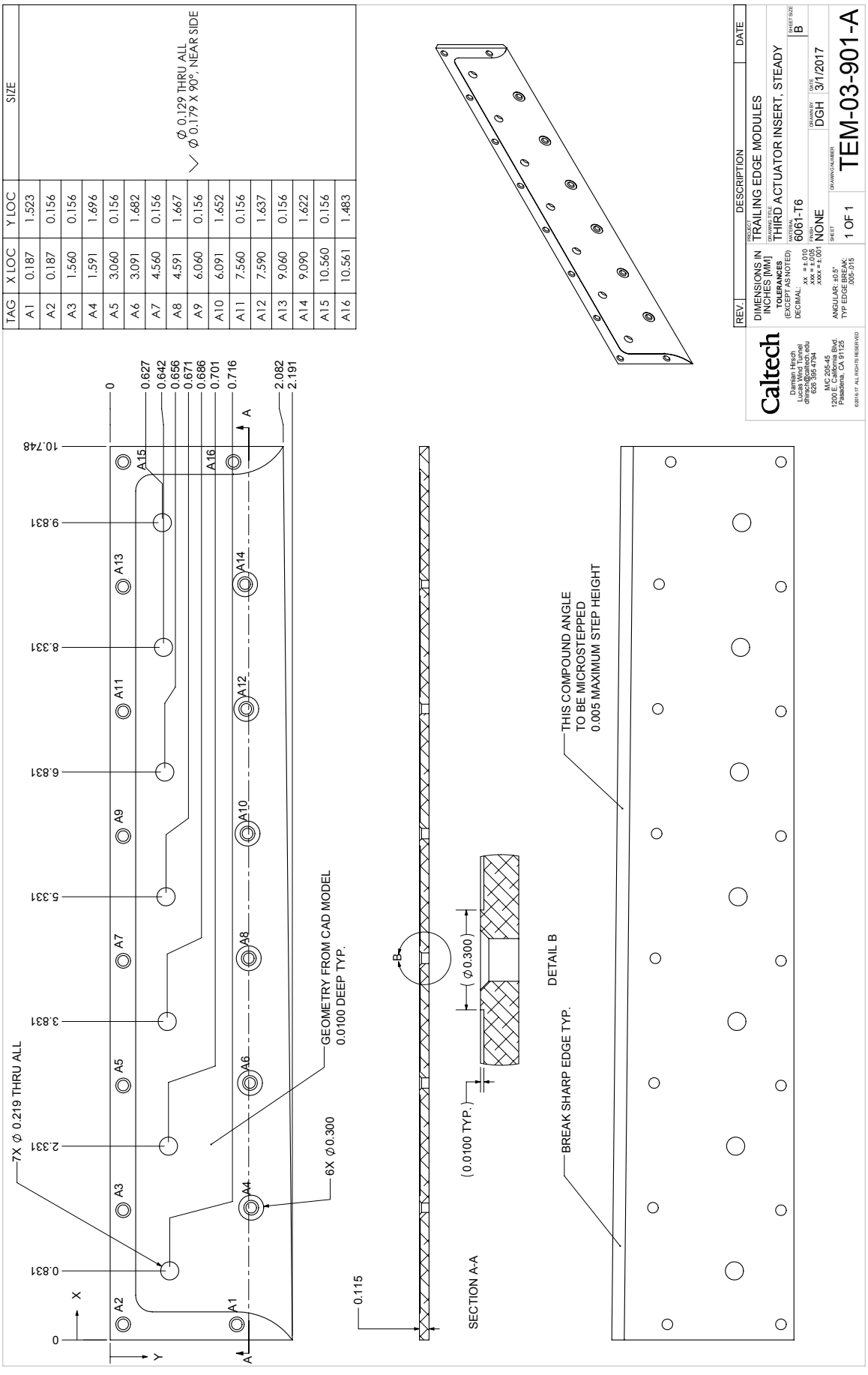
TAG | X LOC | Y LOC | SIZE
A1 | 0.187 | 1.523
A2 | 0.187 | 0.156
A3 | 1.560 | 0.156
A4 | 1.591 | 1.696
A5 | 3.060 | 0.156
A6 | 3.091 | 1.682
A7 | 4.560 | 0.156
A8 | 4.591 | 1.667
A9 | 6.060 | 0.156
A10 | 6.091 | 1.652
A11 | 7.560 | 0.156
A12 | 7.590 | 1.637
A13 | 9.060 | 0.156
A14 | 9.090 | 1.622
A15 | 10.560 | 0.156
A16 | 10.561 | 1.483
Ø 0.129 THRU ALL
Ø 0.179 X 90°, NEAR SIDE
7X Ø 0.219 THRU ALL
6X Ø0.300
GEOMETRY FROM CAD MODEL
0.0100 DEEP TYP.
0.115
(0.0100 TYP.)
(Ø0.300)
SECTION A-A
DETAIL B
THIS COMPOUND ANGLE
TO BE MICROSTEPPED
0.005 MAXIMUM STEP HEIGHT
BREAK SHARP EDGE TYP.
REV. | DESCRIPTION | DATE
DIMENSIONS IN INCHES [MM]
TOLERANCES (EXCEPT AS NOTED)
DECIMAL: XX = ± .010 XXX = ± .005 XXXX = ± .001
PROJECT: TRAILING EDGE MODULES
DRAWING TITLE: THIRD ACTUATOR INSERT, STEADY
MATERIAL: 6061-T6
FINISH: NONE
SHEET: 1 OF 1
SHEET SIZE: B
DRAWN BY: DGH
DATE: 3/1/2017
DRAWING NUMBER: TEM-03-901-A
ANGULAR: ±0.5°
TYP. EDGE BREAK: .005-.015
Caltech
Damian Hinsch
Lucas Wind Tunnel
dhinsch@caltech.edu
626 395 4794
1200 E. California Blvd.
MC 205-45
Pasadena, CA 91125
©2016-17 ALL RIGHTS RESERVED

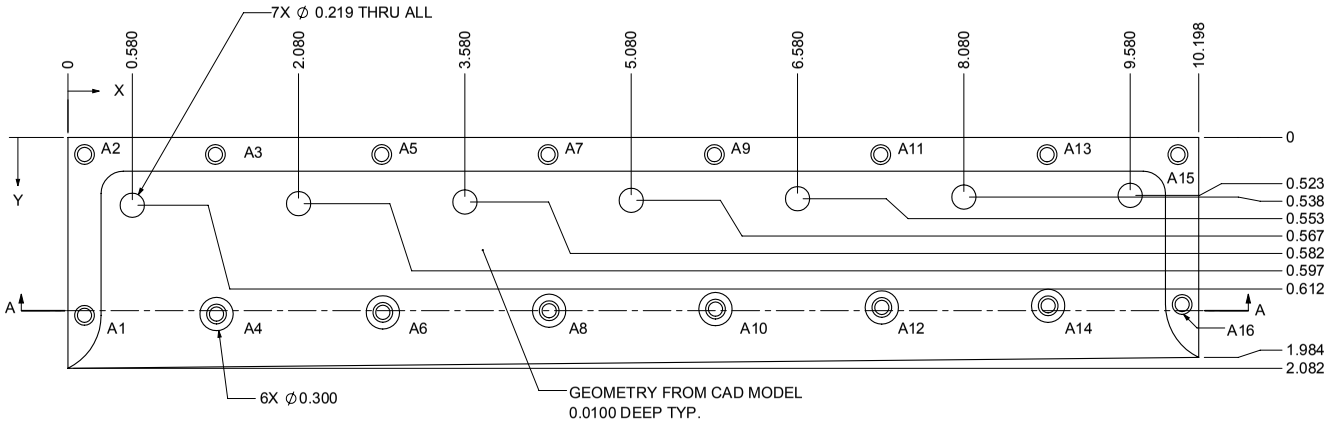

TAG	X LOC	Y LOC	SIZE
A1	0.150	1.604	∅ 0.129 THRU ALL ⌵ ∅ 0.179 X 90°, NEAR SIDE
A2	0.150	0.154	
A3	1.330	0.154	
A4	1.340	1.593	
A5	2.830	0.154	
A6	2.840	1.578	
A7	4.330	0.154	
A8	4.340	1.563	
A9	5.830	0.155	
A10	5.840	1.548	
A11	7.330	0.155	
A12	7.340	1.533	
A13	8.830	0.155	
A14	8.840	1.518	
A15	10.010	0.155	
A16	10.048	1.506	

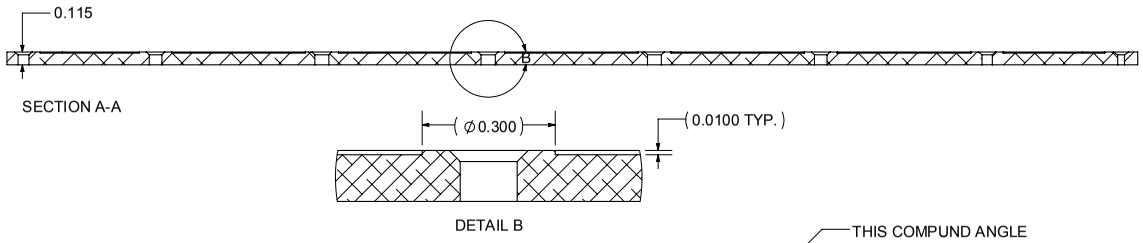

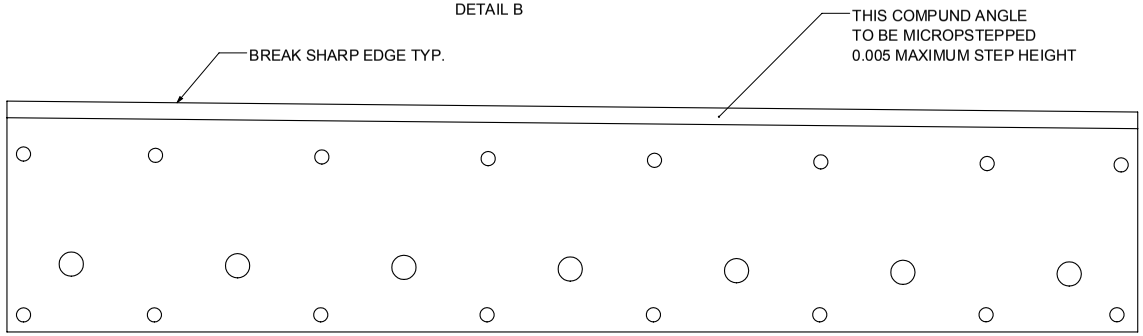

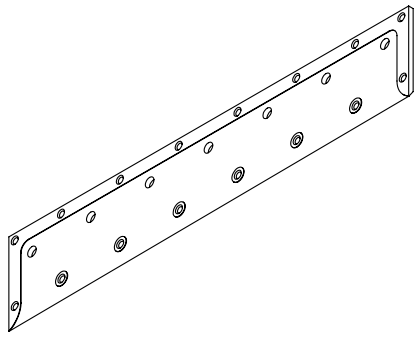

REV.	DESCRIPTION	DATE

Caltech
Damian Hirsch
Lucas Wind Tunnel
dhirsch@caltech.edu
626 395 4794
M/C 205-45
1200 E. California Blvd.
Pasadena, CA 91125

DIMENSIONS IN INCHES [MM]
TOLERANCES (EXCEPT AS NOTED)
DECIMAL:
.xx = ±.010
.xxx = ±.005
.xxxx = ±.001
ANGULAR: ±0.5°
TYP EDGE BREAK: .005-.015

PROJECT: TRAILING EDGE MODULES
DRAWING TITLE: FOURTH ACTUATOR INSERT, STEADY
MATERIAL: 6061-T6
SHEET SIZE: B
FINISH: NONE
DRAWN BY: DGH
DATE: 3/1/2017
SHEET: 1 OF 1
DRAWING NUMBER: TEM-04-901-A

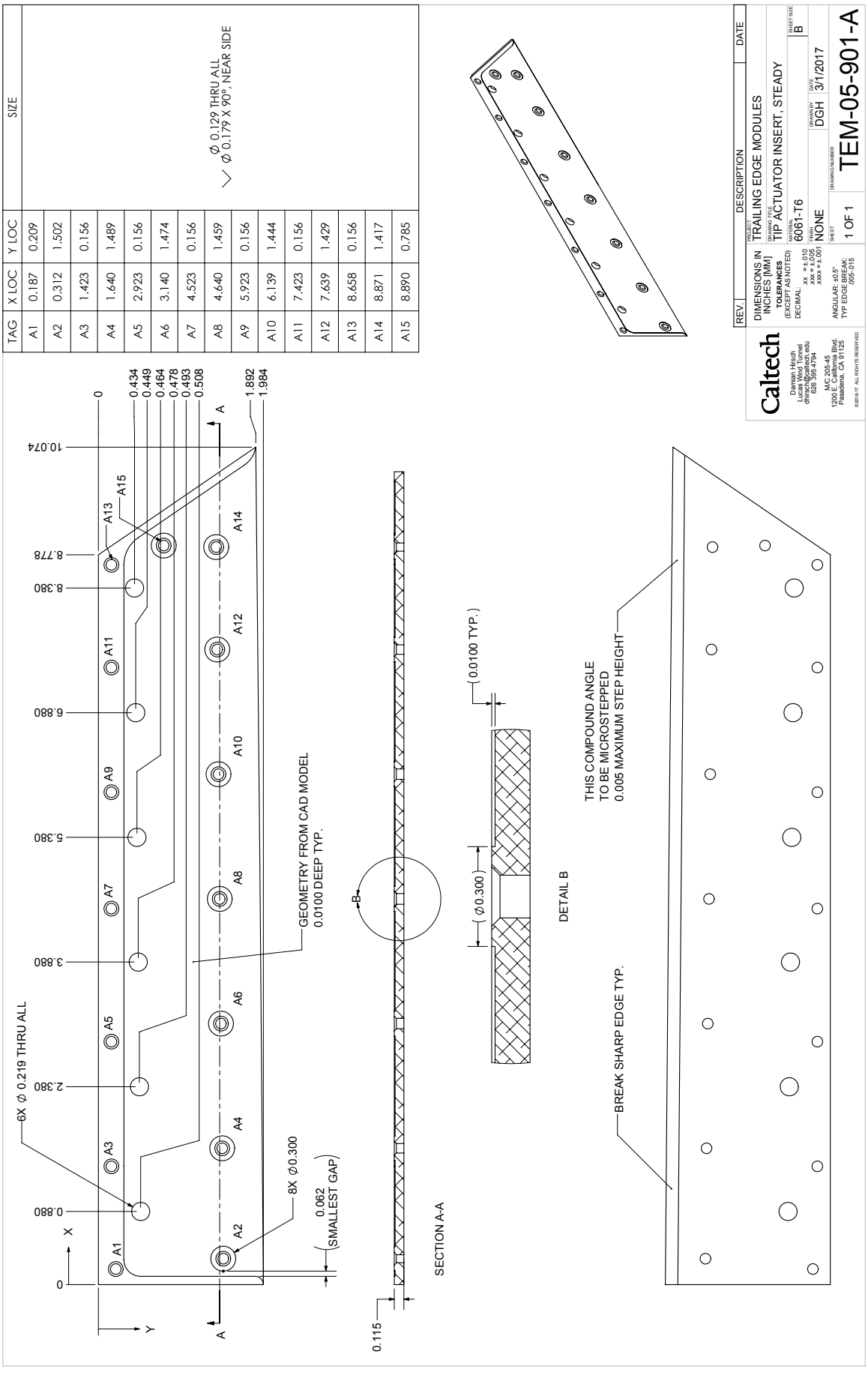
TAG | X LOC | Y LOC | SIZE
A1 | 0.187 | 0.209
A2 | 0.312 | 1.502
A3 | 1.423 | 0.156
A4 | 1.640 | 1.489
A5 | 2.923 | 0.156
A6 | 3.140 | 1.474
A7 | 4.523 | 0.156
A8 | 4.640 | 1.459
A9 | 5.923 | 0.156
A10 | 6.139 | 1.444
A11 | 7.423 | 0.156
A12 | 7.639 | 1.429
A13 | 8.658 | 0.156
A14 | 8.871 | 1.417
A15 | 8.890 | 0.785
Ø 0.129 THRU ALL
Ø 0.179 X 90°; NEAR SIDE
6X Ø 0.219 THRU ALL
8X Ø0.300
0.062
(SMALLEST GAP)
GEOMETRY FROM CAD MODEL
0.0100 DEEP TYP.
SECTION A-A
DETAIL B
(0.0100 TYP.)
(Ø0.300)
THIS COMPOUND ANGLE
TO BE MICROSTEPPED
0.005 MAXIMUM STEP HEIGHT
BREAK SHARP EDGE TYP.
REV. | DESCRIPTION | DATE
DIMENSIONS IN INCHES [MM]
TOLERANCES
(EXCEPT AS NOTED)
DECIMAL:
xx. = ±.010
xxx. = ±.005
xxxx = ±.001
ANGULAR: ±0.5°
TYP. EDGE BREAK:
.005-.015
PROJECT
TRAILING EDGE MODULES
DRAWING TITLE
TIP ACTUATOR INSERT, STEADY
MATERIAL
6061-T6
FINISH
NONE
SHEET
1 OF 1
DRAWN BY
DGH
DATE
3/1/2017
SHEET SIZE
B
DRAWING NUMBER
TEM-05-901-A
Caltech
Damian Hinch
Lucas Wind Tunnel
dhinch@caltech.edu
626 395 4794
1200 E. California Blvd.
MC 205-45
Pasadena, CA 91125
©2016-17 ALL RIGHTS RESERVED

Bibliography

Adrian, R. (2005). "Twenty Years of Particle Image Velocimetry". *Experiments in Fluids*, Vol. 39, No. 2, pp. 159–169.

Altman, J. and Hayter, N.-L. (1951). *A Comparison of the Turbulent Boundary-layer Growth on an Unswept and a Swept Wing*. Tech. rep. DTIC Document.

Anders, S., Sellers III, W., and Washburn, A. (2004). "Active Flow Control Activities at NASA Langley". *2nd AIAA Flow Control Conference*, p. 2623.

Andino, M., Lin, J., Washburn, A., Whalen, E., Graff, E., and Wygnanski, I. (2015). "Flow Separation Control on a Full-Scale Vertical Tail Model Using Sweeping Jet Actuators". *53rd AIAA Aerospace Sciences Meeting*, p. 0785.

Attinello, J. (1961). "Design and Engineering Features of Flap Blowing Installations". *Boundary Layer and Flow Control: Its Principles and Application*. Ed. by G. V. Lachmann. Vol. 1. Pergamon Press, pp. 463–515.

Bailey, S. (1980). "Tradeoffs Complicate Decisions in Selecting Flowmeters". *Control Engineering*, Vol. 27, No. 4, pp. 75–79.

Barlow, J., Rae, W., and Pope, A. (1999). *Low-Speed Wind Tunnel Testing*. 3rd ed. John Wiley & Sons.

Bauer, M., Grund, T., and Nitsche, W. (2014). "Experiments on Active Drag Reduction on a Complex Outer Wing Model". *AIAA Journal*, Vol. 53, No. 7, pp. 1774–1783.

Bertin, J. (2002). *Aerodynamics for Engineers*. 4th ed. Prentice Hall, NJ.

Bezos-O'Connor, G., Mangelsdorf, M., Nickol, C., Maliska, H., Washburn, A., and Wahls, R. (2011). "Fuel Efficiencies Through Airframe Improvements". *3rd AIAA Atmospheric Space Environments Conference*, p. 3530.

Blevins, R. (1984). *Applied Fluid Dynamics Handbook*. Vol. 1. Van Nostrand Reinhold Company.

Bobusch, B., Woszidlo, R., Bergada, J., Nayeri, C., and Paschereit, C. (2013). "Experimental study of the internal flow structures inside a fluidic oscillator". *Experiments in fluids*, Vol. 54, No. 6, p. 1559.

Bright, M., Korntheuer, A., Komadina, S., and Lin, J. (2013). "Development of Advanced High Lift Leading Edge Technology for Laminar Flow Wings". *51st AIAA Aerospace Sciences Meeting including the New Horizons Forum and Aerospace Exposition*, p. 211.

Busemann, A. (1935). "Aerodynamischer Auftrieb bei Überschallgeschwindigkeit". *Luftfahrtforschung*, Vol. 12, No. 6, pp. 210–220.

Campagnuolo, C. and Lee, H. (1969). *Review of Some Fluidic Oscillators*. Tech. rep. Harry Diamond Laboratories.

Canny, J. (1986). "A Computational approach to Edge Detection". *IEEE Transactions on pattern analysis and machine intelligence*, Vol. PAMI-8, No. 6, pp. 679–698.

Cattafesta III, L. and Sheplak, M. (2011). "Actuators for Active Flow Control". *Annual Review of Fluid Mechanics*, Vol. 43, pp. 247–272.

Cerretelli, C., Gharaibah, E., Toplack, G., Gupta, A., and Wuerz, W. (2009). "Unsteady Separation Control for Wind Turbine Applications at Full Scale Reynolds Numbers". *47th AIAA Aerospace Sciences Meeting*, Vol. 380, p. 2009.

Cerretelli, C. and Kirtley, K. (2009). "Boundary Layer Separation Control with Fluidic Oscillators". *Journal of Turbomachinery*, Vol. 131, No. 4, p. 041001.

Chaplin, H. (1956). *Preliminary Investigation of a Jet-Flap Wing Configuration*. David W. Taylor Model Basin Aero Rep.

Chen, C., Seele, R., and Wygnanski, I. (2012). "Separation and Circulation Control on an Elliptical Airfoil by Steady Blowing". *AIAA Journal*, Vol. 50, No. 10, pp. 2235–2247.

Clemons, L. and Wlezien, R. (2016). "Unsteady Active Flow Control on the Leading Edge of a High-lift Configuration Thin Airfoil". *8th AIAA Flow Control Conference*, p. 3310.

Collier, F., Thomas, R., Burley, C., Nickol, C., Lee, C.-M., and Tong, M. (2010). "Environmentally Responsible Aviation – Real Solutions for Environmental Challenges Facing Aviation". *27th International Congress of the Aeronautical Sciences*.

Demauro, E., Dell'Orso, H., Sivaneri, V., Tuna, B., and Amitay, M. (2015). "Measurements of 3-D Stall Cells on 2-D Airfoil". *45th AIAA Fluid Dynamics Conference*, p. 2633.

Desalvo, M., Whalen, E., and Glezer, A. (2012). "High-Lift Enhancement Using Active Flow Control". *6th AIAA Flow Control Conference*, p. 3245.

Elsinga, G., Scarano, F., Wieneke, B., and Oudheusden, B. van (2006). "Tomographic Particle Image Velocimetry". *Experiments in Fluids*, Vol. 41, No. 6, pp. 933–947.

Flatt, J. (1961). "The History of Boundary Layer Control Research in the United States of America". *Boundary Layer and Flow Control: Its Principles and Application*. Ed. by G. V. Lachmann. Vol. 1. Pergamon Press, pp. 122–143.

Freeman, P. (1977). *High Gain Fluid Amplifier*. US Patent 4,000,757.

Gad-el-Hak, M. (2007). *Flow Control: Passive, Active, and Reactive Flow Management*. Cambridge University Press.

Gharib, M. and Kim, D. (2011). *Method to Generate Micro Scale Gas Filled Liquid Bubbles as Tracer Particles or Inhaler Mist for Drug Delivery*. US Patent App. 13/089,910.

Graff, E. and Gharib, M. (2008). "Performance Prediction of Point-Based Three-Dimensional Volumetric Measurement Systems". *Measurement Science and Technology*, Vol. 19, No. 7, p. 075403.

Graff, E. and Wygnanski, I. (2014). *Fluidic Fence for Performance Enhancement*. US Patent App. 14/242,809.

Graham, W. (2013). "Boeing/NASA Test Active Flow-Control Tail". *Aviation Week & Space Technology*.

Greenblatt, D. and Wygnanski, I. (2000). "The Control of Flow Separation by Periodic Excitation". *Progress in Aerospace Sciences*, Vol. 36, No. 7, pp. 487–545.

Gregory, J. and Tomac, M. (2013). "A Review of Fluidic Oscillator Development". *43rd AIAA Fluid Dynamics Conference*, p. 2474.

Guyot, D., Paschereit, C. O., and Raghu, S. (2009). "Active Combustion Control Using a Fluidic Oscillator for Asymmetric Fuel Flow Modulation". *International Journal of Flow Control*, Vol. 1, No. 2, pp. 155–166.

Hemsch, M. and Luckring, J. (1990). "Connection Between Leading-Edge Sweep, Vortex Lift, and Vortex Strength for Delta Wings". *Journal of Aircraft*, Vol. 27, No. 5, pp. 473–475.

Hirsch, D., Graff, E., Pereira, F., and Gharib, M. (2015a). "How Common Transparent Materials Can Affect Image-Based Velocimetry". *11th International Symposium on Particle Image Velocimetry - PIV15*.

Hirsch, D., Graff, E., Pereira, F., and Gharib, M. (2015b). "Influence of Common Transparent Materials on the Accuracy of Image-Based Velocimetry". *Measurement Science and Technology*, Vol. 26, No. 8, p. 087002.

Huerre, P. and Monkewitz, P. (1985). "Absolute and Convective Instabilities in Free Shear Layers". *Journal of Fluid Mechanics*, Vol. 159, pp. 151–168.

Jairam, A., Clemons, L., and Wlezien, R. (2016). "Active Separation Control on the Morphed Leading Edge of a Thin Airfoil in High-lift Configuration". *8th AIAA Flow Control Conference*, p. 3307.

Kelly, M. (1956). *Analysis of Some Parameters Used in Correlating Blowing-Type Boundary-Layer Control Data*. National Advisory Committee for Aeronautics.

Koklu, M. (2015). "The Effects of Sweeping Jet Actuator Parameters on Flow Separation Control". *45th AIAA Fluid Dynamics Conference*, p. 2485.

Lachmann, G. V., ed. (1961). *Boundary Layer and Flow Control: Its Principles and Application*. Vol. 1. Pergamon Press.

Lucas, N., Taubert, L., Woszidlo, R., Wygnanski, I., and McVeigh, M. (2008). "Discrete Sweeping Jets as Tools for Separation Control". *4th Flow Control Conference, Seattle, WA, AIAA*. Vol. 3868, pp. 23–26.

Maas, H.-G., Gruen, A., and Papantoniou, D. (1993). "Particle Tracking Velocimetry in Three-Dimensional Flows". *Experiments in Fluids*, Vol. 15, No. 2, pp. 133–146.

Newman, B. (1961). "The Deflexion of Plane Jets by Adjacent Boundaries – Coanda Effect". *Boundary Layer and Flow Control: Its Principles and Application*. Ed. by G. V. Lachmann. Vol. 1. Pergamon Press, pp. 232–264.

Norris, G. (2014). "Real Results". *Aviation Week & Space Technology*, Vol. 176, No. 3, pp. 44–45.

Norris, G. (2015). "757 EcoDemo Focuses On Laminar And Active Flow". *Aviation Week & Space Technology*.

Ostermann, F., Godbersen, P., Woszidlo, R., Nayeri, C., and Paschereit, C. (2016). *Sweeping Jet from a Fluidic Oscillator in Crossflow*. `https://doi.org/10.1103/APS.DFD.2016.GFM.V0076`.

Ostermann, F., Woszidlo, R., Nayeri, C. N., and Paschereit, C. O. (2015). "Phase-Averaging Methods for the Natural Flowfield of a Fluidic Oscillator". *AIAA Journal*, Vol. 53, No. 8, pp. 2359–2368.

Ostermann, F., Woszidlo, R., Nayeri, C., and Paschereit, C. (2016). "The Time-Resolved Flow Field of a Jet Emitted by a Fluidic Oscillator into a Crossflow". *54th AIAA Aerospace Sciences Meeting*, p. 0345.

Pereira, F. and Gharib, M. (2002). "Defocusing Digital Particle Image Velocimetry and the Three-Dimensional Characterization of Two-Phase Flows". *Measurement Science and Technology*, Vol. 13, No. 5, p. 683.

Pereira, F., Gharib, M., Dabiri, D., and Modarress, D. (2000). "Defocusing Digital Particle Image Velocimetry: A 3-Component 3-Dimensional DPIV Measurement Technique. Application to Bubbly Flows". *Experiments in Fluids*, Vol. 29, S078–S084.

Phillips, E., Woszidlo, R., and Wygnanski, I. (2010). "The Dynamics of Separation Control on a Rapidly Actuated Flap". *5th Flow Control Conference*, p. 4246.

Poisson-Quinton, P. (1948). "Recherches Théoriques et Expérimentales sur le Contrôle de Couche Limites". *VII International Congress of Applied Mechanics, London*.

Prandtl, L. (1904). "Über Flüssigkeitsbewegung bei sehr kleiner Reibung". *Third International Congress of Mathematicians*.

Prasad, A. and Adrian, R. (1993). "Stereoscopic Particle Image Velocimetry Applied to Liquid Flows". *Experiments in Fluids*, Vol. 15, No. 1, pp. 49–60.

Raghu, S. (2013a). "Fluidic Oscillators for Flow Control". *Experiments in Fluids*, Vol. 54, No. 2, p. 1455.

Raghu, S. (2013b). *Method and Apparatus for Aerodynamic Flow Control Using Compact High-Frequency Fluidic Actuator Arrays*. US Patent 8,382,043.

Raman, G., Hailye, M., and Rice, E. J. (1993). "Flip-Fop Jet Nozzle Extended to Supersonic Flows". *AIAA Journal*, Vol. 31, No. 6, pp. 1028–1035.

Raman, G. and Raghu, S. (2000). "Miniature Fluidic Oscillators for Flow and Noise Control – Transitioning from Macro to Micro Fluidics". *Fluids 2000 Conference and Exhibit*, p. 2554.

Raman, G. and Raghu, S. (2004). "Cavity Resonance Suppression Using Miniature Fluidic Oscillators". *AIAA Journal*, Vol. 42, No. 12, pp. 2608–2612.

Rathay, N., Boucher, M., Amitay, M., and Whalen, E. (2014). "Performance Enhancement of a Vertical Tail Using Synthetic Jet Actuators". *AIAA Journal*, Vol. 52, No. 4, pp. 810–820.

Saddoughi, S., Boespflug, M., and Donnelly, S. (2010). *Dual Bimorph Synthetic Pulsator*. US Patent 7,686,257.

Schlichting, H., Gersten, K., Krause, E., Oertel, H., and Mayes, K. (1960). *Boundary-Layer Theory*. Vol. 7. Springer.

Schmidt, H.-J., Woszidlo, R., Nayeri, C., and Paschereit, C. (2015). "Drag Reduction on a Rectangular Bluff Body with Base Flaps and Fluidic Oscillators". *Experiments in Fluids*, Vol. 56, No. 7, p. 151.

Schmidt, H.-J., Woszidlo, R., Nayeri, C., and Paschereit, C. (2016). "Fluidic Oscillators for Bluff Body Drag Reduction in Water". *54th AIAA Aerospace Sciences Meeting*, p. 0591.

Seele, R., Graff, E., Gharib, M., Taubert, L., Lin, J., and Wygnanski, I. (2012). "Improving Rudder Effectiveness with Sweeping Jet Actuators". *6th AIAA Flow Control Conference*, p. 3244.

Seele, R., Graff, E., Lin, J., and Wygnanski, I. (2013). "Performance Enhancement of a Vertical Tail Model with Sweeping Jet Actuators". *51st AIAA Aerospace Sciences Meeting including the New Horizons Forum and Aerospace Exposition*, p. 411.

Seele, R., Tewes, P., Woszidlo, R., McVeigh, M., Lucas, N., and Wygnanski, I. (2009). "Discrete Sweeping Jets as Tools for Improving the Performance of the V-22". *Journal of Aircraft*, Vol. 46, No. 6, pp. 2098–2106.

Seifert, A., Bachar, T., Koss, D., Shepshelovich, M., and Wygnanski, I. (1993). "Oscillatory Blowing: A Tool to Delay Boundary-Layer Separation". *AIAA Journal*, Vol. 31, No. 11, pp. 2052–2060.

Seifert, A., Bachar, T., Wygnanski, I., Kariv, A., Cohen, H., and Yoeli, R. (1999). "Application of Active Separation Control to a Small Unmanned Air Vehicle". *Journal of Aircraft*, Vol. 36, No. 2, pp. 474–477.

Seifert, A., Eliahu, S., Greenblatt, D., and Wygnanski, I. (1998). "Use of Piezoelectric Actuators for Airfoil Separation Control". *AIAA Journal*, Vol. 36, No. 8, pp. 1535–1537.

Seifert, A., Stalnov, O., Sperber, D., Arwatz, G., Palei, V., David, S., Dayan, I., and Fono, I. (2008). "Large Trucks Drag Reduction Using Active Flow Control". *46th AIAA Aerospace Sciences Meeting and Exhibit*, p. 743.

Settles, G. (2001). *Schlieren and Shadowgraph Techniques: Visualizing Phenomena in Transparent Media*. Springer Science & Business Media.

Sieber, M., Ostermann, F., Woszidlo, R., Oberleithner, K., and Paschereit, C. (2016). "Lagrangian Coherent Structures in the Flow Field of a Fluidic Oscillator". *Physical Review Fluids*, Vol. 1, No. 5, p. 050509.

Soloff, S., Adrian, R., and Liu, Z.-C. (1997). "Distortion Compensation for Generalized Stereoscopic Particle Image Velocimetry". *Measurement Science and Technology*, Vol. 8, No. 12, p. 1441.

Spyropoulos, C. (1964). *A Sonic Oscillator*. Tech. rep. Harry Diamond Laboratories.

Stephenson, D. (2013). "A Tail of Innovation". *Boeing: Feature Story*.

Stouffer, R. and Bower, R. (1998). *Fluidic Flow Meter with Fiber Optic Sensor*. US Patent 5,827,976.

Tam, C. and Seiner, J. (1987). "Analysis of Twin Supersonic Plume Resonance". *11th Aeroacoustics Conference*, p. 2695.

Tewes, P. (2015). "Application of Active Flow Control to a Finite Swept Wing". PhD thesis. Technische Universität Berlin.

Tewes, P., Taubert, L., and Wygnanski, I. (2010). "On the Use of Sweeping Jets to Augment the Lift of a Lambda-Wing". *28th AIAA Applied Aerodynamics Conference*, p. 4689.

Tewes, P., Taubert, L., and Wygnanski, I. (2014). "On the Effect of Sweep on Separation Control". *7th AIAA Flow Control Conference*, p. 2513.

Tolhurst, W. (1958). *Full-Scale Wind-tunnel Tests of a 35° Sweptback-Wing Airplane with Blowing from the Shroud Ahead of the Trailing-Edge Flaps*. National Advisory Committee for Aeronautics.

Tsai, R. (1986). "An Efficient and Accurate Camera Calibration Technique for 3D Machine Vision". *Proc. IEEE Conf. on Computer Vision and Pattern Recognition*.

Vatsa, V., Koklu, M., and Wygnanski, I. (2012). "Numerical Simulation of Fluidic Actuators for Flow Control Applications". *6th AIAA Flow Control Conference*, p. 3239.

Viets, H. (1975). "Flip-Flop Jet Nozzle". *AIAA Journal*, Vol. 13, No. 10, pp. 1375–1379.

Warwick, G. (2013). "Trick of the Tail". *Aviation Week & Space Technology*, Vol. 175, No. 13, p. 14.

Whalen, E. A., Lacy, D. S., Lin, J. C., Andino, M. Y., Washburn, A. E., Graff, E. C., and Wygnanski, I. J. (2015). "Performance Enhancement of a Full-Scale Vertical Tail Model Equipped with Active Flow Control". *53rd AIAA Aerospace Sciences Meeting*, p. 0784.

Willert, C. and Gharib, M. (1991). "Digital Particle Image Velocimetry". *Experiments in Fluids*, Vol. 10, No. 4, pp. 181–193.

Willert, C. and Gharib, M. (1992). "Three-Dimensional Particle Imaging with a Single Camera". *Experiments in Fluids*, Vol. 12, No. 6, pp. 353–358.

Woszidlo, R. (2011). "Parameters Governing Separation Control with Sweeping Jet Actuators". PhD thesis. University of Arizona.

Woszidlo, R., Nawroth, H., Raghu, S., and Wygnanski, I. (2010). "Parametric Study of Sweeping Jet Actuators for Separation Control". *AIAA 5th Flow Control Conference*. Vol. 28.

Woszidlo, R., Ostermann, F., Nayeri, C., and Paschereit, C. (2015). "The Time-Resolved Natural Flow Field of a Fluidic Oscillator". *Experiments in Fluids*, Vol. 56, No. 6, p. 125.

Woszidlo, R. and Wygnanski, I. (2011). "Parameters Governing Separation Control with Sweeping Jet Actuators". *29th AIAA Applied Aerodynamics Conference*, p. 3172.

Wygnanski, I., Tewes, P., Kurz, H., Taubert, L., and Chen, C. (2011). "The Application of Boundary Layer Independence Principle to Three-Dimensional Turbulent Mixing Layers". *Journal of Fluid Mechanics*, Vol. 675, pp. 336–346.

Wygnanski, I., Tewes, P., and Taubert, L. (2014). "Applying the Boundary-Layer Independence Principle to Turbulent Flows". *Journal of Aircraft*, Vol. 51, No. 1, pp. 175–182.

Zemtseff, K. and Jensen, B. (2015). "Smaller Tails, Big Breakthroughs". *Boeing: Environment Feature Stories*.